Millimeter-Wave Interferometric Study of Nearby Starburst Galaxies

Satoki MATSUSHITA

Doctor of Science

Department of Astronomical Science
School of Mathematical and Physical Science
The Graduate University for Advanced Studies

1999 (School Year)

Contents

Abstract

In this thesis, we studied about the evolution of starburst from the viewpoint of molecular gas in galaxies.

For the study of the evolution using molecular gas, it is important to know its physical conditions. We first find out a good tracer for estimating the molecular gas temperature using J = 1 – 0 lines, which are observable with millimeter arrays; the HCN(1 – 0)/^{13}CO(1 – 0) intensity ratio tend to show high value ($\gtrsim$ 1) when the molecular gas is dense ($n(H_2) \gtrsim 10^4$ cm^{-3}) and warm ($T_k \gtrsim$ 100 K). The mechanism of this ratio can be explained as follows; HCN(1 – 0) emission is optically thick even at high temperature, but ^{13}CO(1 – 0) emission becomes optically thin when the temperature gets higher. Hence, at high-density and high-temperature region, HCN/^{13}CO ratio tend to have higher value. Indeed, the HCN/^{13}CO ratios are related with other temperature indicators; the physical conditions of molecular gas derived from the HCN/^{13}CO ratios in galaxies are consistent with those derived from high-J molecular lines. The HCN/^{13}CO ratios also have good correlation with the existence of warm ($\sim$ 100 K) dust, and have loose or no correlation with that of cold dust. These observational results support that the HCN/^{13}CO ratio might be a good tracer for molecular gas temperature.

Our statistical study of starburst and non-starburst galaxies shows that the starburst galaxies tend to have higher HCN/^{13}CO ratios than those of the non-starburst galaxies. These starburst galaxies also tend to have higher HCN/^{12}CO and ^{12}CO/^{13}CO ratios. We searched such high intensity ratio objects in Our Galaxy from published data, and show that molecular gas related to shocked regions such as outflows from star forming dense cores or supernova remnants have high ratios. This result indicates that shocked molecular gas is the dominant source of the high intensity ratios that can be seen in the starburst regions. Take their energetics, lifetimes, effecting areas, and numbers into consideration, we concluded that supernova explosions are the most effective heating source in galaxies.

Interferometric ^{13}CO(1 – 0) and 110 GHz continuum observations were carried out toward the prototypical starburst galaxy NGC 253, the starburst galaxy NGC 3504, and the post-starburst galaxy NGC 4736 with Nobeyama Millimeter Array (NMA). Spectrum energy distributions in the starburst galaxies including our 110 GHz continuum emission data are dominated by free-free emission, and the star formation efficiency (SFE) derived from this emission and that from extinction corrected Hα luminosity show good correspondence. HCN(1 – 0)/^{12}CO(1 – 0) intensity ratios (the ratio of the dense gas amount to the total molecular gas amount) and SFEs show good correlation, which support the previously published results that the dense molecular gas is needed for the star formation.

We also observed the prototypical starburst galaxy M82 in detail with NMA, and succeeded to image a few hundred parsec scale outflowing molecular gas (spurs) and an

expanding superbubble for the first time. The features of the spurs are quite similar to the optical dark filaments (dust filaments), which indicates that molecular gas and dust are settled in the similar regions. The superbubble is located $\sim$ 140 pc westward from the nucleus of M82 with its diameter of 210 $\times$ 140 pc in north-south and east-west direction. The energy of the superbubble is about 10^{55} erg, which corresponds to $\sim 10^4$ supernovae. Molecular gas related with the superbubble is offset from rigid rotation, and ionized gas also shows similar kinematics but have much higher velocity. Kinematics of H_2O and OH masers also show similar features, which indicate that molecular gas has undergone strong shock which maybe produced by the interaction with ionized gas and/or by induced star formations. The center of the superbubble is deficient in molecular gas, which means that no more star formation would occur at there. On the other hand, the surrounding regions are rich in molecular gas and show strong free-free emission, suggesting that new starburst might be occurred. From these results, we proposed a new mechanism of continuation and termination of starburst that strong starburst can blow out almost all the molecular gas in and around the starburst region and force to stop the ongoing star formations, but its strong expansion would compress the surrounding molecular gas and make new star forming regions.

Near the center of the superbubble, there are a 2.2 μm secondary peak which cluster is dominated by luminous supergiants, and a X-ray peak which may be radiated from a middle mass ($\sim 10^3 - 10^4$ $M_\odot$) black hole, based on the published positions. The stellar contents, mass, and evolution of the star cluster at 2.2 μm secondary peak based on initial mass function (IMF) suggest that massive stars which have already exploded can explain the energy of the superbubble. In this stellar cluster, it is possible to merge stars to several hundred solar mass with runaway merger within the similar timescale of the superbubble, and it can be a middle mass black hole after an hypernova. Also, the mass of their compact remnants (stellar black holes) are enough higher than that of the middle mass black hole, so that if some of the stellar black holes can merge into one black hole, it would be a middle mass black hole. These results indicate that an intense starburst is possible to make a middle mass black hole, and give a new explanation of the formation of AGN and/or quasars.

SFEs estimated from free-free continuum emission and HCN/^{13}CO ratios in M82 show high values similar to other starburst galaxies, but HCN/^{12}CO ratios show lower values similar to post-starburst galaxies. This result strongly suggests that M82 is in the very late phase of starburst or in the very early phase of post-starburst. Other literatures based on optical and infrared observations also suggest the similar result.

Comparison between published starburst epoch estimated from optical/infrared data and the change in the HCN/^{12}CO, HCN/^{13}CO, and ^{12}CO/^{13}CO intensity ratios, we proposed the evolution of intensity ratios, which corresponds to the evolution of the physical conditions of molecular gas, in accordance with the evolution of starburst. First, the density of molecular gas gets high by the gravitational instability. According to the increment of molecular density, the star formation might occur, and the resultant supernova explosions heat the surrounding gas. The continuance of star formation and the successive supernovae might decrease the dense gas. Even all the dense gas would exhaust or blown out, however, there might still exist the massive stars and therefore the supernova explosions for a short time ($\sim 10^6 - 10^7$ yr), so the temperature of molecular gas might still high. Therefore, there might be a time offset between the changes in molecular gas density and temperature. After the death of the heating sources, molecular

gas might cool down, and finally diffuse and cool molecular gas might mainly remain.

Chapter 1

General Introduction

Gas, especially molecular gas, is very important matter for the universe, because all of the stars are formed from molecular gas. Therefore, studies about molecular gas might give important information for the formation and evolution of stars, galaxies, and much larger structures. In this thesis, we studied the evolution of starburst in galaxies based on the physical conditions of molecular gas. The importance of starburst and physical conditions of molecular gas are described as follows.

1.1 Starburst Galaxy

Galaxies are usually consist of $10^9 - 10^{11}$ stars, so that star formation is one of the most important event in galaxy formation and/or evolution. In large-scale ($\sim 10^2 - 10^3$ pc scale) star formation event in a galaxy, there exist very important phenomenon, so-called "starburst". In starburst phase, enormous stars, especially massive stars, are formed at the starburst region within very short-timescale ($\sim 10^6 - 10^7$ yr; e.g. Rieke et al. 1980), and the galaxy to be very luminous in various wavelength. The successive supernova explosions disturb the surrounding regions, and spread heavy elements to these areas. The energy of vast amount of supernova explosions tend to escape perpendicular to the galactic disk and make large-scale outflows (Tomisaka & Ikeuchi 1988) which even reach to kpc-scale (Lehnert & Heckman 1996). Such large-scale outflows can pollute with heavy elements not only the starburst galaxy itself, but also its galactic halo or even intergalactic medium. Recent high-z observations indicate that galaxies with z> 4 ($t \lesssim 10^9$ yr) are already chemically polluted by heavy elements, which means that short-timescale extensive starbursts were occurred at the very early phase of galaxy formation (e.g. Hamann & Ferland 1999, Dietrich et al. 1999). These observations support that the starburst phenomenon is very important also in the early universe.

The definition of "starburst" is still under discussion, but mainly there are two. One is that a galaxy in which stars are forming intensively at higher star formation rate (SFR) than that averaged over the lifetime of the galaxy (Weedman 1987). Another is that a galaxy whose SFR per unit molecular gas mass available for star formation, or in other words, star formation efficiency (SFE), is high (Young 1987). The former definition might depend on the area and/or activity of star forming region and/or the amount of molecular gas, but the latter one would not depend on these parameters and defines the quality of molecular gas. Indeed, starburst galaxies defined by the near-infrared aperture photometry have high SFRs (Devereux 1989), but show wide range of SFEs (Young &

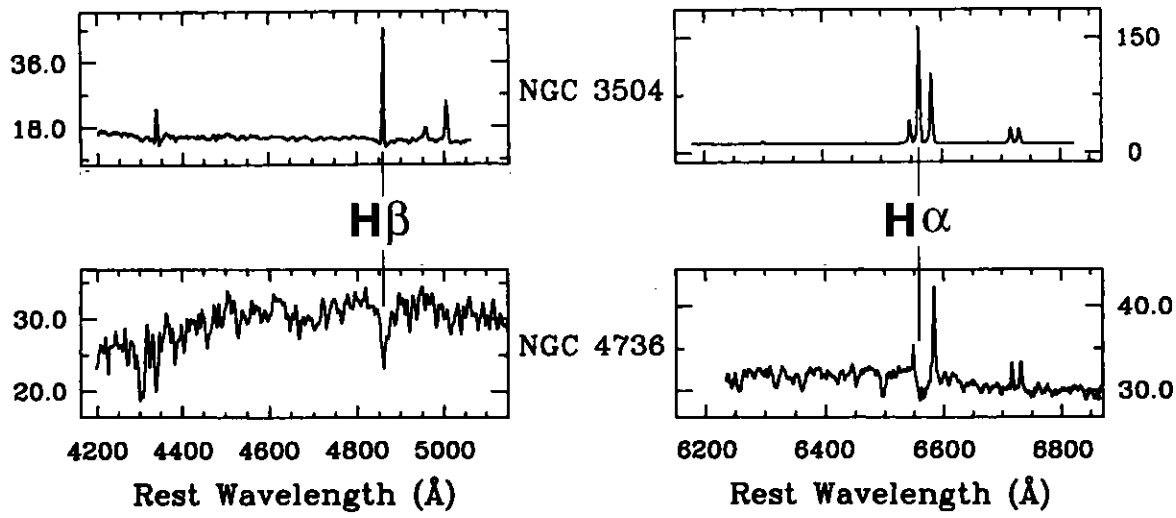

Fig. 1.1: Comparison of optical spectra between a starburst galaxy (NGC 3504; top) and a post-starburst galaxy (NGC 4736; bottom). There are large differences in the strength of Balmer lines (Hα and Hβ lines) that starburst galaxy shows strong emission features, but post-starburst galaxy displays strong absorption features. These spectra are taken from Ho, Filippenko, & Sargent (1995).

Devereux 1991). A dense molecular gas study of high SFR and low SFE galaxy NGC 4527 shows a small amount of dense molecular gas compared with total gas amount, which is similar to those of normal galaxies (Shibatsuka et al. 2000), implies that this galaxy is not a starburst galaxy from the standpoint of molecular gas study. We therefore define the "starburst" in accordance to Young (1987) that an object with high SFE.

A proposition of a burst of star formation or "starburst" at a first time was to explain the low mass-luminosity (M/L) ratio and high infrared luminosity of galaxies such as "prototypical starburst galaxy" M82 and NGC 253 (Rieke & Lebofsky 1979 and references therein). Star formation is tend to form a larger number of lower mass stars than higher mass stars, which might be according to the initial mass function (IMF; Miller & Scalo 1979) of

$$\frac{dN(m)}{dm} \propto m^{-\alpha} \tag{1.1}$$

with the normalization formula of

$$\int_{m_l}^{m_u} dN(m) = 1 \tag{1.2}$$

where N is the number of stars, m stellar mass, α the slope of IMF which has 2.35 at solar neighborhood (Salpeter 1955), and m_u and m_l are upper and lower mass cutoffs, respectively. In the starburst region, lower mass cutoff of $> 1M_\odot$ is needed for the explanation of the low M/L, which implies that starburst galaxies tend to form more massive stars than normal galaxies (e.g. Rieke et al. 1980, Goldader et al. 1997). The timescale of starburst is in the range of $\sim 10^7 - 10^9$ yr, much shorter than the lifetime of galaxies (e.g. Rieke et al. 1980, Goldader et al. 1997).

This short timescale leads to the evolution of a starburst. At the beginning of a starburst, the equivalent width of the Brackett γ line shows a large value because of a large amount of ionized source ($\approx$ OB stars). The lifetime of such massive stars (OB stars) is at most $\sim 10^7 - 10^8$ yr, so that burned out of these stars is almost corresponds to

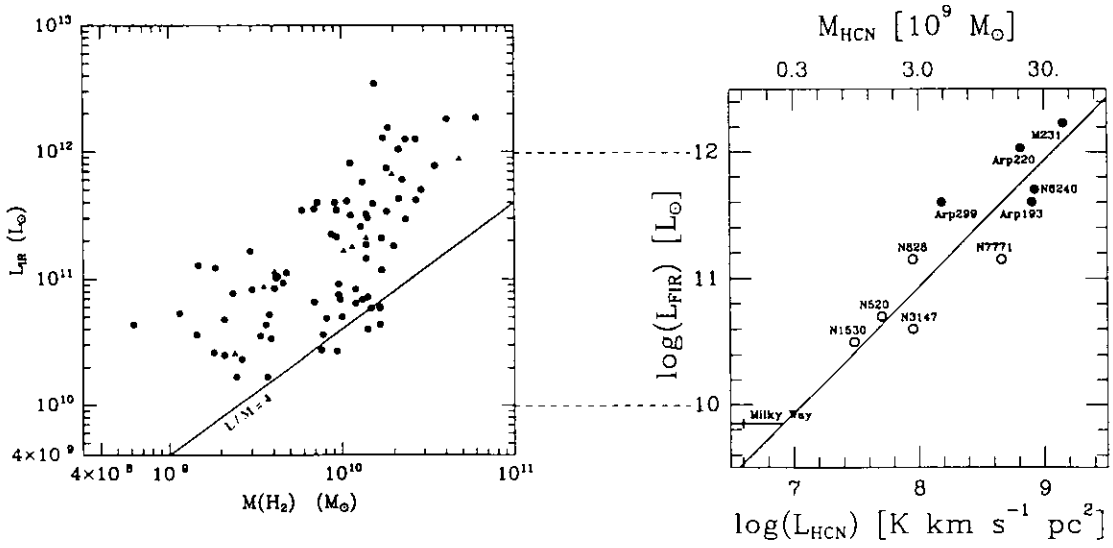

Fig. 1.2: Comparison of correlation diagrams between molecular gas mass derived from ^{12}CO(1 – 0) luminosity and infrared luminosity (left; Sanders, Scoville, & Soifer 1991) and HCN(1 – 0) and infrared luminosity (right; Solomon, Downes, & Radford 1992). HCN luminosity is much tightly correlated with infrared luminosity, which means that HCN (dense gas) emission is much closely related with star formation than ^{12}CO (diffuse gas) emission.

the end of starburst. According to this sequence, the equivalent width of Brackett γ line might decrease. The CO absorption line, which implies the existence of supergiants (late phase of OB stars) might increase at the middle phase of starburst ($\sim 10^6 - 10^7$ yr) but decrease in accordance with the decrement of the number of high mass stars. Molecular hydrogen or Fe II lines, which trace shocked regions, get strong because of the increment of the number of supernova explosions. After the starburst phase, there might remain a lot of A-type stars which show strong Balmer absorption in the spectrum, so-called "post-starburst" phase (figure 1.1). This starburst evolution has been proposed by Rieke et al. (1988) and Rieke (1988) based on optical and near-infrared spectra of their data, and is still believed.

1.2 Physical Conditions of Molecular Gas

Since stars are formed from molecular gas, molecular gas might be a direct fuel of starburst phenomena. Therefore, studies of molecular gas in starburst galaxies might give important knowledge about the evolution of starburst and its effects.

For the formation of stars, the density of molecular gas is a very important factor. Molecular gas has its density from 10^2 cm^{-3} to higher than 10^4 cm^{-3}, sometimes reaches to more than 10^9 cm^{-3}, and the distributions are different between diffuse and dense molecular gas. Diffuse molecular gas distributes widely, and is loosely gravitationally bounded, but dense gas resides in much clumpy and tightly bounded region (e.g. Goldsmith 1987). Observational studies of molecular cloud in Our Galaxy suggest that stars are formed from dense molecular gas, not from diffuse region (e.g. Lada 1992). Extragalactic single-dish molecular gas observations also show similar result that the strength of star formation is much tightly correlated with the amount of dense molecular gas than

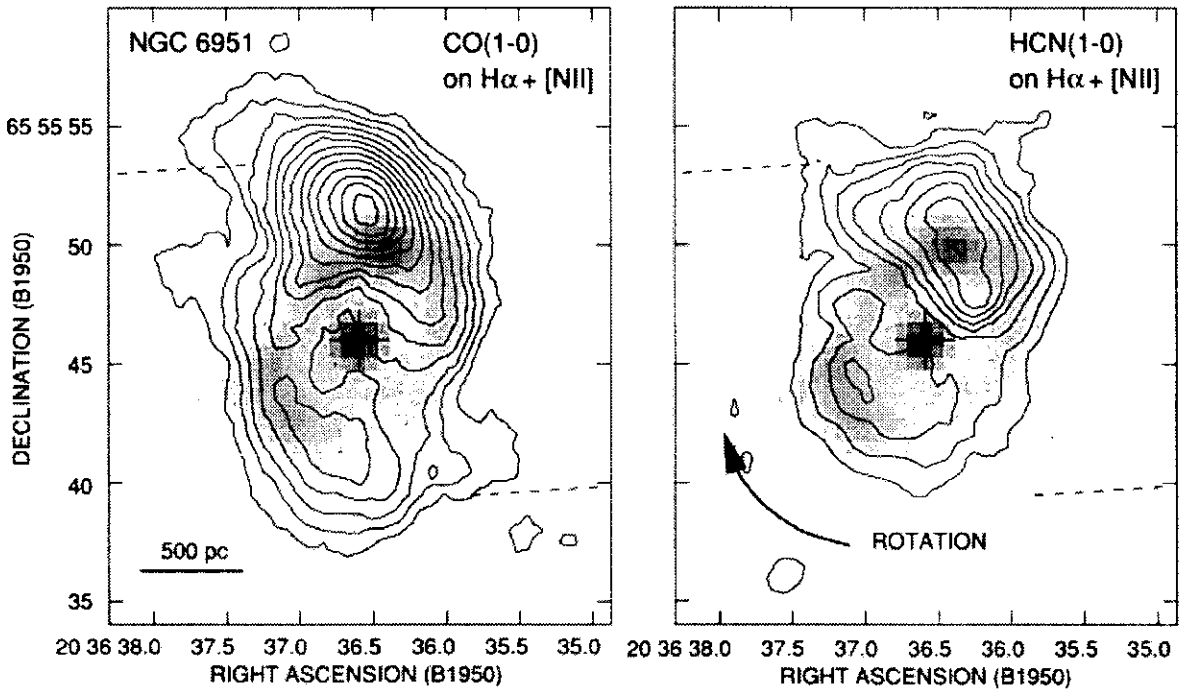

Fig. 1.3: Comparison of ^{12}CO(1 − 0) and HCN(1 − 0) distributions (contour; Kohno, Kawabe, & Vila-Vilaró 1999) with the Hα + [NII] image (greyscale; Wozniak et al. 1995). Dashed lines indicate the trace of dust lanes seen in a $B - I$ color image (Wozniak et al. 1995). These figures clearly show that the distribution of Hα emission show better coincidence with that of HCN emission than that of ^{12}CO emission. These figures are taken from Kohno, Kawabe, & Vila-Vilaró (1999).

that of diffuse molecular gas (figure 1.2; Solomon, Downes, & Radford 1992). Interferometric molecular gas observations show that the distributions of star forming regions are much closely related with those of dense molecular gas than those of diffuse molecular gas (figure 1.3; Kohno, Kawabe, & Vila-Vilaró 1999, Reynaud & Downes 1999). These results strongly imply that the density of molecular gas might control the star formation from small-scale to large-scale.

Kohno (1997) has studied an evolution of star forming regions from the standpoint of molecular gas density. In starburst galaxies, there are a large amount of dense molecular gas, and are strongly concentrated at the starburst regions. In post-starburst galaxies, however, there are almost no dense molecular gases. This result leads to the fact that exhaustion of dense molecular gas by star formation would stop the starburst. On the other hand, the beginning of starburst might cause by the gravitational instability, because starburst galaxies tend to have unstable molecular gas, but normal galaxies have stable gas.

Study of another physical condition parameter, temperature, of molecular gas might also be important information for the studies of star formation. This information would give us the strength of the effect of star formation to surrounding molecular gas. For example, stars might heat surrounding region by their radiation, so that molecular gas in star forming regions might be warmer than that in quiescent regions. Dark clouds, which is quiescent, low mass star forming clouds, have temperature of $\sim$ 10 K. However, cores of giant molecular clouds, which are active high mass star forming clouds, have high temperature, sometimes reach to a few hundred Kelvin (Graf et al. 1990). Molecular

gas temperature in external galaxies also shows similar tendencies that starburst galaxies have higher molecular gas temperature than quiescent, normal galaxies (Wall et al. 1993, Güsten, et al. 1993, Harris et al. 1991). Therefore, temperature would give us the star formation activity of molecular gas.

To obtain temperature information, observations of multi-J molecular lines are the direct way. High-J and low-J lines are, however, in different wave bands, the former lines are in submillimeter wave bands, and the latter in millimeter wave bands. At present, only several single-dish telescopes are available for the submillimeter observations, and no submillimeter interferometers, so that there are only small numbers of statistical observations with low spatial resolutions (insufficient to resolve the active and non-active regions) for the high-J line observations. Hence, studies for molecular gas temperature in galaxies are not active so far.

1.3 Thesis Outline

Due to the difficulty of submillimeter observations, the detail study of molecular gas temperature has still not been done, and therefore the relation with molecular gas density, and the evolution of these physical conditions are still not clear. In this thesis, therefore, we will try to address the issue that "is there any relations between the evolution of starburst and the physical conditions of molecular gas?"

Since many authors have done the study of molecular gas density, we first concentrate to the study of molecular gas temperature. To address the issue indicated above, we have to answer "how to know the molecular gas temperature?" and "what is the heating source?" In chapter 2, we will study about the physical conditions of circumnuclear molecular gas in M51, which was the beginning of this study, and indicate that the HCN(1 – 0)/^{13}CO(1 – 0) integrated intensity ratio might be a good molecular gas temperature probe. There is also a good correlation between HCN/^{13}CO ratios and the amount of 100 K dust, which strongly support this result. The studies of various objects in Our Galaxy suggest that supernova explosions might be the most effective heating source in the starburst regions.

In chapter 3, the case study of prototypical starburst galaxy M82 will be discussed. In the evolutional study of starburst galaxy by Rieke et al. (1988) and Rieke (1988), they have suggested that M82 might be a late phase of starburst, not the typical one. In this section, we will discuss about "is M82 typical starburst galaxy?" from the standpoint of the physical properties of molecular gas. The molecular gas in M82 show that the amount of dense gas is very low, but the star formation efficiency is high comparable to other starburst galaxies, which indicate that M82 would be in the very late phase of starburst, not in the middle of the starburst phase. Since our observations are a few $\times$10 pc resolution, we will also discuss the detail structures of molecular gas in the starburst galaxy. The molecular gas images show very interesting feature, that is, an expanding molecular superbubble. From the study of this superbubble, we propose the new mechanisms of the termination of starburst, the sequential starburst, and the formation of a middle mass black hole.

In chapter 4, we will study about the physical conditions of molecular gas in starburst and non-starburst galaxies, and compare the differences between these galaxies. There are large differences that the density and temperature of molecular gas in starburst galaxies tend to be higher than that in non-starburst galaxies. Even inside of a starburst

galaxy, there are differences in physical conditions. We will also study about $\sim$ 100 GHz continuum emission in millimeter wave, and discuss about the domination of free-free emission in the continuum and usefulness in the estimation of star formation rate (SFR) and star formation efficiency (SFE). The SFR and SFE derived from the free-free emission dominated continuum emission show good correspondence with those derived from the extinction corrected Hα emission, which indicate that millimeter wave ($\sim$ 100 GHz) continuum emission would be a good tool for estimating absorption free SFR and SFE values, if free-free emission is dominated.

In chapter 5, we will propose the evolution of the physical conditions of molecular gas in accordance with the evolution of starburst galaxies using all the results in chapter 2−4. There might be offsets in the evolution of the increment and decrement of molecular density and those of molecular temperature in accordance with the evolution of starburst. First the density would increase because of the gravitational instability, and after that temperature would increase by the explosions of supernovae.

Summary of this thesis will be provided in chapter 6.

Chapter 2

Tracers for Estimating the Physical Conditions of Molecular Gas

2.1 Introduction

Studies of dense molecular gas in galaxies have demonstrated that the physical properties (especially density) of molecular gas in the central regions of starburst galaxies are quite different from those at the centers or disks of normal galaxies. For example, high angular resolution imaging of HCN(1 – 0) and ^{12}CO(1 – 0) emission toward the nuclear regions of the prototypical starburst nuclei NGC 253 and M82 revealed a high HCN(1 – 0)/^{12}CO(1 – 0) intensity ratio of 0.2−0.3 (Paglione, Tosaki, & Jackson 1995, Sorai et al. 2000b, Shen & Lo 1995; but it is not true for M82. See chapter 2.3, 3). These ratios are higher than that in the central region of the Milky Way (the ratio $\sim$ 0.08; Jackson et al. 1996, Helfer & Blitz 1997b), suggesting an enhancement of the gas density in the central hundreds parsec regions of starburst galaxies. This enhancement is closely related to the star-formation efficiency. Galaxies with higher density enhancement tend to have higher star-formation efficiency (Solomon, Downes, & Radford 1992, Kohno 1997). Moreover, there are spatial coincidence between dense molecular gas distributions and star forming regions (Kohno, Kawabe, & Vila-Vilaró 1999). These results strongly support the idea of stars are formed from dense molecular gas. However, from the observations of ^{12}CO and HCN, we can only obtain lower limits to the density conditions, and this is not enough to reveal a whole story of starburst phenomena.

Another important information for the physical conditions of molecular gas is temperature. The difference of temperature between molecular clouds might suggest the difference of the amount of heating source such as massive stars, supernova explosions, and so on. Therefore, the temperature would give us the star formation activity of molecular gas. To obtain the temperature information, observations of high-J molecular lines in the submillimeter wave bands are needed. At present, however, only single-dish telescopes are available for the submillimeter observations (no submillimeter interferometer), so that spatial resolutions (at most one kpc scale) are insufficient to resolve the star forming regions (at most a few hundred pc scale; Jackson et al. 1996) and quiescent regions even in the nearby galaxies, and we cannot obtain the small-scale temperature information. Therefore other ways of measuring temperature are required.

In this chapter, we will propose a new probe to obtain the physical conditions of molecular gas (especially temperature) that can observe with millimeter wave bands,

and therefore can obtain detail information with high spatial resolution interferometer observations (section 2.2). Since the discovery of this new probe is in a part of the study about active galactic nuclei, we will also discuss about these objects. We will show the reliability of the probe (section 2.3), and also discuss about the heating source as well (section 2.4).

2.2 HCN/^{13}CO as Dense and Warm Molecular Gas Tracer I : M51

2.2.1 Background

Recent aperture synthesis mm-wave HCN observations have revealed the existence of the dense gas circumnuclear tori (or disks) in the Seyfert galaxy NGC 1068 (Jackson et al. 1993, Tacconi et al. 1994) and the low-luminosity active galactic nucleus (AGN) M51 (Kohno et al. 1996). These tori have a typical radius of a few hundred parsecs and a H_2 column density of $> 10^{24}$ cm^{-2}, and are thought to be responsible for the obscuration of the direct view of AGN. In both galaxies, the HCN emission from the tori is very bright, and the resultant HCN/^{12}CO intensity ratio is very high (0.6 for NGC 1068, Helfer & Blitz 1995, Helfer & Blitz 1997a; 0.4 for M51, Kohno et al. 1996). The possible interpretation of this high ratio is that the density in the clouds of the tori is very high compared with that of GMCs (giant molecular clouds) in disks of spirals.

In order to understand the physical conditions of the molecular clouds, and also to be able to relate those properties to the AGN phenomena, multi-line observations are essential. The best multi-line observation is to observe multi-J lines with millimeter and submillimeter telescopes, because we do not need to consider any abundance of the molecules, and we can derive physical conditions directly. In addition, since the dense parts of the molecular clouds are confined to relatively smaller regions than is the ^{12}CO emission, the line ratios can be very sensitive to the resolution of the telescope (e.g. Helfer & Blitz 1993). Therefore, millimeter and submillimeter multi-line observations using interferometers are the best way to study these active regions. However, there are still no submillimeter interferometers in this world, so that we have to find other probes in millimeter wave bands to know the physical conditions of molecular gas, and check the validity of the probes with observing multi-J lines in submillimeter wave bands with case studies.

For the study of the circumnuclear molecular tori/disks, M51 is one of the best sample galaxies to observe. It has a low-level activity Seyfert 2 nucleus (e.g. Rose & Cecil 1983, Terashima et al. 1998, Ho, Filippenko, & Sargent 1997), and its nearness (9.6 Mpc; Sandage & Tammann 1975) and face-on view (20°; Tully 1974) make it possible to observe the circumnuclear region with high resolution ($1''$= 47 pc) and small contaminations by outer disk gas. Aperture synthesis HCN(1 – 0) observations by Kohno et al. (1996) have found a dense circumnuclear torus/disk around AGN, and its rotating axis (P.A. $\sim -20°$) is almost parallel to the position angle of the radio jet ($\sim -17°$; Ford et al. 1985). High resolution ($0\farcs8 \times 1\farcs2$) ^{12}CO(2 – 1) observations (Scoville et al. 1998) have also showed a similar image as that of HCN(1 – 0), although the ^{12}CO(2 – 1) distribution is not symmetric. From these circumstances, M51 is one of the best candidates to study the conditions of the nuclear molecular clouds.

Table 2.1: Interferometer observational parameters.

	^{13}CO*	^{12}CO†	HCN†
Observing period	1995 Nov. - 1996 Mar.	1988 Dec. - 1989 Mar.	1994 Apr. - 1994 May, 1995 Jan. - 1995 Mar.
Synthesized beam	5.″9 × 5.″1	5.″1 × 4.″4	7.″1 × 5.″8
(Linear scale§)	(270 pc × 230 pc)	(230 pc × 200 pc)	(330 pc × 270 pc)
Velocity resolution	20.4 km s^{-1}	19.5 km s^{-1}	21.1 km s^{-1}
R.m.s. noise¶	16 mJy beam^{-1} (53 mK)	82 mJy beam^{-1} (340 mK)	10 mJy beam^{-1} (38 mK)

* This work.
† Kohno et al. (1996).
§ For distance 9.6 Mpc (Sandage & Tammann 1975).
¶ R.m.s. noise for channel maps with the velocity resolution listed above.

2.2.2 Observations

Interferometric Observations

Aperture synthesis observations of the central region of M51 were carried out in the ^{13}CO(1 – 0) line (rest frequency = 110.201353 GHz) using the Nobeyama Millimeter Array (NMA) during 1995 December - 1996 March. The ^{13}CO image was obtained using three configurations (D, C, and AB) of six 10m antennas which are equipped with tunerless SIS receivers (Sunada, Kawabe, & Inatani 1994). The receiver noise temperatures were about 50 K (DSB) at 110 GHz. As back-end, we used a 1024 channels FX spectrocorrelator (Chikada et al. 1987), with a total bandwidth of 320 MHz, corresponding to 870 km s^{-1} at the ^{13}CO(1 – 0) frequency. The band-pass calibration was done with 3C273, and 1308+326 was observed every 25 minutes as a phase calibrator. The flux scale of 1308+326 was determined by comparisons with planets of known brightness temperature. The uncertainty in the absolute flux scale is estimated to be $\sim$ 20%.

The data were reduced using the NRO software package "UVPROCII", and the final maps were made and CLEANed with the NRAO software AIPS. All these maps were made with natural weighting. The synthesized beam of the ^{13}CO channel maps was 5.″9 × 5.″1 (270 pc × 230 pc) and the velocity channel maps were made with 20.4 km s^{-1} velocity binning. The typical noise level of the channel maps was 16 mJy beam^{-1}. We briefly summarized the observational parameters of ^{13}CO in table 2.1, together with ^{12}CO and HCN. The detailed observational parameters for the ^{12}CO and HCN are described in Kohno et al. (1996).

Single-Dish Observations

Observations of the central region of M51 using the Nobeyama 45 m telescope were carried out in the HCN(1 – 0), ^{13}CO(1 – 0), and ^{12}CO(1 – 0) lines (rest frequency =

86.6316024 GHz, 110.201353 GHz, and 115.271204 GHz, respectively) during 1997 May – December. The half power beam widths (HPBW) were 17″, 15″, 14″, and the main-beam efficiencies were $\eta_{\rm mb} = 0.47 \pm 0.02, 0.51 \pm 0.03, 0.40 \pm 0.01$, respectively. We used two SIS receivers simultaneously for the observations of two molecular lines with no relative pointing offsets. The telescope pointing was check and corrected every one hour, and the absolute pointing errors were less than 3″ during the observations. The system noise temperatures (SSB) of 87 GHz, 110 GHz, and 115 GHz throughout the observations were 200 – 300 K, 300 – 500 K, and 600 – 700 K, respectively. As back-ends, we used 2048-channel wide band acousto-optical spectrometers (AOS), with a total bandwidth of 250 MHz, corresponds to 650 km s^{-1} at the ^{12}CO(1 – 0) frequency. The line intensity calibration was made by the chopper-wheel method (Ulich & Haas 1976), and the relative intensity errors were calibrated with the intensity of IRC+10216 at every observation.

We also observed in the HCN(3 – 2), ^{13}CO(3 – 2), ^{12}CO(3 – 2), and HCN(4 – 3) lines (rest frequency = 265.886432 GHz, 330.587957 GHz, 345.795991 GHz, and 354.505472 GHz, respectively) using the JCMT 15 m telescope during 1997 April – May. The half power beam widths (HPBW) were 18″, 14″, 13″, and 13″, respectively. We used the Receiver A2 for the HCN(3 – 2) observations, and the Receiver B3 for the rest of the lines. The Receiver B3 has two mixers, Mixer A and Mixer B, and we observed the ^{13}CO(3 – 2) with Mixer B, the ^{12}CO(3 – 2) with Mixer A, and the HCN(4 – 3) with both mixers. The main-beam efficiency of the Receiver A2 was $\eta_{\rm mb} = 0.60 \pm 0.04$, and those of the Mixer A and Mixer B of the Receiver B3 were $\eta_{\rm mb} = 0.64 \pm 0.03$ and 0.61 ± 0.03, respectively. The telescope pointing was check and corrected every two hours, and the absolute pointing errors were less than 3″ during the observations. The system noise temperatures of the Receiver A2 (DSB) and Receiver B3 (SSB) throughout the observations were 500 – 800 K and 400 – 1000 K, respectively. As back-ends, we used 2048-channel digital autocorrelation spectrometer (DAS), with a total bandwidth of 760 MHz, corresponds to 660 km s^{-1} at the ^{12}CO(3 – 2) frequency. The observed spectra were taken using secondary mirror chopping with a beam throw of 3′ in R.A. The line intensity calibration was made by the chopper-wheel method, and the relative intensity errors were calibrated with the intensity of IRC+10216 at every ^{12}CO(3 – 2) and HCN(4 – 3) observations. For the calibrations of the ^{13}CO(3 – 2) observations, the average calibration values for the ^{12}CO(3 – 2) and HCN(4 – 3) lines with IRC+10216 observations were used. We did not calibrate the relative intensity errors for the HCN(3 – 2) observations, but it will be less than 15% (estimated from the standard deviation of the JCMT standard line measurements of the HCN(3 – 2) line in IRC+10216).

We observed six points with the ^{12}CO(3 – 2) line, two points with the ^{12}CO(1 – 0) and ^{13}CO(3 – 2) lines, and one point (center) with the ^{13}CO(1 – 0), HCN(1 – 0), HCN(3 – 2) and HCN(4 – 3) lines. The reference position for the observations is (R.A., Decl.) = ($13^{\rm h}27^{\rm m}46^{\rm s}.327$, 47°27′10″.25), which coincides with 6 cm radio continuum peak (Ford et al. 1985). The grid points of the ^{12}CO(3 – 2) line were spaced by 7″.5 parallel and perpendicular to the major axis of the galaxy at a position angle (P.A.) of −10° (Tully 1974). The observed positions of ^{12}CO(1 – 0) were (0″.0, 0″.0) and (0″.0, 15″.0) in R.A. and Decl. offsets, and those of the ^{13}CO(3 – 2) were (0″.0, 0″.0) and (0″.0, 7″.5) with the same gridding as the ^{12}CO(3 – 2) observations. We briefly summarized the observational parameters of these single-dish observations in table 2.2.

Table 2.2: Single-dish observational parameters.

Molecular lines	Rest frequency (GHz)	Beam size (arcsec)	Linear scale* (pc)	Telescope
^{12}CO (3 – 2)	345.796	$\sim$ 13	620	JCMT 15 m
^{13}CO (3 – 2)	330.588	$\sim$ 14	640	JCMT 15 m
HCN (4 – 3)	354.505	$\sim$ 13	600	JCMT 15 m
HCN (3 – 2)	265.886	$\sim$ 18	850	JCMT 15 m
^{12}CO (1 – 0)	115.271	$\sim$ 14	630	NRO 45 m
^{13}CO (1 – 0)	110.201	$\sim$ 15	690	NRO 45 m
HCN (1 – 0)	88.632	$\sim$ 17	800	NRO 45 m

* For distance 9.6 Mpc (Sandage & Tammann 1975).

2.2.3 Results

The Distribution of ^{13}CO emission

The channel maps of the ^{13}CO emission observed with the NMA are shown in figure 2.1. ^{13}CO emission from the central $\sim$ 1′ region (in diameter) of M51 was detected over a velocity range of $V_{LSR} = 387 - 547$ km s^{-1} (a full velocity range of 160 km s^{-1}), similar to the ^{12}CO (Kohno et al. 1996). Figure 2.2 shows the total integrated intensity map of ^{13}CO obtained by binning the channel maps over the velocity range from $V_{\rm LSR} = 384$ to 546 km s^{-1}, together with the ^{12}CO and HCN maps taken from Kohno et al. (1996). The total flux of ^{13}CO emission in our 68″ beam is 162 Jy km s^{-1}. The ^{13}CO emission detected with the 14m FCRAO telescope (45″ beam) by Young and Sanders (1992) is 2.9±0.21 K km s^{-1} (which corresponding to 122 Jy km s^{-1}). Our ^{13}CO flux within a similar 45″ gaussian beam is 78.7 Jy km s^{-1}, corresponds to $\sim$ 70% of the single-dish flux. In the following intensity calculations, we recovered the missing flux with assuming that the missing flux of 30 % is distributed uniformly.

As can be clearly seen in figure 2.2, the overall distributions of the of ^{13}CO and ^{12}CO emission are very similar. Both are distributed along a pair of spiral arms, and are deficient at the center, clearly different from centrally peaked HCN emission.

Figure 2.3 shows the radial distributions of the ^{12}CO/^{13}CO, HCN/^{13}CO, and HCN/^{12}CO total intensity ratios, respectively. We define the 'intensity' as $I = \int T_B dv$ (K km s^{-1}). All three figures shown in figure 2.3 were made using the tasks "COMB" and "IRING" in the AIPS package; first we made ratio maps with a clipping level of 2σ after the maps convolved to the same beam size, and averaged them over concentric annuli of 4″(180 pc) width. Figure 2.3(a) indicates that the ^{12}CO/^{13}CO ratio is almost constant (except for the center), that is, $\sim$ 7±2 for almost all the region of the field of view. Since we detect almost no ^{13}CO emission from the central 8″in radius, we only obtained the lower limit of ^{12}CO/^{13}CO ratio in this region. The HCN/^{13}CO ratio (figure 2.3(b)) is also obtained with lower limit information, but show a centrally peaked structure. The most remarkable point in this figure is that the HCN/^{13}CO ratio is higher than 3 in the central region (r < 180 pc), namely, the HCN intensity in this region is much brighter than the ^{13}CO intensity in spite of the much larger abundance of the ^{13}CO molecule. On the other hand, in the outer regions (r> 180 pc), the HCN/^{13}CO intensity ratio is only $\sim$

0.5-0.6 which is 5-6 times smaller than in the central 180 pc region. This trend is almost the same as the HCN/^{12}CO ratio (figure 2.3(c)) which is already shown in Kohno et al. (1996).

The Intensities of Multi-J Molecular Lines

We detected ^{12}CO lines with single-dish telescopes in all observed points (figure 2.4). ^{12}CO(3 – 2)/(1 – 0) intensity ratios of the (0.″0, 0.″0) and (0.″0, −15.″0) are $\sim 0.8 \pm 0.1$ and $\sim 0.9 \pm 0.1$, respectively. These values are moderately high compared with starburst galaxies (the mean value of seven starburst galaxies is 0.64 ± 0.06; Devereux et al. 1994) and nearby galaxies (0.2 – 0.7 for 23 nearby galaxies; Mauersberger et al. 1999), and almost comparable to the prototypical starburst galaxy M82 (^{12}CO(3 – 2)/(1 – 0) $\sim 0.9 \pm 0.2$; Tilanus et al. 1991, Wild et al. 1992) and the luminous infrared galaxy Arp 220 (0.9; Mauersberger et al. 1999). ^{12}CO(3 – 2)/(1 – 0) ratio of the center and off-center of M51 in Bash, Jaffe, & Wall (1990) was similar to our result, but in Mauersberger et al. (1999) was 0.62 at the center, somewhat smaller than our measurement. This would be caused by their larger beam size of 21″and/or pointing offset in ^{12}CO(1 – 0) observations, since their spectrum has an asymmetric profile. M51 have weak CO intensity at the center but strong at the off-center (arm) region (e.g. Kohno et al. 1996, Nakai et al. 1994), so that the large beam size or pointing offset easily cause the different line ratios and/or asymmetric profiles.

^{13}CO(3 – 2) was detected both at the center and off-center (0.″0, −7.″5) points, with intensities stronger in off-center point (figure 2.5, solid line). The ^{12}CO(3 – 2)/^{13}CO(3 – 2) intensity ratio of the center is $\sim 22 \pm 7$, but that of the off-center point is $\sim 8 \pm 2$. This ratio is larger than that of other galaxies such as the Seyfert galaxy NGC 1068 ($\sim 14 \pm 3$; Papadopoulos & Seaquist 1999) and the starburst region of M82 ($\sim$ 10; Tilanus et al. 1991). ^{13}CO(1 – 0) was observed only at the center, and detected at that point (figure 2.5, dashed line). The ^{12}CO(1 – 0)/^{13}CO(1 – 0) intensity ratio is $\sim 13 \pm 2$, which is moderately high compared with that of normal galaxies ($\sim$ 10; Sage & Isbell 1991, Young & Sanders 1986). However, as seen in the interferometer image of ^{13}CO (figure 2.2), almost all the ^{13}CO comes from the off-center (arm) region, so that the ratio with much smaller beam size ($\theta \ll 15''$) might be much higher (figure 2.3).

About HCN molecules, J = 1 – 0 was clearly detected (figure 2.6(a)), but J = 3 – 2 (figure 2.6(b)) and J = 4 – 3 (figure 2.6(c)) were marginal detections. The HCN(4 – 3)/^{12}CO(3 – 2) intensity ratio is $\sim 0.03 \pm 0.01$, similar to NGC 253 and IC 342 of $\sim 0.03 - 0.05$, but quite different from M82 of < 0.003 (Jackson et al. 1995). The HCN(3 – 2)/(1 – 0) intensity ratio is $\sim 0.22 \pm 0.06$, similar to NGC 1068, Arp 220, Maffei 2 and IC 342 (~ 0.2), but lower than M82 and NGC 253 ($\sim 0.6 - 0.7$) (Paglione, Jackson, & Ishizuki 1997). Paglione, Jackson, & Ishizuki (1997) also observed M51, but they obtained only a upper limit of 0.1. This might be a beam dilution of HCN(3 – 2) emission caused by their larger beam size. Their beam size is 27″, so the beam dilution effect lowers the intensity of the source smaller than our beam size ($\sim$ 18″) by 45%. Our observed integrated intensity and peak temperature are 1.62 K km s^{-1} and 20 mK, so that the dilution of $\sim$ 45% would result these values as 0.7 K km s^{-1} and 9 mK, respectively. These value are lower than their observed upper limits of < 1.3 K km s^{-1} and < 11 mK, respectively. This estimate indicates that the higher-J HCN emission might also be compact and centrally peaked as HCN(1 – 0) (Kohno et al. 1996). We summarized the results of the observations in table 2.3.

Table 2.3: Single-dish observational results.

Molecular lines	Offsets* ($\Delta\alpha''$, $\Delta\delta''$)	Integrated intensities† (K km s^{-1})
^{12}CO(3 – 2)	(0.0, 0.0)	43.1 ± 2.9
	(7.5, 0.0)	35.6 ± 3.4
	(0.0, 7.5)	50.8 ± 4.2
	(−7.5, 0.0)	33.7 ± 3.7
	(0.0, −7.5)	29.3 ± 3.0
	(0.0, −15.0)	31.8 ± 2.9
^{12}CO(1 – 0)	(0.0, 0.0)	53.8 ± 5.1
	(0.0, −15.0)	37.4 ± 3.0
^{13}CO(3 – 2)	(0.0, 0.0)	1.9 ± 0.6
	(0.0, −7.5)	3.5 ± 0.7
^{13}CO(1 – 0)	(0.0, 0.0)	4.3 ± 0.7
HCN(4 – 3)	(0.0, 0.0)	1.9 ± 0.4
HCN(3 – 2)	(0.0, 0.0)	1.6 ± 0.4
HCN(1 – 0)	(0.0, 0.0)	7.5 ± 0.4

* The reference point (0.″0, 0.″0) is the position of the galactic nucleus determined from the 6 cm radio continuum peak. Other points are offset from the reference point with a P.A. of −10°.
† Quoted uncertainties are 1σ.

2.2.4 Physical Conditions of Dense Gas Disk in the Nucleus of M51

Physical Conditions Derived from HCN/^{13}CO Intensity Ratio

We found that the HCN/^{13}CO intensity ratio of the nuclear dense gas disk of M51 observed with the NMA is much higher than unity, in addition to the high HCN/^{12}CO ratio which has been already obtained by Kohno et al. (1996). Similar results have been obtained from the nuclear molecular clouds of the Seyfert galaxy NGC 1068 and the starburst galaxy M82 as discussed below. We will present below the physical conditions of the dense gas disk in M51 which is estimated from the obtained HCN/^{13}CO intensity ratio.

Calculations based on the Large-Velocity-Gradient (LVG) approximation (e.g. Goldreich & Kwan 1974, Scoville & Solomon 1974) can be used to estimate the physical conditions of the molecular clouds from the observed molecular line data. We derived the physical conditions of the circumnuclear molecular disk in M51 using LVG calculations with the HCN and ^{13}CO data, assuming a one component model in order to make clear under what conditions the HCN emission becomes brighter than that of ^{13}CO. The line intensity ratios and the line opacities were calculated as a function of the H_2 number density, $n(H_2)$, from 10^2 to 10^7 cm^{-3}, and the kinetic temperatures, T_k, from 10 to 1000 K. The collision rates for CO molecule were available from Flower & Launay (1985) ($\leq$ 250 K) and McKee et al. (1982) ($\geq$ 500 K), and that of HCN molecule were available

from Green & Thaddeus (1974) (< 100 K) and Green (1993) (≥ 100 K). We fixed the abundances to the 'standard' relative abundance as $Z(^{13}\mathrm{CO}) = [^{13}\mathrm{CO}]/[\mathrm{H_2}] = 1 \times 10^{-6}$ (Solomon, Scoville, & Sanders 1979) and $Z(\mathrm{HCN}) = [\mathrm{HCN}]/[\mathrm{H_2}] = 2 \times 10^{-8}$ (Irvine, Goldsmith, & Hjalmarson 1987).

We made two kinds of coarse estimations for the velocity gradient dv/dr before the LVG calculations. First, we estimate it from the observational values. The velocity width of the nuclear HCN emission is about 130 km/s and its radius is < 200 pc (Kohno et al. 1996), hence a lower limit to the value of the velocity gradient dv/dr is > 0.7 km s^{-1}pc^{-1}. From Figures 3 & 5 of Kohno et al. (1996), the nuclear disk seems to be resolved, and the separation of the blue and red velocity peaks is about 90 pc. If we assume that this is the lower limit of the radius, an upper limit of dv/dr would be < 1.4 km s^{-1}pc^{-1}. Therefore, the estimated range of the velocity gradient is $0.7 < dv/dr < 1.4$. A second estimate of the velocity gradient comes from assuming that the circumnuclear clouds are virially bound and $n_{H_2} \sim 10^4$ cm^{-3}; then, the velocity gradient can be approximately estimated as

$$\frac{dv}{dr} \sim \frac{\sigma_v}{r_c} = \sqrt{\frac{4\pi G m_{\mathrm{H_2}} n_{\mathrm{H_2}}}{3}} \sim 2 \text{ km s}^{-1} \text{ pc}^{-1}, \tag{2.1}$$

where, σ_v: velocity dispersion (km s^{-1}), r_c: cloud radius (pc), G: gravitational constant, $m_{\mathrm{H_2}}$: mass of molecular hydrogen, and $n_{\mathrm{H_2}}$: number density of molecular hydrogen. These two estimations show $dv/dr \sim 1$, similar to the general value of 1.0. We therefore used $dv/dr = 1$ as a normal value in the following calculations.

The results of the calculations of the density and temperature dependent intensity ratio are shown in figure 2.7. The solid contours in the figure show the curves of constant HCN/^{13}CO intensity ratios; the curves corresponding to a HCN/^{13}CO ratio of 3 were outlined as thick solid curves. These figures clearly indicate that the observed high HCN/^{13}CO ratio can only be produced when both density *and* temperature are high. These results lead to the conclusion that the high HCN/^{13}CO ratio originates in molecular gas of high density ($n(\mathrm{H_2}) \sim 10^{5\pm1}$ cm^{-3}) *and* high temperature ($\mathrm{T_k} \gtrsim 300$ K), for normal velocity gradients and ^{13}CO and HCN abundances.

The LVG calculations with different velocity gradient were also performed, and implied that increasing the velocity gradient of a factor of 3 ($dv/dr = 3$), which is larger value than those estimated above, lowers the temperature of only a factor of ~ 2. On the other hand, the decrease of the velocity gradient raises the temperature. Hence, even if the velocity gradient would change, high HCN/^{13}CO ratio indicates that molecular gas is in high-density and high-temperature conditions. We also carried out the LVG calculations with a low ^{13}CO abundance condition, and the results indicate that reducing the ^{13}CO molecule abundance of a factor of 2 ($[^{12}\mathrm{CO}]/[^{13}\mathrm{CO}] = 100$) lowers the temperature of only a factor of ~ 2. Furthermore, an increase of the $[^{12}\mathrm{CO}]/[^{13}\mathrm{CO}]$ abundance ratio toward the galactic center is opposite from its decreasing trend of Our Galaxy (Wilson & Rood 1994). If we rise the ^{13}CO abundance, the calculated physical conditions show much higher temperature. Hence, even if the ^{13}CO abundance would change, high HCN/^{13}CO ratio indicates that molecular gas is in high-density and high-temperature conditions. On the other hand, since the HCN emission is optically thick, the change in the HCN abundance do not affect to the calculation results. For the following LVG calculations, therefore, we use normal velocity gradient and ^{13}CO and HCN abundances.

Why is HCN Brighter Than ^{13}CO ?

The observed brightness temperature of an emission $T_{\rm B}$ is related to the filling factor f, the excitation temperature $T_{\rm ex}$, and opacity of emission τ by the equation $T_{\rm B} = f(J_\nu(T_{\rm ex}) - J_\nu(T_{\rm bg}))(1 - \exp(-\tau))$, where $J_\nu = (h\nu/k)(\exp(h\nu/kT) - 1)^{-1}$, and $T_{\rm bg}$ is the background radiation temperature. Using the Local-Thermal-Equilibrium (LTE) approximation, the observed HCN/^{13}CO brightness temperature ratio can be expressed as

$$\frac{T_{\rm HCN}}{T_{\rm ^{13}CO}} = \frac{1 - \exp(-\tau_{\rm HCN})}{1 - \exp(-\tau_{\rm ^{13}CO})} \tag{2.2}$$

assuming the same filling factor and excitation temperature for HCN and ^{13}CO. If the opacities of both molecules are optically thick, the brightness temperature ratio tends to 1. However, if the HCN emission line is optically thick and ^{13}CO is thin, the ratio can be > 1.

The opacity ratio of the HCN and ^{13}CO emission is related to the dipole moment μ_i (i denotes the corresponding molecules), rotational constant B, and column density N_i as

$$\frac{\tau_{\rm HCN}}{\tau_{\rm ^{13}CO}} = \frac{\mu^2_{\rm HCN} B_{\rm HCN}\{1 - \exp(-\frac{h\nu_{\rm HCN}}{kT_{ex}})\}N_{\rm HCN}}{\mu^2_{\rm ^{13}CO} B_{\rm ^{13}CO}\{1 - \exp(-\frac{h\nu_{\rm ^{13}CO}}{kT_{ex}})\}N_{\rm ^{13}CO}}. \tag{2.3}$$

For the following calculations, we used $\mu_{\rm CO} = 0.112 \times 10^{-18}$ esu cm, $\mu_{\rm HCN} = 3.0 \times 10^{-18}$ esu cm, $B_{\rm CO} = 57.9$ GHz, $B_{\rm HCN} = 44.3$ GHz, $\nu_{\rm ^{13}CO} = 110$ GHz, $\nu_{\rm HCN} = 88.6$ GHz, and we used the usual abundance ratios mentioned above. Since the dipole moment of HCN is 30 times larger than that of ^{13}CO and the τ is proportional to μ^2, even taking into account the abundance ratios of HCN and ^{13}CO, it is obvious that the $\tau_{\rm HCN}$ will be larger than the $\tau_{\rm ^{13}CO}$. Adopting $T_{\rm ex} = 30$ K (Garcia-Burillo et al. 1993), the calculated opacity ratio of ^{13}CO and HCN is $\tau_{\rm HCN}/\tau_{\rm ^{13}CO} = 9.00$, but these results do not depend severely on the excitation temperature used (even if the excitation temperature is raised by a factor of 3, the opacity ratio differences are less than 1%).

Indeed, inspection of figure 2.7 shows that the opacity of ^{13}CO is optically thin (see dotted line of figure 2.7) and that of HCN is optically thick (not shown in the figure) where HCN/^{13}CO > 3; therefore, the above discussion is appropriate.

Physical Conditions Derived from Multi-Transition Molecular Line Study

Observation results by the single-dish telescopes show that the integrated intensity ratios of ^{12}CO(3 – 2)/(1 – 0) are almost constant in both center and off-center (arm regions), but those of ^{12}CO/^{13}CO are clearly different. This result indicates that the physical properties of the center and arm regions would be different. We again calculated the physical conditions of the molecular clouds from the observed molecular line data based on the LVG approximation.

Line intensity ratios and opacities for CO molecules were calculated as a function of the H_2 number density, $n(H_2)$, from 10^1 to 10^6 cm^{-3}, and the kinetic temperatures, $T_{\rm k}$, from 10 to 2000 K. The collision rates of ≤ 250 K were available from Flower & Launay (1985) and of ≥ 500 K were available from McKee et al. (1982). We fixed the abundances to the 'standard' relative abundance as $Z(^{13}{\rm CO}) = [^{13}{\rm CO}]/[{\rm H_2}] = 1 \times 10^{-6}$ (Solomon, Scoville, & Sanders 1979) and $[^{12}{\rm CO}]/[^{13}{\rm CO}] = 50$. We also fixed the velocity gradient, dv/dr, as a general value of 1.0.

Table 2.4: Two-component model LVG calculation intensities.

Molecular lines	Component (a) (K km s^{-1})	Component (b) (K km s^{-1})	Observed* (K km s^{-1})
^{12}CO(3 – 2)	27.9	12.3	43.1 ± 2.9
^{12}CO(1 – 0)	49.7	8.3	53.8 ± 5.1
^{13}CO(3 – 2)	0.6	1.9	1.9 ± 0.6
^{13}CO(1 – 0)	4.7	0.3	4.3 ± 0.7

* Quoted uncertainties are 1σ.

The LVG calculations assuming a one-component model indicate the molecular gas in the central 300 pc in radius have a density $n(H_2)$ of $\sim 5\times10^2 - 1\times10^3$ cm^{-3}, and a kinetic temperature T_k of $\sim$ 100 – 200 K. This result means that the molecular gas of central region of M51 is dominated by diffuse, warm gas. This result, however, may not reflect the true physical conditions, because the molecular gas emission in this region would come mainly from two different physical condition regions, the spiral arms and the circumnuclear disk. Molecular gas in the spiral arm regions can be clearly seen in the ^{12}CO(1 – 0) and ^{13}CO(1 – 0) interferometer maps (figure 2.2), and would resemble to Galactic GMCs ($n(H_2) \sim 10^3 - 10^4$ cm^{-3}, $T_k \sim$ 15 – 40 K) or GMC complexes ($n(H_2) \sim 1 - 3\times10^2$ cm^{-3}, $T_k \sim$ 7 – 15 K) (Goldsmith 1987). On the other hand, the molecular gas in the circumnuclear disk is rich in dense gas ($n(H_2) \sim 10^5$ cm^{-3}), which can also be seen in the interferometer HCN(1 – 0) image (figure 2.2). Since the physical conditions of these two distinct components may be different from the calculation result, it would be better to calculate physical conditions assuming a two-component model.

According to this point of view, we run LVG calculations assuming a two-component model. This model did not concern geometrical effects. The best fit to the data is obtained by the following: (a) a low-density ($n(H_2) \sim 3 - 6\times10^2$ cm^{-3}) and low-temperature ($T_{kin} \sim$ 20 – 50 K) component, and (b) a high-density ($n(H_2) \gtrsim 10^4$ cm^{-3}) and high-temperature ($T_{kin} \gtrsim$ 500 K) component. We briefly summarized the LVG calculation results in table 2.4.

Almost all of the ^{12}CO(1 – 0) and ^{13}CO(1 – 0) emissions and two-thirds of the ^{12}CO(3 – 2) emission comes from the component (a). In addition, the physical properties of the component (a) are consistent with those of the Galactic GMCs or GMC complexes, and of the low density molecular gas in the nearby galaxies ($n(H_2)$ of $< 10^3$ cm^{-3} and T_{kin} of 50 K; Mauersberger et al. 1999). Furthermore, the interferometric results indicate that the arm regions are dominated by the ^{12}CO(1 – 0) and ^{13}CO(1 – 0) emissions. These results suggest that the component (a) is a main component of the spiral arm regions. On the other hand, almost all of the ^{13}CO(3 – 2) emission, one-third of the ^{12}CO(3 – 2) emission, and almost no ^{13}CO(1 – 0) emission comes from the component (b). The deficiency of the ^{13}CO(1 – 0) emission and the physical properties of the component (b) are consistent with the situations of the circumnuclear molecular disk observed by NMA observations as indicated above ($n(H_2)$ of $\sim 10^5 \pm 1$ cm^{-3} and T_{kin} of $\gtrsim$ 300 K). Stronger in higher-J emission lines in ^{13}CO molecule and therefore the high-density and high-temperature conditions can also be seen in the massive star forming regions of Orion A and NGC 2024 (Graf et al. 1990).

Table 2.5: Comparison of HCN/^{13}CO intensity ratio with other galaxies.

Location	M51	NGC 1068	IC 342	Our Galaxy		
				Inner region	Sgr A	Sgr B2
Nuclear region :						
Ratio	> 3.3 (3σ)†	> 2.3 (3σ)¶	$\sim 0.5 - 0.9$**	~ 0.8§§	~ 0.8§§	~ 0.4‡‡
Linear scale*	360 pc§	140 pc‡	10 – 50 pc††	$\sim$ 600 pc¶¶	4.1 pc¶¶	4.7 pc¶¶
Arm or ring	$\sim 0.5 - 0.6$†	—	—	—	—	—

* Linear scale of the region which HCN/^{13}CO intensity ratio was obtained.
† This work. The value of nuclear region was derived with 3σ upper limit.
§ For distance 9.6 Mpc (Sandage & Tammann 1975).
¶ Helfer & Blitz 1995. This value was derived with 3σ upper limit.
‡ For distance 14 Mpc (Helfer & Blitz 1995).
** Downes et al. 1992.
†† For distance 1.8 Mpc (McCall 1989).
§§ See text.
¶¶ For distance 8.5 kpc.
‡‡ Linke, Stark, & Frerking 1981.

Same as CO molecules, line intensity ratios and opacities for HCN molecules were calculated as a function of $n(H_2)$ ($10^2 - 10^7$ cm^{-3}) and T_k (10 – 1000 K). The collision rates of < 100 K were available from Green & Thaddeus (1974) and of ≥ 100 K were available from Green (1993). We again fixed dv/dr as 1.0, and the HCN abundances as $Z(\mathrm{HCN}) = [\mathrm{HCN}]/[\mathrm{H_2}] = 2 \times 10^{-8}$ (Irvine, Goldsmith, & Hjalmarson 1987) which is the 'standard' relative abundance. The LVG calculation results for HCN(3 – 2)/(1 – 0) $\sim 0.22 \pm 0.06$ indicates $n(H_2) \sim 4{\times}10^2 - 2{\times}10^4$ cm^{-3}. This density range is consistent with the CO results.

The intensities of the two-component LVG calculation results and those of the observational results suggest that the beam filling factor of the component (a) is ~ 0.02, but that of the component (b) is only < 0.00036. The beam size of about 600 pc and the beam filling factor calculated above implies that the area of the component (a) is ~ 6000 pc^2, which is equivalent to the area of 20 molecular clouds with radius of 10 pc (equivalent to $\sim$ 20 GMCs) in the central $\sim$ 300 pc in radius. On the other hand, the area of the component (b) is less than 110 pc^2, which is equivalent to the area of one molecular cloud with a radius of only < 6 pc.

2.2.5 Comparison with Other Galaxies

From the study of physical conditions of molecular lines in the central region of M51, we indicate that the HCN/^{13}CO intensity ratio is good warm and dense molecular gas tracer as high-J lines. To confirm this result, we studied the previously published data of other galaxies. The summary for the results of the previously published data is in table 2.5.

NGC 1068. — The nuclear region of NGC 1068 has a Seyfert 2 nucleus and star-forming inner spiral arms (or ring) (Wilson & Ulvestad 1982, Telesco et al. 1984), but the strength of the star-formation is lower than M82. The ^{12}CO emission is mainly

distributed in the inner spiral arms, and some in the nucleus. The ^{13}CO distribution is similar to that of ^{12}CO but there is no clear emission in the nucleus. On the other hand, the HCN emission is strongly concentrated near the nucleus. Therefore, this object resembles M51. In Helfer & Blitz (1995), the effective peak temperature of a nuclear source of size 2″ is given from the direct comparison of the ^{12}CO, ^{13}CO, and HCN emissions. Using these values, it is clear that the ^{12}CO/^{13}CO ratio is greater than 5 and the HCN/^{13}CO ratio is greater than 2.3. This value is rather smaller than that of M51, but the HCN/^{13}CO is anyway much larger than unity. In the star-forming inner spiral arms, Helfer & Blitz mentioned that the HCN/^{12}CO intensity ratio is $\sim$ 5 times smaller than in the nucleus. If there is no depletion of ^{13}CO, the HCN/^{13}CO will be therefore smaller than unity. Tacconi et al. (1994) estimated the kinetic temperature and density of the circumnuclear molecular gas as $>$ 70 K and $\sim 10^{4-5}$ cm^{-3} from ^{12}CO(4 – 3) and (1 – 0) observations. Our LVG estimations are $\gtrsim$ 200 K and $\sim 10^{5\pm1}$ cm^{-3}, if we use HCN/^{13}CO $>$ 2.3 (Tacconi et al. 1994) and normal ^{13}CO and HCN abundances. If we compare our estimations of both kinetic temperature and density with those of Tacconi et al. (1994), we can say that these are in good agreement with each other.

Merger candidate ultraluminous infrared galaxies. — From single dish observations, it has become clear that merger candidate ultraluminous infrared galaxies have very large ^{12}CO/^{13}CO (Aalto et al. 1991a, Aalto et al. 1991b, Casoli, Dupraz, & Combes 1992a, Casoli, Dupraz, & Combes 1992b, Aalto et al. 1995) and HCN/^{12}CO (Solomon, Downes, & Radford 1992) ratios, so that merging galaxies will also have high HCN/^{13}CO ratios. Indeed, high angular resolution interferometric observations of ^{12}CO(1 – 0), ^{13}CO(1 – 0), and HCN(1 – 0) emission in Arp 299 (IC 694 and NGC 3690; Aalto et al. 1997) have shown the distributions of these emission lines in this merging system, and proved that there exist high HCN/^{13}CO ratio regions. These high ratio regions are seen in the starburst regions of Arp 299 where the interacting pair is highly overlapping, and at the nuclei of two galaxies (one is a possible AGN and the other is a possible starburst nucleus: Gehrz et al. 1983). These results are only for one object, so that much more high spatial resolution interferometric observations of merging galaxies are necessary to make clear these suggestions and problems.

IC 342. — There is no clear nuclear concentration in any of the maps of the three emission lines. Instead, there exist five evident molecular clouds, and the HCN/^{13}CO intensity ratios of these clouds range 0.5-0.9 (Downes et al. 1992). These values are twice as high as the values at 400-1400 pc from the center of M51 (inner arm), but much lower than those of the central region. The nuclear region of IC 342 has a population of young stars and experienced recent star formation, as suggested from strong FIR emission (Becklin et al. 1980) and 2 cm and 6cm radio continuum emission (Turner & Ho 1983). However, the degree of star formation is much lower than in M82, since only one out of five of the dense molecular clouds has an OB star association (Downes et al. 1992), and the star formation rate of the nuclear region calculated from the 6 cm thermal radio flux (Turner & Ho 1983) is estimated to be 0.15 M$_\odot$ yr^{-1}. Harris et al. (1991) have detected ^{12}CO(6 – 5) emission from the nucleus. Incorporating the observations of Eckart et al. (1990) and their 6 – 5 observations, they have estimated the molecular gas temperature and density as T_k = 30 K and $n(H_2) > 5 \times 10^3$. These values are much lower than NGC 1068 or M51. Our estimations from the HCN/^{13}CO ratio lower than 1 indicate that the molecular gas of IC 342 is not warm, and these estimations are also consistent with the high-J ^{12}CO line estimations.

Our Galaxy. — The inner $\sim$ 600 pc region of the Milky Way has an average HCN/^{12}CO intensity ratio of $\sim$ 0.08 (Jackson et al. 1996, Helfer & Blitz 1997b). Using a ^{12}CO/^{13}CO ratio of $\sim$ 9 – 10 ($\sim$ 9 for inner 1 kpc, Bronfman, Bitran, & Thaddeus 1988; $\sim$ 10 for inner 300 pc, Aalto et al. 1991a), the HCN/^{13}CO intensity ratio in the inner region of the Milky Way is $\sim$ 0.8. This value is very similar to that of IC 342. In addition, there are data for Sgr A and Sgr B2. In Sgr A, the brightness temperature of the ^{13}CO emission is $\sim$ 9.3 K (Bally et al. 1988) and that of the HCN emission is $\sim$ 7.1 K (Lee 1996), therefore the HCN/^{13}CO is $\sim$ 0.8. The beam size for the ^{13}CO observations was 100″ and that of HCN 61″. Since HCN is clearly more extended than the 61″ beam, the HCN/^{13}CO ratio would still be $\sim$ 0.8, if the beam size was extended to match that of the ^{13}CO observations. In Sgr B2, the ^{13}CO and HCN data was observed by Linke, Stark, & Frerking (1981). The $T_{\rm A}$ of ^{13}CO is 7.5 K and that of HCN is 2.9 K, therefore the HCN/^{13}CO is $\sim$ 0.4.

From the previous results, we can broadly divide galaxies into two groups; those that have a HCN/^{13}CO ratio $\lesssim$ 1 and those with a ratio $>$ 1. The nucleus of M51 has a low-luminosity AGN (LINER) (Rose & Searle 1982, Rose & Cecil 1983, Palumbo et al. 1985, Makishima et al. 1990, Terashima et al. 1998). As described above NGC 1068, and merger candidate ultraluminous infrared galaxies also have an active region. On the other hand, the central regions of IC 342 and Our Galaxy have neither an AGN nor an active starburst. Although we compared small samples, these results suggest that high activity regions such as AGNs and intense starburst regions tend to have higher HCN/^{13}CO ratios than in the regions of lower activities.

2.2.6 How are High-Density and High-Temperature Molecular Clouds Made ?

The physical properties of the nuclear dense molecular gas disk are very different from what is usually seen in the GMCs or the disk region of galaxies. In this section, we discuss about the heating mechanism of this component. From our observations, however, we cannot rule out either of these possibilities.

M51 has a low luminosity Seyfert 2 nucleus (Sect. 2.2.1), and therefore emitting a hard X-ray (Palumbo et al. 1985, Makishima et al. 1990, Terashima et al. 1998). The X-ray luminosity, $L_{\rm X}$, and the estimated hydrogen column density, $N_{\rm H}$, toward the nucleus of M51 are $\sim 10^{41}$ erg s^{-1} and $\gtrsim 5 \times 10^{23}$ cm^{-2}, respectively (Makishima et al. 1990, Terashima et al. 1998). According to the model calculations of Maloney, Hollenbach, & Tielens (1996) using the observed $L_{\rm X}$ and $N_{\rm H}$, the AGN of M51 can heat the molecular gas within a radius of $\sim$ 5 pc to a temperature higher than a few hundred Kelvin. This result is consistent with that of the LVG calculation results based on this work and our NMA observations.

M51 has a radio jet emitting from the nucleus with the pressure of $\sim 10^{-9}$ dyn cm^{-2} (Ford et al. 1985, Crane & van der Hulst 1992). If the molecular gas around nucleus is in pressure equilibrium with the pressure of the radio jet, the gas with the density of $\gtrsim 10^4$ cm^{-3} would be heated up to $\lesssim$ 700 K. Hence, this mechanism can also be a heating source of the dense gas disk. This is consistent with the result of Scoville et al. (1998), and supports the idea of the molecular torus/disk collimates the jet (e.g. Scoville et al. 1998, Kohno, Kawabe, & Vila-Vilaró 1999). Since the temperature is inversely proportional to the density, however, the density of higher than 10^5 cm^{-3} cannot heat

up to the temperature higher than 100 K.

The jet can also cause shocks to the surrounding gas. Therefore, the shock heating would also be possible, since this mechanism can also heat up the gas to a few thousand Kelvin. Indeed, the infrared molecular hydrogen emission line observations suggest that the molecular gas in the nuclear region of M51 may be shocked, possibly by outflows from the AGN (Lester and Thompson, 1990).

The near-infrared (near-IR) nuclear color observations of the Seyfert galaxies indicates the existence of hot ($T = 1000 - 1300$ K) dust reddened by $A_V \approx 5 - 30$ magnitude (e.g. Alonso-Herrero et al. 1998 and references therein) near AGNs. This result suggests that the collisional heating by dust around AGNs can be one of the heating mechanisms of circumnuclear molecular gas. Because of no near-IR nuclear color observation for M51, however, we cannot estimate the possibility of this heating mechanism.

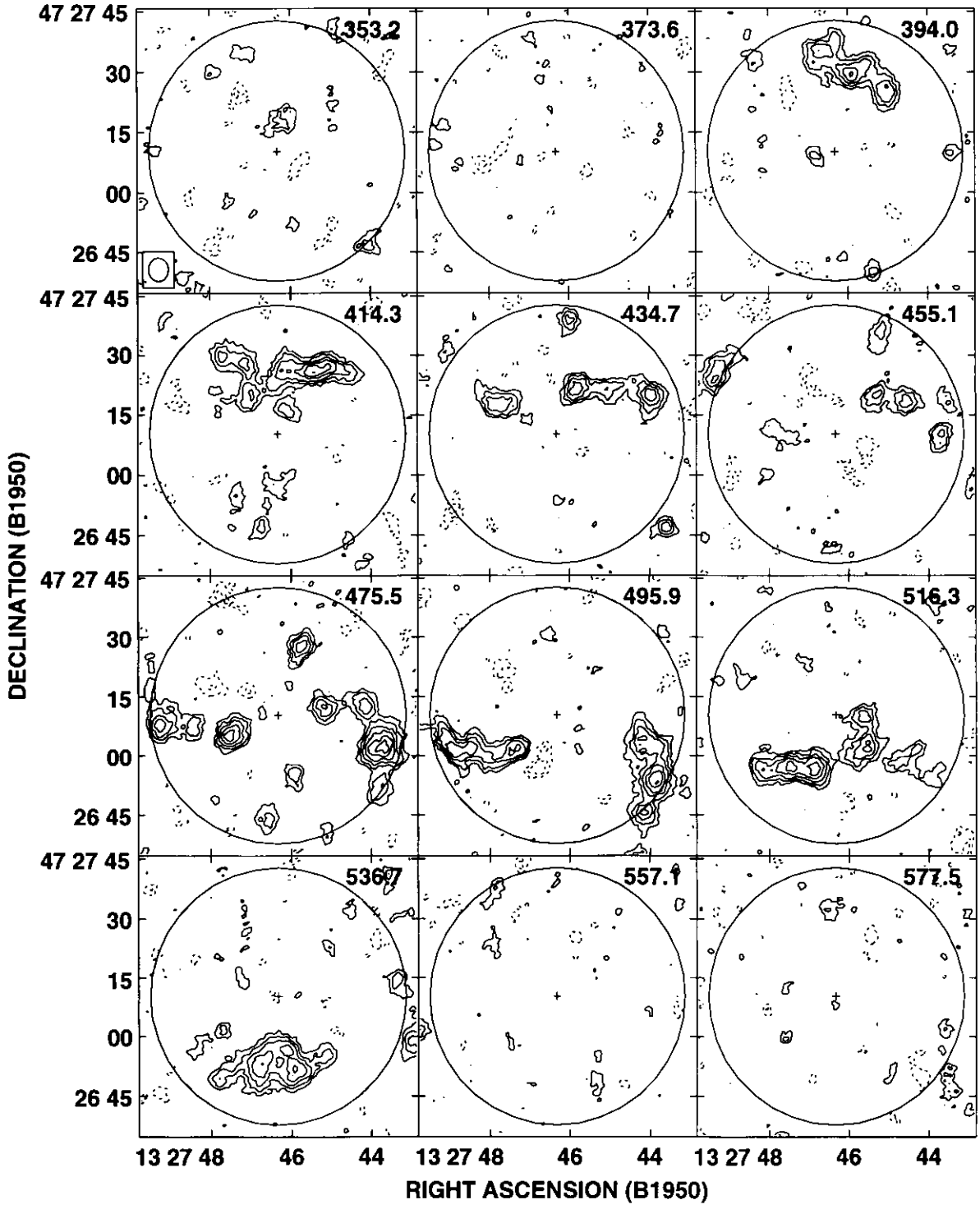

Fig. 2.1: Channel maps of ^{13}CO emission. LSR velocities are shown in the upper-right corner of each map. Synthesized beam is shown in the lower-left corner of the first channel map. The cross of each map indicates the position of the galactic nucleus determined from the peak of 6 cm radio continuum source of α(B1950)=$13^h27^m46^s.327$, δ(B1950)=$47°27'10''.25$ (Ford et al. 1985). A circle of 68″of each map is the field of view. The rms noise is $\sigma = 16$ mJy beam^{-1} = 53 mK, and the contour interval is 1 σ, with the lowest contour at 2 σ.

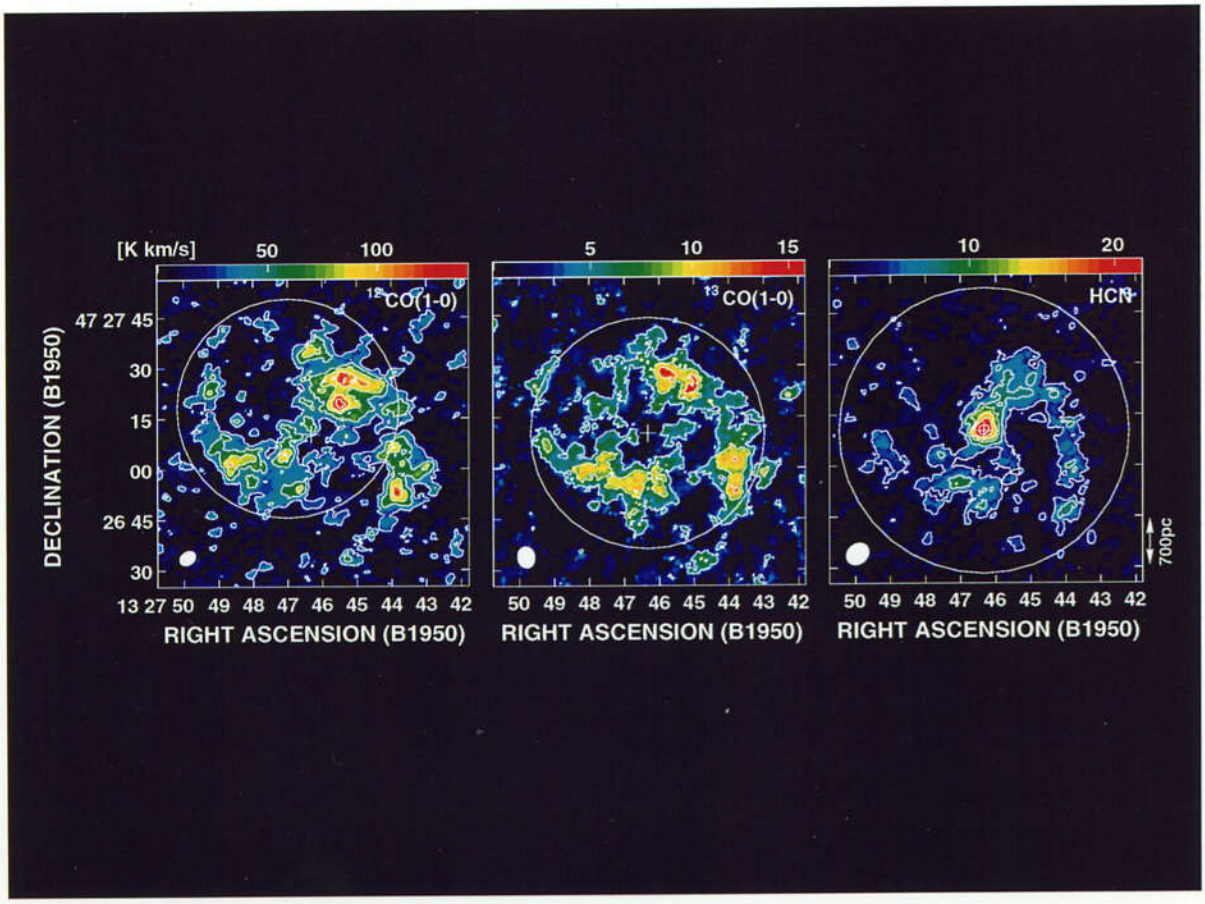

Fig. 2.2: Integrated intensity maps of ^{12}CO, ^{13}CO, and HCN lines of the central region of M51. The color scale is shown at the top of each map. The cross of each map marks the 6 cm continuum emission peak. ^{12}CO and HCN maps were taken by Kohno et al. (1996). *Left*: ^{12}CO$(1-0)$ moment map. Synthesized beam ($5\farcs1 \times 4\farcs4$, P.A. $= 138°$) is shown at the bottom-left corner. The field of view ($65''$) is indicated with a circle. The contour levels are $1.5, 3, 4.5, \cdots, 9\sigma$, where $1\ \sigma = 4.6$ Jy beam^{-1} km s^{-1} [$= 19$ K km s^{-1}]. *Middle*: ^{13}CO$(1-0)$ moment map. Synthesized beam ($5\farcs9 \times 5\farcs1$, P.A. $= 9°$) is shown at the bottom-left corner. The field of view ($68''$) is indicated with a circle. The contour levels are $1.5, 3, 4.5, \cdots, 9\sigma$, where $1\ \sigma = 0.9$ Jy beam^{-1} km s^{-1} [$= 3.0$ K km s^{-1}]. *Right*: HCN$(1-0)$ moment map. Synthesized beam ($7\farcs1 \times 5\farcs8$, P.A. $= 138°$) is shown at the bottom-left corner. The field of view ($84''$) is indicated with a circle. The contour levels are $1.5, 3, 4.5, \cdots, 9\sigma$, where $1\ \sigma = 0.6$ Jy beam^{-1} km s^{-1} [$= 2.3$ K km s^{-1}].

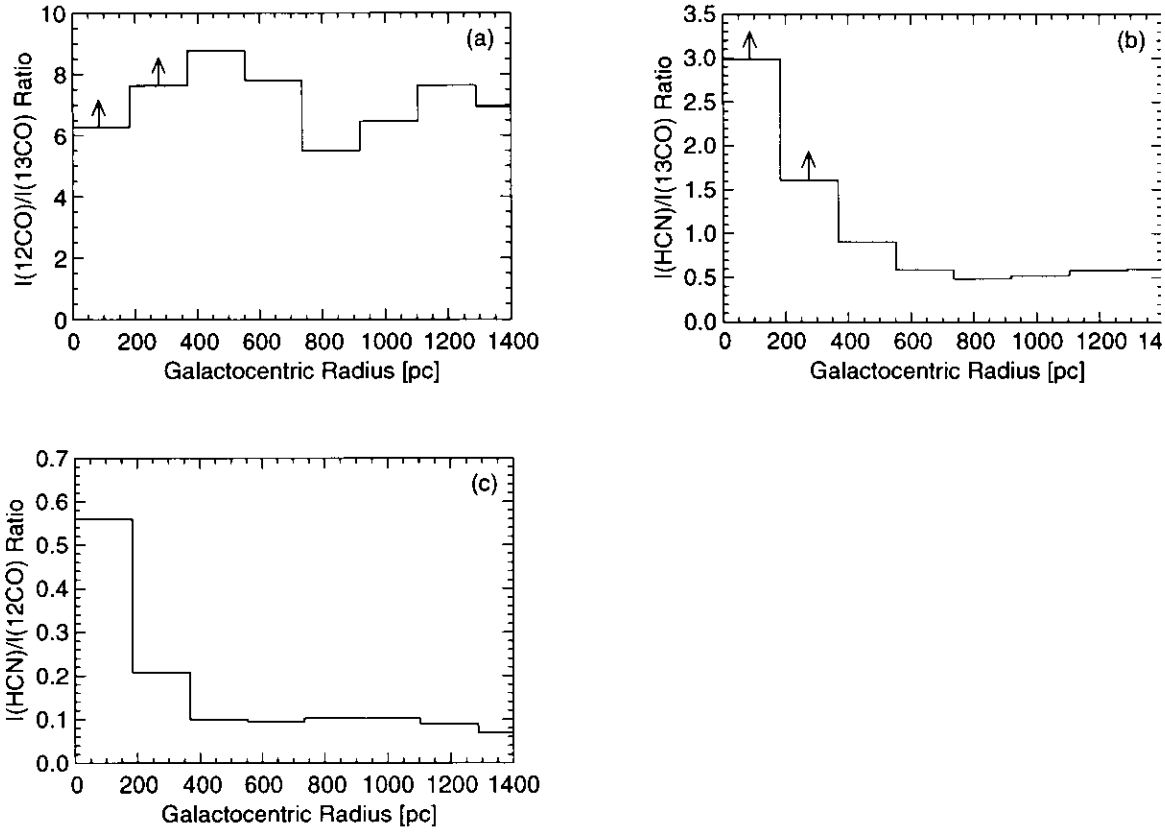

Fig. 2.3: Radial distributions of total intensity ratio. All figures were made using a task "COMB" in AIPS package to divide images each other with clipping level of 2σ, and using a task "IRING" to averaged over concentric annuli of 4″(180 pc) wide. (a) Radial distribution of ^{12}CO/^{13}CO total intensity ratio. (b) Radial distribution of HCN/^{13}CO total intensity ratio. (c) Radial distribution of HCN/^{12}CO total intensity ratio.

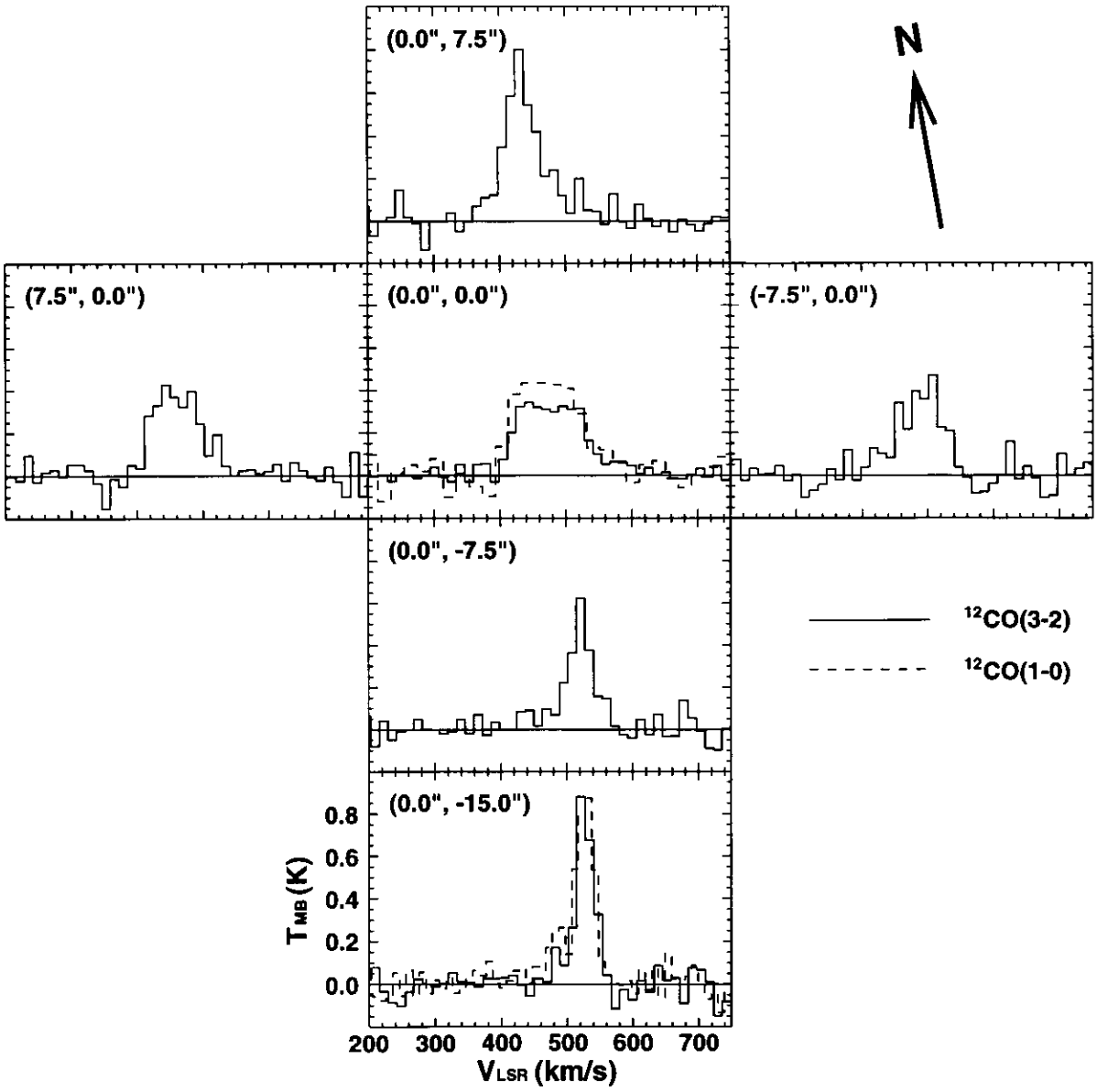

Fig. 2.4: Spectra of ^{12}CO(3 – 2) (solid line) and ^{12}CO(1 – 0) (dashed line) emission. Horizontal axis is LSR velocity, $V_{\rm LSR}$, and vertical axis is main beam temperature, $T_{\rm MB}$. The reference point (0.″0, 0.″0) is the position of the galactic nucleus determined from the peak of 6 cm radio continuum source. Other points are offset from the reference point with a P.A. of $-10°$.

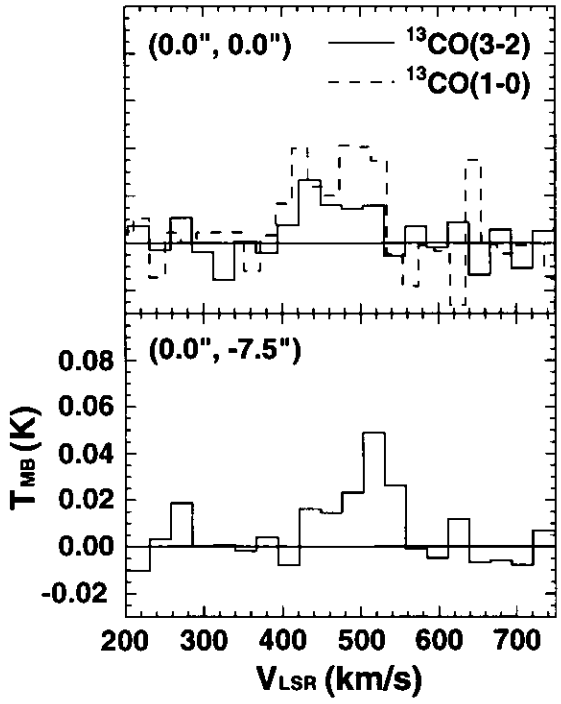

Fig. 2.5: Spectra of ^{13}CO(3 – 2) (solid line) and ^{13}CO(1 – 0) (dashed line) emission. Formats are same as in figure 2.4.

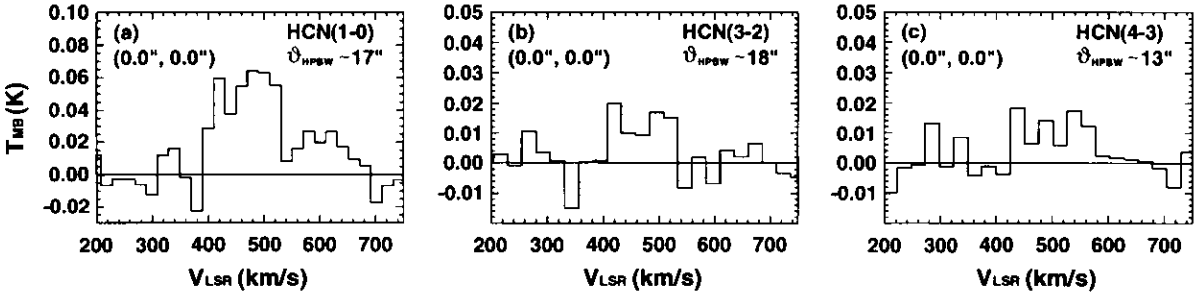

Fig. 2.6: Spectra of (a) HCN(1 – 0), (b) HCN(3 – 2), and (c) HCN(4 – 3) emission. Formats are same as in figure 2.4.

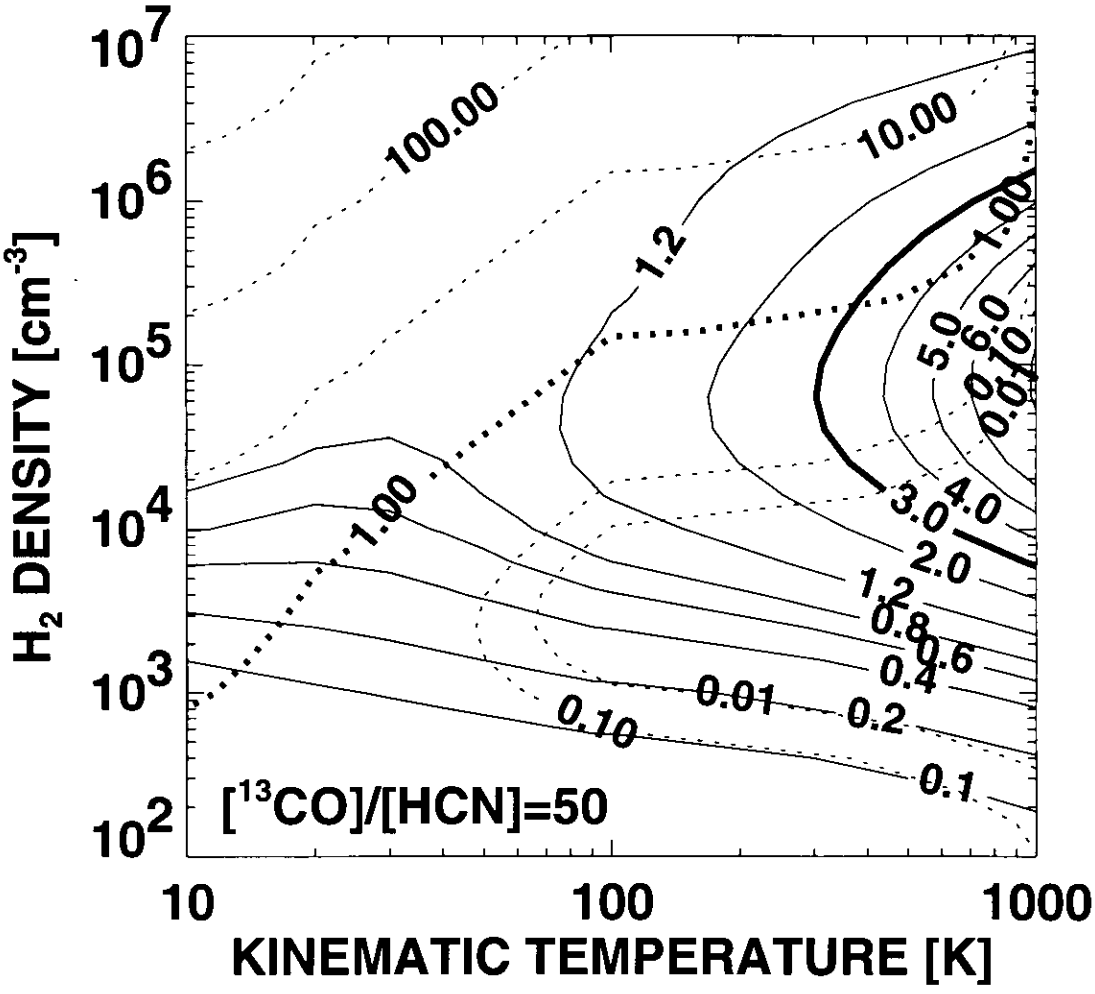

Fig. 2.7: Density (vertical axis) and temperature (horizontal axis) dependence of HCN($1-0$)/^{13}CO($1-0$) intensity ratio. Solid contours show curves of constant HCN/^{13}CO intensity ratio, and thick solid curve indicates HCN/^{13}CO ratio of 3.0. Dotted curves show ^{13}CO opacity, and thick dotted curve indicates ^{13}CO opacity of 1.0.

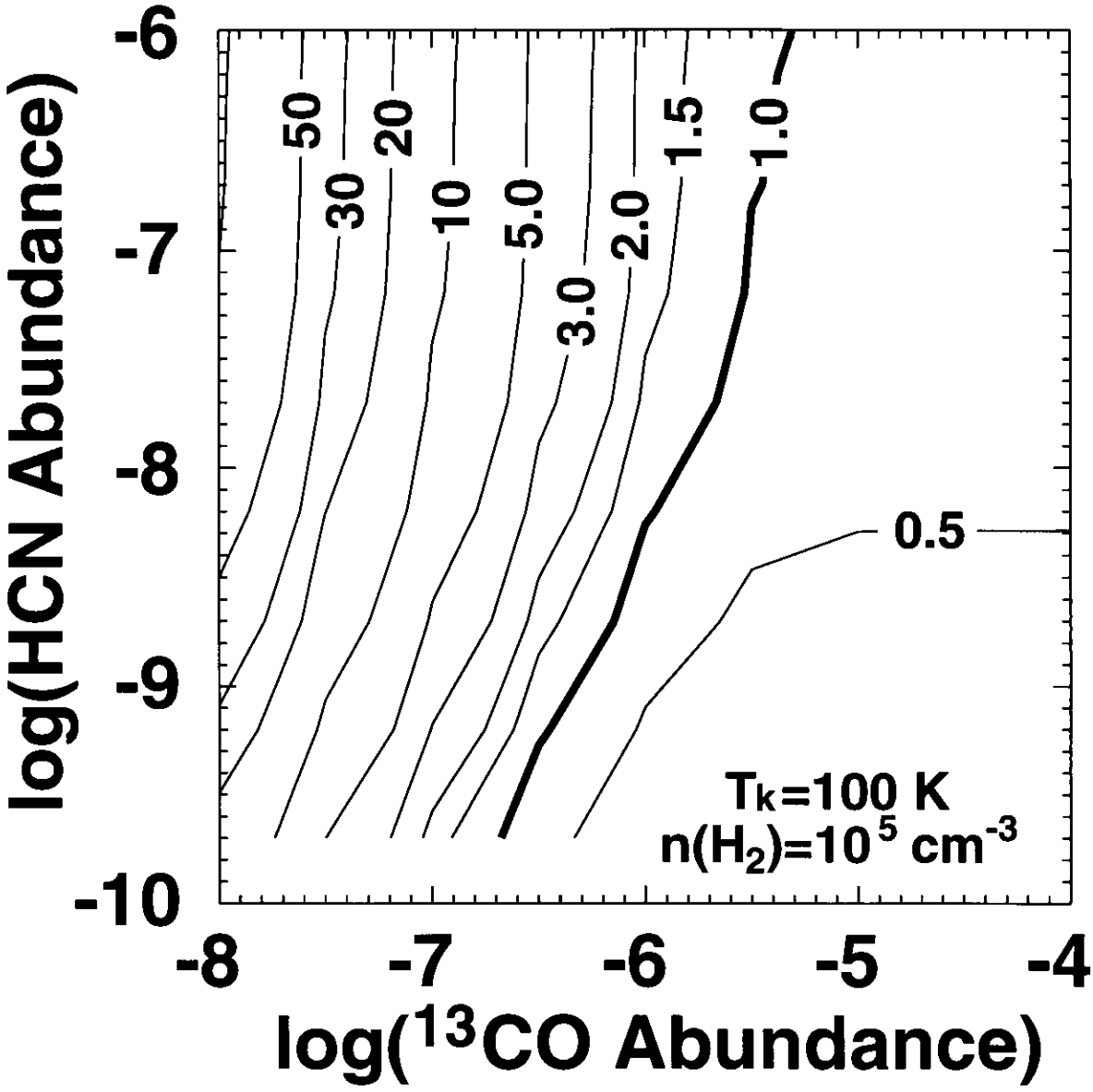

Fig. 2.8: HCN (vertical axis) and ^{13}CO (horizontal axis) abundance dependence of HCN(1 – 0)/^{13}CO(1 – 0) intensity ratio. Solid contours show curves of constant HCN/^{13}CO intensity ratio, and thick solid curve indicates HCN/^{13}CO ratio of 1.0. This figure clearly shows that the HCN abundance do not affect to the HCN/^{13}CO intensity ratios.

2.3 HCN/^{13}CO as Dense and Warm Molecular Gas Tracer II : NRO 45 m Extragalactic HCN/^{13}CO Survey

2.3.1 Background

In the previous section, we found a new probe (HCN/^{13}CO integrated intensity ratio) to get the information of the physical conditions of molecular gas, and proved by the qualitative discussions. In this section, we will discuss about this probe quantitatively. For the quantitative discussions, we perform a HCN/^{13}CO survey with observing starburst and non-starburst galaxies. These sample galaxies cover a wide range of star formation activity. We summarized the sample galaxies with basic parameters in table 2.6–2.7.

M82 and NGC 253 are located near from Our Galaxy (3.25 Mpc and 3.4 Mpc, respectively; Sandage & Tammann 1975) and show energetic properties in many wavelengths. These galaxies, therefore, have been studied by many authors, and known as prototypical starburst galaxies (e.g. Rieke et al. 1980, Rieke, Lebofsky, & Walker 1988, Devereux 1989). NGC 2146 and NGC 3504 have star formation activities comparable to M82 and NGC 253 on the basis of 1.65, 2.2, and 10 μm photometric observations (Devereux 1989, Devereux et al. 1994). NGC 2903 is one of the Sérsic-Pastoriza galaxy (a catalogue of galaxies with peculiar or complex nuclei such as "hot spots" or "amorphous nucleus"; Sérsic & Pastoriza 1965, Sérsic & Pastoriza 1967, Sérsic 1973) and its nuclear appearance was classified as "hot spot". This "hot spot" nuclear region is a powerful infrared source, and it has been proposed that this activity would be caused by a starburst (Rieke et al. 1980, Telesco & Harper 1980). This model has been supported by radio and infrared observations (Wynn-Williams & Becklin 1985). NGC 6946 has a centrally peaked molecular gas structure (Ishizuki et al. 1990, Regan & Vogel 1995), and a starburst is now ongoing at this nuclear gas concentrated region (Turner & Ho 1983, Engelbracht et al. 1996). NGC 6951 is also a Sérsic-Pastoriza galaxy, and has a $9'' \times 6''$ ($\sim 1.0 \times 0.7$ kpc assuming a distance of 24.1 Mpc; Tully 1988) circumnuclear "hot spot" ring (Barth et al. 1995, Elmegreen et al. 1999). This ring is bright in Hα (Wozniak et al. 1995, González-Delgado et al. 1997) and shows high star formation rate (SFR) of $\sim 3 - 4$ M$_\odot$yr^{-1} and also high star formation efficiency (SFE) which is comparable to those in the central regions of nearby starburst galaxies (Kohno, Kawabe, & Vila-Vilaró 1999, Kohno 1997, Wozniak et al. 1995).

Optical spectra of the central regions of both NGC 4736 and NGC 5195 show strong Balmer absorption lines (Ho, Filippenko, & Sargent 1995, Taniguchi et al. 1996, Sauvage et al. 1996, Greenawalt et al. 1998). Since these strong Balmer absorption lines are the typical spectra of A-type stars, the stellar populations of galaxies that have these absorption lines would be dominated by these stars. Indeed the stellar population synthesis implies that stellar populations of NGC 4736 and NGC 5195 are extend up to at most A4 to A7, and optical light is dominated by these stellar populations (Pritchet 1977, Warner 1974). The possible mechanism of making the A-type star dominated galaxies is as follows; starburst would produce enormous numbers of early to late-type stars, assuming a normal initial mass function. Early-type stars (OB stars) would live at most 10^8 years, so that at the time of 10^9 years after the beginning of the starburst, early-type stars would be burned out, and the vast numbers of A-type stars would remain. Therefore

Table 2.6: Basic parameters of the starburst galaxy sample.

Galaxy	Type*	α(B1950)	δ(B1950)	Ref.†	Dist.§	Ref.¶
NGC 253	SAB(s)c	$00^h45^m05^s.63$	$-25°33'40''.5$	1	3.4	8
NGC 2146	SB(s)ab pec	$06^h10^m41^s.10$	$+78°22'28''.1$	2	17.2	9
NGC 2903	SAB(rs)bc	$09^h29^m20^s.26$	$+21°43'20''.74$	3	7.6	8
M82	I0 sp	$09^h51^m43^s.5$	$+69°55'00''.0$	4	3.25	8
NGC 3504	(R)SAB(s)ab	$11^h00^m28^s.53$	$+28°14'31''.2$	5	26.5	9
NGC 6946	SAB(rs)cd	$20^h33^m49^s.2$	$+59°58'49''.5$	6	10.5	8
NGC 6951	SAB(rs)bc	$20^h36^m36^s.59$	$+65°55'46''.0$	7	24.1	9

* Morphological type taken from RC3.
† References for the positions.
§ Distance in Mpc.
¶ References for distance.
References — (1) Keto et al. 1993. (2) Condon et al. 1982. (3) 2.2 μm peak of Wynn-Williams & Becklin 1985. (4) Shen & Lo 1995. (5) Condon et al. 1990. (6) Turner & Ho 1983. (7) Saikia et al. 1994. (8) Sandage & Tammann 1975. (9) Tully 1988.

the galaxies with numerous A-type stars would be explained as post-starburst galaxies (Rieke 1988, Rieke, Lebofsky, & Walker 1988, Walker, Lebofsky, & Rieke 1988). Recent millimeter wave molecular gas observations support this suggestion that there is little molecular gas (Tosaki & Shioya 1997), or even exist, molecular gas is stable against gravitational instability (Shioya et al. 1998) and almost no high-density gas (Kohno 1997) in the Balmer absorption dominated regions. Therefore, we classified NGC 4736 and NGC 5195 as "post-starburst" as other literatures classified. NGC 4826 is classified as a type 2 transition object (which has the middle of stellar and non-stellar excitation and with no broad wing; Ho, Filippenko, & Sargent 1997). Even if all of the Hα emission of this galaxy originates from star forming regions, the extinction corrected total Hα luminosity, L(Hα), of 5.7×10^{40} erg s^{-1} (Young et al. 1996) indicates the SFR of only ~ 0.5 M$_\odot$ yr^{-1}, using the relationship between the SFR and the L(Hα) of (Kennicutt 1983)

$$\mathrm{SFR} = \frac{L(\mathrm{H}\alpha)}{1.12 \times 10^{41} \mathrm{ergs}^{-1}} \mathrm{M}_\odot \mathrm{yr}^{-1}. \quad (2.4)$$

Hence this galaxy might be regarded as a non-starburst galaxy.

2.3.2 Observations

Observations of the central regions of nearby galaxies using the Nobeyama 45 m telescope were carried out in the HCN(1 – 0), ^{13}CO(1 – 0), and ^{12}CO(1 – 0) lines (rest frequency = 86.6316024 GHz, 110.201353 GHz, and 115.271204 GHz, respectively) during 1997 February – April and 1997 December for starburst sample, 1998 March – April for non-starburst sample and M82, and 1999 March – April for NGC 6951. We observed ^{13}CO and HCN simultaneously for the starburst sample and NGC 6951, and ^{13}CO and ^{12}CO for the non-starburst sample and M82. Since we observed two lines simultaneously with using two SIS receivers, there are no relative pointing offsets between these two lines. The half power beam widths (HPBW) for the ^{13}CO and HCN simultaneous observations (except NGC 6951) were 15″and 17″, and the main-beam efficiencies were $\eta_{\mathrm{mb}} = 0.51 \pm 0.03$

Table 2.7: Basic parameters of the non-starburst galaxy sample.

Galaxy	Type*	α(B1950)	δ(B1950)	Ref.†	Dist.§	Ref.¶	Activity‡
NGC 4736	(R)SA(r)ab	$12^h48^m31^s.910$	$+41°23'31''.78$	1	4.3	3	Post-SB
NGC 4826	(R)SA(rs)ab	$12^h35^m16^s.07$	$+21°57'13''.5$	2	4.1	3	(LINER)
NGC 5195	I0 pec	$13^h27^m53^s.27$	$+47°31'25''.5$	2	9.3	3	Post-SB

* Morphology types taken from RC3.
† References for the positions.
§ Distance in Mpc.
¶ References for distance.
‡ Star formation activity. "SB" indicates starburst.
References — (1) Turner & Ho 1994. (2) Hummel et al. 1987. (3) Tully 1988.

and 0.47 ± 0.02, respectively. The HPBW for NGC 6951 observations with ^{13}CO and HCN lines were 15″and 18″, and the main-beam efficiencies were $\eta_{\rm mb} = 0.48 \pm 0.02$ and 0.49 ± 0.02, respectively. The HPBW for the ^{13}CO and ^{12}CO simultaneous observations were both 14″, and the main-beam efficiencies were $\eta_{\rm mb} = 0.40 \pm 0.03$ and 0.51 ± 0.03, respectively. The telescope pointing was check and corrected every one hour, and the absolute pointing errors were less than 4″ during the observations. As back-ends, we used 2048-channel wide band acousto-optical spectrometers (AOS), with a total bandwidth of 250 MHz, corresponds to 650 km s^{-1} at the ^{12}CO(1 – 0) frequency. The line intensity calibration was accomplished by the chopper-wheel method (Ulich & Haas 1976), and the relative intensity errors were calibrated at every observation with the intensity of W51 main for NGC 6951 and IRC+10216 for the rest of the observations.

We observed central regions of sample galaxies pointed to the nuclei except for M82. M82 was observed toward five points for ^{13}CO and HCN lines, and three points for ^{12}CO lines. Observed positions for M82 were the nucleus (0″, 0″), and (-15″, -3″) and (-30″, -6″) in R.A. and Decl. offset from the nucleus with three lines. In addition, ^{13}CO and HCN observations were pointed toward (-45″, -9″) and (10″, -6″) offset from the nucleus. The basic parameters of the starburst galaxy sample are summarized in table 2.6, and those of non-starburst galaxy sample are summarized in table 2.7.

2.3.3 Results

We detected the observed lines from all of the sample galaxies. The observed properties (peak temperature and integrated intensity) are summarized in table 2.8, and calculated integrated intensity ratios are summarized in table 2.9. Since we did not observe HCN lines for the non-starburst galaxy sample, we use the HCN data taken by Kohno (1997).

Figure 2.9 shows the ^{12}CO, ^{13}CO, and HCN line spectra of the observed points of the central region of M82, which is one of the starburst galaxy sample. Overall lineshapes of each observed points are similar between these three lines, but line intensity ratios are clearly different. ^{13}CO is weak compared with other two lines at the center (high HCN/^{13}CO and ^{12}CO/^{13}CO integrated intensity ratios), but on the other hand, HCN is very weak at off-center (low HCN/^{13}CO and HCN/^{12}CO ratios). The changes of the intensity ratios are gradual. Intensity ratios at the center are high, but the ratios get gradually lower as the offsets get larger.

Figures 2.10–2.11 show ^{13}CO(1 – 0) and HCN(1 – 0) line spectra of other starburst

Table 2.8: Observed properties for sample galaxies.

Galaxy	Position*	$T_{MB}(^{12}CO)$†	$T_{MB}(^{13}CO)$†	T_{MB}(HCN)†	I(^{12}CO)§	I(^{13}CO)§	I(HCN)§
NGC 253	(0″, 0″)	—	0.43 ± 0.03	0.42 ± 0.02	—	168 ± 15	258 ± 22
NGC 2146	(0″, 0″)	—	0.074 ± 0.015	0.072 ± 0.007	—	16.0 ± 1.3	12.3 ± 0.7
NGC 2903	(0″, 0″)	—	0.074 ± 0.008	0.066 ± 0.009	—	9.1 ± 0.7	9.8 ± 0.6
M82	(0″, 0″)	3.52 ± 0.08	0.23 ± 0.03	0.27 ± 0.02	565 ± 33	34.5 ± 2.6	55.4 ± 2.6
	(+10″, +6″)	—	0.76 ± 0.04	0.70 ± 0.04	—	66.1 ± 4.4	71.2 ± 3.6
	(−15″, −3″)	6.02 ± 0.13	0.49 ± 0.03	0.39 ± 0.03	646 ± 38	45.2 ± 2.9	36.2 ± 1.9
	(−30″, −6″)	2.61 ± 0.33	0.27 ± 0.05	0.17 ± 0.02	288 ± 20	29.0 ± 2.8	12.2 ± 0.9
	(−45″, −9″)	—	0.17 ± 0.05	< 0.08	—	12.7 ± 2.2	< 3.2
NGC 3504	(0″, 0″)	—	0.052 ± 0.005	0.060 ± 0.009	—	7.7 ± 0.5	10.1 ± 0.6
NGC 6946	(0″, 0″)	—	0.152 ± 0.012	0.151 ± 0.008	—	21.9 ± 1.4	21.4 ± 1.0
NGC 6951	(0″, 0″)	—	0.055 ± 0.009	0.034 ± 0.007	—	8.1 ± 0.6	6.1 ± 0.5
NGC 4736	(0″, 0″)	0.26 ± 0.01	0.043 ± 0.012	—	44.1 ± 2.7	6.3 ± 1.4	—
NGC 4826	(0″, 0″)	0.53 ± 0.05	0.11 ± 0.03	—	87.0 ± 5.9	17.2 ± 3.6	—
NGC 5195	(0″, 0″)	0.26 ± 0.04	0.10 ± 0.02	—	37.9 ± 2.8	12.0 ± 2.2	—

* Offset from the position of the nucleus indicated in table 2.6–2.7.
† Peak main-beam temperature in K. Quoted uncertainties are 1σ and upper limits are 2σ.
§ Integrated intensity in K km s^{-1}. We define integrated intensity as $I = \int T_{MB} dv$. Quoted uncertainties are 1σ and upper limits are 2σ.

galaxy sample, and Figure 2.12 shows ^{13}CO(1 − 0) and ^{12}CO(1 − 0) line spectra of non-starburst galaxy sample. I(^{12}CO) of NGC 4736 agrees with that of Kohno (1997), but I(^{12}CO) of NGC 4826 and NGC 5195 differ 67% and 46% from his results. These disagreements may be due to pointing error and/or calibration error. Pointing error of our observations was $\sim$ 4″, larger than that of Kohno (1997) of $\sim$ 2″. On the other hand, Kohno (1997) did not observe any intensity calibrator as we did with IRC+10216. Therefore, the intensity ratios of HCN and other lines of these galaxy may have $\sim$ 30% and $\sim$ 50% error. As mentioned above, since other galaxies are observed HCN and ^{13}CO lines simultaneously, there are no HCN/^{13}CO integrated intensity ratio errors caused by the relative pointing offsets.

The average HCN/^{13}CO ratio of the center ((0″, 0″) point) of the starburst galaxy sample is 1.15, and that of the starburst region of M82 ((+10″,+6″), (0″, 0″), and (-15″, -3″) points) is also similar value of 1.16. However, the average HCN/^{13}CO ratios of the center of the non-starburst galaxy sample and the non-starburst region of M82 ((-30″, -6″) and (-45″, -9″) points) are only 0.31 and 0.34, respectively. Even we consider about the intensity error of NGC 4826 and NGC 5195, the average HCN/^{13}CO ratio is quite different between starburst and non-starburst regions. On the other hand, the average ^{12}CO/^{13}CO ratio of the starburst region of M82 is 15.4, but those of the non-starburst galaxy sample and the non-starburst region of M82 are 5.1 and 9.9, respectively. Since the average value of the ^{12}CO/^{13}CO ratio at the center of galaxies is about 10 (Sage & Isbell 1991, Young & Sanders 1986), the starburst regions of M82 have higher ^{12}CO/^{13}CO ratios but the non-starburst regions do not. These results show that both the HCN/^{13}CO and ^{12}CO/^{13}CO ratio have higher values at the active star forming regions than the non-starburst regions, indicate that the physical conditions of molecular gas in starburst regions would be different from that of non-starburst regions.

Table 2.9: Integrated intensity ratios for sample galaxies.

Galaxy	Position*	HCN/^{13}CO†	^{12}CO/^{13}CO†	HCN/^{12}CO†
NGC 253	$(0'', 0'')$	1.53 ± 0.19	5.6 ± 0.5§	0.274 ± 0.024§
NGC 2146	$(0'', 0'')$	0.77 ± 0.08	—	—
NGC 2903	$(0'', 0'')$	1.08 ± 0.11	—	—
M82	$(0'', 0'')$	1.61 ± 0.14	16.4 ± 1.6	0.098 ± 0.007
	$(+10'', +6'')$	1.08 ± 0.09	—	—
	$(-15'', -3'')$	0.80 ± 0.07	14.3 ± 1.2	0.056 ± 0.004
	$(-30'', -6'')$	0.42 ± 0.05	9.9 ± 1.2	0.042 ± 0.004
	$(-45'', -9'')$	0.25 ± 0.04	—	—
NGC 3504	$(0'', 0'')$	1.32 ± 0.12	—	—
NGC 6946	$(0'', 0'')$	0.98 ± 0.08	—	—
NGC 6951	$(0'', 0'')$	0.75 ± 0.08	—	—
NGC 4736	$(0'', 0'')$	< 0.32¶	7.0 ± 1.6	< 0.042‡
NGC 4826	$(0'', 0'')$	0.48 ± 0.10¶	5.0 ± 1.1	0.063‡
NGC 5195	$(0'', 0'')$	0.13 ± 0.06¶	3.2 ± 0.6	0.018‡

* Offset from the position of the nucleus indicated in table 2.6–2.7.
† Ratios of integrated intensity indicated in table 2.8. Quoted uncertainties are 1σ, and upper limits are 2σ.
§ ^{12}CO(1 – 0) intensity data taken from Sorai et al. (2000a).
¶ HCN(1 – 0) intensity data taken from Kohno (1997).
‡ HCN/^{12}CO intensity ratio data taken from Kohno (1997).

2.3.4 Discussions

Physical conditions of molecular gas in sample galaxies

For the detail comparisons between the physical conditions of the molecular gas in starburst and non-starburst galaxies, we derived those from the observed line ratios (table 2.9) based on the LVG approximation. As we discussed in section 2.2.4, the HCN/^{13}CO ratio can give constraint on both temperature and density to only high HCN/^{13}CO ratio objects, and give no constraint on temperature to low HCN/^{13}CO ratio objects. Hence, to give temperature information on the low HCN/^{13}CO ratio objects, we have to derive the physical conditions with other line ratios. Since we observed ^{12}CO(1 – 0) lines for non-starburst galaxies and a part of M82, we can obtain additional constraint on the physical properties from ^{12}CO(1 – 0)/^{13}CO(1 – 0) ratios and HCN(1 – 0)/^{12}CO(1 – 0) ratios for these objects. We therefore newly calculated the physical conditions based on the LVG approximation for ^{12}CO/^{13}CO and HCN/^{12}CO ratios.

Line intensity ratios for CO and HCN molecules were calculated as a function of the H_2 number density, $n(H_2)$, from 10^1 to 10^6 cm^{-3}, and the kinetic temperatures, T_k, from 10 to 1000 K. The collision rates of the CO molecule of $\leq$ 250 K were available from Flower & Launay (1985) and of $\geq$ 500 K were available from McKee et al. (1982). Those of the HCN molecule of $<$ 100 K were available from Green & Thaddeus (1974) and of $\geq$ 100 K were available from Green (1993). We fixed the abundances to the 'standard'

relative abundance as $Z(^{13}\mathrm{CO}) = [^{13}\mathrm{CO}]/[\mathrm{H_2}] = 1 \times 10^{-6}$ (Solomon, Scoville, & Sanders 1979), $Z(\mathrm{HCN}) = [\mathrm{HCN}]/[\mathrm{H_2}] = 2 \times 10^{-8}$ (Irvine, Goldsmith, & Hjalmarson 1987) and $[^{12}\mathrm{CO}]/[^{13}\mathrm{CO}] = 50$. We also fixed the velocity gradient, dv/dr, as a general value of 1.0. The calculated results are shown in figure 2.13.

Using the LVG calculation results shown in the figures 2.7 and 2.13, we derived the physical conditions of molecular gas in the sample galaxies. We summarized the derived properties in table 2.10. The results clearly show that galaxies with higher HCN/^{13}CO ratio tend to have higher temperature, and also show that the starburst galaxies tend to have higher density ($n(\mathrm{H_2}) \gtrsim 10^4$ cm^{-3}) and higher temperature ($T_\mathrm{k} \gtrsim 50$ K) than those of the non-starburst galaxies of $n(\mathrm{H_2}) \sim 10^3$ cm^{-3} and $T_\mathrm{k} \lesssim 60$ K. We therefore suggest that the star formation activity might be closely related with high-density and high-temperature molecular gas.

Similar to the HCN/^{13}CO ratio, galaxies (or regions) with higher ^{12}CO/^{13}CO ratios also tend to have higher temperature. High ^{12}CO/^{13}CO ratios in merging galaxies are also reported by many authors (Aalto et al. 1991a, Aalto et al. 1991b, Casoli, Dupraz, & Combes 1992a, Casoli, Dupraz, & Combes 1992b, Aalto et al. 1995, Aalto et al. 1997). These merging galaxies have ultraluminous infrared properties, so that these galaxies might also have active star forming regions. These results indicates that the ^{12}CO/^{13}CO ratio might also be a good tracer for the temperature (or star formation activity) of molecular gas. This can be explained by the similar mechanism as the HCN/^{13}CO ratio that ^{12}CO is optically thick line as HCN even the temperature is high. On the other hand, ^{13}CO would be getting optically thin (the populations of the energy level would move to higher level) when the kinetic temperature is getting high, and therefore the intensity of ^{13}CO line would be weak, and the ^{12}CO/^{13}CO ratio would be high. One problem in this ratio is that, as can be seen in the figure 2.13, ^{12}CO/^{13}CO ratio cannot decide the detail physical conditions of molecular gas with only this ratio. To know the physical conditions, the observations of high-density tracers such as HCN would be needed. In this point, the HCN/^{13}CO ratio is a better tracer than the ^{12}CO/^{13}CO ratio.

Relation between molecular gas and dust

Since the ratios of the infrared flux taken by Infrared Astronomical Satellite (IRAS) would be one of the good indicators for the star formation activities (Helou 1986; see also reviews of Soifer, Houck, & Neugebauer 1987, Telesco 1993), we compared the HCN/^{13}CO ratios with the IRAS flux ratios. Since the 12 μm flux is dominated by the radiation from IR cirrus clouds heated by general interstellar radiation field, and from outflow materials of OH/IR stars (Cox, Krügel, & Mezger 1986), these radiation do not depend on the star formation activities, and it is reasonable to assume that the 12 μm flux exist constantly in all galaxies. We therefore made IRAS flux ratios between 12 μm and other wavelength ($\log(F_{12}/F_{25})$, $\log(F_{12}/F_{60})$, and $\log(F_{12}/F_{100})$), which ratios mean 25 μm, 60 μm, and 100 μm flux densities normalized by 12 μm flux density. The IRAS data and infrared flux ratios of sample galaxies are summarized in table 2.11.

Using the HCN/^{13}CO ratios and infrared flux ratios of sample galaxies listed in table 2.9 and table 2.11, respectively, we made correlation diagrams in figures 2.14–2.15. The figure 2.14 clearly shows that the HCN/^{13}CO ratios strongly correlate with the IRAS $\log(F_{12}/F_{25})$ ratios, and indicates that lower $\log(F_{12}/F_{25})$ ratio (steep spectrum with large 25 μm flux excess from 12 μm flux) galaxies tend to have higher HCN/^{13}CO ratios. These low $\log(F_{12}/F_{25})$ ratio and high HCN/^{13}CO ratio galaxies are dominated

Table 2.10: Physical conditions of molecular gas in the sample galaxies.

Galaxy	Position*	$n(\mathrm{H_2})^\dagger$	$T_\mathrm{k}^\S$
NGC 253	$(0'', 0'')$	$\sim 2-3\times10^4$	~ 100
NGC 2146	$(0'', 0'')$	$\lesssim 5\times10^4$	—
NGC 2903	$(0'', 0'')$	$\gtrsim 10^4$	$\gtrsim 50$
M82	$(0'', 0'')$	$\sim 6\times10^3 - 2\times10^4$	$\sim 200-300$
	$(+10'', +6'')$	$\gtrsim 10^4$	$\gtrsim 50$
	$(-15'', -3'')$	$\sim 3-5\times10^3$	~ 200
	$(-30'', -6'')$	$\sim 2-3\times10^3$	~ 100
	$(-45'', -9'')$	$\lesssim 5\times10^3$	—
NGC 3504	$(0'', 0'')$	$\gtrsim 10^4$	$\gtrsim 100$
NGC 6946	$(0'', 0'')$	$\gtrsim 10^4$	$\gtrsim 50$
NGC 6951	$(0'', 0'')$	$\lesssim 5\times10^4$	—
NGC 4736	$(0'', 0'')$	$\lesssim 2\times10^3$	$\lesssim 60$
NGC 4826	$(0'', 0'')$	$\sim 3-5\times10^3$	$\sim 50-60$
NGC 5195	$(0'', 0'')$	$\sim 0.8-2\times10^3$	$\sim 10-20$

* Offset from the position of the nucleus indicated in table 2.6–2.7.
† Molecular hydrogen number density in $\mathrm{cm^{-3}}$.
§ Kinetic temperature in K.

by starburst galaxies. On the other hand, non-starburst galaxies tend to have high $\log(F_{12}/F_{25})$ ratios (flat spectrum) and low HCN/^{13}CO ratios. This correlation does not hold in NGC 5195. We will discuss this galaxy later. The figure 2.15 shows that the IRAS $\log(F_{12}/F_{60})$ ratios are loosely correlated with HCN/^{13}CO ratios, and IRAS $\log(F_{12}/F_{100})$ ratios have almost no correlation. These results indicates that warmer dust (shorter infrared wavelength components) would be related with HCN/^{13}CO ratios.

For the detail comparison of the physical conditions of molecular gas and dust, we fit blackbody spectra to the infrared spectral energy distribution (SED) of sample galaxies. Since the infrared SED of Our Galaxy can be fit by mainly three components, cold dust of $T \sim 15-25$ K, warm dust of $T \sim 30-40$ K, and hot dust of $T \sim 250-500$ K (Cox, Krügel, & Mezger 1986), we used similar blackbody temperature of $T = 20$ K, 50 K, and 350 K for the infrared SED fitting. These three blackbody components are, however, not enough to fit the low $\log(F_{12}/F_{25})$ ratio galaxies. Hence, we also used 100 K component in addition to other three blackbody components, Examples of the blackbody fitting results of sample galaxies are shown in figure 2.16. The fitting results clearly show that the $\log(F_{12}/F_{25})$ ratio indicates the fraction of the 100 K dust component relative to hot dust component. The infrared SED of the starburst galaxy M82, which is one of the lowest $\log(F_{12}/F_{25})$ ratio galaxy in the sample galaxies, have large amount of the 100 K dust component, but that of the post-starburst galaxy NGC 4736, which is one of the highest $\log(F_{12}/F_{25})$ ratio galaxy, have almost no 100 K dust component. The moderate $\log(F_{12}/F_{25})$ ratio galaxy NGC 6951 have moderate amount of 100 K dust component, not so large amount as M82 but larger amount than NGC 4736.

As discussed in the previous subsection, the HCN/^{13}CO ratio traces the temperature

Table 2.11: IRAS data and infrared flux ratios of sample galaxies.

Galaxy	F^*_{12}	F^*_{25}	F^*_{60}	F^*_{100}	$\log(F_{12}/F_{25})$	$\log(F_{12}/F_{60})$	$\log(F_{12}/F_{100})$
NGC 253	24.02	119.7	784.2	993.1	−0.70	−1.51	−1.62
NGC 2146	6.228	17.58	131.0	184.2	−0.45	−1.32	−1.47
NGC 2903	1.428	2.896	35.83	100.8	−0.31	−1.40	−1.85
M82	57.38	267.8	1089	1150	−0.67	−1.28	−1.30
NGC 3504	1.060	3.726	21.20	32.70	−0.55	−1.30	−1.49
NGC 6946	2.545	6.745	53.89	160.0	−0.42	−1.33	−1.80
NGC 6951	0.6169	1.374	13.21	37.47	−0.35	−1.33	−1.78
NGC 4736	5.33	6.13	69.20	121.52	−0.06	−1.11	−1.36
NGC 4826	1.913	2.538	34.38	74.50	−0.12	−1.25	−1.59
NGC 5195	0.7211	1.453	10.35	< 74.38	−0.30	−1.16	> -2.01

$*$ Flux densities in Jy, taken by IRAS.

(and also density) of molecular gas. High HCN/^{13}CO ratio indicates the presence of the $\gtrsim$ 100 K molecular gas. On the other hand, the low $\log(F_{12}/F_{25})$ ratio indicates the existence of $\sim$ 100 K dust component. Taking the correlation between $\log(F_{12}/F_{25})$ ratios and HCN/^{13}CO ratios, and the similarity of the temperature of molecular gas and dust into consideration, the existence of the 100 K dust component would be closely related with the existence of $\gtrsim$ 100 K molecular gas, and both materials might be located in the same place, well mixed, and therefore in temperature equilibrium. Because of the tight correlation of the existence of dense molecular gas and the star formation activity (Solomon, Downes, & Radford 1992, Kohno, Kawabe, & Vila-Vilaró 1999), the 100 K dust component would also closely related with star formation activity. The most effective heating source in the star forming regions is supernova explosions (section 2.4.5), so that the heating mechanisms of dust and molecular gas would be shock heating and/or cosmic ray heating. As mentioned in section 2.2.6, shock can heat the gas to more than a few hundred Kelvin, so that shock heating can be the heating mechanism of molecular gas and dust. Cosmic ray from supernova explosions can also heat the gas up to a few hundred Kelvin (Suchkov, Allen, & Heckman 1993), so that this mechanism can also be the heating mechanism.

Comments on NGC 5195

As mentioned above, NGC 5195 is one of the post-starburst galaxy which shows strong Balmer line absorptions and a small amount of dense gas, and so on. The nuclear region of this galaxy, however, is very bright in infrared. Infrared Space Observatory (ISO) 15 μm observations show very bright point-like source, although this source do not show any correspondence with Hα distribution as the sources of NGC 5194 (M51) do (Sauvage et al. 1996). Dust temperature indicates unusually high value of $\sim$ 65 K, relative to M51 and Our Galaxy of $\sim 20 - 30$ K (Smith 1982). Hα images show diffuse, filamentary structures, which is similar to that seen in the outflows from the starburst region of M82 (Greenawalt et al. 1998). The X-ray image also shows extended structure in north-south direction as the Hα image (Ehle, Pietsch, & Beck 1995, Greenawalt et al. 1998), which is also similar to the Hα–X-ray configuration of M82. These observational results suggest

that NGC 5195 might be a very early phase of post-starburst (or a very late phase of starburst), which have almost no dense molecular gas and massive star formations, but still have stronger interstellar radiation field (ISRF) than other non-starburst galaxies. Indeed, the strength of the ISRF of this galaxy is possible to heat the dust to the observed properties (Boulade et al. 1996).

However, our molecular line observations suggest that the temperature of molecular gas would be only $\sim 10-20$ K, three times or more lower than that of dust. One of the possible explanations of this difference would be that molecular gas and dust are located at the different regions and therefore these materials are not in temperature equilibrium, and also the molecular gas emission comes from mainly cold component and the dust emission comes from warm component. NGC 5195 is interacting with NGC 5194 and the molecular gas of the arm of NGC 5194 is overlapping (Sage 1989, Sage 1990), so that there is a possibility of the molecular gas emission comes from cold molecular gas located in the arm of NGC 5194 and the dust emission comes from the nucleus of NGC 5195. However, the velocity component of the molecular gas in NGC 5195 (velocity range of $\sim 500-800$ km s^{-1}) and that of the arm of NGC 5194 (velocity range of $\sim 350-500$ km s^{-1}) are obviously different (Sage 1989, Sage 1990), and our data mainly come from NGC 5195, this explanation would be in difficulty. Other possibility is that the warm dust component is located at the circumnuclear ring seen in the optical B-band minus 15 μm image which have a radius of 12″(Block et al. 1997), or diffuse H II regions located around the nucleus (Greenawalt et al. 1998), because these structures are located well outside of our beam size. The post-starburst region of NGC 5195 is only the central several arcsec, and our observations are looking just at this region. Therefore our observational results tend to indicate the post-starburst properties. To make clear this problem, high spatial-resolution mapping observations of NGC 5195 with multi-molecular line, and derive the spatial physical conditions of molecular gas would be needed.

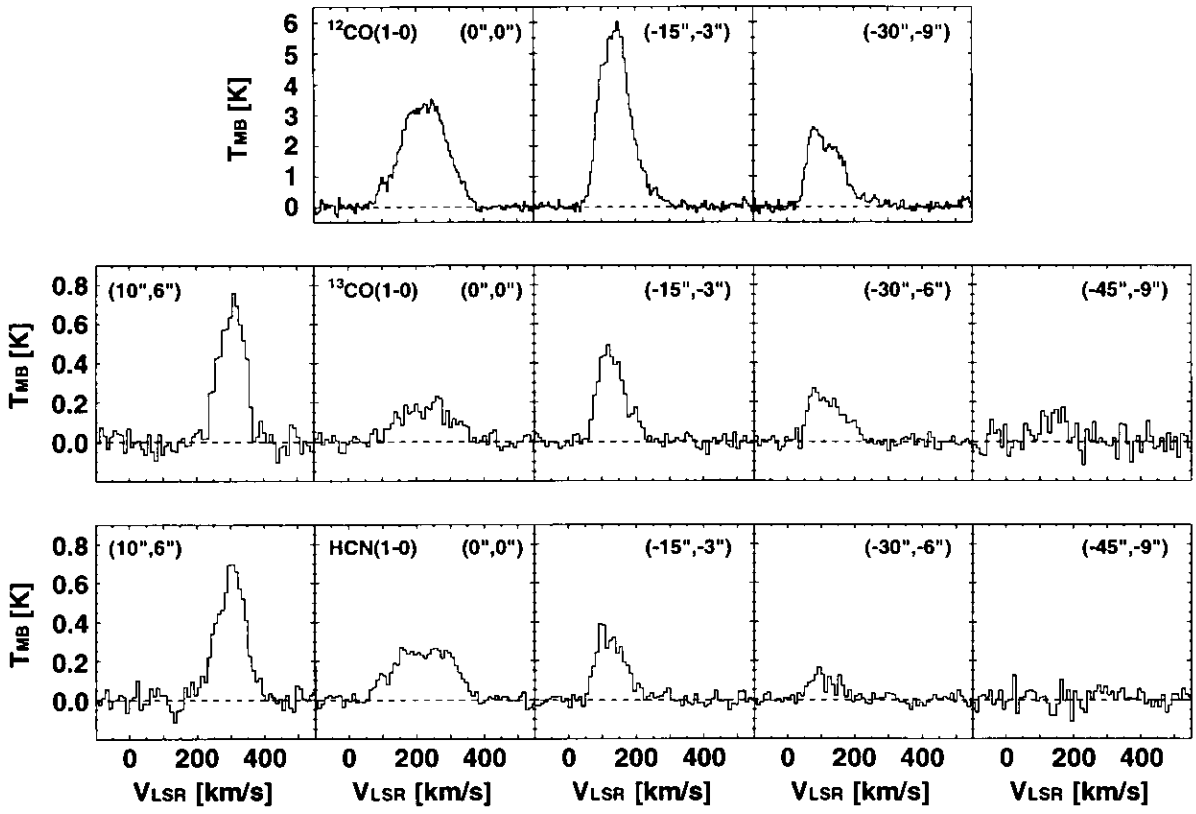

Fig. 2.9: ^{12}CO(1 – 0) (top row), ^{13}CO(1 – 0) (middle row), and HCN(1 – 0) (bottom row) spectra of the central region of the prototypical starburst galaxy M82. Horizontal axis is LSR velocity, $V_{\rm LSR}$, and vertical axis is main beam temperature, $T_{\rm MB}$. The reference point (0″, 0″) is the position of the galactic nucleus determined from the peak of 2.2 μm source (see table 2.6). Other points are in R.A. and Decl. offset from the reference point.

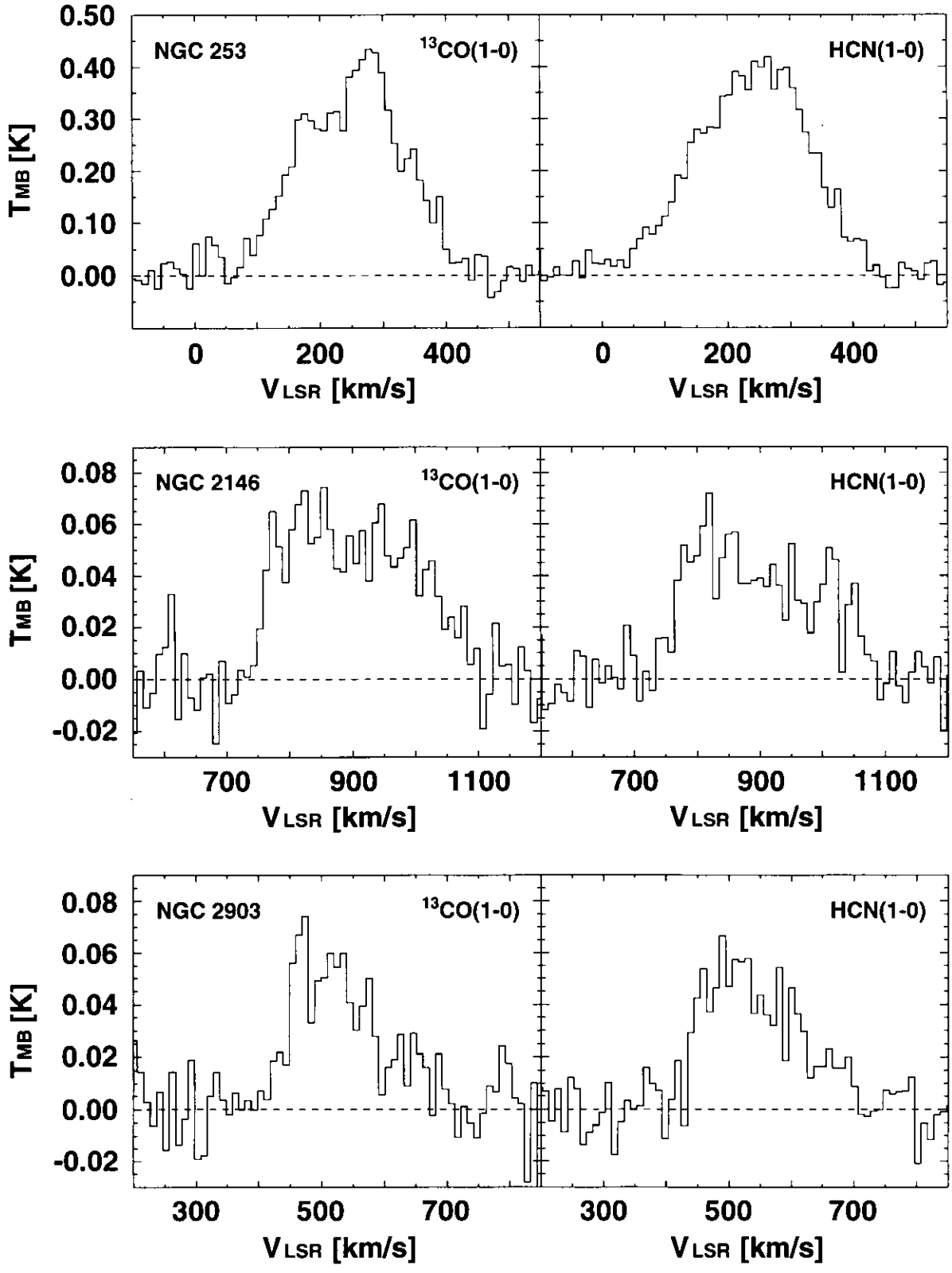

Fig. 2.10: ^{13}CO(1 – 0) (left side) and HCN(1 – 0) (right side) spectra of the center of starburst sample. Horizontal axis is LSR velocity, $V_{\rm LSR}$, and vertical axis is main beam temperature, $T_{\rm MB}$. Scale for the vertical axis is same between ^{13}CO and HCN. Top row: NGC 253. Middle row: NGC 2146. Bottom row: NGC 2903.

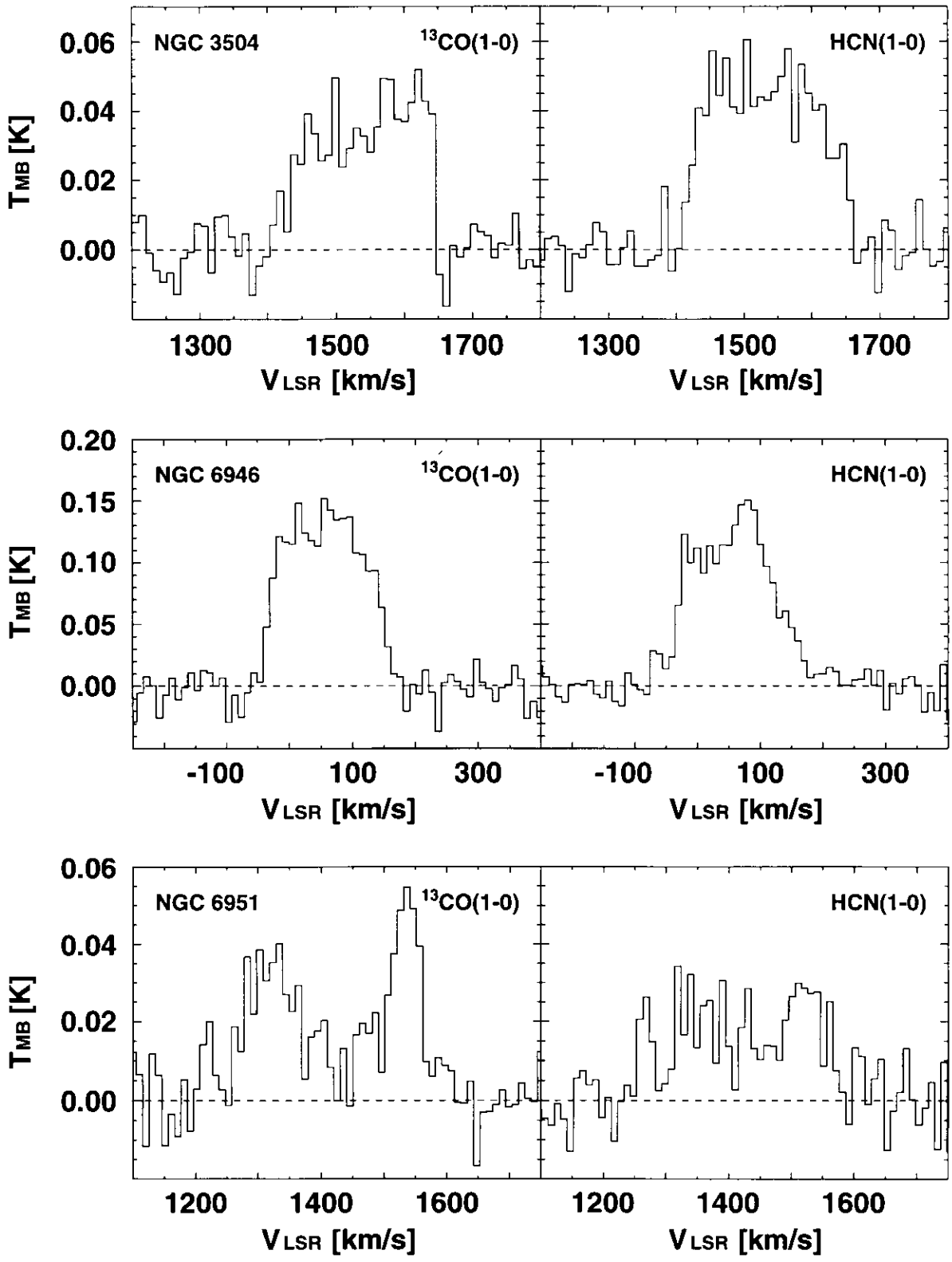

Fig. 2.11: ^{13}CO(1 – 0) (left side) and HCN(1 – 0) (right side) spectra of the center of starburst sample. Formats are same as figure 2.9. Top row: NGC 3504. Middle row: NGC 6946. Bottom row: NGC 6951.

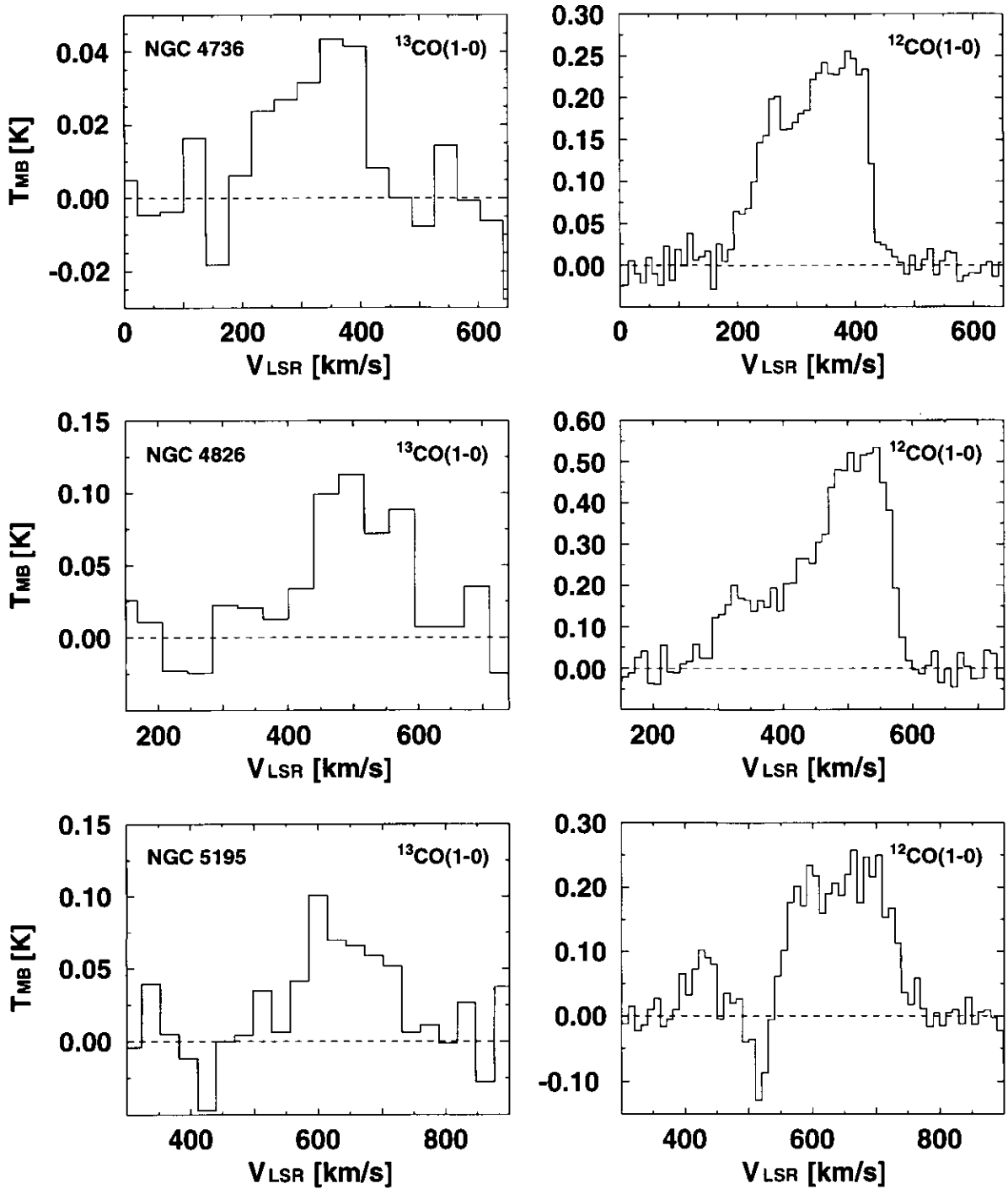

Fig. 2.12: $^{13}CO(1-0)$ (left side) and $^{12}CO(1-0)$ (right side) spectra of the center of normal and post-starburst sample. Horizontal axis is LSR velocity, V_{LSR}, and vertical axis is main beam temperature, T_{MB}. Top row: NGC 4736. Middle row: NGC 4826. Bottom row: NGC 5195.

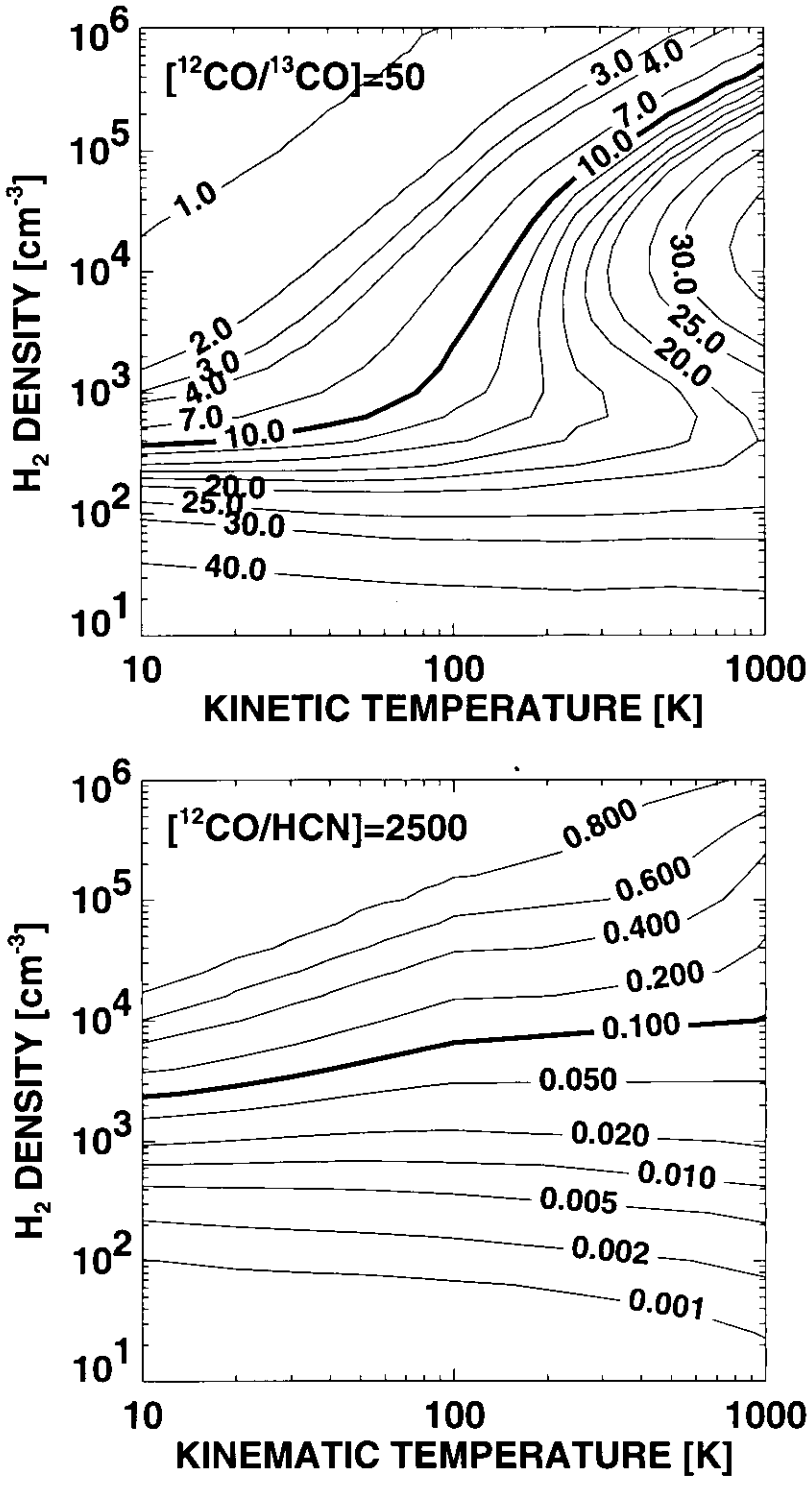

Fig. 2.13: (Top) Density (vertical axis) and temperature (horizontal axis) dependence of ^{12}CO(1 – 0)/^{13}CO(1 – 0) intensity ratio. Solid contours show curves of constant ^{12}CO(1 – 0)/^{13}CO intensity ratio, and thick solid curve indicates ^{12}CO(1 – 0)/^{13}CO ratio of 10.0. (Bottom) Density (vertical axis) and temperature (horizontal axis) dependence of HCN(1 – 0)/^{12}CO(1 – 0) intensity ratio. Solid contours show curves of constant HCN/^{12}CO intensity ratio, and thick solid curve indicates HCN/^{12}CO ratio of 0.1.

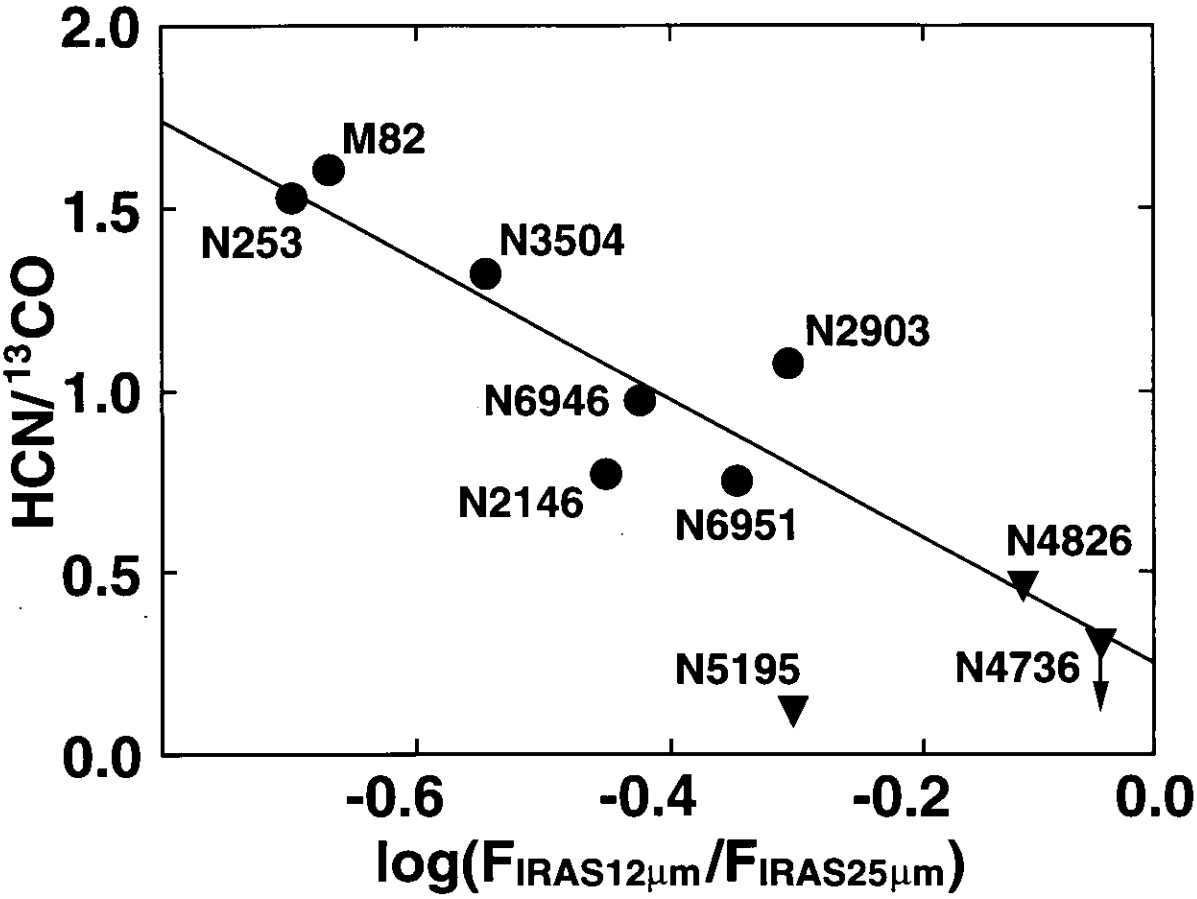

Fig. 2.14: Relation between IRAS $\log(F_{12}/F_{25})$ flux ratios and HCN(1 – 0)/^{13}CO(1 – 0) integrated intensity ratios. Filled circles and triangles indicate starburst galaxy sample and non-starburst galaxy sample, respectively. The solid line indicates the calculated linear regression using all sample galaxies except NGC 5195, which largely offsets from the correlation.

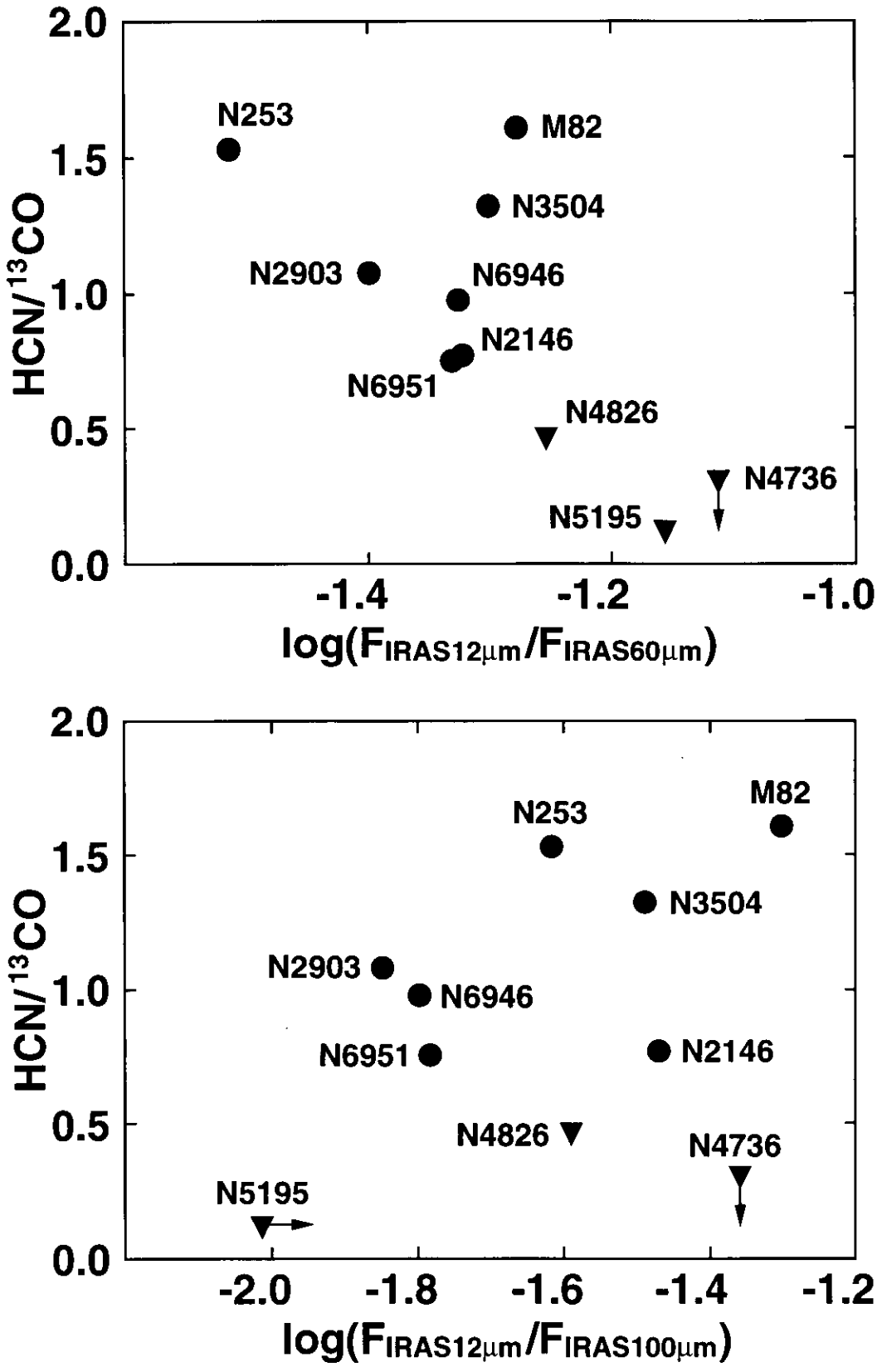

Fig. 2.15: Relation between HCN(1 – 0)/^{13}CO(1 – 0) integrated intensity ratios and (Top) IRAS $\log(F_{12}/F_{60})$ ratios, (Bottom) IRAS $\log(F_{12}/F_{100})$ ratios. Circles and triangles marks indicate starburst galaxy sample and non-starburst galaxy sample, respectively.

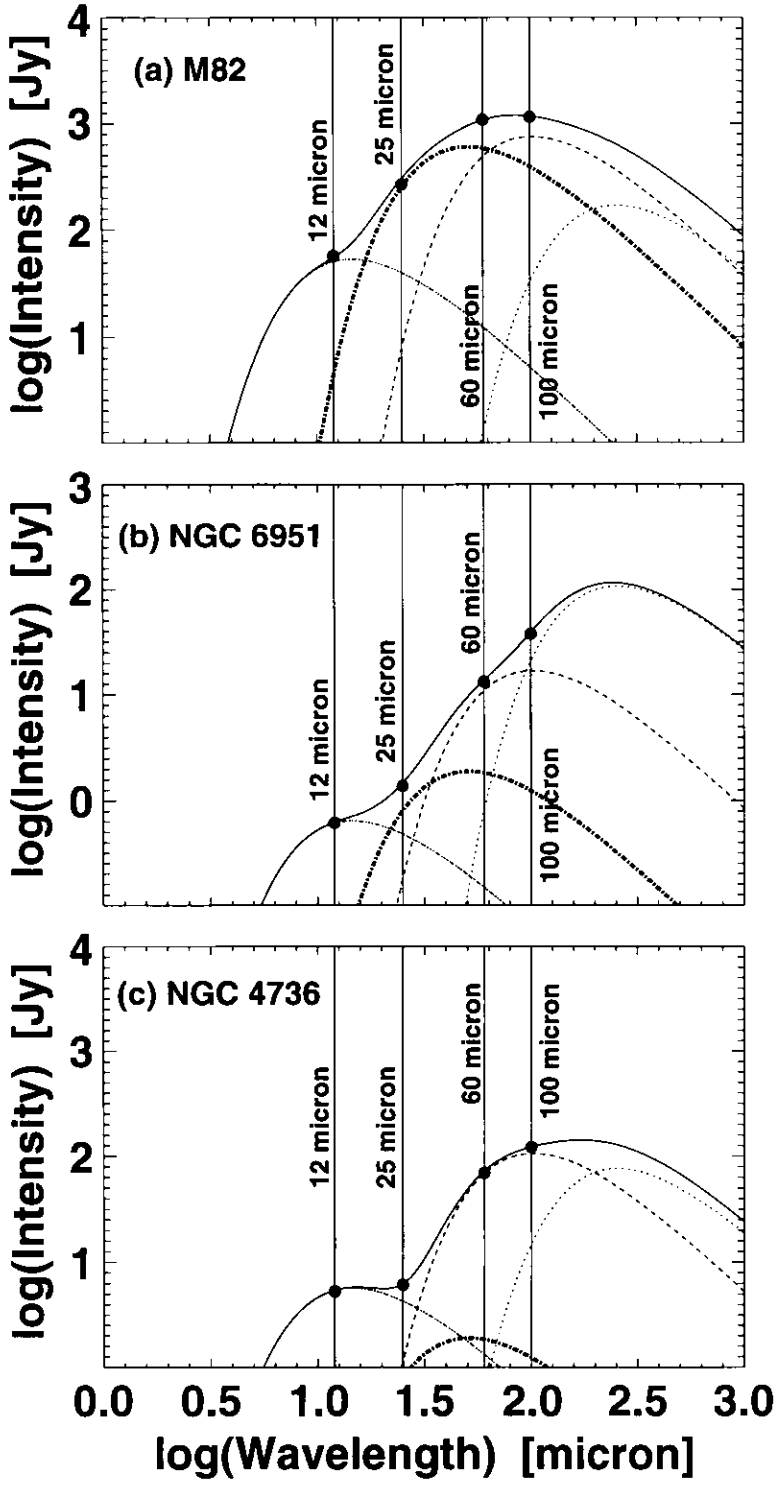

Fig. 2.16: Examples of black body temperature fitting on IRAS flux of observed galaxies. Filled circles indicate observed IRAS fluxes. The fitting was done with 20 K (dotted lines), 50 K (dashed lines), 100 K (dash-dot lines), and 350 K (dash-dot-dot-dot lines) black body temperatures, and the sum of these fitting were indicated with solid lines. (a) The fitting result of starburst galaxy M82. (b) The fitting result of moderate starburst galaxy NGC 6951. (c) The fitting result of post-starburst galaxy NGC 4736. These figures suggest that the IRAS $\log(F_{12}/F_{25})$ ratio indicates the fraction of the 100 K component. The strong starburst galaxy ($\approx$ M82) is clearly dominated by the 100 K component, but non-starburst galaxy ($\approx$ NGC 4736) has almost no 100 K component.

2.4 HCN/^{13}CO as Dense and Warm Molecular Gas Tracer III : High HCN/^{13}CO Objects in Our Galaxy

2.4.1 Background

In the previous section (section 2.3), we show that starburst regions have high HCN/^{13}CO, ^{12}CO/^{13}CO and HCN/^{12}CO integrated intensity ratios, and indicate there are good relations between physical conditions of molecular gas derived from the intensity ratios and star formation activities. In this section, we will discuss about the high intensity ratio sources in these active regions.

Because of the limited spatial resolution for the observations of external galaxies, we may observe many star forming regions, supernova remnants, and so on in one beam, and therefore it is very difficult to make clear what is the heating sources in the starburst regions. On the other hand, these objects in Our Galaxy can observe and discuss separately and in detail, it might be good samples to discuss about the heating sources in the starburst galaxies. Since there are many observations of the active regions in Our Galaxy, we studied these regions with previously published data. For this study, we searched high HCN/^{13}CO, ^{12}CO/^{13}CO and/or HCN/^{12}CO intensity ratio objects (similar to the extragalactic starburst regions) in star forming regions (section 2.4.2), supernova remnants (section 2.4.3), and high mass-loss carbon stars (section 2.4.4).

2.4.2 Star forming regions

In star forming regions, there are three active components; (1) star forming dense cores, (2) outflows from the cores, and (3) shock fronts and/or dense photodissociation regions between neutral layers and ionization (H II regions) fronts. We will discuss these three components in order.

Star forming dense cores

Stars are made from dense molecular cores rather than diffuse molecular envelopes (e.g. Lada 1992). This is also seen in the larger spatial scale that star formation activity in the star forming regions of external galaxies has a better spatial and quantitative correlation with dense molecular gas (i.e. HCN) than tenuous molecular gas (i.e. ^{12}CO; Kohno, Kawabe, & Vila-Vilaró 1999, Solomon, Downes, & Radford 1992). Therefore it is expected that dense cores have high HCN/^{12}CO ratios. Indeed, Giant Molecular Cloud (GMC) mapping observations with ^{12}CO(1 – 0), HCN(1 – 0), and CS(1 – 0) lines shows that the cores of the GMCs (S88, S140, S269, and Orion B) have high HCN/^{12}CO ratios of 0.1 – 0.3 (Helfer & Blitz 1997b) which is similar ratio to those of the extragalactic starburst regions.

On the other hand, ^{12}CO(1 – 0) and ^{13}CO(1 – 0) observations of high mass star forming cores of NGC 2071, S140, and Orion show the ^{12}CO/^{13}CO intensity ratios of $\sim$ 2.7, 3.1, and 9.8, respectively, at the systemic velocity component (Snell et al. 1984, see also figure 2.17). ^{12}CO and ^{13}CO observations towards young low mass stars of T Tauri and AS 353 A show the ^{12}CO/^{13}CO intensity ratios of $\sim$ 2.5 and 2.3, respectively, around the systemic velocity component (Edwards & Snell 1982). ^{12}CO and ^{13}CO observations

Table 2.12: $^{12}CO/^{13}CO$ intensity ratios of star forming dense cores and associated outflows .

Objects	Cores*	Outflows*	Notes	References
NGC 2071	2.7	21	High mass star forming core	1
S140	3.1	20	High mass star forming core	1
Orion	9.8	55	High mass star forming core	1
T Tau	2.5	10 – 20	T Tauri type star	2
AS 353 A	2.3	> 40	T Tauri type star	2
Haro 6 – 10	1.3	15	Herbig-Haro object	3
HH 19 – 27	1.5	—	Herbig-Haro object	3
RNO 43	—	11.5 – 51	Herbig-Haro object	3
LK Hα 234	2.3	36	Herbig-Haro object	4
HH 7 – 11	2.5	> 84	Herbig-Haro object	5

* $^{12}CO/^{13}CO$ intensity ratios of star forming dense cores and associated outflows
References — (1) Snell et al. 1984. (2) Edwards & Snell 1982. (3) Edwards & Snell 1984. (4) Edwards & Snell 1983. (5) Snell & Edwards 1981.

towards Herbig-Haro objects of Haro 6 – 10 in Taurus, HH 19 – 27 which lie ~ 10′ south of NGC 2068, LK Hα 234 in the reflection nebula NGC 7129, and HH 7 – 11 which lie south of NGC 1333 show the $^{12}CO/^{13}CO$ intensity ratios of ~ 1.3, 1.5, 2.3 and 2.5, respectively, around the systemic velocity component (Edwards & Snell 1984, Edwards & Snell 1983, Snell & Edwards 1981). To summarize, these nine objects show low $^{12}CO/^{13}CO$ ratios from ~ 1 to at most ~ 10 (see table 2.12), and an average ratio of only 3.1, three times lower than those of the central regions of normal galaxies of about 10.

$HCN/^{12}CO$ ratios of 0.1 – 0.3 and an average $^{12}CO/^{13}CO$ ratios of 3.3 indicate the $HCN/^{13}CO$ ratio of about 0.3 – 1.0, similar to the central regions of the normal galaxies or disk regions of galaxies.

The results of these three ratios indicate that only $HCN/^{12}CO$ ratio of the star forming dense core is similar to that of the starburst galaxies, but other ratios cannot explain the ratios which can be seen in the starburst galaxies. Therefore, the forming stars in the dense core would not be the dominant high intensity ratio sources of the molecular gas in starburst galaxies.

Outflows from star forming dense cores

Outflows associated with star forming dense cores are one of the energetic activities in the star forming regions. These outflows have the energies of ~ $10^{41} - 10^{47}$ erg (Bally & Lada 1983, Edwards & Snell 1984, Edwards & Snell 1983, Snell & Edwards 1981, Solomon, Huguenin, & Scoville 1981), large enough to affect the surrounding gas. These outflows can be seen as the high velocity (wing) components in the spectra.

$^{12}CO(1-0)$ and $^{13}CO(1-0)$ observations of outflows associated with high mass star forming cores of NGC 2071, S140, and Orion, associated with young low-mass stars of T Tauri and AS 353 A, and associated with Herbig-Haro objects of Haro 6 – 10, RNO 43, LK Hα 234, and HH 7 – 11 show the $^{12}CO/^{13}CO$ intensity ratios of about 21, 20,

55, 10 – 20, > 40, 15, 11.5 – 51, 36, and > 84, respectively (Snell et al. 1984, Edwards & Snell 1982, Edwards & Snell 1984, Edwards & Snell 1983, Snell & Edwards 1981, see also figure 2.17). These ratios are much higher than those of the dense core (table 2.12), which means that little of the ^{13}CO emission is associate with the outflows (see also figure 2.18 and next paragraph), contrary to the dense cores. In addition, these ratios are higher than those of the normal galaxies, and comparable or higher than those of starburst or merger candidate ultraluminous infrared galaxies (see section 2.3.4).

Since HCN emission line has hyperfine components, observations of objects in Our Galaxy with HCN emission are very little compared with other non-hyperfine lines. However, there are a few observations with HCN lines for these outflows. Umemoto et al. (1992) observed a highly collimated outflow in the dark cloud L1157 with ^{12}CO(1 – 0), ^{13}CO(1 – 0), and HCN(1 – 0) lines (figure 2.18). In ^{12}CO spectrum, we fit the gaussian to the outflow component and derive the integrated intensity. HCN spectrum show almost no emission from the quiescent component as can be seen in the ^{12}CO spectra because of the self-absorptions at the systemic velocity. Hence we assume that the HCN emission is only from outflow component. On the other hand, since ^{13}CO spectra show no outflow component, we derived the 3σ upper limit of $\sim$ 0.3 K. From these data, we calculated HCN/^{12}CO and HCN/^{13}CO ratios of 0.9 and > 260 (3σ lower limit), respectively. Interferometric observations of Orion-KL high velocity outflow (Wright, Plambeck, & Wilner 1996) were done with HCN and ^{12}CO lines, and also show high HCN/^{12}CO intensity ratios of 0.4 – 0.5. These ratios are also much higher than those of starburst galaxies (see section 2.3.4).

These intensity ratios at the outflows associated with star forming dense cores show similar or much higher values than those of extragalactic starburst regions. These results imply that the outflows can be one of the high intensity ratio sources of the molecular gas in starburst galaxies.

Photodissociation regions

Ionization fronts between ionized gas and molecular gas are one of the good samples for the study of photodissociation regions (PDRs) and shocked molecular gas (interactions between expansion of ionized gas and quiescent molecular gas). The multi-line (^{12}CO(1 – 0), ^{13}CO(1 – 0), and HCN(1 – 0)) observations of the Orion bright bar, which is a prominent ionization front located at the south-east of the Orion nebula, was done by Omodaka et al. (1994). The observations were slit scan perpendicular to the Orion bright bar (figure 2.19). The northwest region is a HII region ionized by the Trapezium stars (Becklin et al. 1976), and the southeast region is a molecular cloud region. The ^{12}CO/^{13}CO, HCN/^{12}CO, and HCN/^{13}CO intensity ratios along this slit scans are shown in figure 2.20. The ^{12}CO/^{13}CO ratios have higher ratios around H II region side, but lower than those of the extragalactic starburst regions. The HCN/^{12}CO and HCN/^{13}CO ratios, on the other hand, have higher ratios around molecular cloud side. These higher HCN/^{12}CO ratios of 0.2 – 0.25 are very similar to those of the extragalactic starburst regions, but HCN/^{13}CO ratios of 0.7 – 0.8 are somewhat lower than those of the extragalactic starburst regions.

Similar to the star forming dense cores, only the HCN/^{12}CO ratio is similar to that of the starburst galaxies, but other ratios are lower than which can be seen in the starburst galaxies. Therefore, the PDRs ionized by the early-type stars would not be the dominant high intensity ratio sources of the molecular gas in starburst galaxies. However, since

the observations of the PDRs with $^{12}CO(1-0)$, $^{13}CO(1-0)$, and HCN(1 – 0) lines are only Omodaka et al. (1994), it would be needed to confirm this conclusion.

2.4.3 Supernova remnants

Molecular gas associated with supernova remnants are known as one of the good laboratory for the study of shocked molecular gas. Since the shocked molecular gas has high temperature, the chemical reactions in the shocked gas might be very different from low temperature molecular gas. Therefore, the shocked molecular gas observations with many molecules and transitions were done by many authors for the study of shock chemistry. The sample of molecular clouds which have clear evidence of the association with supernova remnants are, however, very rare at present, and these multi-line, multi-transition observations were mainly done toward IC443, and some observations toward W51C. Hence we will look at these two samples in this section.

Shocked molecular gas in the supernova remnant IC443 is the best-studied sample. There are several clumps that can be seen in the molecular gas observations (figure 2.21). $^{12}CO(1-0)$ and $^{13}CO(1-0)$ observations of clump B show the $^{12}CO/^{13}CO$ intensity ratios of 61 ± 6 (DeNoyer & Frerking 1981) and 62 (Dickman et al. 1992), and those of clump C show $^{12}CO/^{13}CO > 12$ (DeNoyer 1979). Moreover, $HCN(1-0)/^{12}CO(1-0)$ intensity ratios at clump GI (north part of clump G) and clump B are both 0.25 (van Dishoeck, Jansen, & Phillips 1993), and that at southeast edge of clump C is 0.18 (White et al. 1987). Sample spectra of ^{12}CO, ^{13}CO and HCN emission at clump B are shown in figure 2.22. Since both of the $^{12}CO/^{13}CO$ and $HCN/^{12}CO$ ratios shows high value, $HCN/^{13}CO$ ratios would inevitably show high ratios (larger than unity). These high values at the shocked molecular gas are quite similar to those of extragalactic starburst regions.

W51C is also one of the supernova remnants associated with shocked molecular gas (Koo & Moon 1997a). There are five molecular clumps, and the $^{12}CO(1-0)$ and $^{13}CO(1-0)$ observations were done toward clump 2 and 4 (Koo & Moon 1997b). The resultant intensity ratios are 53 ± 18 and 62 ± 25, respectively, which are also similar to those of extragalactic starburst regions. HCN(1 – 0) observations of W51C are not available so that the intensity ratios related to HCN are not clear.

The ^{12}CO, ^{13}CO, and HCN intensity ratios of these two objects show similar results as those of extragalactic starburst regions, which indicate that the supernova explosions would be one of the high intensity ratio sources of the molecular gas in starburst galaxies.

2.4.4 High mass-loss carbon stars

Asymptotic giant branch (AGB) stars are the dominant sources of mass-loss objects, which return the materials to the interstellar space with a mass-loss rate of $3-6 \times 10^{-10}$ $M_\odot$ pc^{-2} yr^{-1} (Jura & Kleinmann 1989). Carbon stars are one of the AGB stars with [C]/[O] abundance ratio of > 1, which constitute about half of the high mass-loss AGB stars (Jura & Kleinmann 1989), and IRC+10216 is one of the most famous and common high mass-loss carbon star. We observed this source with $^{12}CO(1-0)$, $^{13}CO(1-0)$, and HCN(1 – 0) for the intensity calibrations of starburst galaxies. Details of the observations are in section 2.3.2. The observed spectra are shown in figure 2.23, and the resultant $^{12}CO/^{13}CO$, $HCN/^{12}CO$, and $HCN/^{13}CO$ ratios are $\sim$ 11, 1.3, and 15, respectively. The $^{12}CO/^{13}CO$ ratio is similar to the normal galaxies. Other high mass-loss carbon stars

also show ^{12}CO/^{13}CO ratio of $\sim 11 \pm 4$ in 8 objects out of 13 (Greaves & Holland 1997), although their observations were J = 2 – 1 lines (but may have similar ratio with J = 1 – 0. For example, IRC+10216 have ^{12}CO(1 – 0)/^{13}CO(1 – 0) = 11 and ^{12}CO(2 – 1)/^{13}CO(2 – 1) = 15). On the other hand, HCN/^{12}CO and HCN/^{13}CO ratios show quite high values compared to those of extragalactic starburst regions.

These results indicate that ^{12}CO/^{13}CO ratio cannot explain the ratios in the starburst galaxies. In addition, AGB stars are evolved from intermediate mass stars (from 1 to $5-8$ M$_\odot$ stars) and are abundant in normal galaxies, but these galaxies do not have high HCN/^{12}CO and HCN/^{13}CO ratios. Therefore the high mass-loss carbon stars would not the source of high intensity ratios in the starburst galaxies.

2.4.5 Discussions

From the standpoint of ^{12}CO/^{13}CO, HCN/^{12}CO, and HCN/^{13}CO intensity ratios, the high intensity ratio source of the molecular gas in the starburst galaxies would be outflows associated with star forming dense cores and/or supernova explosions. As discussed in section 2.2 and 2.3, these high intensity ratios indicate that the molecular gas have high-density and high-temperature physical conditions. Both of these sources are related to shock phenomena, so that the "shock" would be the most important mechanism for these conditions. To distinguish the dominant source of these conditions in starburst regions, we have to consider the intrinsic parameters of both of these outflows and supernova remnants such as source sizes, dynamical timescales, energies and so on. Hence, we next discuss which is the dominant source in the starburst regions with considering these intrinsic parameters.

The outflows have the energies of $\sim 10^{41} - 10^{47}$ erg and the typical source sizes of $0.1 - 1$ pc (Bally & Lada 1983, Edwards & Snell 1984, Edwards & Snell 1983, Goldsmith et al. 1984, Snell et al. 1984, Snell & Edwards 1981, Solomon, Huguenin, & Scoville 1981) with the dynamical timescale of typically 10^{5-6} yr (Richer et al. 2000). On the other hand, the supernova remnants have the energies of $\sim 10^{51}$ erg, and the source sizes of $10^0 - 10^2$ pc at the dynamical timescale of $10^3 - 10^5$ yr (Jones et al. 1998, Weiler & Sramek 1988). From these values, we will calculate the heating efficiencies in the starburst regions for each source.

At first, we will calculate stellar mass function in the starburst regions. Since the outflow phenomena are the angular momentum ejections for the mass accretion onto the embedded stars in the dense cores, all the star forming cores would form the outflows (André 1994, Bachiller 1996), and therefore these do not depend on the stellar mass function. However, the progenitor of the supernova explosions might be only stars with the stellar mass of $\gtrsim 8$ M$_\odot$, so that the number of the objects would depend on the stellar mass function. For the calculation of the stellar mass function, we adopted the initial mass function (IMF) of the extended Millar-Scalo function (Kennicutt 1983),

$$\psi(m) = \frac{dN(m)}{dm} = km^{-2.5} \quad (1 \leq m \leq 100 \text{ M}_\odot) \tag{2.5}$$

$$= km^{-1.4} \quad (0.1 \leq m \leq 1 \text{ M}_\odot) \tag{2.6}$$

where m is the stellar mass in unit of M$_\odot$ and $N(m)$ is the number count of the stars with a mass of m. k is a normalization constant defined by

$$\int_{m_l}^{m_u} \psi(m) dm = 1 \tag{2.7}$$

where m_l is a lower mass cutoff and m_u is an upper mass cutoff. We adopted the upper mass cutoff of 100 $M_\odot$, and the lower mass cutoff of 1 $M_\odot$ (which means we only use equation (2.5)) because starburst regions tend to be deficient in low-mass stars less than $\sim$ 1 $m_\odot$ (Goldader et al. 1997). With these mass cutoff, k would be determined as 1.5. As mentioned above, stars with their mass larger than 8 $M_\odot$ would finish their life with the supernova explosion, so that we have to derive the number count of these high-mass stars for the estimations of supernova heating efficiency. The calculation was done as

$$N(8 \leq m \leq 100\ M_\odot) = \int dN = \int_8^{100} \psi(m)dm = \int_8^{100} 1.5m^{-2.5}dm = 0.04 \qquad (2.8)$$

which means only 4% of the formed stars have their mass of $> 8\ M_\odot$.

Next we will calculate the energy input efficiency to the starburst regions. We assume that one starburst phase would continue 10^8 yr (Rieke et al. 1980, Goldader et al. 1997), and the spatial extent of the starburst region would have a radius of $\sim$ 100 pc (Jackson et al. 1996, Devereux 1989) with a thin disk-like structure (which means we do not consider thickness of the disk). For the outflow, we adopt an energy of 10^{47} erg, a timescale of 10^6 yr, a radius of 0.5 pc, and assume that all the stars (100 % of the formed stars) would eject outflows in their star formation phase. Using these values, the energy input by the outflow to the starburst region in one starburst phase normalized by the stellar number count would calculate as

$$\begin{aligned} \varepsilon_{outflow} &\sim 10^{47}\ [\mathrm{erg}] \times \frac{10^6\ [\mathrm{yr}]}{10^8\ [\mathrm{yr}]} \times \frac{(0.5\ [\mathrm{pc}])^2}{(10^2\ [\mathrm{pc}])^2} \times \frac{100\ [\%]}{100\ [\%]} \\ &\sim 2.5 \times 10^{40}\ [\mathrm{erg/starburst}]. \end{aligned} \qquad (2.9)$$

For the supernova explosion, we adopt an energy of 10^{51} erg, a timescale of 10^5 yr, a radius of 10 pc, and as calculated in equation (2.8) that 4 % of the formed stars would explode. These high-mass stars would be short-lived (similar to the timescale of a starburst), so that almost all of these stars would explode enough within the starburst phase of 10^8 yr. Using these values, the energy input by the supernova explosion to the starburst region in one starburst phase normalized by the stellar number count would calculate as

$$\begin{aligned} \varepsilon_{SN} &\sim 10^{51}\ [\mathrm{erg}] \times \frac{10^5\ [\mathrm{yr}]}{10^8\ [\mathrm{yr}]} \times \frac{(10\ [\mathrm{pc}])^2}{(10^2\ [\mathrm{pc}])^2} \times \frac{4\ [\%]}{100\ [\%]} \\ &\sim 4.0 \times 10^{44}\ [\mathrm{erg/starburst}]. \end{aligned} \qquad (2.10)$$

These calculation results clearly shows that $\varepsilon_{SN} \gg \varepsilon_{outflow}$, and suggest that the supernova explosions are the most efficient heating source in the starburst regions. Therefore, it is concluded that the high $^{12}CO(1-0)/^{13}CO(1-0)$, $HCN(1-0)/^{12}CO(1-0)$, and $HCN(1-0)/^{13}CO(1-0)$ ratios which indicate high-density and high-temperature conditions of molecular gas in the starburst galaxies would mainly caused by the supernova explosions of high-mass stars.

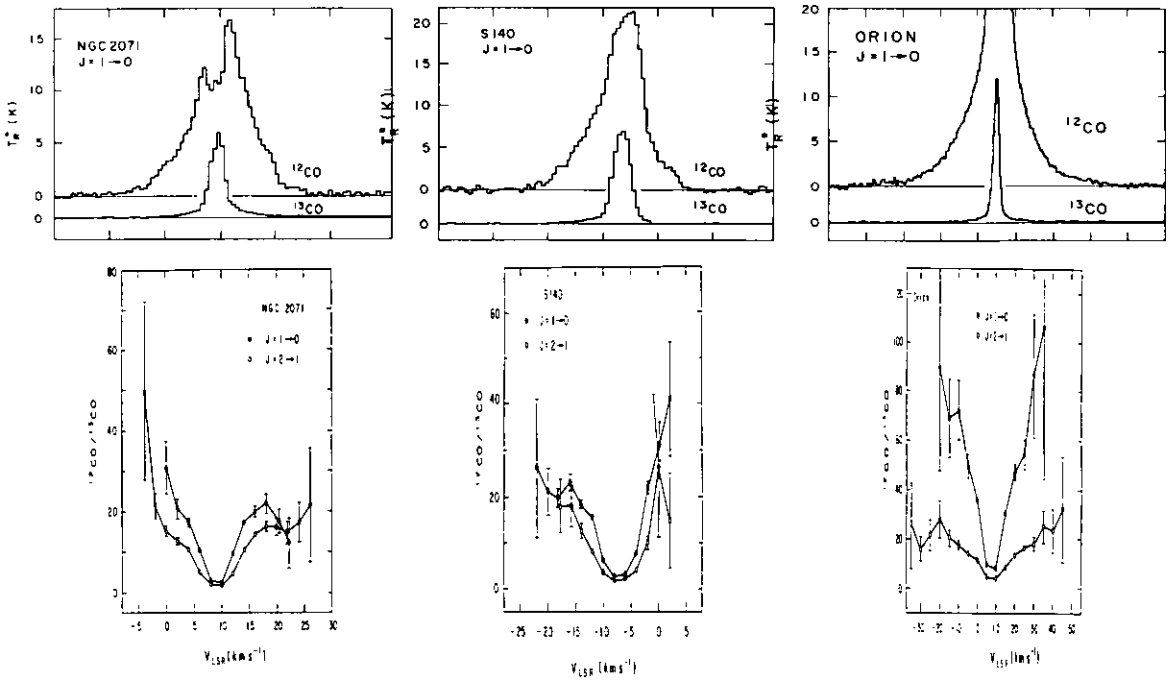

Fig. 2.17: ^{12}CO and ^{13}CO Spectra (top) and ^{12}CO/^{13}CO intensity ratios (bottom) of high mass star forming cores and associated outflows. The ratios clearly show low intensity ratios at the cores, but high at outflows (wing components). These figures are taken from Snell et al. (1984).

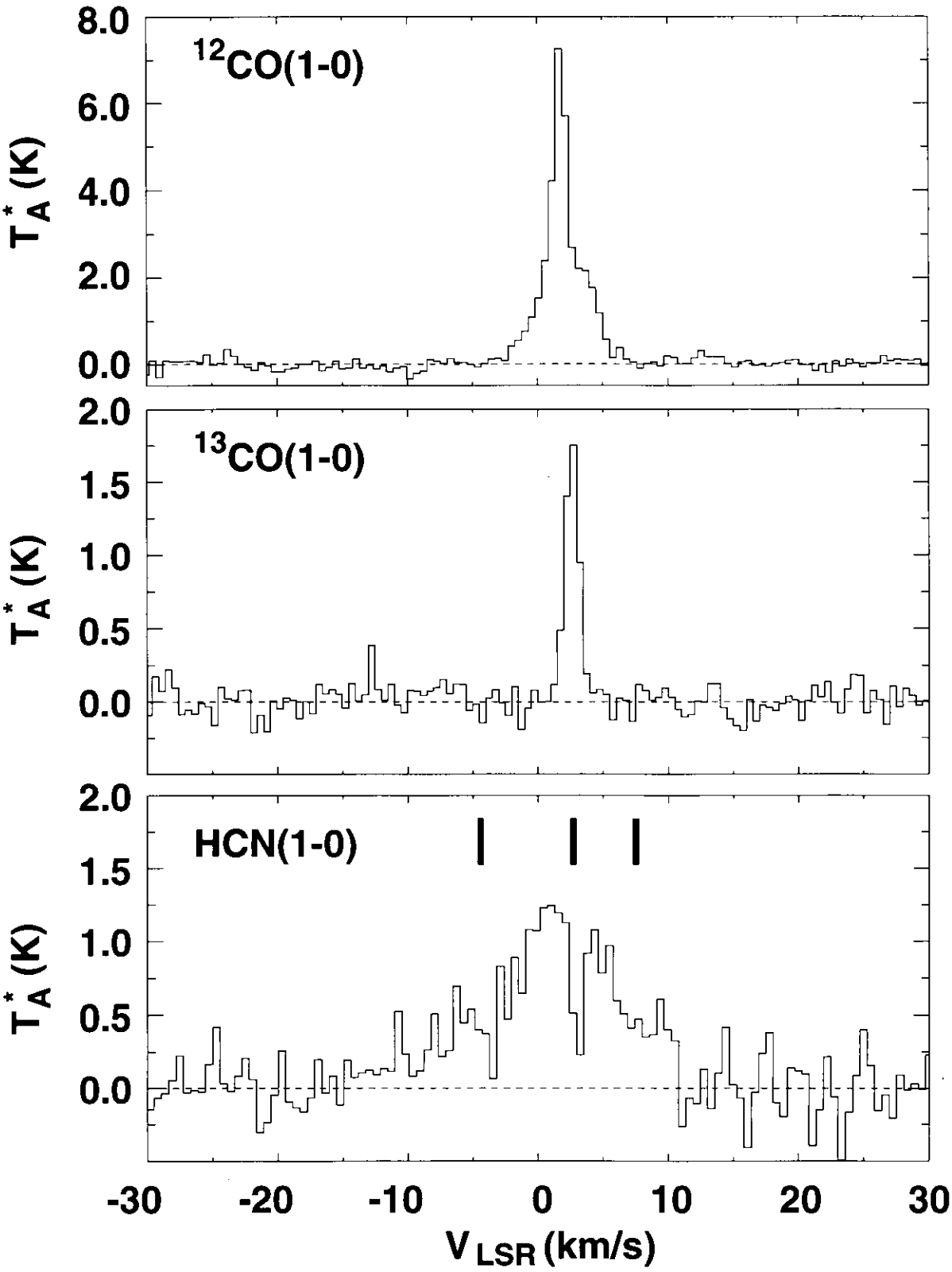

Fig. 2.18: Spectra of ^{12}CO(1 – 0) (top), ^{13}CO(1 – 0) (middle), and HCN(1 – 0) (bottom) lines toward the outflow in the dark cloud L1157 ($V_{sys} \sim 2.7$ km s^{-1}). The position of the spectra is (+45″, −1′45″) offset from the IRAS 20386 + 6751 (α(B1950) = $20^h38^m39.^s6$, δ(B1950) = 67°51′33″) which might be the progenitor of this outflow. Thick vertical lines in the HCN spectrum indicate the hyperfine components. The ^{12}CO and HCN lines show clear outflow (high velocity or wing) components, but ^{13}CO line shows no such component. These figures are taken from Umemoto et al. (1992).

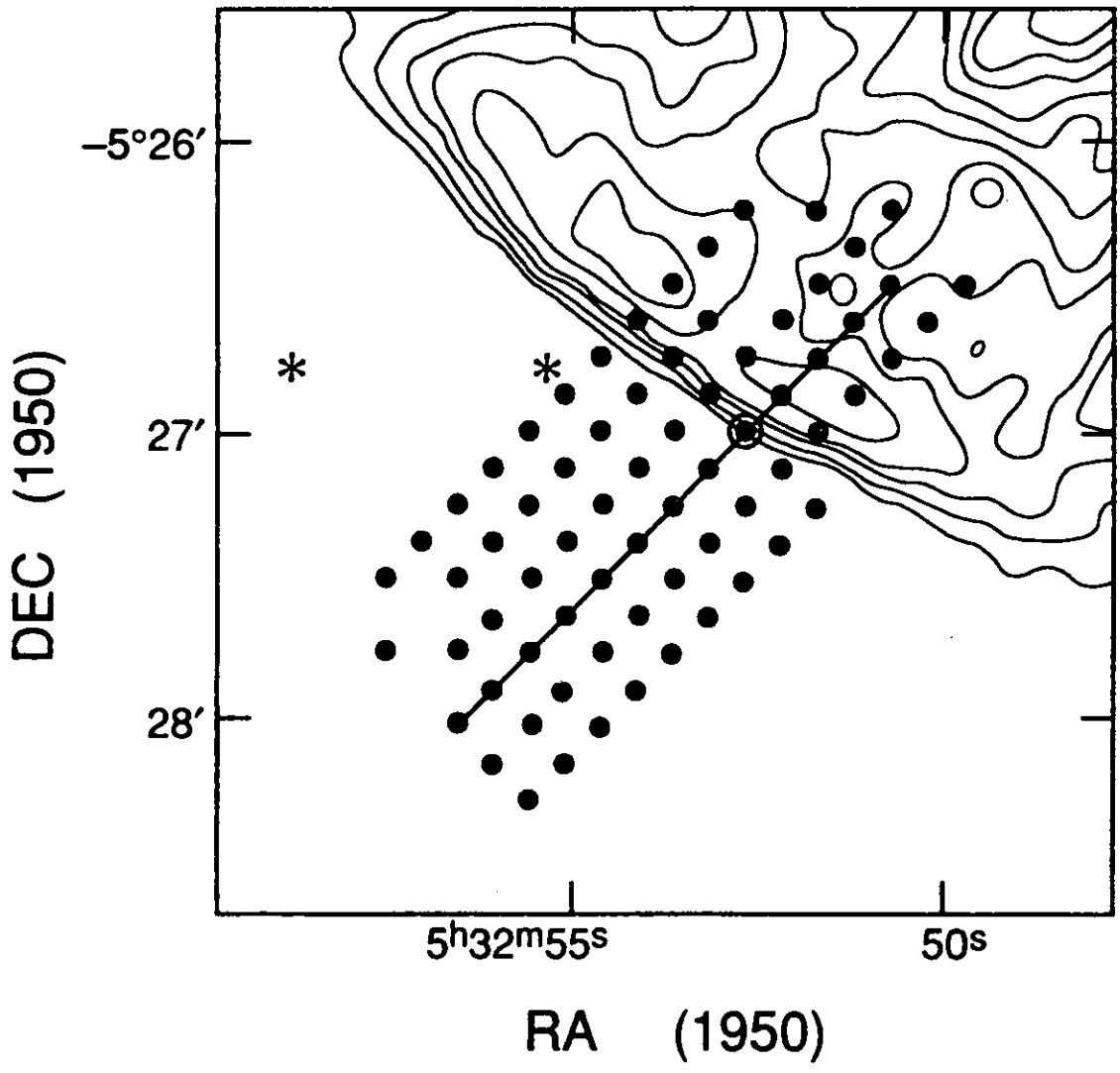

Fig. 2.19: The map of Orion bright bar region. Black dots with a thick straight line are strip scanned positions of ^{12}CO(1 − 0), ^{13}CO(1 − 0), and HCN(1 − 0) emission. A circled dot is a reference position of $(0'', 0'')$ = (α(B1950) = $5^h32^m52.^s7$, δ(B1950) = $-5°27'00''$). Thin solid contours are the 6 cm continuum emission (free-free emission; Johnston et al. 1983), and the asterisks indicate the positions of θ^2 Ori A and θ^2 Ori B. The northwest region is a HII region, and the southeast region is a molecular cloud region. This figure is taken from Omodaka et al. (1994).

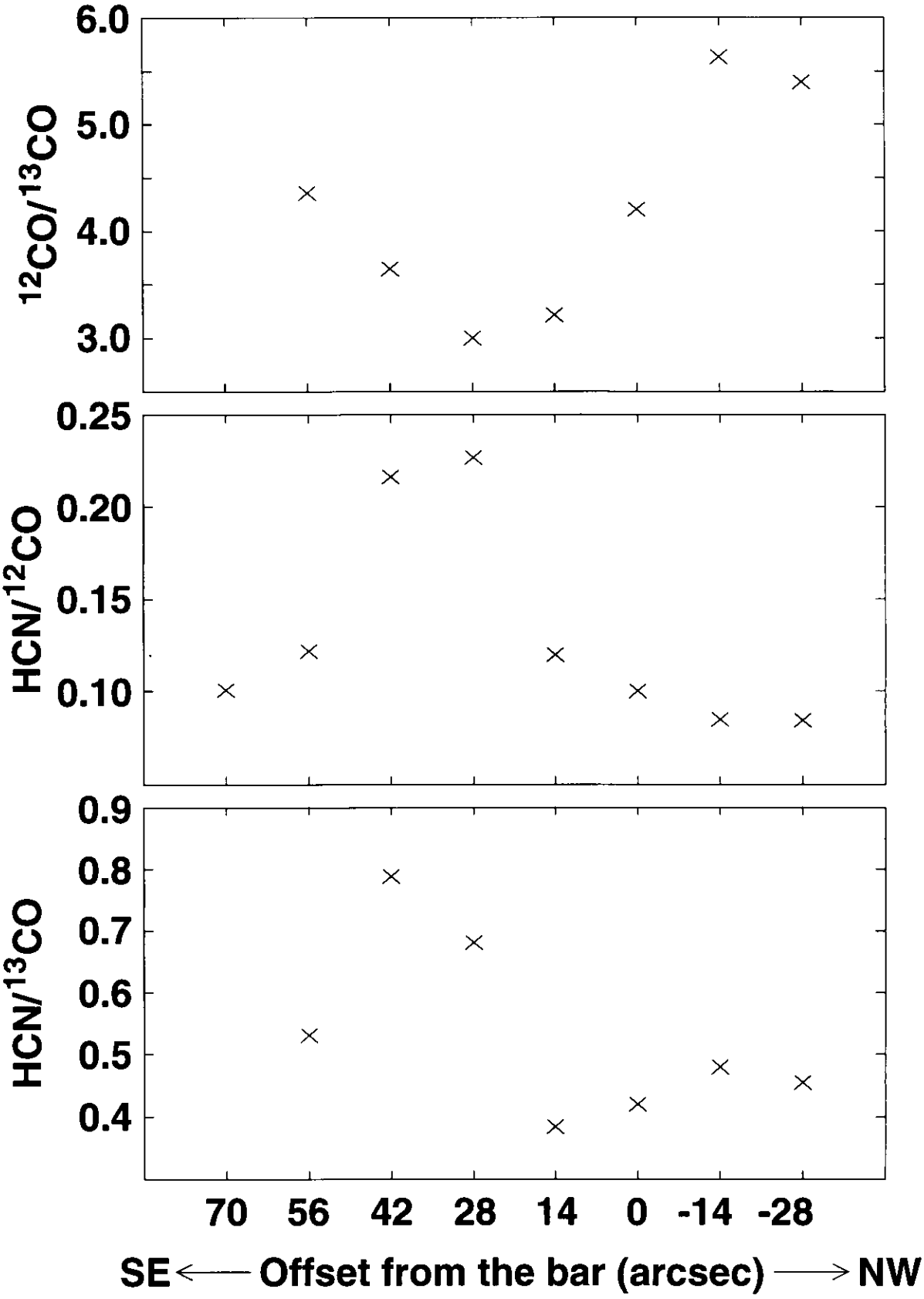

Fig. 2.20: Variations of the $^{12}CO/^{13}CO$ (top), $HCN/^{12}CO$ (middle), and $HCN/^{13}CO$ (bottom) intensity ratios perpendicular to the Orion bright bar. $0''$ is a reference position of α(B1950) = $5^h32^m52.^s7$, δ(B1950) = $-5°27'00''$. The northwest region is a HII region, and the southeast region is a molecular cloud region. The intensity data are taken from Omodaka et al. (1994).

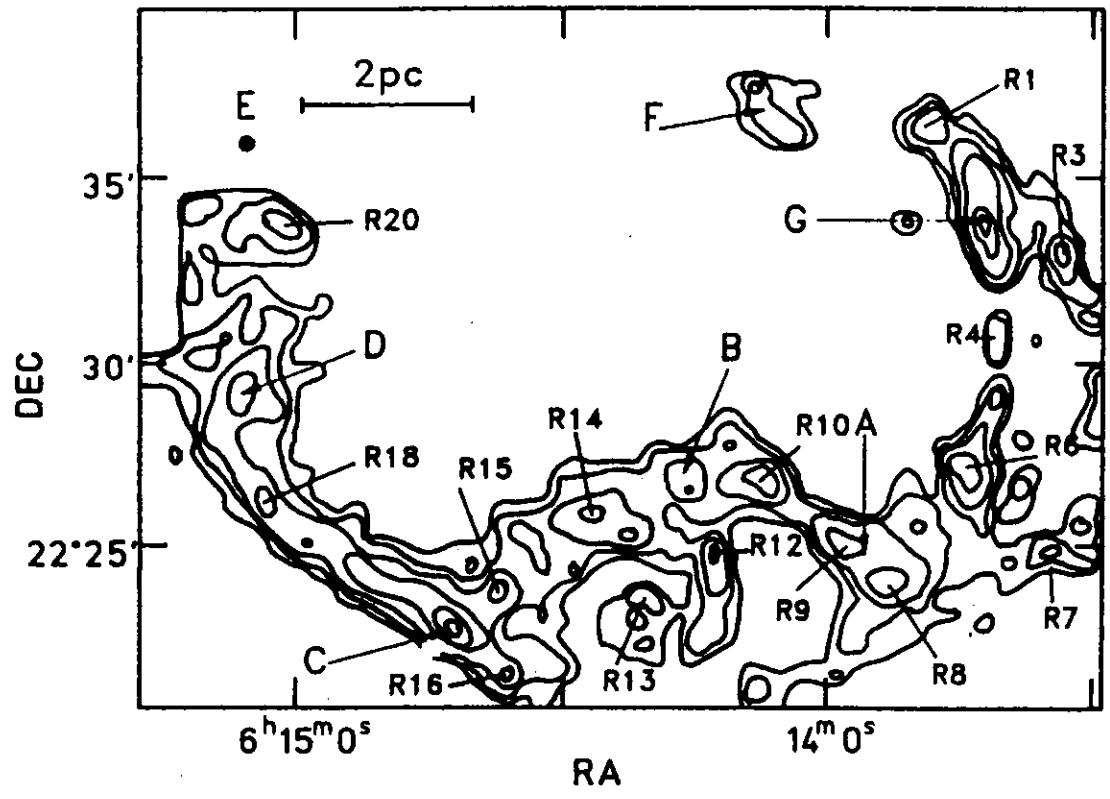

Fig. 2.21: Shocked molecular gas region in IC 443. This image was mapped with 2.1 μm shocked molecular hydrogen emission. Names and positions of the clumps are indicated in the map. (From Burton 1987, van Dishoeck, Jansen, & Phillips 1993)

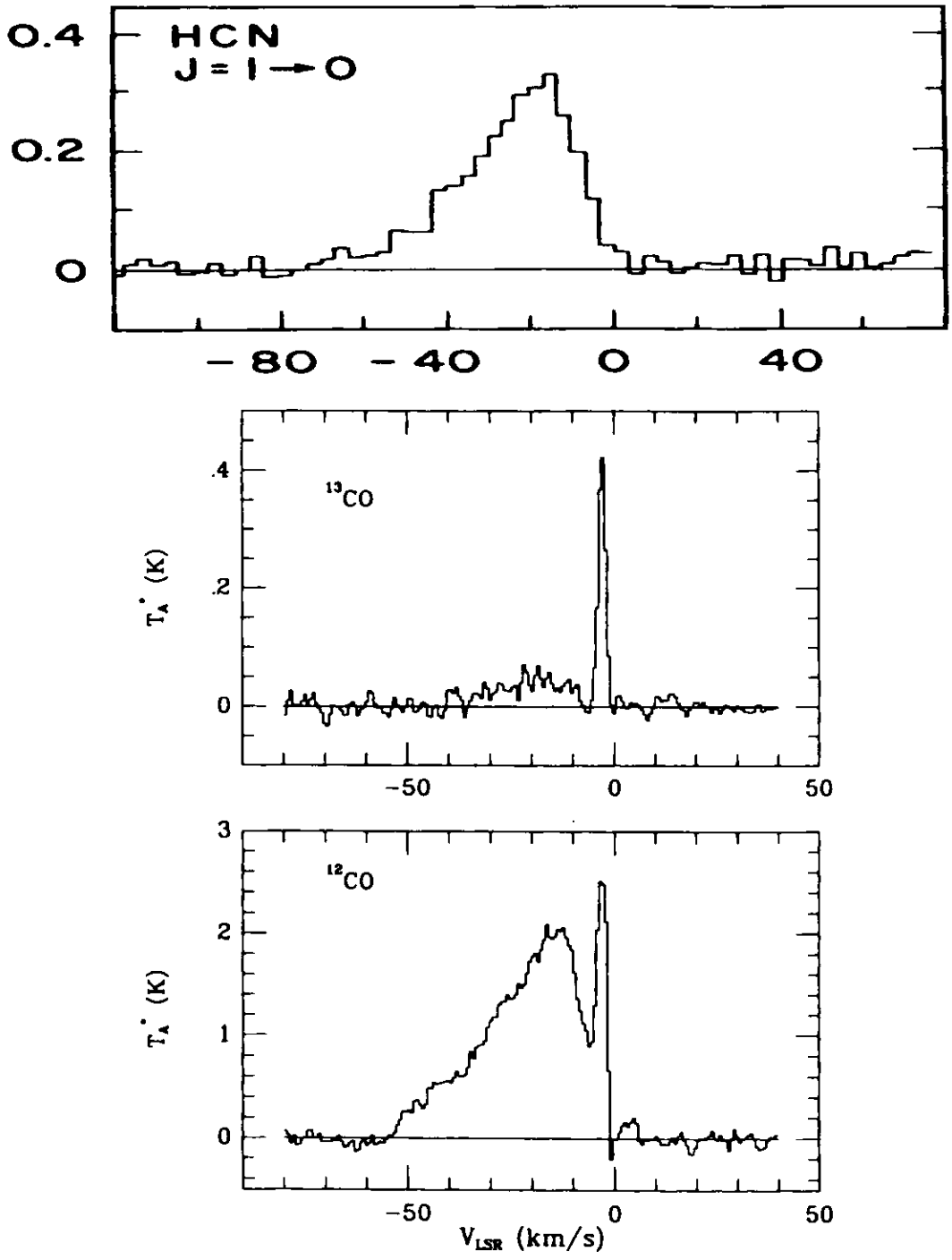

Fig. 2.22: HCN(1 – 0), ^{13}CO(1 – 0), and ^{12}CO(1 – 0) spectra of IC 443 B. The horizontal axis indicates the LSR velocity and the vertical axis indicates the antenna temperature. These spectra clearly show strong HCN and weak ^{13}CO emission. HCN data are taken from Ziurys et al. (1989), and other data are from Dickman et al. (1992).

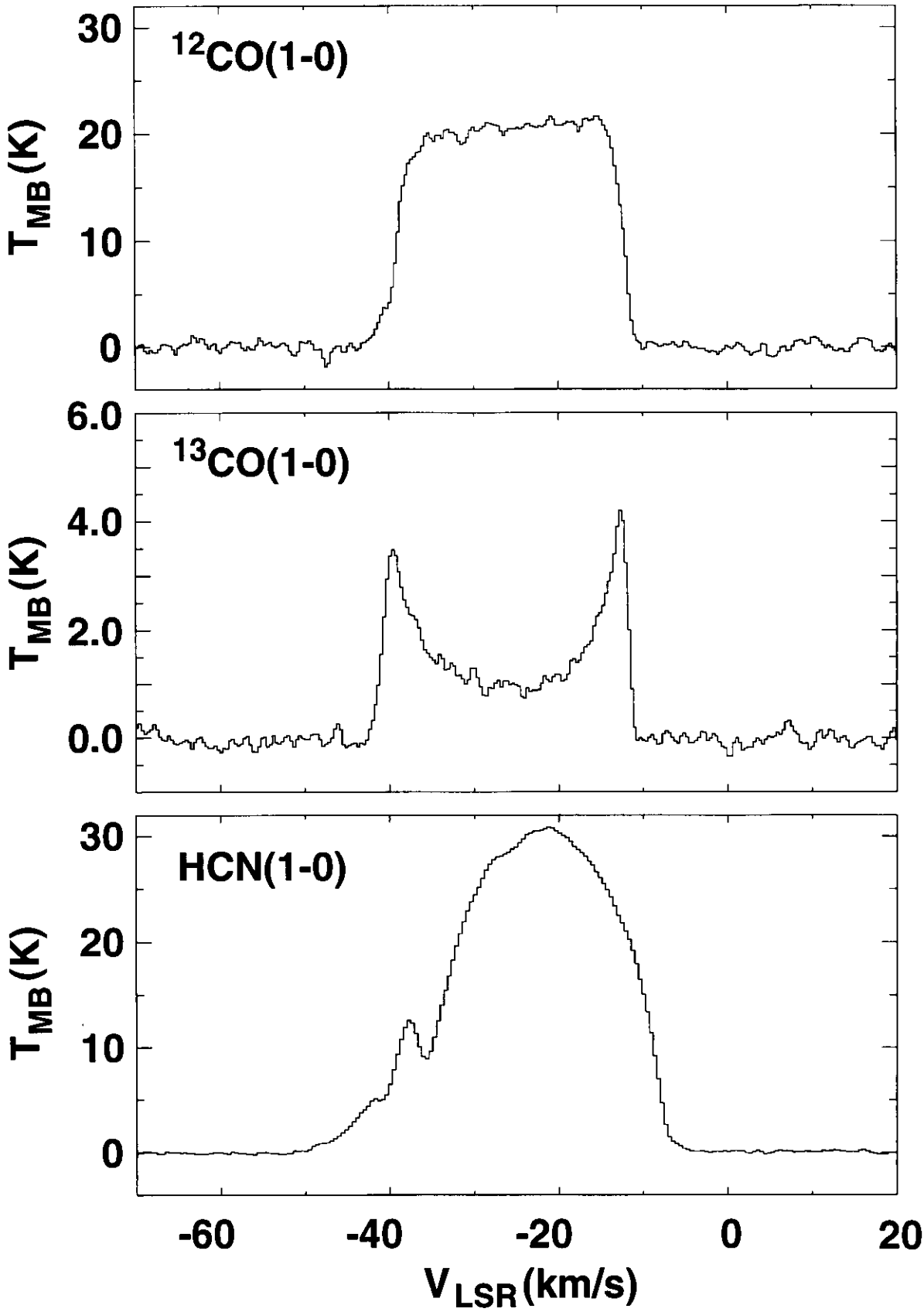

Fig. 2.23: ^{12}CO(1 – 0), ^{13}CO(1 – 0), and HCN(1 – 0) spectra of IRC+10216. The horizontal axis indicates the LSR velocity and the vertical axis indicates the main-beam temperature. These spectra clearly show strong ^{12}CO and HCN, and weak ^{13}CO emission.

Chapter 3

Molecular Gas in Prototypical Starburst Galaxy M82

3.1 Introduction

Messier 82 (NGC 3034, Cigar Galaxy) is known as one of the nearby (3.25 Mpc; Sandage & Tammann 1975) bright irregular galaxies, and therefore has been studied by many authors and by many wavelength. Optical photographic observations (Lynds & Sandage 1963) show remarkable features of filaments extend along the minor axis to a height of 3 kpc above and below the disk of this galaxy. They suggest that these filamentary structures are the resultant of an expulsion occurred at the central region. Infrared observations suggest that M82 is one of the luminous infrared galaxies of $\sim 3 \times 10^{10}$ $L_{\odot}$ (Rieke & Lebofsky 1979). The mass-to-luminosity ratio, M/L, of this galaxy shows extremely low value (< 0.02, Rieke & Lebofsky 1979; ≈ 0.04, Telesco 1993) compared with typical values of $5-10$ and other nearby starburst values of ~ 0.2 (Rieke & Lebofsky 1978). This extremely low M/L ratio can be explained by bursts of star formation (or starburst; Rieke & Lebofsky 1978, Rieke et al. 1980).

Soft X-ray observations show extended structures along the minor axis of M82, which is similar to the optical extensions (Watson, Stanger, & Griffiths 1984, Kronberg, Biermann & Schwab 1985, Fabbiano 1988, Bregman, Schulman, & Tomisaka 1995, Shopbell, & Bland-Hawthorn 1998). Large-scale molecular gas (^{12}CO(1 - 0); Nakai et al. 1987) and dust (2 mm, Kuno & Matsuo 1997; 450 μm and 850 μm, Alton, Davies, & Bianchi 1999) observations also show filamentary structures outside the disk region. Radio (centimeter-wavelength) continuum observations show over 40 sources within central $\sim$ 300 pc region (Kronberg, Biermann & Schwab 1985). Multi-frequency radio observations (Wills et al. 1997) and high-resolution VLBI observations (Bartel et al. 1987, Wilkinson & de Bruyn 1990, Muxlow et al. 1994) of these sources indicate that most of these sources are supernova remnants with their average age of a few hundred years. Ages and numbers of the supernova remnants indicate the supernova rate of $0.05 - 0.1$ yr^{-1}, much higher than that of Our Galaxy of $\sim 0.01 - 0.02$ (Condon 1992). These results also support that the central starburst and the resultant supernova explosions cause the large-scale filamentary structures.

Inside the disk region, there is a 2.2 μm peak which is dominated by late type stars (late type supergiants; Rieke et al. 1980, Dietz et al. 1986, Joy, Lester, & Harvey 1987, Lester et al. 1990) located at the dynamical center (Weliachew, Fomalont, & Greisen

1984). Around this region, there are luminous super star clusters with low $M/L_V \sim 0.1$ which suggest young ages of $\lesssim 5 \times 10^7$ yr (O'Connell et al. 1978, O'Connell et al. 1995). However, this region is strongly absorbed by dust even in 2.2 μm (K-band), e.g. $A_K \sim 1.4$ (McLeod et al. 1993), $\lesssim 0.8$ (Telesco et al. 1991), ≈ 0.6 (Joy, Lester, & Harvey 1987), these correspond to $A_V \sim 14$, $\lesssim 8$, and ≈ 6, respectively, if we assume $A_V/A_K = 10$ (Draine 1989), so that it is difficult to discuss in detail by these wavelength.

On the other hand, since mid-infrared to millimeter wave bands are not affected by absorption, it is very suitable to study such heavily absorbed starburst regions. Mid-infrared, far-infrared and submillimeter continuum ($\approx$ dust itself) features show double lobe structure which emission is weak at the 2.2 μm peak but strong at the surrounding regions (Rieke et al. 1980, Telesco et al. 1991, Smith et al. 1991). Molecular gas (^{12}CO $J = 1-0, 2-1, 3-2$) observation also show double lobe structure (Nakai et al. 1987, Lo et al. 1987, Loiseau et al. 1990, Tilanus et al. 1991), but tend to have larger radius than infrared lobe (Telesco et al. 1991). Detail interferometric molecular observations show central peak around the center of the double lobe, but somewhat offset to west from the 2.2 μm peak (Carlstrom 1988, Shen & Lo 1995). These observations indicate that dust and molecular gas structure have a ring-like structure (Nakai et al. 1987) or tightly wound spiral arms (Shen & Lo 1995). Multi-line observations indicate that molecular gas temperature and density are $\sim 20 - 70$ K and $\sim 10^{4-5}$ cm^{-3}, respectively (Nguyen-Q-Rieu, Nakai, & Jackson 1989, Harris et al. 1991, Wild et al. 1992, Güsten, et al. 1993, Seaquist, Frayer, & Bell 1998). In addition, there are OH and H_2O masers at the central regions (Weliachew, Fomalont, & Greisen 1984, Baudry, & Brouillet 1996, Seaquist, Frayer, & Frail 1997), so that there would be much dense and warm gas. Atomic gas also indicates dense ($\approx 10^4$ cm^{-3}) and warm (≈ 200 K) condition (Lugten et al. 1986). 92 GHz free-free emission shows strong intensity which is equivalent to the flux from 5×10^5 O5 stars (Carlstrom & Kromberg 1991). These absorption-free observations also suggest active star formations at the central region of M82.

Recent interferometric observations suggest the existence of a superbubble, which may be formed by the massive supernova explosions (Weiβ et al. 1999, Neininger et al. 1998, Wills et al. 1999). ^{12}CO(1 - 0) and ^{13}CO(1 - 0) observations suggest the existence of superwind around this region (Kikumoto et al. 1998). Inside of this superbubble, there is a strongest radio point source, 41.95+575, which may be a supernova remnant (Bartel et al. 1987, Wilkinson & de Bruyn 1990, Wills et al. 1997, Pedlar et al. 1999), and a middle mass black hole candidate (Matsumoto & Tsuru 1999, Ptak & Griffiths 1999).

These results are, however, still not explained each other systemically, so that the starburst in M82 is still not clear so far. We therefore performed high-resolution ($2''.8 \times 2''.3$), multi-line, deep imaging observations of the central region (450 pc in radius) of M82 with the Nobeyama Millimeter Array for understanding the starburst phenomena in M82.

3.2 Observations

Aperture synthesis observations of the central region of M82 were carried out in the ^{12}CO(1 - 0), ^{13}CO(1 - 0), C^{18}O(1 - 0), CS(2 - 1), HCO$^+$(1 - 0), and HCN(1 - 0) lines (rest frequency = 115.271 GHz, 110.201 GHz, 109.782 GHz, 97.981 GHz, 89.189 GHz, and 88.632 GHz, respectively) with the Nobeyama Millimeter Array (NMA) during 1997 November - 1999 March. All the images were obtained using three configurations

(D, C, and AB) of six 10m antennas which are equipped with tunerless SIS receivers (Sunada, Kawabe, & Inatani 1994). The system noise temperatures in the single side band were about 950 K, 850 K, 500 K, and 450 K at 115 GHz, 110 GHz, 98 GHz, and 89 GHz, respectively. As back-end, we used a XF-type spectro-correlator Ultra Wide Band Correlator (UWBC; Okumura et al. 2000), with a total bandwidth of 512 MHz and 256 channels for ^{12}CO observations (corresponding to 1300 km s^{-1} bandwidth with 5.2 km s^{-1} velocity resolution), and with a total bandwidth of 1024 MHz and 126 channels for other observations (corresponding to 2800 km s^{-1}, 3100 km s^{-1}, and 3500 km s^{-1} bandwidths with 22 km s^{-1}, 24 km s^{-1}, and 27 km s^{-1} velocity resolutions for 110 GHz, 98 GHz, and 89 GHz, respectively). Since the NMA receiver system has an intermediate frequency (IF) of 6 GHz, and the UWBC can obtain both the upper side band (USB) and the lower side band (LSB) with 1024 MHz bandwidth, it is possible to observe (a) ^{13}CO(1 – 0), C^{18}O(1 – 0), and CS(2 – 1) lines, and (b) HCO$^+$(1 – 0) and HCN(1 – 0) lines, simultaneously (figure 3.1). The band-pass calibration was done with 3C273, and 0923+392 was observed every 10 minutes as a phase and amplitude calibrator. The flux scale of 0923+392 was determined by comparisons with Mars and Uranus. The uncertainty in the absolute flux scale is estimated to be $\sim$ 20%.

The data were analyzed using the NRO software package "UVPROCII", and the final maps were made and CLEANed with the NRAO software AIPS. All these maps except C^{18}O were made with natural weighting. Since C^{18}O emission is weak, the map was made with the UV tapering of 60 kλ to increase the signal-to-noise ratio at the cost of the spatial resolution. The spatial resolutions, their linear scale, and the typical noise level of the channel map of the ^{12}CO, ^{13}CO, C^{18}O, CS, HCO$^+$, and HCN maps were summarized in table 3.1. We also obtained 100 GHz continuum with USB of HCO$^+$ and HCN simultaneous observations. The central frequency and the bandwidth of the continuum are 100.884 GHz and 1024 MHz, respectively. The spatial resolutions of the 100 GHz continuum is 3.″7 × 3.″3, which corresponds to a linear scale of 56 pc × 50 pc. The typical noise level of the map was 1.6 mJy beam^{-1}. We also summarize the continuum observational parameters in table 3.1.

3.3 Results

3.3.1 Distributions of Observed Gas

Total integrated intensity maps of observed molecular lines and 100 GHz continuum are shown in figure 3.2. The plus and cross marks indicate the positions of the galactic nucleus (dynamical center) determined from the peak of the strongest 2.2 μm source (Lester et al. 1990) and the centimeter-wave continuum point source 41.95+57.5 which would be a young supernova remnant (Bartel et al. 1987, Wilkinson & de Bruyn 1990). The overall distributions of molecular gas are coincident with previously identified (Carlstrom 1988, Shen & Lo 1995) three prominent peaks, so-called double lobes (or North-East [NE] and South-West [SW] lobes) and a central peak. These distributions are briefly summarized in figure 3.3.

^{12}CO and ^{13}CO molecular gas tend to reside in SW lobe, but neutral dense molecular gas (HCN and CS) tend to reside in opposite side of the lobe (NE lobe). 100 GHz continuum is strong in central peak and inner side (east side) of the SW lobe, and some weak emission is in NE lobe. The distribution of HCO$^+$ tend to have the characteristics

Table 3.1: Observational parameters.

	Synthesized beam (Linear scale*)	Velocity resolution	R.m.s. noise	
			Channel map†	Moment map
^{12}CO(1 – 0)	2.″8 × 2.″3 (42 pc × 35 pc)	5.2 km s^{-1}	37.7 mJy beam^{-1} (540 mK)	1.6 Jy km s^{-1} (23 K km s^{-1})
^{13}CO(1 – 0)	3.″9 × 3.″4 (59 pc × 51 pc)	22 km s^{-1}	10.7 mJy beam^{-1} (82 mK)	0.93 Jy km s^{-1} (7.1 K km s^{-1})
C^{18}O(1 – 0)	5.″1 × 4.″4 (77 pc × 66 pc)	22 km s^{-1}	8.9 mJy beam^{-1} (40 mK)	0.73 Jy km s^{-1} (3.3 K km s^{-1})
CS(2 – 1)	4.″3 × 3.″6 (65 pc × 45 pc)	24 km s^{-1}	5.8 mJy beam^{-1} (48 mK)	0.51 Jy km s^{-1} (4.2 K km s^{-1})
HCO$^+$(1 – 0)	4.″0 × 3.″6 (60 pc × 54 pc)	27 km s^{-1}	6.3 mJy beam^{-1} (67 mK)	0.64 Jy km s^{-1} (6.8 K km s^{-1})
HCN(1 – 0)	4.″1 × 3.″6 (62 pc × 54 pc)	27 km s^{-1}	6.4 mJy beam^{-1} (67 mK)	0.62 Jy km s^{-1} (6.5 K km s^{-1})
100 GHz continuum	3.″7 × 3.″3 (56 pc × 50 pc)	——	1.6 mJy beam^{-1} (16 mK)	——

* For distance 3.25 Mpc (Sandage & Tammann 1975).
† The noise level of a 8 MHz bandwidth. For 100 GHz continuum, the noise level of a 1 GHz bandwidth is displayed.

of the distributions of both neutral dense molecular gas and 100 GHz continuum. The detail line ratios will be discuss in next subsection (section 3.3.2).

We also identified diffuse spurs north and south (minor axis direction) of the galaxy, which can be clearly seen in ^{12}CO map. As shown in figure 3.4, the spurs well trace dark filaments which can be seen in optical B-band image (Alton, Davies, & Bianchi 1999). Since the dark filaments might be the absorption of dust, the spatial coincidence of the distributions of molecular gas and dark filaments indicates that molecular gas and dust might reside in similar regions. Similar structures (= spurs) have been detected further out in the filaments by low spatial resolution single-dish ^{12}CO(1 – 0) (Nakai et al. 1987) and millimeter and submillimeter continuum (dust emission; Kuno & Matsuo 1997, Alton, Davies, & Bianchi 1999) observations, but ours is the first detection close to the disk.

3.3.2 Molecular Line Intensity Ratios

To know the physical conditions of molecular gas in M82, we derived the intensity ratios of these lines. For the comparison with the 100 GHz continuum, we derived the ratios from the total integrated intensity maps. Since M82 is the edge-on galaxy, this comparison would be a rather crude way than the comparison with the position-velocity maps, but continuum emission has no velocity information, this way is the only way to compare.

Table 3.2: Intensity ratios of observed molecular gas at specific regions.*

Position	HCN/^{12}CO	HCN/^{13}CO	^{12}CO/^{13}CO
NE lobe	0.073 ± 0.004	1.29 ± 0.10	18.1 ± 1.1
Central peak	0.067 ± 0.005	1.54 ± 0.15	23.1 ± 2.0
SW lobe (E)	0.044 ± 0.004	0.82 ± 0.08	18.4 ± 1.1
SW lobe (W)	0.047 ± 0.004	0.57 ± 0.05	12.2 ± 0.5

* Quoted uncertainties are 1σ.

In this way, we only made the ratio maps of ^{12}CO, ^{13}CO, and HCN emission. We define the 'integrated intensity' as $I = \int T_B dv$ (K km s^{-1}). All the ratio maps were made using the tasks "COMB" and "IMEAN" in the AIPS package; first we corrected the primary beam attenuations, recovered the missing fluxes from the single dish observations (^{12}CO – Young et al. 1995; ^{13}CO – Young & Scoville 1984; HCN – this work (section 2.3)), and convolved all the maps to the same beam size of $4''.1 \times 3''.6$ corresponds to the spatial resolution of the HCN map which have the largest beam size. Next we made ratio maps with a clipping level of 2σ, and then averaged the ratios at specific regions. We divided the molecular gas distribution to four areas, that is, the NE lobe, central peak, SW lobe (E), and SW lobe (W) for the rough comparisons of the regional differences. Since the SW lobe is elongated to the east-west direction, we divided to the east side and west side. Table 3.2 summarized the integrated intensity ratios of the HCN/^{12}CO, HCN/^{13}CO, ^{12}CO/^{13}CO.

The HCN/^{12}CO ratios in all the regions of M82 clearly have lower values of < 0.1 than those of other starburst galaxies of > 0.1, rather similar to those of the normal or post-starburst galaxies of < 0.1 (Solomon, Downes, & Radford 1992, Kohno 1997). Although these ratios have low values, there are some tendencies between these four regions, that is, the NE lobe and central peak have somewhat higher values than those of the SW lobe (E) and (W). These differences are much clearly seen in other ratios. The HCN/^{13}CO ratios show that the central peak have the highest value of ~ 1.5, well corresponds to the single dish observations (section 2.3). The NE lobe and the central peak have high ratios of > 1 similar to those of starburst galaxies NGC 253 and NGC 3504, the SW lobe (E) has a ratio of ~ 0.8 similar to those of starburst galaxies NGC 2146, NGC 2903, NGC6946, and NGC 6951, and the SW lobe (W) has a low ratio similar to non-starburst regions or galaxies (see section 2.3). The ^{12}CO/^{13}CO ratios also have the highest value of ~ 23 at the central peak, which is similar to merging galaxies (Aalto et al. 1991a, Aalto et al. 1991b, Casoli, Dupraz, & Combes 1992a, Casoli, Dupraz, & Combes 1992b, Aalto et al. 1995, Aalto et al. 1997). The NE lobe and the SW lobe (E) also have high ratios of ~ 18, but SW lobe (W) has low ratio of ~ 12 similar to those of the normal galaxies (Sage & Isbell 1991, Young & Sanders 1986).

To sum up the major characteristics of these four regions, HCN/^{12}CO ratios are very low similar to those of the non-starburst galaxies. For HCN/^{13}CO and ^{12}CO/^{13}CO ratios, the central peak has high intensity ratios similar to those of other starburst galaxies, the NE lobe and SW lobe (E) have somewhat lower ratios than the central peak but in the range of the ratios of starburst galaxies, and the SW lobe (W) has the lowest ratios similar to those of the non-starburst galaxies.

3.3.3 100 GHz continuum

The 100 GHz continuum emission in M82 is dominated by free-free emission (figure 3.5), so that the strength of the 100 GHz continuum directly related with star formation activities like Hα emission in optical wavelength. Moreover, since the 100 GHz continuum observation would not be affected by the dust absorption as optical or near-infrared observations, there are great advantages in the observations of the star forming regions in edge-on galaxies or central region of galaxies where a large amount of dust hinder the star forming regions. Indeed, the central region of M82 are deeply obscured by dust even in the K-band (e.g. $A_{\rm K} \sim 1.4$, McLeod et al. 1993; $A_{\rm K} \lesssim 0.8$, Telesco et al. 1991; $A_{\rm K} \approx 0.6$, Joy, Lester, & Harvey 1987; these correspond to $A_{\rm V} \sim 14$, $\lesssim 8$, and ≈ 6, respectively, if we assume $A_{\rm V}/A_{\rm K} = 10$, Draine 1989), so that it is very hard to derive the flux of recombination lines in optical or near-infrared.

From the flux of the free-free emission, we can estimate the production rate of Lyman continuum photons, $N_{\rm Ly}$, from

$$\left(\frac{N_{\rm Ly}}{[{\rm s}^{-1}]}\right) \gtrsim 6.3 \times 10^{52} \left(\frac{T_{\rm e}}{10^4[{\rm K}]}\right)^{-0.45} \left(\frac{\nu}{[{\rm GHz}]}\right)^{0.1} \left(\frac{L_{\rm T}}{10^{20}[{\rm WHz}^{-1}]}\right), \qquad (3.1)$$

where $T_{\rm e}$ is the electron temperature, ν the frequency, and $L_{\rm T}$ the thermal (free-free) spectral luminosity (Condon 1992). Since $L_{\rm T} = 4\pi D^2 S_{\rm T}$ where D is the distance and $S_{\rm T}$ is the thermal (free-free) flux density, we can rewrite the equation (3.1) as

$$\left(\frac{N_{\rm Ly}}{[{\rm s}^{-1}]}\right) \gtrsim 7.6 \times 10^{52} \left(\frac{T_{\rm e}}{10^4[{\rm K}]}\right)^{-0.45} \left(\frac{\nu}{[{\rm GHz}]}\right)^{0.1} \left(\frac{D}{[{\rm Mpc}]}\right)^{2} \left(\frac{S_{\rm T}}{[{\rm Jy}]}\right). \qquad (3.2)$$

Using the equation (3.2) and the peak flux density of 100 GHz continuum ($\nu = 100.884$ GHz; see section 3.2) averaged over the beam size of $4\farcs1 \times 3\farcs6$ (62 pc $\times$ 54 pc), we calculated the minimum $N_{\rm Ly}$ at specific regions in M82, assuming $T_{\rm e} \sim 10^4$ K and $D \sim 3.25$ Mpc (Sandage & Tammann 1975). We also estimated the number of O8 stars ($M \sim 20$ M$_\odot$) assuming their $N_{\rm Ly}$ of $\sim 10^{48.35}$ s^{-1} (Panagia 1973). The results are summarized in table 3.3.

The star formations in M82 are very active at the central peak where the HCN/^{13}CO and ^{12}CO/^{13}CO ratios are relatively high compared with other regions. On the other hand, the star formation activity in the SW lobe (W), where the ratios are similar to non-starburst galaxies, is low. Those of the NE lobe and SW lobe (E), where the ratios are not so high but in the range of the ratios of starburst galaxies, are moderate. The calculated $N_{\rm Ly}$ are about a factor of 5 lower than those estimated by Carlstrom & Kronberg (1991), but this may due to their large beam size of $6\farcs8 \times 6\farcs1$.

3.4 Expanding Molecular Superbubble

3.4.1 Spatial and Kinematical Structure

At the innermost region of the spurs around the central peak and the SW lobe, there are arc-like features connecting these two peaks (figure 3.4). A position-velocity (PV) diagram cut along the major axis of the galaxy (figure 3.6b) shows an arc-like deviation from the rigid rotation at this region. It can be explained by the expanding superbubble. If there is an expanding bubble, the velocity of the line of sight can be seen as a

Table 3.3: 100 GHz continuum flux densities and corresponding Lyman continuum photons at specific regions.

Position	$F_{\rm T}^{*}$	$N_{\rm Ly}^{\dagger}$	$N_{\rm O8}^{\S}$
NE lobe	38.7	4.9×10^{52}	2.20×10^{4}
Central peak	56.8	7.2×10^{52}	3.23×10^{4}
SW lobe (E)	45.4	5.8×10^{52}	2.58×10^{4}
SW lobe (W)	29.2	3.7×10^{52}	1.66×10^{4}

$*$ Peak 100 GHz continuum flux [mJy beam^{-1}] in the specific regions. The beam size is $4\farcs1 \times 3\farcs6$. 1σ uncertainties are 1.3 mJy beam^{-1}.
† Production rate of Lyman continuum photons [s^{-1}] calculated with $F_{\rm T}^{*}$ averaged over the beam size. 1σ uncertainties are 0.2 s^{-1}. See text for detail.
§ Number of O8 stars ($M \sim 20$ M$_{\odot}$) whose total production rate of Lyman continuum photons is equivalent to the calculated $N_{\rm Ly}$. 1σ uncertainties are 0.07×10^{4}.

gradual change toward the center of the superbubble as shown in the schematic diagram (figure 3.6d), which is similar to the arc-like deviation in the PV diagram. Indeed, such gradual deviation in the PV diagram is one of the common features of the expanding HI superbubbles (Deul & den Hartog 1990). In addition, recent literatures also argued that this deviation is the implication of molecular superbubble, but they do not show any spatial evidence for it (Neininger et al. 1998, Weiβ et al. 1999, Wills et al. 1999). They argued that the superbubble has already broken toward the minor axis direction of this galaxy, and therefore do not show any shell structure in their figures. We made a channel map binning over the velocity range from $V_{\rm LSR} = 118$ to 212 km s^{-1}, which corresponds to the range deviates from the rigid rotation (figure 3.7c). The map clearly shows a shell-like structure between the two peaks (correspond to the central peak and the inner side of the SW lobe) with a diameter of ~ 210 pc $\times$ 140 pc ($\sim 14'' \times 9''$) along the north-south and east-west directions. This structure is also visible in other molecular lines such as ^{13}CO and HCN (figures 3.7d-e), as was previously argued by Neininger et al. 1998. Because of the spatially distinct shell structure (figures 3.7c-e) which cannot be seen in the previous observations and the gradual deviation in the PV diagram (figure 3.6b), this shell-like structure might be the first clear imaging of an expanding molecular superbubble.

3.4.2 Physical Properties

We first derive the expanding velocity and the dynamical timescale of the superbubble. The velocity field of the southern shell (figure 3.6c) is very close to rigid rotation. If we assume that the shell structure is the edge-brightening effect (Wills et al. 1999), the southern shell would be moving perpendicular to the line-of-sight, and this velocity might be the systemic velocity of the molecular superbubble (figure 3.6d). We can also assume that the systemic velocity of the superbubble is on the rigid rotation, since the PV diagram shows almost all of the molecular gas except that of the superbubble is on the rigid rotation (figure 3.6b). These reasons lead to the expanding velocity of the superbubble would be the most deviated velocity from the rigid rotation in PV

diagram (figure 3.6b), and the resultant expanding velocity would be $\sim$ 100 km s^{-1}. Similar discussions are also argued in Wills et al. (1999). However, we cannot reject the possibility of the expanding velocity of $\sim$ 50 km s^{-1} which is the mean deviation velocity in the PV diagram (Weiβ et al. 1999), so that we use the velocity of $50 - 100$ km s^{-1} for the following calculations. Assuming a constant velocity expansion, this expanding velocity and the size of the superbubble (radius of $\sim$ 105 pc) indicate that the elapsed time from the explosion can be estimated as $\sim 1 - 2 \times 10^6$ years.

Next, we will estimate the energetics of the superbubble. Using the intensity ratios between the ^{12}CO line and the ^{13}CO and HCN lines, we calculated CO-to-H_2 conversion factor based on the Large-Velocity-Gradient (LVG) approximation (Sakamoto 1999). Before the intensity ratio calculations, we recovered missing flux of each of three line images using single-dish observations (^{12}CO – Young et al. 1995; ^{13}CO – Young & Scoville 1984; HCN – this work (section 2.3)). The resultant conversion factor is $1.4 \pm 0.6 \times 10^{20}$ cm^{-2} (K km s^{-1})$^{-1}$, assuming normal [^{12}CO]/[H_2] abundance ratio and velocity gradient ranges of $50 - 100$ and $1 - 2$ km s^{-1} pc^{-1}, respectively. However, the kinetic temperature for the conversion factor of $\sim 0.8 \times 10^{20}$ (K km s^{-1})$^{-1}$ is $\sim 500 - 700$ K, which would be somewhat unusual at star forming regions, and also inconsistent with the results of the single dish observations of $\sim 100 - 300$ K (section 2.3). Also, that for the conversion factor of $\sim 2.0 \times 10^{20}$ (K km s^{-1})$^{-1}$ is < 100 K, also inconsistent with the results of the single dish observations. On the other hand, the temperature for the conversion factor of $\sim 1.4 \times 10^{20}$ cm^{-2} (K km s^{-1})$^{-1}$ is $\sim 100 - 200$ K, consistent with the results discussed in section 2.3. In addition, the conversion factor at this region taken from other literatures are $\sim 1.0 \times 10^{20}$ and $\sim 1.2 \times 10^{20}$ cm^{-2} (K km s^{-1})$^{-1}$ estimated from optically thin C^{18}O line (Wild et al. 1992) and 450 μm continuum (Smith et al. 1991), respectively, which are consistent with our result. Hence, we adopted 1.4×10^{20} cm^{-2} (K km s^{-1})$^{-1}$ as the CO-to-H_2 conversion factor for the following calculations. Using this conversion factor, the calculated molecular superbubble mass is $\sim 1.8 \times 10^8$ $M_\odot$. Total molecular mass inside the radius of 450 pc (observed region) is estimated to be $\sim 5.5 \times 10^8$ $M_\odot$, assuming same CO-to-H_2 conversion factor. These results indicate that about one-third of the molecular gas is affected by the explosion. From this molecular superbubble mass and the expanding velocity, we derived the kinetic energy of the superbubble as $\sim 0.5 - 2 \times 10^{55}$ erg. This energy is equivalent with the total energy of $\sim 10^3 - 10^4$ supernovae, assuming one supernova has a kinetic energy of $\sim 10^{51}$ erg and all the supernovae energy is used for the expansion of the superbubble. Since the transformation efficiency of the supernovae explosions energy to the kinetic energy of the superbubble would be smaller than 100%, the number of the exploded supernovae would be much larger. This energetics is more than an order of magnitude larger than that of HI superbubble in other galaxies, such as Our Galaxy, Large and Small Magellanic Clouds, M31, M33, and M101 which have $< 10^{54}$ erg (Tenorio-Tagle & Bodenheimer 1988 and the references therein).

3.4.3 Comparisons with Other Observations

This molecular superbubble is strong in the south region, but diffuse in the north region. On the other hand, the shell-like structure in the 408 MHz continuum (synchrotron emission; Wills et al. 1997), [Ne II] line (ionized gas; Achtermann & Lacy 1995), and the radio recombination line (H41α; Seaquist et al. 1996) images at similar spatial scales are strong in the northern part (figure 3.8a). These evidences seem to indicate that the southern part of it would be dominated by molecular gas but northern part by ionized

gas.

A PV diagram compared with the molecular gas and the recombination line (figure 3.8b) shows that the deviation from the rigid rotation in the recombination lines is much larger than that of the molecular gas. [Ne II] line kinematics also shows similar features (Wills et al. 1999). OH and H_2O masers (Weliachew, Fomalont, & Greisen 1984, Baudry, & Brouillet 1996, Seaquist, Frayer, & Frail 1997) are strongly concentrated at the boundary between the molecular gas and the recombination line in the PV diagram (figure 3.8b). Pumping mechanisms for OH masers are collision ($\approx$ shock) and/or IR/UV radiation ($\approx$ radiation from H II region), and for H_2O masers are basically shocks (Elitzur 1992). Indeed, OH masers can see just at the shocked region of the supernova remnant (Arikawa et al. 1999) and around the H II regions (Gaume & Mutel 1987), and H_2O masers is also distributed at the shocked regions of bow shocks (outflows from star forming dense cores; Claussen et al. 1998). Therefore, molecular gas and ionized gas would be strongly interacting at the boundary of the superbubble, and producing many shocked regions and/or induced star forming regions. This is consistent with the result of 100 GHz continuum observations discussed above (section 3.3.3).

Inside the superbubble (figure 3.7c), there is a 2.2 μm secondary peak (Dietz et al. 1986) which emission may be dominated by luminous supergiants (Joy, Lester, & Harvey 1987). A strong X-ray peak also locates at the center of the superbubble (Collura et al. 1994). Soft X-ray emission can be explained by the thermal emission from hot gas ($\approx 10^7$ K) heated by active star formations and supernova explosions (Watson, Stanger, & Griffiths 1984, Bregman, Schulman, & Tomisaka 1995). Hard X-ray observations show the time variability of its intensity, which indicate the existence of a middle mass black hole (heavier than stellar mass black holes but lighter than the supermassive black holes) with a mass of $\sim 460 - 2 \times 10^8$ $M_\odot$ (Matsumoto & Tsuru 1999, Ptak & Griffiths 1999).

The high-resolution ($2\farcs3 \times 1\farcs9$) 100 GHz continuum image superposed on the ^{12}CO superbubble contour shows clear offset between the ^{12}CO peaks and the 100 GHz continuum peaks. The 100 GHz continuum peaks tend to reside inside of the superbubble. The OH and H_2O masers distribute close to these 100 GHz continuum peaks. The center of the superbubble, on the other hand, the 100 GHz continuum is weak, where the 2.2 μm secondary peak and the X-ray peak are located.

3.4.4 Starburst at 2.2 μm Secondary Peak

We calculated the stellar population of the 2.2 μm secondary peak cluster, which located near the center of the superbubble, using the initial mass function (IMF) for the estimation of the starburst evolution at this cluster. Since the 2.2 μm secondary peak is dominated by the luminous supergiants (Joy, Lester, & Harvey 1987), we would estimate the number of stars for the K-band at the peak using the luminosity of a M2 I (M2 type supergiant) star. The luminosity of the 2.2 μm secondary peak at K-band (Dietz et al. 1986) with its extent (full width at half maximum (FWHM)) of $4''$ (McLeod et al. 1993) would be calculated as $\sim 3.0 \times 10^{27}$ erg s^{-1} Hz^{-1}. The absolute bolometric magnitude, $M_{\rm bol}$, bolometric correction, BC, and $V - K$ of a M2 I star are -8.3, -1.57, and 4.29, respectively (Pickles 1998), so that its absolute V magnitude, $M_{\rm V}$, and absolute K magnitude, $M_{\rm K}$, can be calculated as

$$M_{\rm V} = M_{\rm bol} - BC = -6.73 \tag{3.3}$$

and

$$M_{\rm K} = M_{\rm V} - (V - K) = -11.02, \tag{3.4}$$

respectively. Since 0.0 mag of $M_{\rm K}$ is equivalent to the flux of $10^{-20.20}$ erg s^{-1} cm^{-2} Hz^{-1} or to the luminosity of 7.5×10^{19} erg s^{-1} Hz^{-1}, the luminosity of a M2 I star might be 1.9×10^{19} erg s^{-1} Hz^{-1}. Therefore, the luminosity of the 2.2 μm secondary peak at K-band is equivalent to that of $\sim$ 1500 M2 I stars.

We next calculate the stellar content at the 2.2 μm secondary peak cluster. Since the timescale of the superbubble is only $\sim 1 - 2 \times 10^6$ yr, we assume that the stars with their mass larger than 20 M$_\odot$ (short-live stars with their lifetime of $\lesssim 10^7$ yr) are already exploded by supernovae, and that the remained high mass stars with their mass of 15 – 20 M$_\odot$ are now M2 I stars. Using an extended Millar-Scalo IMF (Kennicutt 1983) of $dN/dm \propto m^{-2.5}$ with lower and upper mass limits of 1 and 100 (see section 2.3.4 for detail), and assuming that there are 1500 stars whose mass are 15 – 20 M$_\odot$, the total stellar numbers and mass formed at the 2.2 μm secondary peak cluster can be calculated as $\sim 2 \times 10^5$ stars and $\sim 7 \times 10^5$ M$_\odot$, respectively. The number of $\gtrsim$ 20 M$_\odot$ stars which would have already exploded in this cluster are $\sim 3 \times 10^3$ stars, consistent with the estimated numbers of supernovae of $10^3 - 10^4$ which are needed to create the superbubble.

The efficiency of star formation in molecular clouds is generally $\sim$ 5 – 25% (Rieke 1988), so that molecular gas used to form the 2.2 μm secondary peak cluster would be $\sim 3 \times 10^6 - 1 \times 10^7$ M$_\odot$. If we assume the size of this cluster is corresponds to FWHM in K-band of 4″ (McLeod et al. 1993), the size might be about 60 pc. Compared with giant molecular clouds in Our Galaxy which have their size and mass of 20 – 80 pc and $8 \times 10^4 - 2 \times 10^6$ M$_\odot$, respectively (Goldsmith 1987), the molecular cloud which formed the 2.2 μm secondary peak cluster had similar size but had an order of magnitude heavier mass than those in Our Galaxy. In addition, since the mass of the superbubble is $\sim 1.8 \times 10^8$ M$_\odot$, that of the molecular cloud which formed the 2.2 μm secondary peak cluster is 1 – 2 order of magnitude smaller. This means that such a small-scale, localized starburst affected very massive, large-scale regions.

From these observational evidences and IMF calculations, it is obvious that this expanding molecular superbubble might be made as a result of localized starbursts occurred around the 2.2 μm secondary peak. Inside the superbubble, hot ionized gas created by the supernova explosions might be compressing the surrounding molecular gas outwards.

3.4.5 Effects of Superbubble to Starburst

As mentioned elsewhere, stars are believed to be made from the dense part of molecular gas (Lada 1992). Extragalactic observations also suggest that star formation activity has a better spatial and quantitative correlation with dense molecular gas (i.e. HCN) than tenuous molecular gas (i.e. ^{12}CO; Kohno, Kawabe, & Vila-Vilaró 1999, Kohno 1997, Solomon, Downes, & Radford 1992). Therefore, it is natural to think that the termination of star formation is caused by the exhaustion of dense molecular gas by making stars. However, as can be seen in the figure 3.7, almost all the molecular gas is blown away from the center of the superbubble by its explosion, so that star formation at the center of the superbubble would stop because of the lack of dense molecular gas. Indeed, the 100 GHz continuum at the center of the superbubble is weaker than the surrounding region, which support this discussion (figure 3.9). Hence, this superbubble

tells us that expulsion of dense molecular gas from star forming regions is another possible mechanism for the termination of star formation.

On the other hand, the swept up molecular gas is concentrated at the central peak and the SW lobe, and the inner side of these two peaks, there is strong 100 GHz continuum (free-free) emission (figure 3.9) equivalent to the flux from $\sim 10^5$ O8 stars (Carlstrom & Kromberg 1991), and also have the star formation efficiencies similar to or higher than other starburst galaxies (figure 3.11). This situation indicates that other starbursts are now ongoing at the inner side of these two peaks. Since these peaks correspond to the minor axis of the bubble and the diameter is about 70 pc smaller than that of the major axis, this difference suggests that the expansion toward the galactic disk might be suppressed by the molecular gas resides in the disk. This condition quite resembles to the hydrodynamical simulations (Tomisaka & Ikeuchi 1988), although the initial conditions would be somewhat different from that of the superbubble in M82. Therefore, it is reasonable to think that these two peaks might be formed by the expansion of the superbubble, and other starbursts might be induced by the compression.

3.4.6 Middle Mass Black Hole

As mentioned above, recent hard X-ray observations show the time variability of the intensity of the strongest X-ray peak in M82 (Matsumoto & Tsuru 1999, Ptak & Griffiths 1999), which locates near the 2.2 μm secondary peak. This time variability indicates the existence of a middle mass black hole with a mass of $\sim 460 - 2 \times 10^8$ $M_\odot$. We therefore discuss about the possibilities of this middle mass black hole formation at this 2.2 μm secondary peak cluster.

There would be two possibilities of making a middle mass black hole, (1) one is the merging of stellar black holes, and (2) another is the merging of stars before the supernovae and make a very high mass star, and produce a black hole after its supernova. The timescale of an object sink into the center of the stellar cluster by the dynamical friction (Binney & Tremaine 1987) can be estimated as $< 10^7$ yr in the 2.2 μm secondary peak cluster. Therefore, it would be possible to concentrate some of the stars or black holes (but not all of these) at the center of this cluster in the timescale of the superbubble of $1 - 2 \times 10^6$ yr.

We then discuss about the black hole mass with these merging process. We first discuss about the possibility (1). If we assume that stars with their mass larger than 25 $M_\odot$ would create stellar black holes of almost same mass (Brown & Bethe 1994), there would be 2×10^3 black holes with their total mass of 7×10^4 $M_\odot$ in this 2.2 μm secondary peak cluster, based on IMF calculations discussed in the previous section. A problem is the possibility of merging. Since stellar black holes have very small radii ($1 - 10$ km), it would be very hard to merge because of the angular momentum ejection and merging timescale ($\sim 10^9$ yr), the total mass of the stellar black holes will be the upper limit of the middle mass black hole. This upper mass limit is well within the range of that of the middle mass black hole estimated from the hard X-ray observations. Next, about the possibility (2), since stars have large radii ($\gtrsim 10^6$ km), it would be much easier for stars to be merged than stellar black holes. There are simulations of stellar merging (runaway merger) in compact clusters to create a very massive star ($\gtrsim 100$ $M_\odot$) in less than $3 - 4 \times 10^6$ years (Portegies-Zwart et al. 1999). If we assume that the stellar merging probability of 0.1% which is similar probability to the stellar merger simulations, it is possible to make a ~ 700 $M_\odot$ object in the 2.2 μm secondary peak cluster. Such a high

mass object would evolve to a similar mass ($\sim$ 700 $M_\odot$) black hole after the hypernova ($\gtrsim 10^{52}$ erg). This mass is also within the range of that of the middle mass black hole. To summarize, either possibilities are possible to create a black hole within the mass range decided by the hard X-ray observations, and we can also limit the black hole mass, $M_{\rm BH}$, in this cluster as $460 \lesssim M_{\rm BH} \lesssim 7 \times 10^4$ $M_\odot$, whose upper limit has estimated from the IMF calculations, and lower limit from the hard X-ray observations.

Since the cluster mass, $M_{\rm cluster}$, are calculated as 7×10^5 $M_\odot$ from IMF as calculated in the previous subsection, the ratio of $M_{\rm BH}$ over $M_{\rm cluster}$ would be $-3.2 \lesssim \log(M_{\rm BH}/M_{\rm cluster}) \lesssim -0.95$. We compared this ratio with those of other galaxies. We used the data of $M_{\rm bulge}$ ($\approx M_{\rm cluster}$) and $M_{\rm BH}$ in Magorrian et al. (1998) except their upper limit data. As shown in the figure 3.10, the estimated range of the middle mass black hole in M82 is on the $M_{\rm bulge}$-$M_{\rm BH}$ relation for galaxies with supermassive black holes.

Our results related to the superbubble and middle mass black hole might give a new explanation to the observations and discussions such as many of the quasar-like and AGN activities are related with starburst activities (AGN-starburst connection; Terlevich et al. 1992, Lawrence 1999), some of the quasars are embedded in interacting (and therefore active star forming) galaxies (Boyce et al. 1996, Boyce et al. 1998), strong γ-ray bursts (hypernova) with its energy of $\gtrsim 10^{52}$ erg (Mészáros 1999), and middle mass black holes located either at or offset from galactic nuclei (Colbert & Mushotzky 1999). According to our results, these would be created/ongoing with the similar mechanism (=localized starburst) which occurred in the 2.2 μm secondary peak cluster in M82.

3.5 Starburst in M82

To derive the physical conditions of molecular gas in M82, we calculated those using the observed line ratios based on LVG approximation. Detail modeling and the results of the LVG calculations are discussed in sections 2.2.4 and 2.3.4, and shown in figures 2.7 and 2.13. The intensity ratios at specific regions are shown in table 3.2, and the resultant physical conditions are summarized in table 3.4.

There are some differences in physical conditions of molecular gas between the specific regions. Molecular density in the NE lobe and the central peak tend to have somewhat (factor of two) higher than the SW lobe. Temperature is lower in SW lobe (W) than other regions. These tendencies are very similar to the 100 GHz continuum flux (and therefore Lyman continuum photons) shown in table 3.3. As discussed above (section 2.3.4 and section 3.3.1), molecular gas and dust are spatially correlated, so that it might be natural to have similar tendencies.

Although there are some differences in physical conditions between the regions, these differences are within the order of magnitudes of $\sim 10^3$ cm^{-3} and $\sim 10^2$ K. Compared with those of other galaxies in table 2.10, density of M82 is an order of magnitude lower than starburst galaxies but similar to non-starbursts. On the other hand, temperature is similar to or higher than starbursts, and an order of magnitude higher than non-starbursts. Hence, it is obvious that molecular gas in M82 has low-density and high-temperature conditions.

Since star formation activity is well correlated with the quantity of dense molecular gas (Kohno 1997, Solomon, Downes, & Radford 1992), molecular gas in the starburst galaxy M82 is expected to be rich in high-density gas. However, above results indicate

Table 3.4: Physical conditions of molecular gas in M82.

Position	$n(H_2)^{\dagger}$	$T_k^{\S}$
NE lobe	$\sim (5-7) \times 10^3$	~ 300
Central peak	$\sim (4-6) \times 10^3$	$\sim 400-500$
SW lobe (E)	$\sim (2-3) \times 10^3$	$\sim 300-400$
SW lobe (W)	$\sim 3 \times 10^3$	$\sim 100-200$

$*$ Molecular hydrogen number density in cm^{-3}.
† Kinetic temperature in K.

that M82 is dominated by tenuous gas. To discuss quantitatively, we calculated star formation efficiency (SFE) and compared with other galaxies observed by Kohno (1997). The SFE usually calculate using Hα luminosity, but it is very difficult to calculate for M82 because of the deep dust absorption. We therefore calculate the SFE using 100 GHz continuum data.

The calculations from 100 GHz continuum flux to SFE are as follows; The thermal flux density, S_T, is related with Hβ line flux, $F_{H\beta}$, as

$$\left(\frac{F_{H\beta}}{10^{-12}\ \mathrm{erg\ cm^{-2}\ s^{-1}}}\right) \sim 0.28 \left(\frac{T_e}{10^4\ \mathrm{K}}\right)^{-0.52} \left(\frac{\nu}{\mathrm{GHz}}\right)^{0.1} \left(\frac{S_T}{\mathrm{mJy}}\right), \tag{3.5}$$

and the $F_{H\beta}$ is related with Hα line flux, $F_{H\alpha}$, as

$$\frac{F_{H\alpha}}{F_{H\beta}} = 2.86 \left(\frac{T_e}{10^4\ \mathrm{K}}\right)^{-0.07}, \tag{3.6}$$

where T_e is the electron temperature and ν is the frequency of S_T (Condon 1992). Therefore, the relation between Hα luminosity, $L_{H\alpha}$, and S_T can be written as

$$\left(\frac{L_{H\alpha}}{\mathrm{erg\ s^{-1}}}\right) \sim 9.61 \times 10^{37} \left(\frac{D}{\mathrm{Mpc}}\right) \left(\frac{T_e}{10^4\ \mathrm{K}}\right)^{-0.59} \left(\frac{\nu}{\mathrm{GHz}}\right)^{0.1} \left(\frac{S_T}{\mathrm{mJy}}\right), \tag{3.7}$$

where D is the distance to the object. The star formation rate (SFR) is correlate with $L_{H\alpha}$ by (Kennicutt 1983)

$$\frac{\mathrm{SFR}}{\mathrm{M_\odot\ yr^{-1}}} = \frac{L_{H\alpha}}{1.12 \times 10^{41} \mathrm{ergs^{-1}}}. \tag{3.8}$$

Dividing this SFR by the beam size, we can obtain the SFR column density in unit of $M_\odot$ yr^{-1} pc^{-2}. On the other hand, the gas column density, Σ_{gas}, can be obtained assuming Galactic ^{12}CO-to-H_2 conversion factor of 3.0×10^{20} $cm^{-2}(K\ km\ s^{-1})^{-1}$ as

$$\left(\frac{\Sigma_{gas}}{M_\odot \mathrm{pc^{-2}}}\right) = 1.36 \times 500 \left(\frac{I_{CO}}{\mathrm{Jy\ km\ s^{-1}\ arcsec^{-2}}}\right), \tag{3.9}$$

where I_{CO} is ^{12}CO integrated intensity, and a factor of 1.36 is for the inclusion of He and other elements (Kohno 1997). The SFE (in unit of yr^{-1}) can obtain from the

equation (3.8) divide by the equation (3.9). If we assume the conversion factor of 1.4×10^{20} $cm^{-2}(K\ km\ s^{-1})^{-1}$ which is the derived value for the superbubble (section 3.4.2), the gas column density would be a factor of 1.4/3.0 smaller, and the SFE would be a factor of 1.4/3.0 larger than the derived values using the above equations.

We calculated the SFE for some regions in M82 and plotted on the HCN/CO-SFE correlation diagram (figure 3.11). Other galaxy data plotted on the diagram are taken from Kohno (1997). The data of M82 are largely offset from the correlation derived by Kohno (1997), and the SFE are similar to those of the starburst galaxies, but the HCN/^{12}CO ratios are similar to those of the non-starburst galaxies. Since the SFE is calculated from the Hα luminosity and the Hα emission is originate from the early type stars (OB stars), it is clear that M82 formed a large amount of early type stars as other starburst galaxies. However, the amount of dense gas is very small compared with starburst galaxies and similar to those of non-starburst galaxies. The stars believe to be formed from dense part of the molecular gas (Lada 1992), hence it is natural to think that dense gas is exhausted or blown away by the starburst activity, and therefore star formation in M82 would stop because of the lack of dense gas. We therefore suggest that M82 is now in the very late phase of starburst or in the very early phase of post-starburst. This suggestion is also supported by the results of near-infrared spectroscopy that M82 is in the late phase of starburst (Rieke, Lebofsky, & Walker 1988, Rieke 1988) whose age is about 5×10^7 yr (Rieke et al. 1980).

Model calculations of superbubbles show that the last phase (timescale of $\sim 10^7$ yr) of superbubbles have elongated, chimney-like structures which extend over 1 kpc (Tomisaka & Ikeuchi 1988). At this timescale, the shell (or wall) of this chimney-like structure is quite similar to the molecular spurs in M82, so that the spurs would be the remnants of broken superbubbles. Single-dish dust observations of M82 revealed that the dust extends at least 800 pc away from the galactic disk (Alton, Davies, & Bianchi 1999). Assuming that the expanding velocity of the dust is the same as our estimated expanding velocity of the superbubble, the expanding timescale would be $0.8 - 1.6 \times 10^7$ years, similar to the model calculations of Tomisaka & Ikeuchi (1988), but about one order of magnitude longer timescale than that of the molecular superbubble which can be seen in our image.

Since the large-scale outflow originate from at least two different burst regions (Shopbell, & Bland-Hawthorn 1998), the molecular spurs extend everywhere from the molecular disk (figure 3.7b), and there are about an order of magnitude difference in the expanding timescale between the superbubble and the large-scale outflow (previous paragraph), it is reasonable to suggest that the energetic explosions and the sequential starbursts similar to the superbubble region (section 3.4.5) have been occurred many times at the central region of M82 in this $\sim 10^7$ years. In addition, repeats of these energetic starburst cycles might create the spurs and the kpc-scale outflows. Now M82 has little dense gas in the starburst region, these starburst cycles might stop near future, and the formations of the large-scale outflows might also stop. This starburst cycle would be very important for other starburst galaxies, since many of these galaxies have similar large-scale outflows (Lehnert & Heckman 1996) as M82.

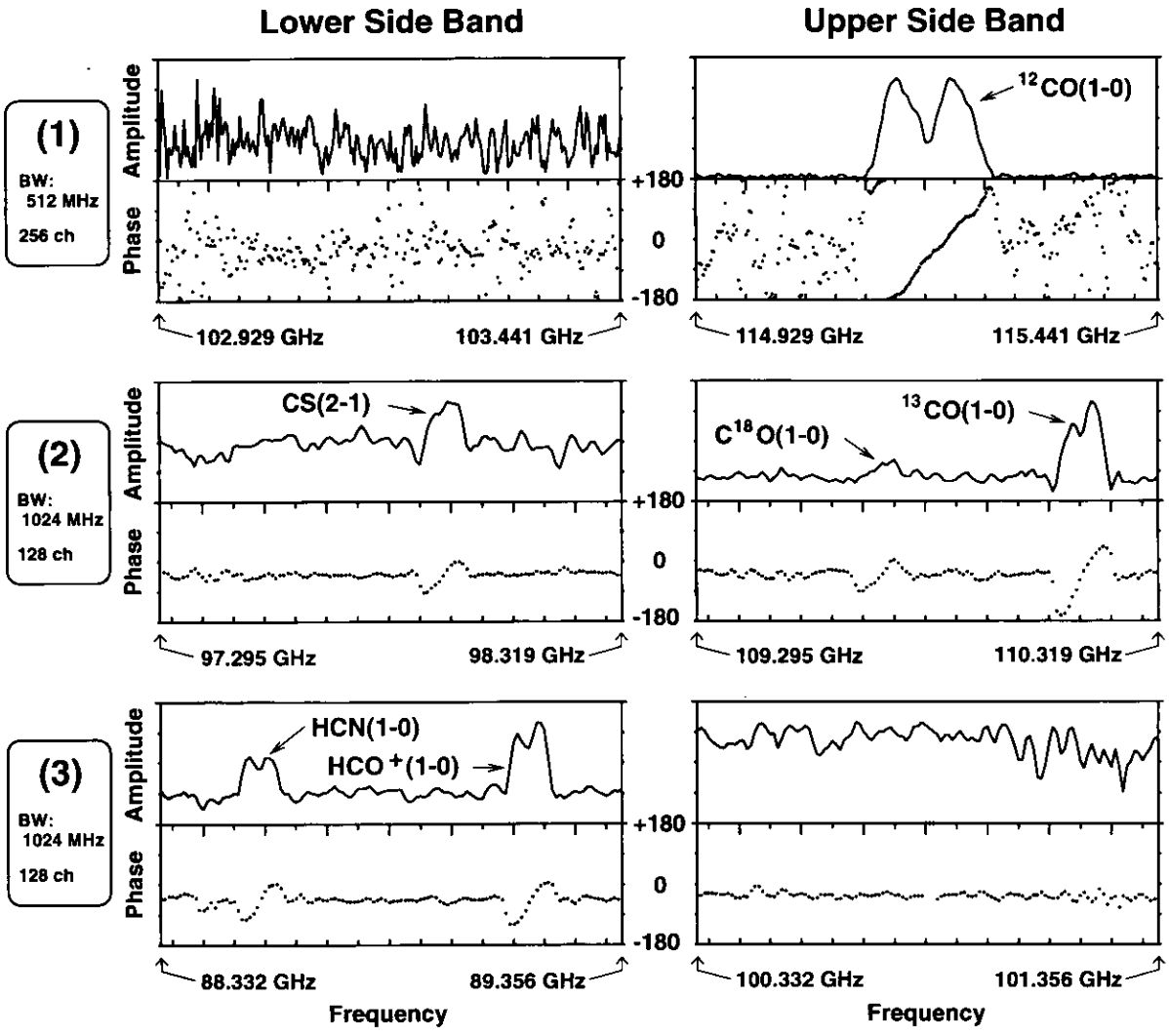

Fig. 3.1: Examples of the simultaneous observations with UWBC (Ultra Wide Band Correlator). Left side and right side columns of the figure indicate lower side band (LSB) and upper side band data (USB), respectively. Each row indicate one observation. *1st row* — LSB : continuum. USB : $^{12}CO(1-0)$ line. *2nd row* — LSB : CS(2 – 1) line. USB : $^{13}CO(1-0)$ and $C^{18}O(1-0)$ lines. *3rd row* — LSB : $HCO^{+}(1-0)$ and HCN(1 – 0) lines. USB : continuum.

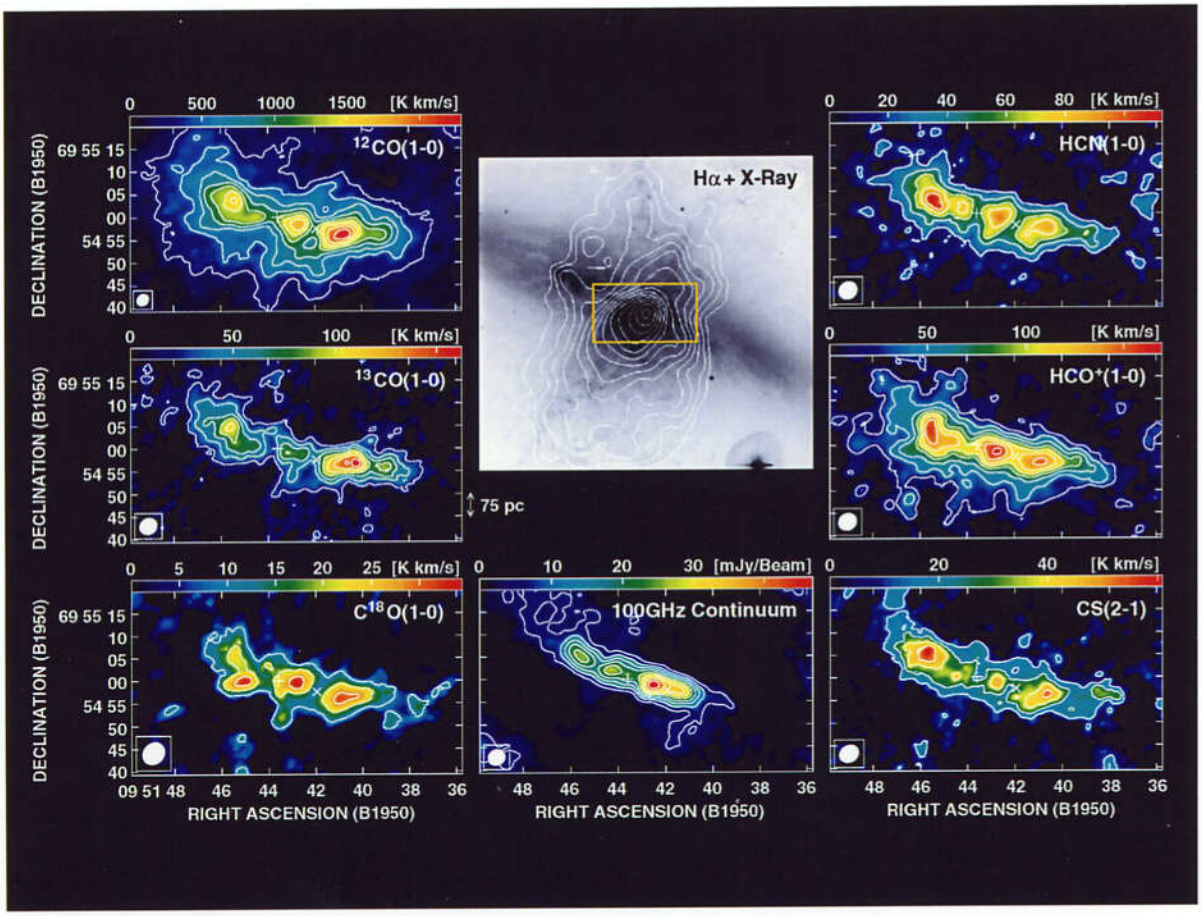

Fig. 3.2: Integrated intensity (moment) maps of ^{12}CO(1 – 0), ^{13}CO(1 – 0), C^{18}O(1 – 0), CS(2 – 1), HCO$^+$(1 – 0), HCN(1 – 0) lines, and 100 GHz continuum of the central region of M82. The region of these maps are indicated with a box in Hα (grayscale) and X-ray (white contours) images, which are taken from Shopbell & Bland-Hawthorn (1998) and Bregman, Schulman, & Tomisaka (1995), respectively. The color scale is shown at the top of each map. Synthesized beam is shown at the bottom-left corner of each map. The contour levels for ^{12}CO(1 – 0) map are $10\sigma, 20\sigma, 30\sigma, \cdots$, and those for other maps are $3\sigma, 6\sigma, 9\sigma, \cdots$. Detail observational parameters are indicated in table 3.1. The plus mark indicates the position of the galactic nucleus determined from the peak of the strongest 2.2 μm source (Lester et al. 1990) of α(B1950)=$9^h51^m43^s.6$, δ(B1950)=69°55′00″. The cross mark indicates the position of the centimeter-wave continuum point source 41.95+57.5 of α(B1950)=$9^h51^m41^s.95$, δ(B1950)=69°54′57″.5, which would be a young supernova remnant (e.g. Bartel et al. 1987).

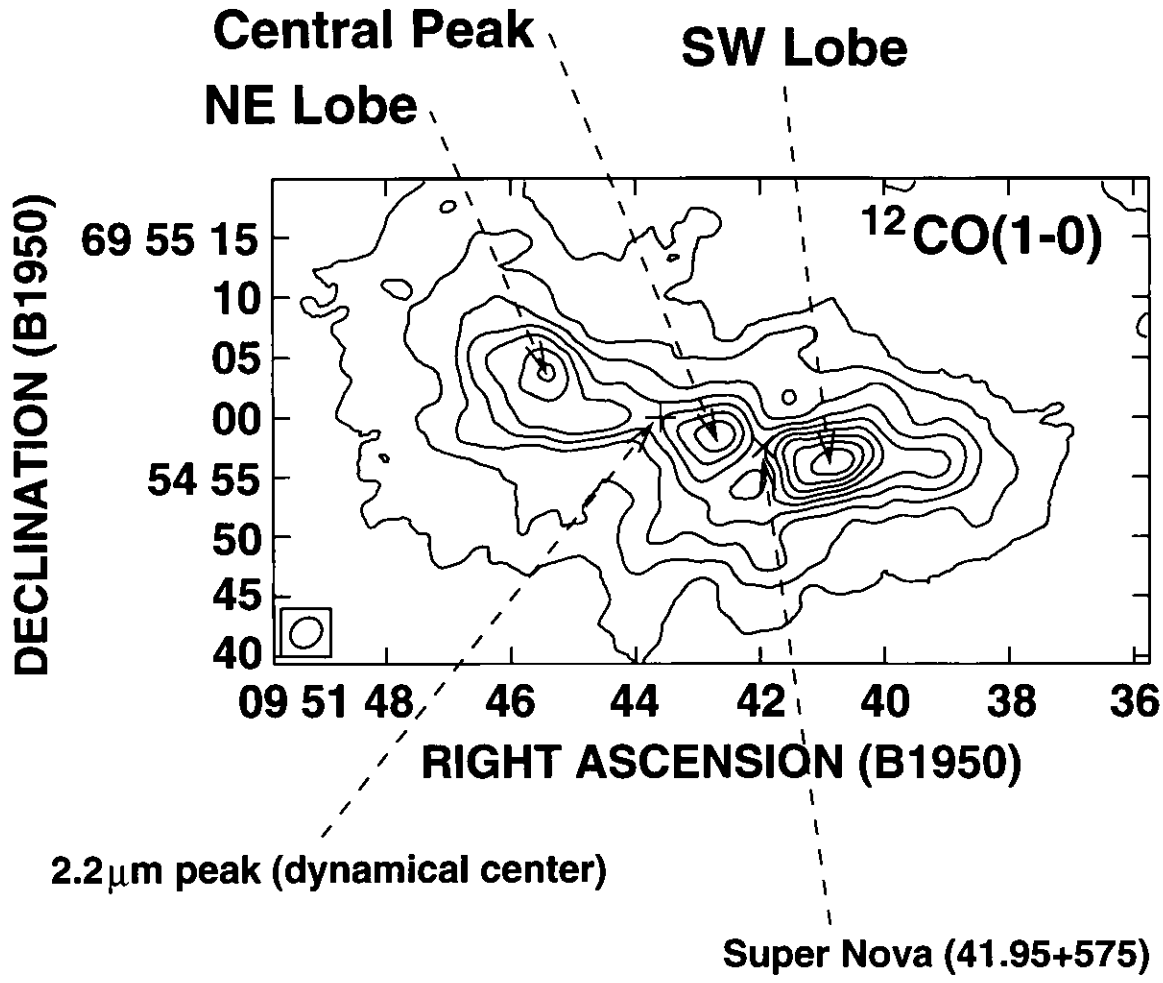

Fig. 3.3: Identifications of the molecular gas peaks and other important sources. The contour map is the integrated intensity map of $^{12}CO(1-0)$.

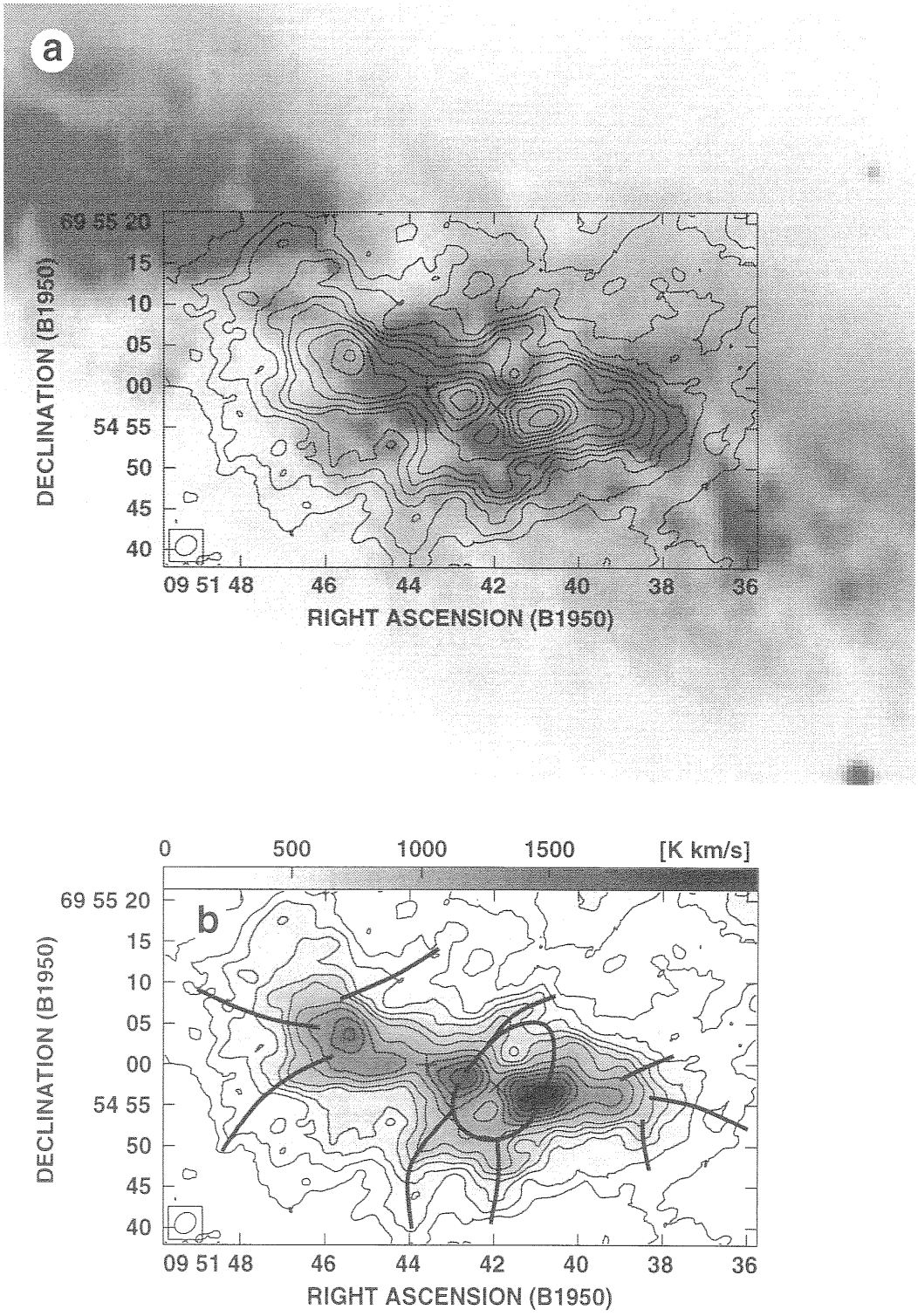

Fig. 3.4: Distribution of diffuse spurs. (a) ^{12}CO integrated intensity map (contours) superimposed on an optical B-band image (grayscale; Alton, Davies, & Bianchi 1999). The contour levels of the ^{12}CO map are $5, 10, 15, 20, 25, 30, 40, 50, \cdots, 90\sigma$, where 1 σ = 1.64 Jy beam^{-1} km s^{-1} [= 23 K km s^{-1}]. Bright regions of the grayscale are indicated in black and dark regions are in white. (b) Positions of the molecular spurs (thick lines) superimposed on the ^{12}CO integrated intensity map (contours and grayscale). Values for the grayscale are indicated on the top of the figure. The contour levels are same as (a). These figures clearly show the good coincidence in the distributions between molecular gas and optical dark filaments.

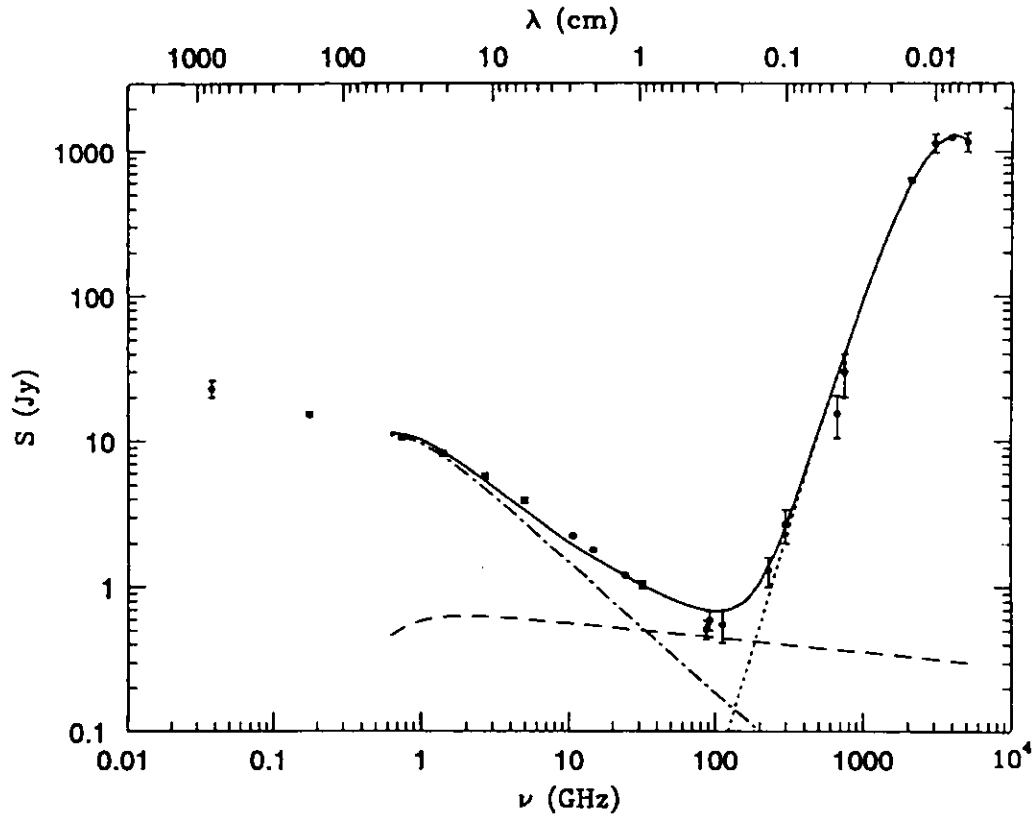

Fig. 3.5: Spectral energy distribution (from radio to far infrared) of M82. Total spectrum (solid line) consists of synchrotron (dot-dash line), free-free (dashed line), and dust (dotted line) emission. This figure clearly shows that the 100 GHz continuum emission is dominated by free-free emission. This figure is taken from Condon (1992).

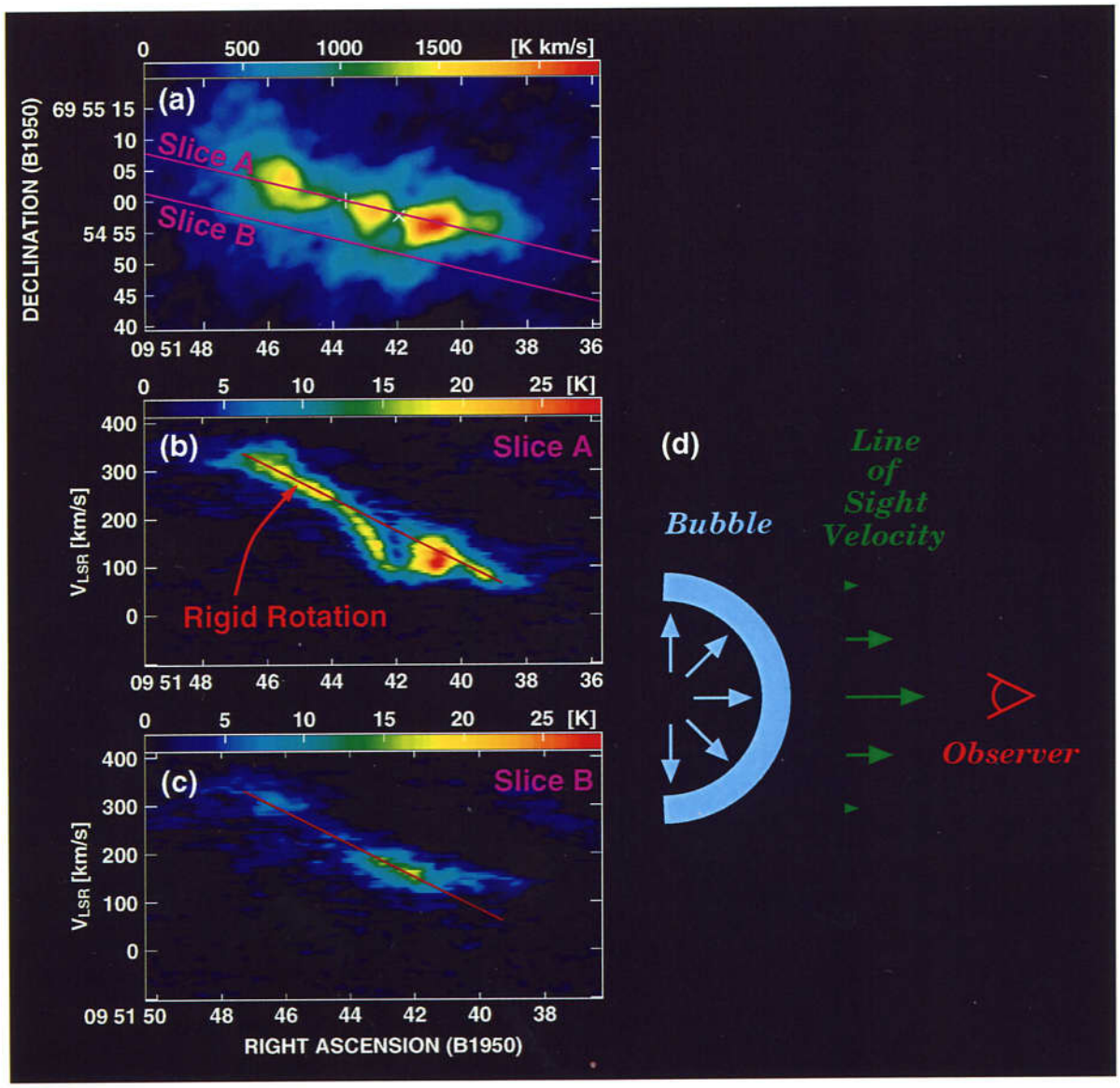

Fig. 3.6: The position-velocity (PV) diagrams of ^{12}CO(1 – 0) along the major axis of M82. (a) Integrated intensity map of ^{12}CO. Pink solid lines indicate the sliced regions for PV diagrams indicated below. (b) A PV diagram at slice A. A red solid line indicates rigid rotation velocity. The region of the superbubble (α(B1950)$\sim 9^{h}51^{m}43^{s}.6$) is clearly deviate from the rigid rotation velocity. (c) A PV diagram at slice B. A red solid line indicates rigid rotation velocity. Almost all of the gas at this slice is on the rigid rotation velocity. (d) A schematic diagram of expanding superbubble. If there is an expanding superbubble, the velocity of the line of sight can be seen as a gradual change toward the center of the superbubble. On the other hand, the edge of the superbubble would have same velocity as the systemic velocity.

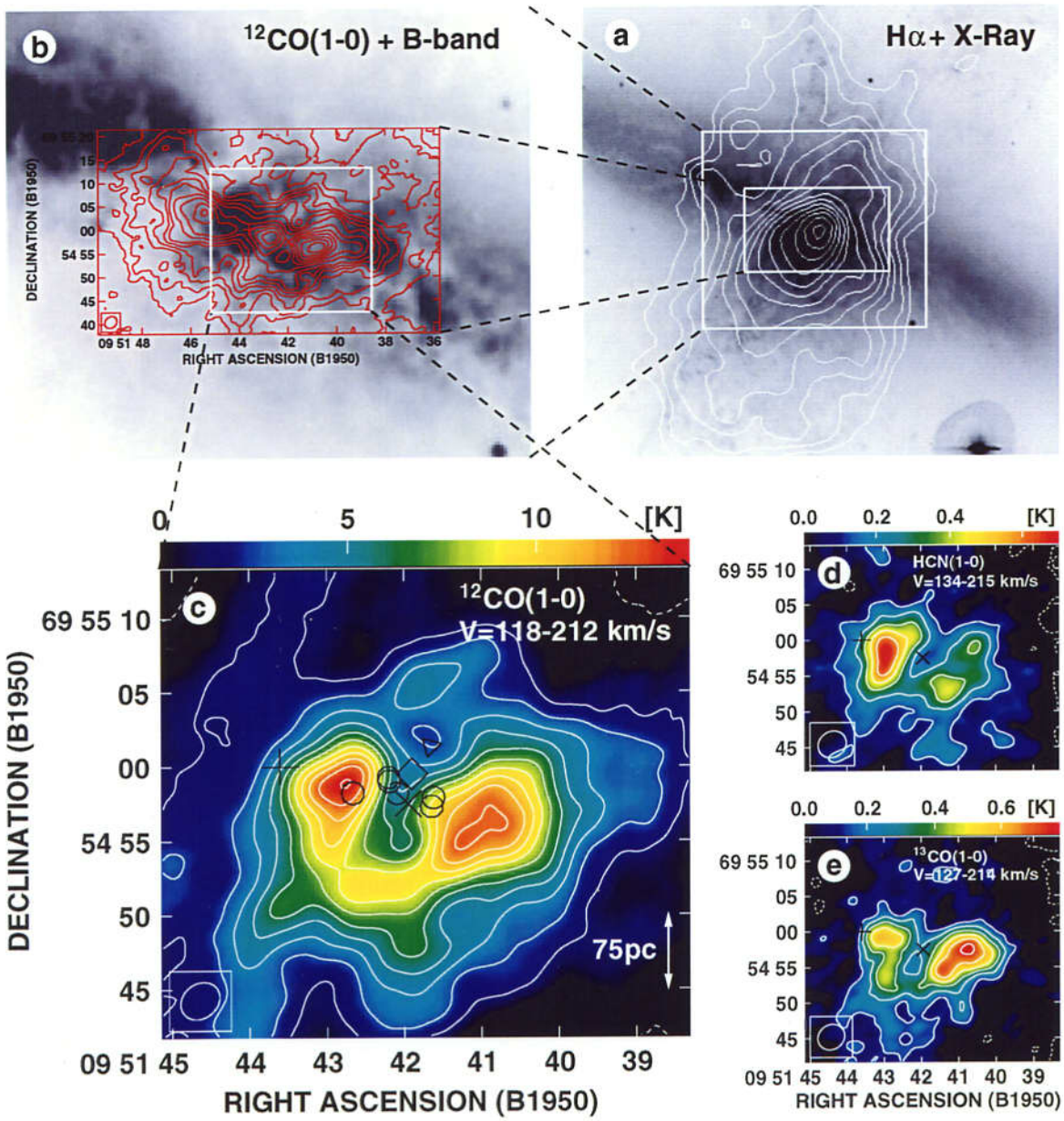

Fig. 3.7: (a) The X-ray image (contours) superimposed on the Hα image (grayscale), which is same as figure 3.2. (b) ^{12}CO integrated intensity map (contours) superimposed on optical B-band image (grayscale), which is same as figure 3.4. (c) The ^{12}CO molecular superbubble image binning over the velocity range of $118-212$ km s^{-1}. The contour levels of the ^{12}CO map are $-10, 10, 20, 30, \cdots, 110\sigma$, where 1 σ = 8.9 mJy beam^{-1} [= 127 mK]. Values for the color scale is indicated on the top of the figure. The synthesized beam size, and the plus and cross marks are the same as figure 3.2. The circle marks indicate the positions of OH and H_2O masers (Weliachew, Fomalont, & Greisen 1984, Baudry & Brouillet 1996, Seaquist, Frayer, & Frail 1997). The diamond and triangle marks indicate the positions of 2.2 μm secondary peak (Dietz et al. 1986) and the strongest X-ray peak (Bregman, Schulman, & Tomisaka 1995), respectively. This figure clearly shows that all these sources are well inside the molecular superbubble. (d) The HCN molecular superbubble image binning over the velocity range of $134-215$ km s^{-1}. The contour levels of the HCN map are $-6, -3, 3, 6, \cdots, 15\sigma$, where 1 σ = 3.7 mJy beam^{-1} [= 39 mK]. (e) The ^{13}CO molecular superbubble image binning over the velocity range of $127-214$ km s^{-1}. The contour levels of the ^{13}CO map are $-3, 3, 6, \cdots, 18\sigma$, where 1 σ = 5.4 mJy beam^{-1} [= 41 mK].

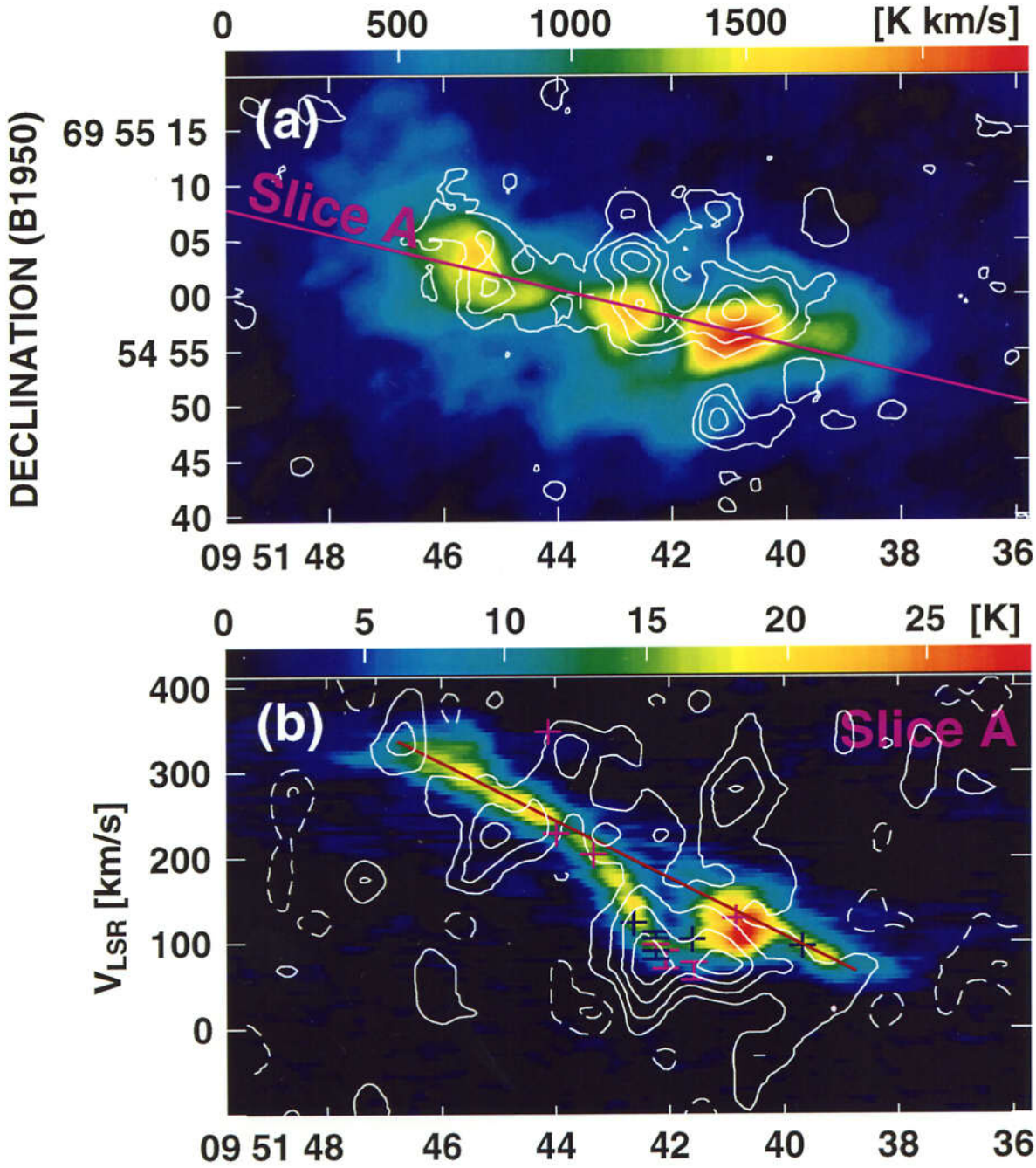

Fig. 3.8: H41α images (contours; Seaquist et al. 1996) superimposed on the ^{12}CO integrated intensity images (color scale). Values for the color scale is indicated on the top of the figure. (a) Integrated intensity maps. Pink solid lines indicate the sliced regions for position-velocity (PV) diagrams indicated below. This figure indicates that molecular gas (^{12}CO) is concentrated mainly on south (lower) side, but ionized gas (H41α) is concentrated mainly on north (upper) side. (b) PV diagram at slice A. Red solid line indicates rigid rotation velocity. Pink and blue marks indicate OH and H_2O masers, respectively. Plus marks indicate masers with small position and velocity range that cannot be indicated by the bars. Bar marks indicate masers with small position range but have large velocity range as indicated by the bars. The region of the superbubble (α(B1950)$\sim 9^h51^m43^s.6$) is clearly deviate from the rigid rotation velocity, and H41α emission have much larger deviation. At this region, masers are clearly concentrated.

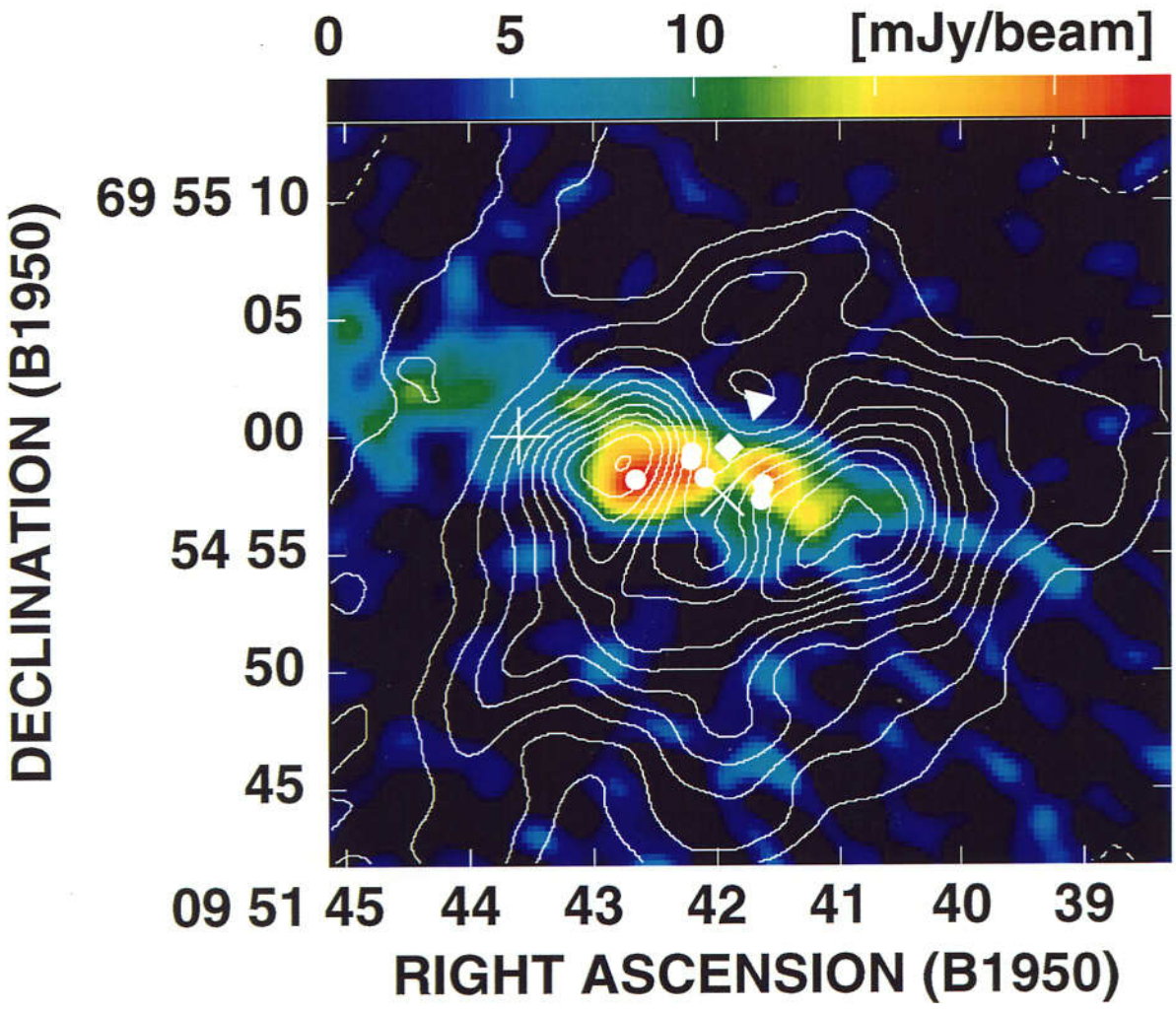

Fig. 3.9: The ^{12}CO integrated intensity image (contour) superimposed on the 100 GHz continuum image (color scale). The plus and cross marks indicate the positions of the nucleus and the strongest centimeter continuum peak 41.95+57.5. The circle, diamond and triangle marks indicate the positions of OH and H_2O masers, 2.2 μm secondary peak, and the strongest X-ray peak, respectively.

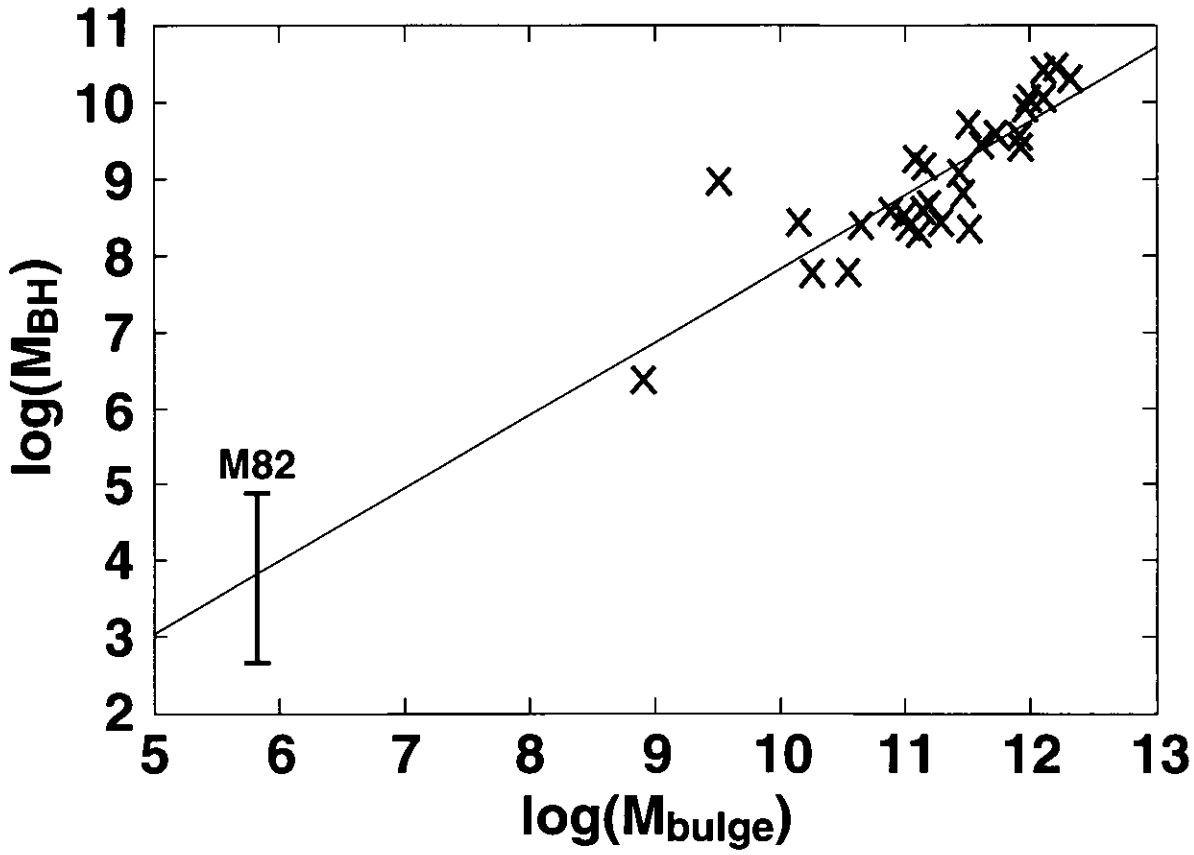

Fig. 3.10: A correlation diagram between bulge mass ($M_{\rm bulge}$) and black hole mass ($M_{\rm BH}$) in galaxies. Cross marks indicate the data taken from Magorrian et al. (1998), and a solid line is a linear fitting of their data. The upper limit and the lower limit of the data of M82 has estimated from the IMF calculations of the 2.2 μm secondary peak and the hard X-ray observations, respectively. The data of M82 is on the correlation derived from the data of supermassive black holes in galaxies (Magorrian et al. 1998).

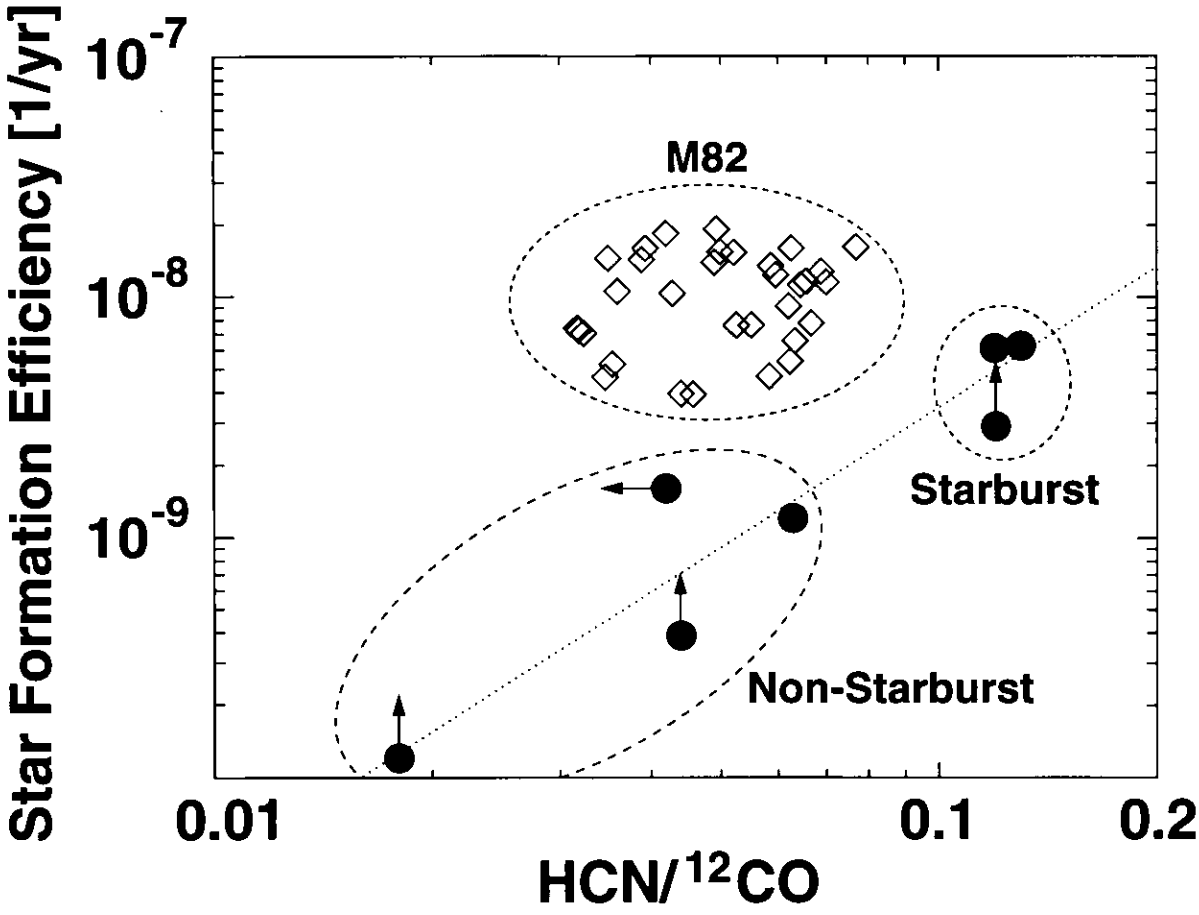

Fig. 3.11: A correlation diagram between HCN/^{12}CO intensity ratio and star formation efficiency in galaxies. Open diamonds are the data of M82 in many regions, filled circles indicate the data taken from Kohno (1997), and a dotted line is a linear fitting of his data. The data of M82 are largely offset from the correlation derived by Kohno (1997). The data of M82 have the SFE similar to those of the starbursts, but the HCN/^{12}CO ratios are similar to those of the non-starbursts.

Chapter 4

Molecular Gas in Nearby Galaxies

4.1 Introduction

To know about the physical conditions of molecular gas in starburst galaxies, we observed and discussed about the "prototypical" starburst galaxy M82 for the case study in the previous chapter. However, the results imply that M82 is not a typical starburst galaxy as we expected, which have very small amount of dense molecular gas. To obtain the further knowledge of the physical conditions of molecular gas in starburst regions, we observed additional three galaxies, another "prototypical" starburst galaxy NGC 253, the starburst galaxy NGC 3504, and the post-starburst galaxy NGC 4736 with Nobeyama Millimeter Array.

The "prototypical" starburst galaxy NGC 253 is one of the nearby (3.4 Mpc; Sandage & Tammann 1975) starburst galaxies, and therefore studied by many authors and in many wavelengths together with another "prototypical" starburst galaxy M82. Far infrared luminosity calculated from IRAS 60 μm and 100 μm data is $\sim 1.4 \times 10^{10}$ $L_{\odot}$, which is comparable with 1.6×10^{10} $L_{\odot}$ for M82 (see also Telesco & Harper 1980). Near-infrared Brackett line observations of the central region of NGC 253 show that the line strengths are similar to those of M82 (Rieke, Lebofsky, & Walker 1988), and suggest that the bolometric luminosity of the central region is probably produced by recently formed OB stars (Wynn-Williams et al. 1979, Beck & Beckwith 1984), which strongly implies the existence of starburst. However, the extent of the infrared source and nonthermal radio source are smaller than those of M82 (Rieke, Lebofsky, & Walker 1988), which suggests a smaller extent of the starburst region. Diffuse X-ray emission (Fabbiano & Trinchieri 1984, Fabbiano 1988, Cappi et al. 1999), optical emission lines (McCarthy, Heckman, & van Breugel, Lehnert & Heckman 1996), and dust emission (Alton, Davies, & Bianchi 1999) show outflow features but show smaller extent than M82, which also indicate that active starburst is now ongoing at the center but this active region is smaller. NGC 253 has a small-scale ($\sim$ 700 pc) bar (stellar and molecular bar; Canzian, Mundy, & Scoville 1988, Paglione, Tosaki, & Jackson 1995, Peng et al. 1996, Engelbracht et al. 1998) inside a large-scale ($\sim$ 4 kpc) bar (also stellar and molecular bar; Scoville et al. 1985, Engelbracht et al. 1998). This small-scale bar is rich in dense molecular gas (Paglione, Tosaki, & Jackson 1995, Peng et al. 1996), and suggested to have high temperature ($\gtrsim$ 100 K; Paglione, Tosaki, & Jackson 1995). These molecular properties are also supported by the low-resolution multi-molecular-line observations (Mauersberger, Henkel, & Sage 1990, Wall et al. 1991, Harrison, Henkel, & Russell 1999).

NGC 3504 is one of the Devereux starburst sample which have the characteristics of "M82 type" starburst in mid-infrared surface brightness viewpoint (Devereux 1989), and its near-infrared line observations suggest the large numbers of UV photons of $\sim 2.5 \times 10^{53}$ s^{-1} (Puxley, Hawarden, & Mountain 1988, Puxley, Hawarden, & Mountain 1990) which corresponds to 1.1×10^5 O8 stars (using $\log(N_{\rm UV}) \sim 48.35$ for O8 stars; Panagia 1973). It has a large-scale stellar bar with offset dust lanes along this bar (Buta & Crocker 1991, Kenney, Carlstrom, & Young 1993). Interferometric molecular gas observations show a centrally peaked structure, and the dust lanes are connecting to the edge of this molecular gas concentration (Kenney, Carlstrom, & Young 1993, Ishizuki 1993). Dense molecular gas distribution also shows a centrally peaked structure (Kohno 1997) and radio continuum observations also show similar features (Condon et al. 1990, Saikia et al. 1994), and therefore considered as nuclear starburst galaxy. However, recent high-resolution optical and near-infrared observations show circumnuclear star formation features (radius of about 2″or 250 pc) rather than star formation at the nucleus (Planesas, Colina, & Pérez-Olea 1997, Elmegreen et al. 1997).

Nuclear region of NGC 4736 spectra show Balmer line absorption features (Ho, Filippenko, & Sargent 1995, Taniguchi et al. 1996) which suggest that A-type stars are mainly dominated at this region (Taniguchi et al. 1996, Pritchet 1977), and absorption-corrected Hα luminosity requires only six O6 stars (Taniguchi et al. 1996) which implies very low star formation activity. Molecular gas observations suggest that nuclear gas is stable against the gravitational instability (Shioya et al. 1998), which also support the low star formation activity. Such a A-type star dominated region can be a site of a starburst in a very late phase (Rieke, Lebofsky, & Walker 1988, Rieke 1988, Walker, Lebofsky, & Rieke 1988); about 10^9 yr after the beginning of starburst, OB stars (short-lived stars of $\lesssim 10^8$ yr) would already burned out, but vast amount of A-type stars may be still alive, and therefore the spectra of old starburst regions would be dominated by those of the A-type stars. Because of these reasons, NGC 4736 is classified as a post-starburst galaxy.

Since stars are made from molecular gas, it is natural to think that these various starburst and non-starburst galaxies would have different molecular physical conditions, and therefore suitable to study about the relations of the physical properties of molecular gas and star forming activities.

4.2 Observations

Aperture synthesis observations of the central regions of NGC 253, NGC 3504, and NGC 4736 were carried out in ^{13}CO(1 – 0) line (rest frequency = 110.201 GHz) and 110 GHz continuum (using line free channels) with the Nobeyama Millimeter Array (NMA) during 1998 November - 1999 May. All the images were obtained using three configurations (D, C, and AB) of six 10 m antennas, which are equipped with tunerless SIS receivers (Sunada, Kawabe, & Inatani 1994). The system noise temperatures in the single side band at 110 GHz were about 420 K, 320 K, and 420 K for NGC 253, NGC 3504, and NGC 4736, respectively. As back-end, we used an XF-type spectro-correlator Ultra Wide Band Correlator (UWBC; Okumura et al. 2000), with a total bandwidth of 1024 MHz and 126 channels for other observations (corresponding to 2800 km s^{-1} bandwidths with a 22 km s^{-1} velocity resolution for 110 GHz). The band-pass calibrations for the observations of these galaxies were done with 3C273. Phase and amplitude calibrators were 0048-097, 1156+295, and 1308+326 for NGC 253, NGC 3504, and NGC 4736, respectively. The

Table 4.1: Observational parameters.

Galaxy	Line/Cont.	Weighting*	Synthesized beam (Linear scale†)	R.m.s. noise Channel map§	R.m.s. noise Moment map
NGC 253	^{13}CO(1 – 0)	NA	10.″9 × 5.″2 (180 pc × 86 pc)	7.8 mJy beam^{-1} (14 mK)	0.72 Jy km s^{-1} (1.3 K km s^{-1})
		RB	6.″8 × 3.″3 (110 pc × 54 pc)	18.4 mJy beam^{-1} (83 mK)	1.6 Jy km s^{-1} (7.0 K km s^{-1})
	110 GHz continuum	NA	10.″9 × 5.″2 (180 pc × 86 pc)	2.1 mJy beam^{-1} (3.7 mK)	— —
		RB	6.″8 × 3.″3 (110 pc × 54 pc)	3.2 mJy beam^{-1} (14 mK)	— —
NGC 3504	^{13}CO(1 – 0)	TP	4.″6 × 3.″8 (590 pc × 490 pc)	8.5 mJy beam^{-1} (49 mK)	0.67 Jy km s^{-1} (3.9 K km s^{-1})
	110 GHz continuum	TP	4.″5 × 3.″8 (580 pc × 490 pc)	1.2 mJy beam^{-1} (7.1 mK)	— —
NGC 4736	^{13}CO(1 – 0)	TP	5.″0 × 4.″4 (100 pc × 92 pc)	5.4 mJy beam^{-1} (25 mK)	0.39 Jy km s^{-1} (1.8 K km s^{-1})
	110 GHz continuum	TP	5.″0 × 4.″4 (100 pc × 92 pc)	0.84 mJy beam^{-1} (3.9 mK)	— —

* NA ··· natural weighting, RB ··· robust weighting (robust parameter = −1.5), TP ··· UV tapering with 60 kλ.
† Assuming distances as follows; NGC 253 ··· 3.4 Mpc (Sandage & Tammann 1975), NGC 3504 ··· 26.5 Mpc (Tully 1988), NGC 4736 ··· 4.3 Mpc (Tully 1988).
§ The noise level of a 8 MHz bandwidth. For 110 GHz continuum, the noise level of a 1 GHz bandwidth is displayed.

calibrators were observed every 10 minutes, and the flux scales of these calibrators were determined by comparisons with Mars and Uranus. The uncertainty in the absolute flux scale is estimated to be $\sim$ 20%.

The data were analyzed using the NRO software package "UVPROCII", and the final maps were made and CLEANed with the NRAO software AIPS. ^{13}CO(1 – 0) and 110 GHz continuum images of NGC 253 were made with natural weighting. Since the images of NGC 253 have high signal-to-noise (S/N) ratios, we also made robust weighting (robust parameter = −1.5) maps to increase spatial resolutions at the cost of the S/N ratios. The intensities of ^{13}CO(1 – 0) and 110 GHz continuum of NGC 3504 and NGC 4736 were very weak, so that we made these maps with the UV tapering of 60 kλ to increase the S/N ratio at the cost of the spatial resolution. The spatial resolutions, their linear scale, and the typical noise level of the channel maps of these images were summarized in table 4.1.

4.3 Results

4.3.1 Prototypical Starburst Galaxy NGC 253

We made high (10.″9×5.″2) and low (6.″8×3.″3) spatial resolution moment maps of observed ^{13}CO(1 – 0) line and intensity maps of 110 GHz continuum with natural weighting and robust weighting (robust parameter = −1.5). These are shown in figure 4.1. The plus mark indicates the position of the galactic nucleus determined from the 2 and 1.3 cm continuum peak (Ulvestad & Antonucci 1997). The high resolution 110 GHz continuum peak is located at α(B1950)=$00^h45^m05^s.73$, δ(B1950)=-25°33′37.″2, 2.″1 northwest of the 2 and 1.3 cm continuum peak and 2.″9 north of the 94 GHz continuum peak (Peng et al. 1996). The disagreement of the position between our 110 GHz continuum peak and 94 GHz continuum peak of Peng et al. (1996) is not clear. The ^{13}CO image of our data also show a few arcsec offset to the north from other ^{13}CO image (Hüttemeister & Aalto 1998), so that the offset maybe caused by artificial errors. One possibility of this artificial error is that the large separation between NGC 253 and the phase calibrator. There are no bright calibrators near NGC 253 so that the phase calibrator far from NGC 253 was used for the observations. We used 0048 − 097 (∼ 16° from NGC 253) for the phase calibrator, but Peng et al. (1996) used 0108 + 015 (∼ 27° from NGC 253) which have much larger elongation than our calibrator. Such a large separation between a calibrator and an object of ∼ 30 degree would cause some positional errors $\gtrsim$ 20% of synthesized beam, if baseline vectors are not very accurately determined (r.m.s. > 0.2 λ). This would be one of the reasons of the positional difference. For the following discussions, we will compare within our data or with other low-resolution observations and do not compare in detail with other high-resolution observations, because we cannot clarify the origin of the position offset between our data and other data.

The 110 GHz continuum shows a single peak in the low-resolution map, but shows a double peak structure elongated toward ∼ 3″ west in the high-resolution map. There is also weak emission along the previously identified "molecular bar" (Canzian, Mundy, & Scoville 1988). ^{13}CO emission shows bar-like structure consistent with the molecular bar. Low-resolution map implies that there is weak emission along the molecular bar at the edge of the field of view that is not previously identified. Detection of this emission may be due to our high sensitivity (∼ 70σ) observations. High-resolution map implies that strong peaks are located westward relative to the 110 GHz continuum peak. The strongest peak of the ^{13}CO emission is clearly offset from the peak of the 110 GHz continuum emission, which means that the ^{13}CO emission is weak at the star forming regions.

4.3.2 Starburst Galaxy NGC 3504

A moment map of the observed ^{13}CO(1 – 0) line and an intensity map of 110 GHz continuum are shown in figure 4.2. ^{12}CO(1 – 0) and HCN(1 – 0) images (Ishizuki 1993, Kohno 1997) are also shown in this figure. The plus mark indicates the position of the galactic nucleus determined from the 6 cm continuum peak (Saikia et al. 1994). The peak of ^{13}CO emission is clearly offset westward from the nucleus, which is different from the centrally peaked ^{12}CO and HCN distributions. These displacements between ^{13}CO emission and ^{12}CO and HCN emission can be seen in other galaxies, such as the central peak of M82 (see figure 3.2; ^{12}CO and HCN emission have a single peak, but

^{13}CO emission have double peaks), and overall distributions of Arp 299 (Aalto et al. 1997).

The peak of 110 GHz continuum also offsets from the nucleus but to the northeast direction. This offset is different from the molecular line emissions indicated above, and also different from the Hα distribution (Planesas, Colina, & Pérez-Olea 1997, Kenney, Carlstrom, & Young 1993). The Hα emission is distributed at southwest of the nucleus, and very weak at northeast. Since the northeast region of the nucleus is dominated by dust (Buta & Crocker 1991, Kenney, Carlstrom, & Young 1993), there are two possible causes of the offset between 110 GHz continuum and Hα emission distributions; one is that the Hα emission is strongly absorbed by dust, and another is that the 110 GHz emission is dominated by the dust emission. As discussed below (section 4.4.1), 110 GHz continuum emission is dominated by free-free emission which means that starburst is ongoing at the 110 GHz peak and therefore there might be Hα emission if there are no dust absorption. Hence, the first possibility would be plausible.

In figure 4.3, we show the radial distributions (averaged over concentric annuli of $1'' = 130$ pc width) of the HCN/^{13}CO, ^{12}CO/^{13}CO, and HCN/^{12}CO intensity ratios. Details about making these figures are described at section 2.2.3. We also show the starburst region traced by the 110 GHz continuum (central $\sim 5'' = 650$ pc region) with thick solid lines in each figure. All these ratios show high values at the starburst region. The HCN/^{13}CO ratio (figure 4.3(a)) shows higher than unity at the starburst region, which indicates that the molecular gas in the central region of NGC 3504 is in high-density and high-temperature condition. The ^{12}CO/^{13}CO and HCN/^{12}CO ratios (figure 4.3(b) and (c)) also shows high values of over 20 and 0.1 at the starburst region, which also support the high-density and high-temperature condition. These results are consistent with the results of single dish observations (section 2.3.4). On the other hand, these ratios show low values (HCN/^{13}CO $\lesssim 1$, ^{12}CO/^{13}CO $\lesssim 10$, and HCN/^{12}CO $\lesssim 0.1$) at the outer region (r$>$ 650 pc).

The extent of the molecular gas in NGC 3504 is only 10″, barely resolved with our $\sim 5 - 6''$ beam, so that it is very hard to discuss the spatial variation of the physical conditions based on integrated intensity maps in detail. We therefore calculate the intensity ratios using position-velocity (PV) diagrams of each molecular line, which means we will separate the molecular gas in NGC 3504 kinematically and discuss the physical conditions. We made the PV diagram intensity ratios with 2σ clipping, and divided to seven region with a 30 km s^{-1} width (VR1-VR7). The resultant ratios are summarized in table 4.2. The intensity ratios around the systemic velocity (VR4) are similar to those of NGC 253 which have high HCN/^{13}CO and HCN/^{12}CO of > 1 and > 0.2, respectively, but have low ^{12}CO/^{13}CO of $\lesssim 10$ (see table 2.9). On the other hand, the intensity ratios of other velocity ranges (except VR3) have high HCN/^{13}CO and ^{12}CO/^{13}CO ratios of > 1 and > 10, respectively, but have somewhat low HCN/^{12}CO values of ~ 0.1. These ratios are similar to those of M82. All the ratios of the range VR3 have high values. Since the positions of the molecular gas except VR4 (systemic velocity component) are located offset from the nucleus (Kenney, Carlstrom, & Young 1993), these components would be related with the circumnuclear star forming regions (Planesas, Colina, & Pérez-Olea 1997, Elmegreen et al. 1997).

We derived the physical conditions of molecular gas with the LVG calculations assuming normal molecular abundances, which are discussed in detail at section 2.2.4, using the intensity ratios in table 4.2. All the components except VR3 and VR4 have a density

Table 4.2: Integrated intensity ratios on position-velocity diagrams in NGC 3504.

Region	Velocity*	HCN/^{13}CO	^{12}CO/^{13}CO	HCN/^{12}CO
VR1	1430 – 1460	1.7	17.3	0.109
VR2	1460 – 1490	1.7	16.3	0.098
VR3	1490 – 1520	3.0	15.6	0.158
VR4	1520 – 1550	2.5	9.6	0.253
VR5	1550 – 1580	1.8	17.0	0.117
VR6	1580 – 1610	1.5	14.6	0.115
VR7	1610 – 1640	1.6	12.6	0.101

* Velocity range for intensity ratios in km s^{-1}. Velocity range VR4 corresponds to the systemic velocity region ($V_{\rm sys}$ = 1535 km s^{-1}; Kenney, Carlstrom, & Young 1993).

Table 4.3: Physical conditions of molecular gas in NGC 3504.

Region	$n(H_2)$*	$T_k^\dagger$
VR1	$\sim 1 \times 10^4$	$\sim 200 - 300$
VR2	$\sim 0.6 - 1 \times 10^4$	$\sim 200 - 300$
VR3	$\sim 1 - 4 \times 10^4$	$\sim 200 - 500$
VR4	$\sim 2 - 6 \times 10^4$	$\sim 150 - 300$
VR5	$\sim 1 \times 10^4$	$\sim 200 - 300$
VR6	$\sim 1 \times 10^4$	$\sim 200 - 300$
VR2	$\sim 0.7 - 1 \times 10^4$	$\sim 200 - 300$

* Molecular hydrogen number density in cm^{-3}.
† Kinetic temperature in K.

of $\sim 1 \times 10^4$ cm^{-3} and a temperature of $\sim 200 - 300$ K. The nearby systemic velocity component VR3 has higher density condition of $\sim 1 - 4 \times 10^4$ cm^{-3}, and also higher temperature condition of $\sim 200 - 500$ K. These physical properties of non-systemic velocity components would be related with ongoing circumnuclear starburst, since these components would be spatially related with these regions mentioned above. The systemic velocity component VR4 has higher density condition of $\sim 2 - 6 \times 10^4$ cm^{-3}, but temperature is similar to other components.

4.3.3 Post-Starburst Galaxy NGC 4736

A moment map of observed ^{13}CO(1 – 0) line and an intensity map of 110 GHz continuum are shown in figure 4.4. ^{12}CO(1 – 0) and HCN(1 – 0) images (Sakamoto et al. 1999, Kohno 1997) are also shown in this figure. The plus mark indicates the position of the galactic nucleus determined from the 6 cm continuum peak (Turner & Ho 1994). There are two peaks in ^{13}CO map, one is the north peak which resides near the nucleus $\sim 1.5''$ offset to the north direction, and another is the south peak which is $\sim 10''$ offset to the south

of the nucleus and on the southern part of the molecular arcs (Sakamoto et al. 1999). The positions of these peaks disagree with those of ^{12}CO emission which are similar to the situations of NGC 3504 or other galaxies mentioned above (section 4.3.2). The nuclear peak of ^{12}CO map separates to two peaks in the higher resolution map, and one of the peaks coincides with the nucleus and another peak is $\sim 3''$ offset to north from the nucleus (Sakamoto et al. 1999). These two peaks are similar to the twin peaks in the UV map (Maoz et al. 1995). These results indicate that the ^{13}CO north peak resides between the two peaks. The position of the south peak also disagrees with those of ^{12}CO peaks which locate at the molecular arcs. On the other hand, the 110 GHz continuum map show no clear emission ($\lesssim 2\sigma$) inside the field of view. HCN also show no clear emission (figure 4.4, Kohno 1997).

Figure 4.5 indicates the radial distributions (averaged over concentric annuli of $3'' = 63$ pc width) of the HCN/^{13}CO, ^{12}CO/^{13}CO, and HCN/^{12}CO intensity ratios. Detail descriptions for the making of these figures are mentioned at section 2.2.3. Balmer absorption dominated region (central $\lesssim 10'' = 210$ pc region; Pritchet 1977) is also indicated with thick horizontal lines in each figure. The HCN/^{13}CO and HCN/^{12}CO ratios at the Balmer absorption dominated region show low values of < 0.6 and < 0.1, respectively. The ^{12}CO/^{13}CO ratio shows $\sim 7 - 11$ at the Balmer absorption dominated region, and much lower values ($\lesssim 6$) at the outer region ($\gtrsim 210$ pc).

4.4 Discussions

4.4.1 110 GHz continuum emission

For the estimations of star formation activities, Hα emission is one of the most useful data, since the Hα emission is in the optical wave band and therefore a lot of published data are available. The Hα emission is, however, easy to be affected by the dust absorption, it is not useful for the studies of dusty objects such as edge-on galaxies (e.g. M82 and NGC 253). On the other hand, the free-free emission in millimeter wave bands is useful for these objects because millimeter wave do not affected by the dust absorption. Problems for the free-free emission are the weakness of its intensity and the contaminations with synchrotron and dust emission. Therefore, there are little studies of the millimeter free-free emission. However, the newly installed UWBC in the NMA backend made the detections of weak continuum emission possible by its wide frequency bandwidth of 1 GHz. Also a great amount of centimeter (e.g. Condon 1992 and references therein) and far-infrared (IRAS) continuum observations, and the recent submillimeter dust observations by many authors made it possible to extract free-free emission from the observed millimeter continuum emission. Using published data and our continuum data (for NGC 253, however, there exist some missing flux in our data, so that we used the single-dish observation of Jura, Hobbs, & Maran 1978. See next subsection), we make decomposition of the spectrum into three components, i.e. synchrotron, free-free, and dust emission.

We made spectral energy distributions (SEDs) of NGC 253 and NGC 3504 using previously published flux data from 20 cm to 60 μm, and separated to synchrotron, free-free, and dust components. Synchrotron emission and free-free emission is assumed as $\propto \nu^{\alpha}$ and $\propto \nu^{-0.1}$, respectively, where synchrotron spectrum index α is a free parameter. The intensity of dust emission can be written as $\propto (1-e^{-\tau})B_{\nu}(T)$, where τ is dust opacity

and $B_\nu(T)$ is black body radiation at frequency ν and temperature T. In far-infrared, submillimeter, and millimeter wave bands, dust opacity is $\tau \ll 1$, and the opacity might be in proportion to ν^β and $\beta \sim 2$ (Hildebrand 1983, Draine & Lee 1984, Braine & Hughes 1999), so that we can write the intensity of dust emission as $\propto \nu^2 B_\nu(T)$, and T is a free parameter. The fitting result is shown in figures 4.6 and 4.7. The synchrotron spectral index and the dust temperature were fitted as ~ -0.8 and $T \sim 25$ K for NGC 253 and ~ -1.1 and $T \sim 33$ K for NGC 3504. In these figures, it is clear that 110 GHz continuum emission is dominated by free-free emission for both galaxies, which means that starburst is ongoing where the 110 GHz continuum detected.

Our NGC 4736 image does not show any millimeter continuum emission. Because of this non-detection of 110 GHz continuum emission, and no published submillimeter dust observations, there would be a large error to fit three components, and therefore we did not separate the SED of NGC 4736. Since $\sim$ 110 GHz continuum emission in NGC 253 and NGC 3504 (and also M82, figure 3.5, Condon 1992) are dominated by free-free emission, we assume that 110 GHz continuum emission in NGC 4736 also dominated by free-free emission. The r.m.s. of this image would give a good upper limit of the free-free emission. The HCN observations show no clear emission (figure 4.4, Kohno 1997) and Balmer lines show absorption features (Ho, Filippenko, & Sargent 1995, Taniguchi et al. 1996). Since stars are formed from dense gas (e.g. Lada 1992), the lack of HCN emission (dense gas) implies there would be no active star formations at this region. The existence of Balmer absorptions which indicate this region is mainly dominated by A-type stars, and the absorption-corrected Hα luminosity requires only six O6 stars (Taniguchi et al. 1996, Pritchet 1977). These results indicate that there are no active star formations at the center of NGC 4736, and are consistent with the weak free-free emission.

4.4.2 Relations between Dense Gas Fraction and Star Formation Efficiency

Kohno (1997) suggest that there is a rough correlation between HCN/^{12}CO ratios and star formation efficiencies (SFEs). Since the SFEs of his data are calculated using Hα emission data, there would be some possibilities of errors caused by the dust absorption effect as mentioned above. We therefore derive the SFEs using free-free ($\sim$ 100 GHz continuum) emission and discuss about the merit and demerit of this emission compared with optical Hα line, and after that we will discuss about the correlation between HCN/^{12}CO ratios and star formation efficiencies.

Both NGC 3504 and NGC 4736 have previously published Hα data and our 110 GHz continuum data, so that we can compare SFEs derived from both emission for these two galaxies. The calculation method of SFEs from Hα and free-free emission has mentioned in section 3.5. We assumed the electron temperature as 10^4 K in the following calculations. The extinction corrected Hα luminosity of NGC 3504 is $\sim 1.4 \times 10^{41}$ erg s^{-1} with $4'' \times 2''$ (510 pc $\times$ 260 pc in linear scale, assuming distance as 26.5 Mpc; Tully 1988) aperture (Ho, Filippenko, & Sargent 1997). This corresponds to the SFR column density of 8.6×10^{-6} M$_\odot$ yr^{-1} pc^{-2}, which has been calculated using the equation (3.8) and dividing by the linear scale of the aperture size. The SFE can be calculated with dividing by the gas column density (equation (3.9)), and the resultant SFE is $\sim 6.1 \times 10^9$ yr^{-1} (Kohno 1997). The Hα luminosity estimated from free-free emission, on the other hand, would be 6.7×10^{41} erg s^{-1} within the beam size of $5''.8 \times 4''.6$ which is the same as

the HCN/^{12}CO ratio discuss below. The corresponding SFR column density is 1.2×10^{-5} $M_\odot$ yr^{-1} pc^{-2}, and the SFE can be calculated as 3.9×10^{-9} yr^{-1}, only a factor of two lower than that calculated from Hα emission. The absorption corrected Hα luminosity of NGC 4736 is $\sim 1.3 \times 10^{38}$ erg s^{-1} with $3''.0 \times 1''.8$ (63 pc $\times$ 38 pc in linear scale, assuming distance as 4.3 Mpc; Tully 1988) aperture (Taniguchi et al. 1996), which corresponds to the SFR column density of 3.8×10^{-7} $M_\odot$ yr^{-1} pc^{-2} and the SFE of $\sim 1.6 \times 10^{9}$ yr^{-1} (Kohno 1997). The 2σ upper limit of the 110 GHz continuum observations implies the Hα luminosity of $< 6.6 \times 10^{39}$ erg s^{-1} with the beam size of $11'' \times 7''$, and therefore the SFR column density and the SFE would be $< 1.6 \times 10^{-6}$ $M_\odot$ yr^{-1} pc^{-2} and $< 2.5 \times 10^{-9}$ yr^{-1}, respectively. This SFE upper limit is higher than the SFE derived from Hα emission, so that both results do not contradict each other. These two results indicate that SFEs derived from free-free emission and extinction (or absorption) corrected Hα emission is consistent each other, and both are useful for the studies of star formation activities. We summarized these values in table 4.4.

We next calculate the SFE of the edge-on galaxy NGC 253 from 110 GHz continuum emission. Before this calculation, we compared our 110 GHz continuum flux with single-dish flux to see the amount of missing flux of our data. The single-dish 87.2 GHz continuum flux is 0.314 Jy with $75''$ beam size (Jura, Hobbs, & Maran 1978), whereas our $75''$ flux is 0.253 Jy. Assuming 87.2 GHz and 110 GHz continuum flux have almost same values, this indicates that our data recovers about 80% of the single-dish flux. We corrected the missing flux of 20% assuming this flux is distributed uniformly, and calculated Hα luminosity, SFR, and SFE according to the method mentioned in section 3.5. The equivalent Hα luminosity would be $\sim 3.2 \times 10^{41}$ erg s^{-1} within the beam size of $15'' \times 15''$ (same as that of the Nobeyama 45m observations). The calculated SFR column density and SFE would be 4.1×10^{-5} $M_\odot$ yr^{-1} pc^{-2} and 1.6×10^{-8} yr^{-1}, respectively. As mentioned above, these results might be good absorption-free values. From this absorption-free Hα luminosity, we can calculate the visual extinction, A_V, at the central region of NGC 253. Absorption uncorrected Hα luminosity is 1.0×10^{39} erg s^{-1} within $16''$ beam (Sorai et al. 2000a), and our Hα luminosity is 3.3×10^{41} erg s^{-1} within the same $16''$ beam. The difference between the logarithm of these values imply the absorption at Hα wave length, $A_{H\alpha}$, and the resultant $A_{H\alpha}$ is ~ 2.5. According to the average interstellar reddening relation of $A_{H\alpha}/A_V \sim 0.81$, the A_V can be estimated as ~ 3.1. Since NGC 253 is edge-on galaxy, the estimations of the visual extinctions from optical and infrared wave length are very difficult, and the published values imply very different values, such as $A_V = 5 - 6$ (I-, J-, and K-band observations toward the central $22''$ region; Uyama, Matsumoto, & Thomas 1984), $7 - 19$ (near- and mid-infrared observations. Wide A_V range caused by the various methods; Engelbracht et al. 1998), $35 - 80$ (radio recombination lines; Puxley et al. 1997), and so on. Our estimated A_V is lower than other published A_V. The estimated $L_{H\alpha}$, SFR, and SFE are summarized in table 4.4. Since A_V implies large variations depend on the observations, we do not show any Hα derived $L_{H\alpha}$, SFR, and SFE in this table.

We plotted HCN/^{12}CO-SFE correlation diagram using our HCN/^{12}CO ratios and SFEs data and those of Kohno (1997) in figure 4.8. This figure clearly shows that the SFEs for NGC 3504 and NGC 4736 which derived from Hα lines and 110 GHz continuum show good correspondence, and strongly suggest that $\sim$ 100 GHz continuum is very useful data for estimating the star formation activities, as mentioned above. Our newly obtained NGC 253 data strongly confirmed the correlation between HCN/^{12}CO intensity

Table 4.4: Hα luminosities, star formation rates and star formation efficiencies in nearby galaxies

	Hα*			110 GHz continuum†		
Galaxy	$L_{H\alpha}$	SFR	SFE	$L_{H\alpha}$	SFR	SFE
NGC 253	—	—	—	3.2×10^{41}	4.1×10^{-5}	1.6×10^{-8}
NGC 3504	1.4×10^{41}	8.6×10^{-6}	6.1×10^{-9}	6.7×10^{41}	1.2×10^{-5}	3.9×10^{-9}
NGC 4736	1.3×10^{38}	3.8×10^{-7}	1.6×10^{-9}	$< 6.6 \times 10^{39}$	$< 1.6 \times 10^{-6}$	$< 2.5 \times 10^{-9}$

* Hα luminosities ($L_{H\alpha}$), star formation rates (SFR) and star formation efficiencies (SFE) in erg s^{-1}, $M_\odot$ yr^{-1} pc^{-2}, and yr^{-1}, respectively, estimated from Hα line data.
† $L_{H\alpha}$, SFR, and SFE in erg s^{-1}, $M_\odot$ yr^{-1} pc^{-2}, and yr^{-1}, respectively, estimated from 110 GHz continuum flux data.

ratios and SFEs in a few hundred parsec scale, which indicate that star formations are closely related with the existence of the dense molecular gas.

4.4.3 Relations between Molecular Gas Intensity Ratios

In the previous section and in section 2.3, we derived a few hundred parsec resolution HCN/^{13}CO, ^{12}CO/^{13}CO, and HCN/^{12}CO ratios of nearby galaxies. Using these values, we plotted the correlation diagrams.

Figure 4.9 shows the correlation diagram of HCN/^{12}CO and HCN/^{13}CO intensity ratios. We also plotted the rough boundaries between low density ($n(H_2) < 10^4$ cm^{-3}) and high density ($n(H_2) \gtrsim 10^4$ cm^{-3}) of HCN/^{12}CO = 0.1, and between low temperature ($T_k < 100$ K) and high temperature ($T_k \gtrsim 100$ K) of HCN/^{13}CO = 1.0 with dotted lines. Starburst galaxies (NGC 253, NGC 3504, NGC 6946, and NGC 6951) tend to have high HCN/^{12}CO and HCN/^{13}CO ratios, but non-starburst galaxies (NGC 4736, NGC 4826, and NGC 5195) have low ratios. The velocity divided intensity ratios of NGC 3504 is also plotted at this figure. It is clear that the components around systemic velocity (VR3 and VR4) are largely offset from other components. Intensity ratios of starburst galaxies are scattered, particularly NGC 253 and NGC 3504 VR3 and VR4,

Figure 4.10 shows the correlation diagrams of HCN/^{12}CO-^{12}CO/^{13}CO and ^{12}CO/^{13}CO-HCN/^{13}CO intensity ratios. Also in these diagrams, the rough boundaries of HCN/^{12}CO = 0.1 and HCN/^{13}CO = 1.0 which mentioned above are plotted. We set the rough boundary for ^{12}CO/^{13}CO ratio as 10, which is the average values of nearby galaxies (e.g. Young & Sanders 1986, Sage & Isbell 1991), and larger than this value tend to relate with active star forming galaxies such as merging galaxies (Aalto et al. 1991a, Aalto et al. 1991b, Casoli, Dupraz, & Combes 1992a, Casoli, Dupraz, & Combes 1992b, Aalto et al. 1995, Aalto et al. 1997). As can be seen in these diagrams, ^{12}CO/^{13}CO ratios of NGC 253 and NGC 3504 VR4 are below the border of 10, although other ratios (HCN/^{12}CO and HCN/^{13}CO ratios) show higher values similar to other starburst galaxies.

The physical conditions of molecular gas in NGC 253 are $n(H_2) \sim 2 - 3 \times 10^4$ cm^{-3} and $T_k \sim 100$ K (table 2.10), which are higher density but lower temperature than the several velocity components (except VR3 and VR4) in NGC 3504 of $n(H_2) \sim 1 \times 10^4$ cm^{-3} and $T_k \sim 200 - 300$ K (table 4.3). The physical conditions of molecular gas in NGC 3504 VR4 show similar tendencies as NGC 253, which are the results of similar intensity ratios. Those of NGC 3504 VR3, on the other hand, show higher-density and

higher-temperature than the several velocity components in NGC 3504, which are the results of higher values in all three intensity ratios. Since the merging galaxies also show high intensity ratios in ^{12}CO, ^{13}CO, and HCN lines (section 2.2.5), molecular gas in these galaxies also have high-density and high-temperature.

All of the intensity ratios of molecular gas in non-starburst galaxies show lower values than the boundaries, and the resultant physical conditions imply low-density and low-temperature, as discussed in section 2.3.4.

These results indicate that (1) the physical conditions of molecular gas in starburst galaxies and non-starburst galaxies are different. Those of non-starburst galaxies have quiescent conditions (low-density and low-temperature), but those of starburst galaxies have higher-density and/or higher-temperature than non-starbursts. (2) Molecular gas in starburst galaxies have wide range of physical conditions like higher-density and lower-temperature (NGC 253 and NGC 3504 VR4), lower-density and higher-temperature (NGC 3504 VR1 $-$ 2 and VR5 $-$ 7), and higher-density and higher-temperature (NGC 3504 VR3 and maybe merging galaxies).

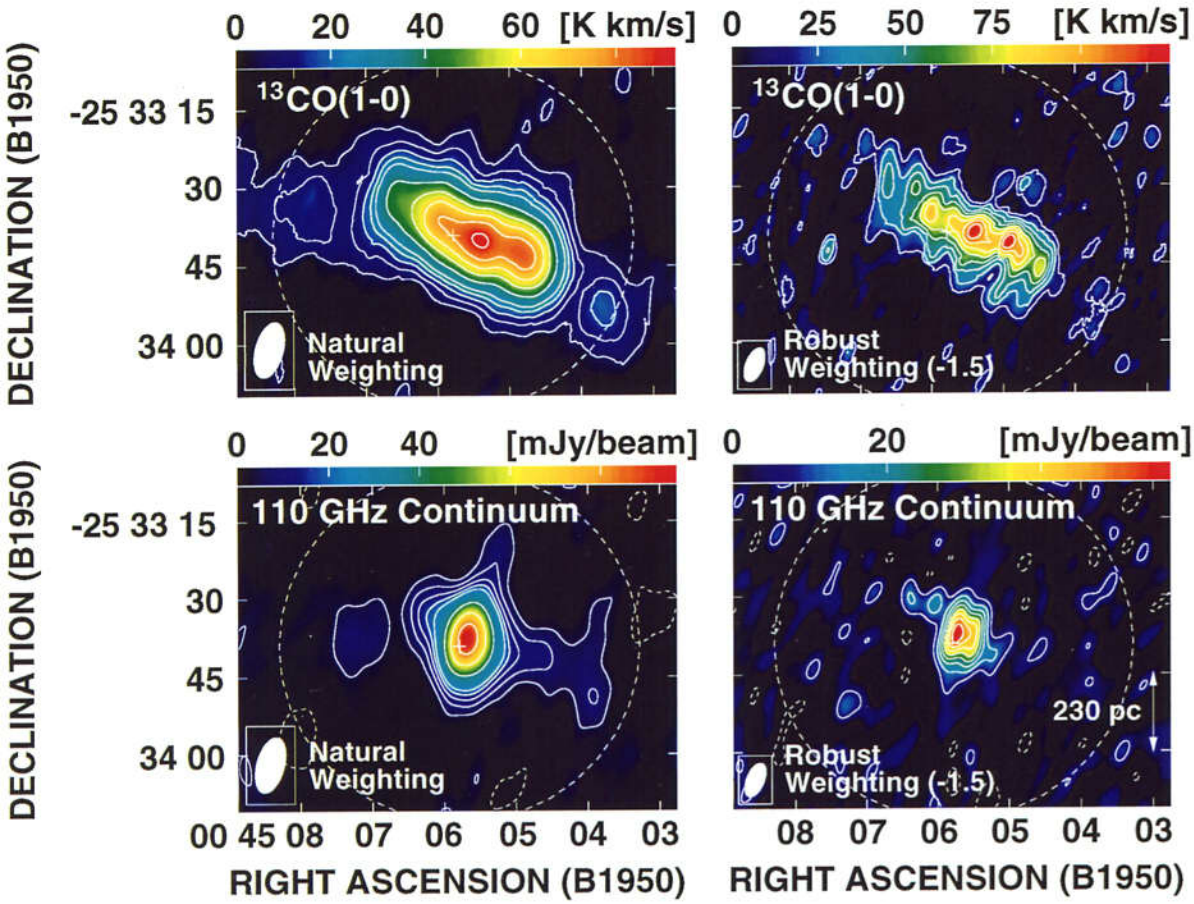

Fig. 4.1: High and low resolution images of ^{13}CO and 110 GHz continuum emission of the central region of the prototypical starburst galaxy NGC 253. The color scale is shown at the top of each map. The cross of each map marks the position of the galactic nucleus determined from the 2 cm and 1.3 cm continuum emission peak of α(B1950)=$00^{\rm h}45^{\rm m}05^{\rm s}.79$, δ(B1950)=$-25°33'39''.1$ (Ulvestad & Antonucci 1997). The field of view ($68''$) is indicated with a dashed circle. *Top left*: Low-resolution ^{13}CO$(1-0)$ moment map. This figure is made with natural weighting. Synthesized beam ($10''.9 \times 5''.2$, P.A. $= 165°$) is shown at the bottom-left corner. The contour levels are $4, 8, 12, 16, 20, 30, \cdots, 70\sigma$, where $1\ \sigma = 0.72$ Jy beam^{-1} km s^{-1} [$= 1.3$ K km s^{-1}]. *Top right*: High-resolution ^{13}CO$(1-0)$ moment map. This figure is made with robust weighting of -1.5. Synthesized beam ($6''.8 \times 3''.3$, P.A. $= 158°$) is shown at the bottom-left corner. The contour levels are $2, 4, 6, \cdots, 16\sigma$, where $1\ \sigma = 1.6$ Jy beam^{-1} km s^{-1} [$= 7.0$ K km s^{-1}]. *Bottom left*: Low-resolution 110 GHz continuum map. This figure is made with natural weighting. Synthesized beam ($10''.9 \times 5''.2$, P.A. $= 165°$) is shown at the bottom-left corner. The contour levels are $-2, 2, 4, 6, 8, 10, 20, 30$, and 40σ, where $1\ \sigma = 2.1$ mJy beam^{-1} [$= 3.7$ mK]. *Bottom right*: High-resolution 110 GHz continuum map. This figure is made with robust weighting of -1.5. Synthesized beam ($6''.8 \times 3''.3$, P.A. $= 158°$) is shown at the bottom-left corner. The contour levels are $-2, 2, 4, 6, \cdots, 16\sigma$, where $1\ \sigma = 3.2$ mJy beam^{-1} [$= 14$ mK].

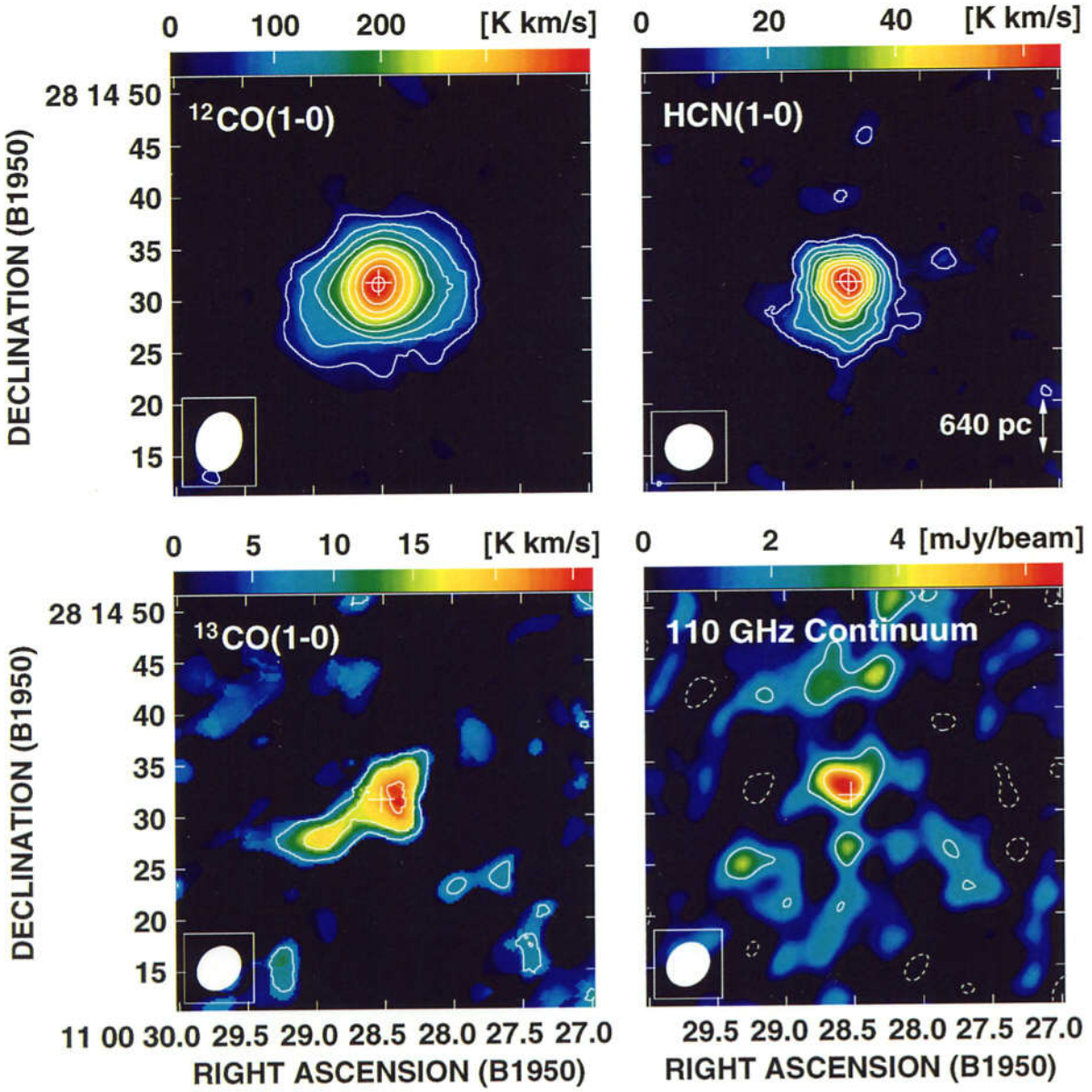

Fig. 4.2: Images of ^{12}CO, HCN, ^{13}CO, and 110 GHz continuum emission of the central region of the starburst galaxy NGC 3504. The color scale is shown at the top of each map. The cross of each map marks the position of the galactic nucleus determined from the 6 cm continuum emission peak of α(B1950)=$11^{\rm h}00^{\rm m}28^{\rm s}.52$, δ(B1950)=$28°14'31''.4$ (Saikia et al. 1994). The field of views of these maps are much larger than the indicated area. ^{12}CO and HCN maps are taken from Ishizuki (1993) and Kohno (1997), respectively. *Top left*: ^{12}CO(1 – 0) moment map. Synthesized beam ($5''.8 \times 4''.3$, P.A. = 164°) is shown at the bottom-left corner. The contour levels are $2, 4, 6, \cdots, 18\sigma$, where 1 σ = 6.3 Jy beam^{-1} km s^{-1} [= 23 K km s^{-1}]. *Top right*: HCN(1 – 0) moment map. Synthesized beam ($4''.6 \times 4''.3$, P.A. = 109°) is shown at the bottom-left corner. The contour levels are $2, 4, 6, \cdots, 18\sigma$, where 1 σ = 0.46 Jy beam^{-1} km s^{-1} [= 3.6 K km s^{-1}]. *Bottom left*: ^{13}CO(1 – 0) moment map. Synthesized beam ($4''.6 \times 3''.8$, P.A. = 137°) is shown at the bottom-left corner. The contour levels are $2, 4$, and 6σ, where 1 σ = 0.67 Jy beam^{-1} km s^{-1} [= 3.9 K km s^{-1}]. *Bottom right*: 110 GHz continuum map. Synthesized beam ($4''.5 \times 3''.8$, P.A. = 139°) is shown at the bottom-left corner. The contour levels are $-2, 2$, and 4σ, where 1 σ = 1.2 mJy beam^{-1} [= 7.1 mK].

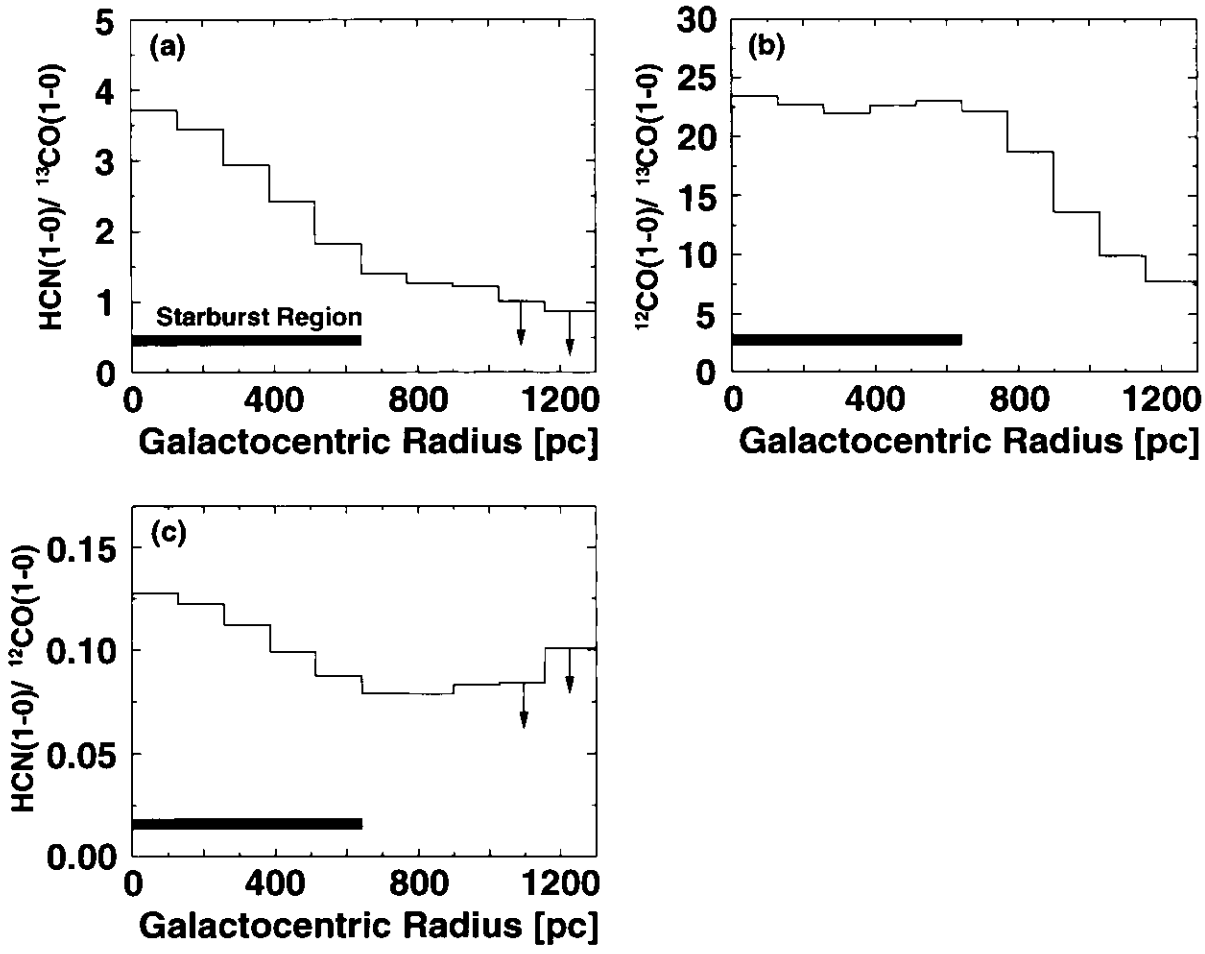

Fig. 4.3: Radial intensity ratio distributions in the central region of NGC 3504. All figures were made using a task "COMB" in AIPS package to divide images each other with clipping level of 2σ, and using a task "IRING" to averaged over concentric annuli of $1''$(130 pc) wide. Thick solid lines indicate the extent of starburst region determined by the 110 GHz continuum emission. (a) Radial distribution of HCN/^{13}CO intensity ratio. (b) Radial distribution of ^{12}CO/^{13}CO intensity ratio. (c) Radial distribution of HCN/^{12}CO intensity ratio.

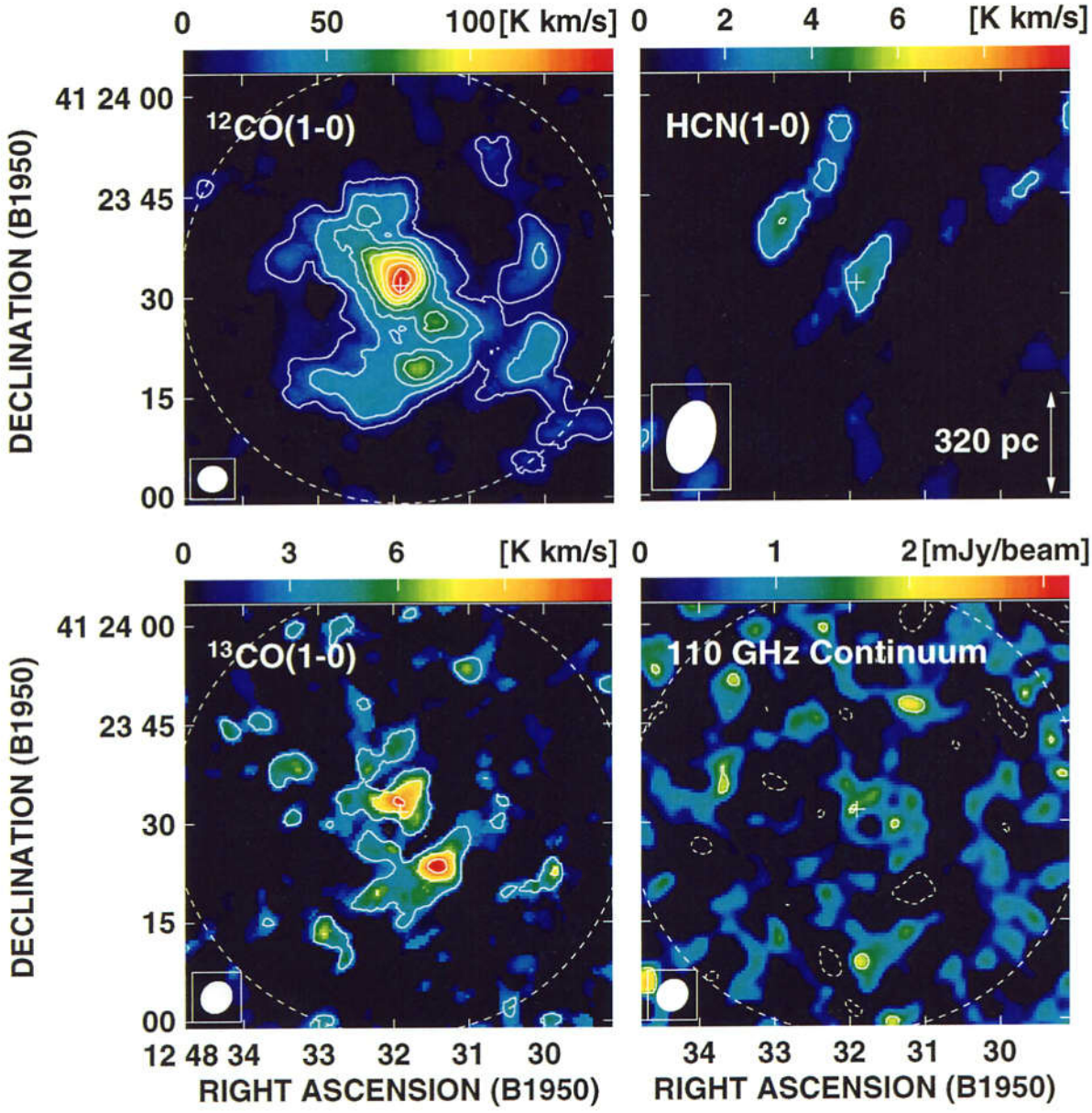

Fig. 4.4: Images of ^{12}CO, HCN, ^{13}CO, and 110 GHz continuum emission of the central region of the starburst galaxy NGC 4736. The color scale is shown at the top of each map. The cross of each map marks the position of the galactic nucleus determined from the 6 cm continuum emission peak of α(B1950)=$12^{\rm h}48^{\rm m}31^{\rm s}.89$, δ(B1950)=41°23′31″.8 (Turner & Ho 1994). ^{12}CO and HCN maps are taken from Sakamoto et al. (1999) and Kohno (1997). *Top left*: ^{12}CO$(1-0)$ moment map. Synthesized beam (4″.3 × 3″.8, P.A. = 96°) is shown at the bottom-left corner. The field of view (65″) is indicated with a dashed circle. The contour levels are $2, 4, 6, \cdots, 16\sigma$, where 1 σ = 1.5 Jy beam^{-1} km s^{-1} [= 8.5 K km s^{-1}]. *Top right*: HCN$(1-0)$ moment map. Synthesized beam (11″.0 × 7″.0, P.A. = 165°) is shown at the bottom-left corner. The field of view is larger than the indicated area. The contour levels are 2 and 4σ, where 1 σ = 0.55 Jy beam^{-1} km s^{-1} [= 1.1 K km s^{-1}]. *Bottom left*: ^{13}CO$(1-0)$ moment map. Synthesized beam (5″.0 × 4″.4, P.A. = 144°) is shown at the bottom-left corner. The field of view (68″) is indicated with a dashed circle. The contour levels are $2, 4$, and 6σ, where 1 σ = 0.39 Jy beam^{-1} km s^{-1} [= 1.8 K km s^{-1}]. *Bottom right*: 110 GHz continuum map. Synthesized beam (5″.0 × 4″.4, P.A. = 139°) is shown at the bottom-left corner. The field of view (68″) is indicated with a dashed circle. The contour levels are -2 and 2σ, where 1 σ = 0.84 mJy beam^{-1} [= 3.9 mK].

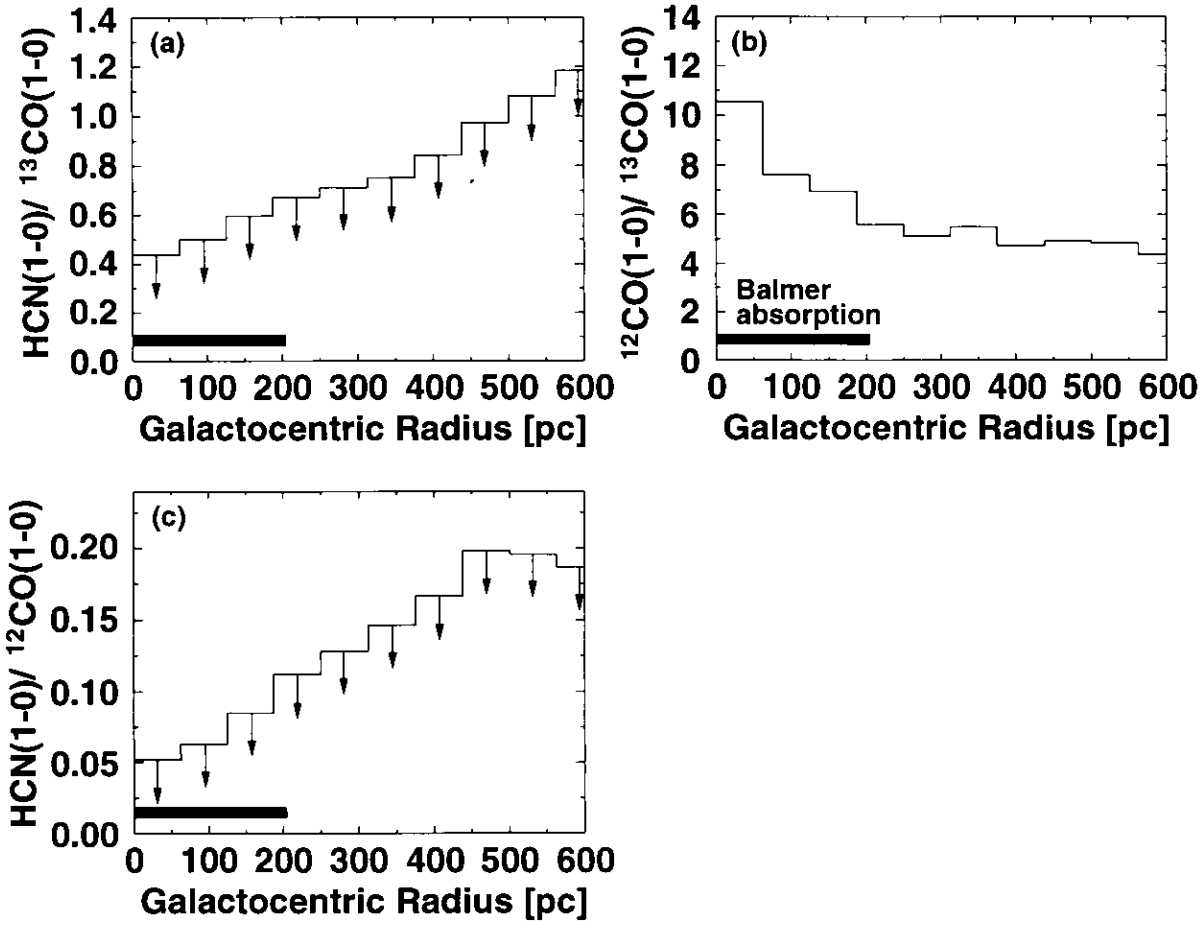

Fig. 4.5: Radial intensity ratio distributions in the central region of NGC 4736. All figures were made using a task "COMB" in AIPS package to divide images each other with clipping level of 1σ, and using a task "IRING" to averaged over concentric annuli of $3''$(63 pc) wide. Thick horizontal lines indicate the maximum extent of Balmer absorption dominated region (coincident with the aperture of Pritchet 1977). (a) Radial distribution of HCN/^{13}CO intensity ratio. (b) Radial distribution of ^{12}CO/^{13}CO intensity ratio. (c) Radial distribution of HCN/^{12}CO intensity ratio.

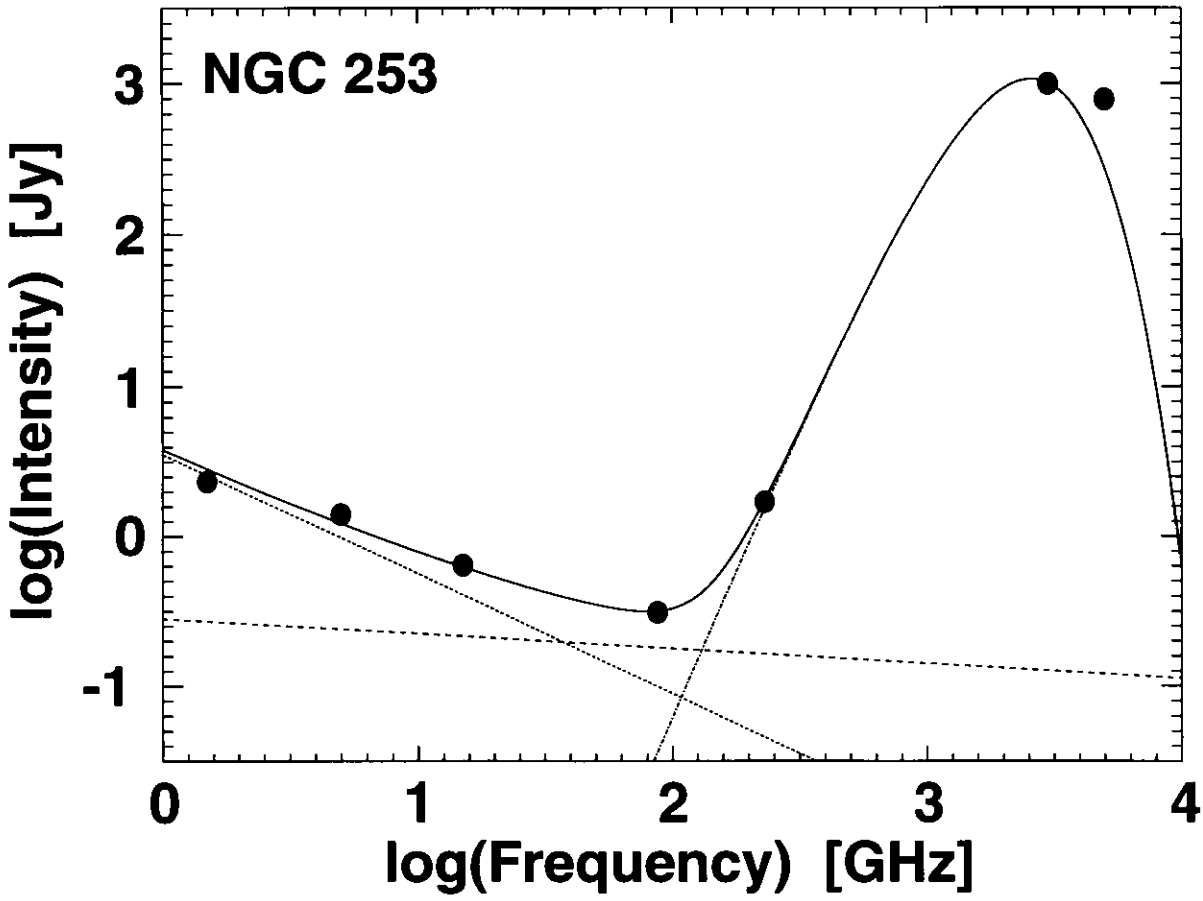

Fig. 4.6: Spectral energy distribution (SED) of the central region of NGC 253. Filled circles indicate the observed flux, and the solid line indicates the sum of synchrotron, free-free, and dust emission. 110 GHz emission is clearly dominated by the free-free emission. *Solid line*: Fitted SED. *Dashed line*: free-free emission ($\propto \nu^{-0.1}$). *Dotted line*: synchrotron emission ($\propto \nu^{-0.8}$). *Dash-dot line*: dust emission ($\propto \nu^2 B_\nu(T)$, $T \sim 25$ K). Flux data are taken from following papers; 1.5 GHz (20 cm) $\cdots$ Condon et al. (1982). 5 GHz (6 cm) $\cdots$ Turner & Ho (1983). 15 GHz (2 cm) $\cdots$ Turner & Ho (1983). 87 GHz (3.4 mm) $\cdots$ Jura, Hobbs, & Maran (1978). 230 GHz (1.3 mm) $\cdots$ Krügel et al. (1990). 3 THz (100 μm), 5 THz (60 μm) $\cdots$ IRAS.

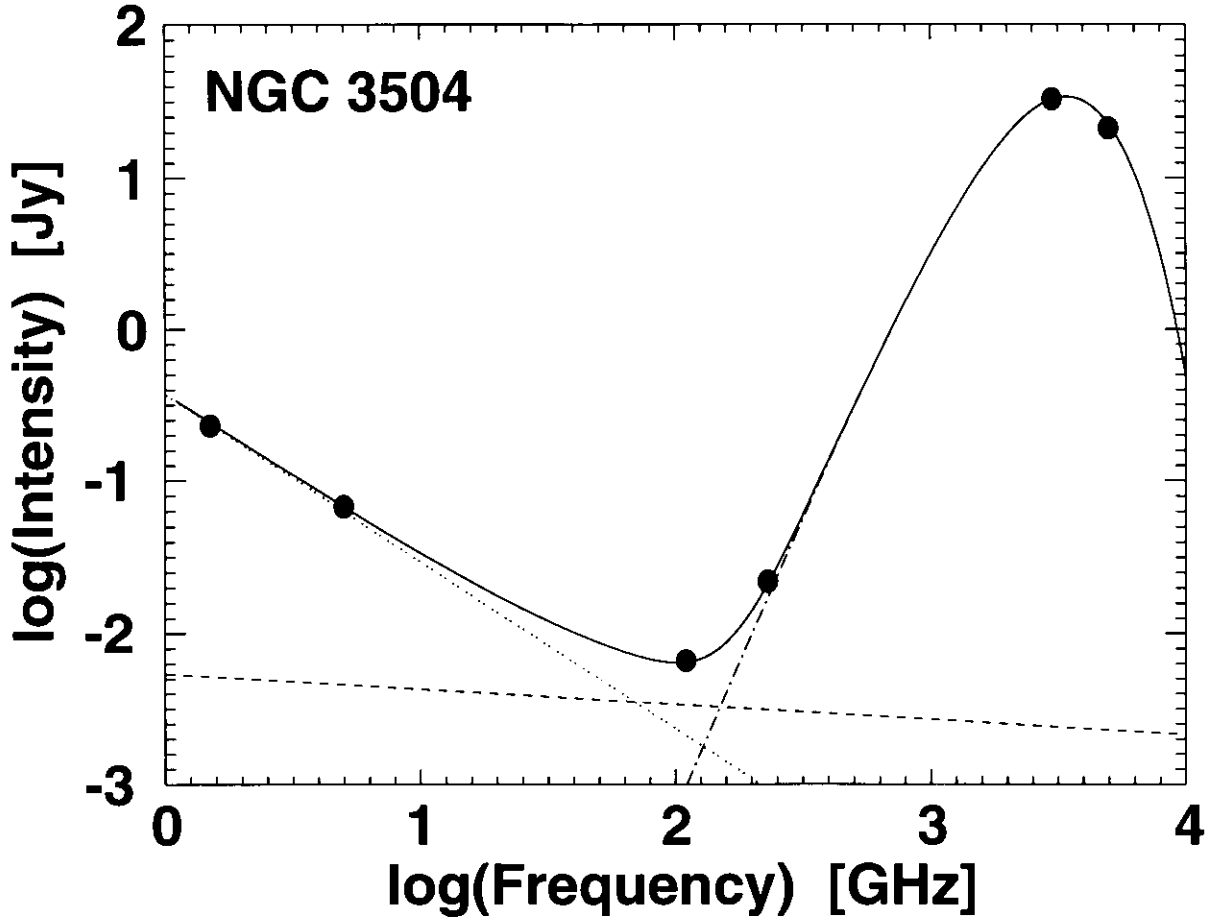

Fig. 4.7: Spectral energy distribution (SED) of the central region of NGC 3504. Filled circles indicate the observed flux, and the solid line indicates the sum of synchrotron, free-free, and dust emission. 110 GHz emission is clearly dominated by the free-free emission. *Solid line*: Fitted SED. *Dashed line*: free-free emission ($\propto \nu^{-0.1}$). *Dotted line*: synchrotron emission ($\propto \nu^{-1.1}$). *Dash-dot line*: dust emission ($\propto \nu^2 B_\nu(T)$, $T \sim 33$ K). Flux data are taken from following papers; 1.5 GHz (20 cm) $\cdots$ Condon et al. (1990). 5 GHz (6 cm) $\cdots$ Saikia et al. (1994). 110 GHz (2.7 mm) $\cdots$ our data. 230 GHz (1.3 mm) $\cdots$ Chini, Krügel, & Lemke (1996). 3 THz (100 μm), 5 THz (60 μm) $\cdots$ IRAS.

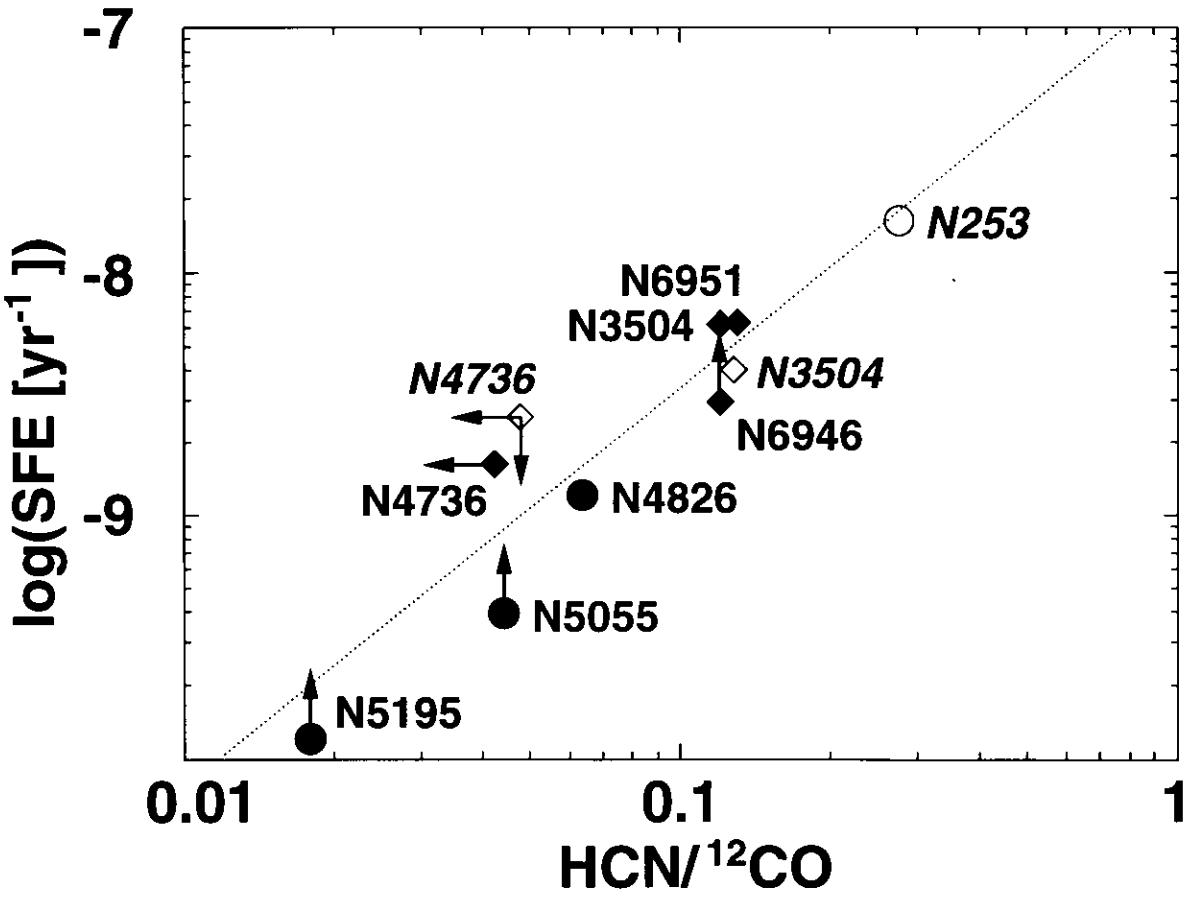

Fig. 4.8: Correlation diagram between HCN/^{12}CO ratios and star formation efficiencies (SFEs). Open marks indicate our data whose SFEs are estimated from our interferometric 110 GHz continuum observations. Filled marks indicate the data taken from Kohno (1997) whose SFEs are estimated from Hα intensities. Diamonds and circles indicate the data taken by the interferometer (Nobeyama Millimeter Array) and the single-dish (Nobeyama 45 m), respectively. A dotted line is a linear fitting of these data.

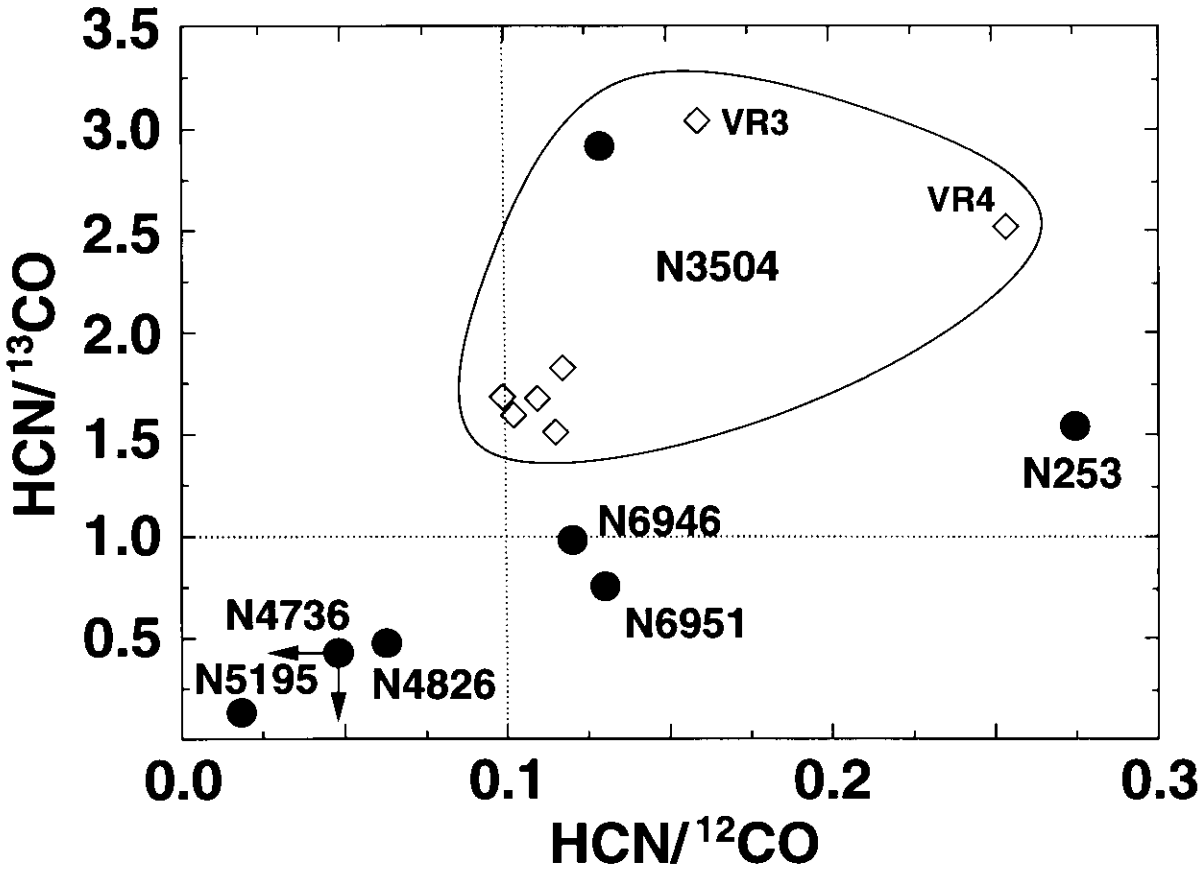

Fig. 4.9: Correlation diagram between HCN/^{12}CO and HCN/^{13}CO ratios. Filled circles indicate the integrated intensity ratios toward the galactic centers, and the open diamonds indicate the velocity divided intensity ratios for NGC 3504. The velocity range of VR3, VR4, and other points are indicated in table 4.2. Vertical dotted line indicates HCN/^{12}CO ratios of 0.1, which is the rough boundary of low density ($n(H_2) < 10^4$ cm^{-3}) and high density ($n(H_2) \gtrsim 10^4$ cm^{-3}). Horizontal dotted line indicates HCN/^{13}CO ratios of 1.0, which is the rough boundary of low temperature ($T_k < 100$ K) and high temperature ($T_k \gtrsim 100$ K).

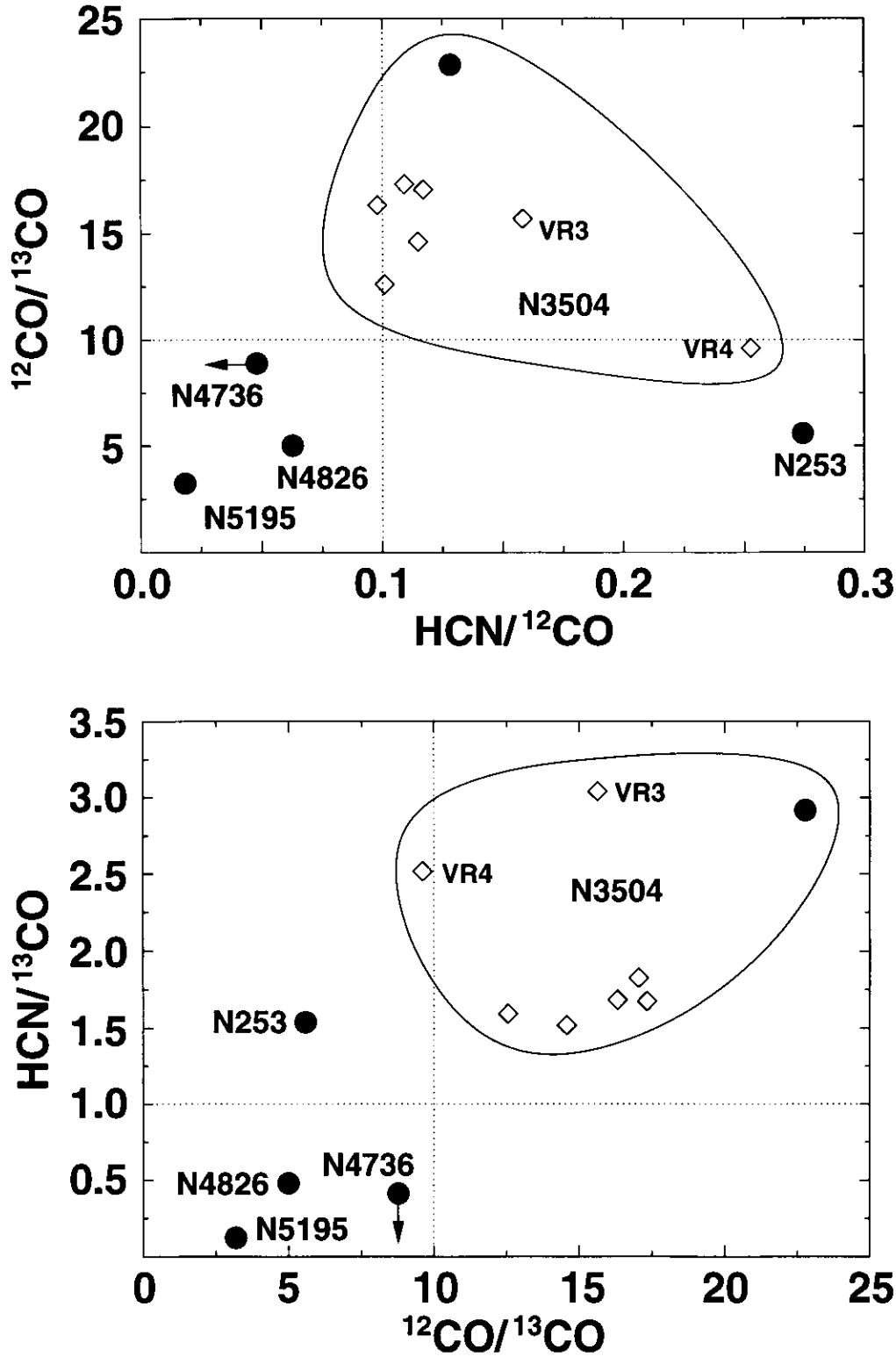

Fig. 4.10: Correlation diagrams between HCN/^{12}CO and ^{12}CO/^{13}CO ratios (top), and ^{12}CO/^{13}CO and HCN/^{13}CO ratios (bottom). Filled circles indicate the integrated intensity ratios toward the galactic centers, and the open diamonds indicate the velocity divided intensity ratios for NGC 3504. The velocity range of VR3, VR4, and other points are indicated in table 4.2. The dotted line of HCN/^{12}CO = 0.1 indicates the rough boundary of low density ($n(H_2) < 10^4$ cm^{-3}) and high density ($n(H_2) \gtrsim 10^4$ cm^{-3}). The dotted line of HCN/^{13}CO = 1.0 indicates the rough boundary of low temperature ($T_k < 100$ K) and high temperature ($T_k \gtrsim 100$ K). The dotted line of ^{12}CO/^{13}CO = 10 indicates the average value of nearby galaxies, and active star forming galaxies tend to have > 10 and quiescent galaxies tend to have < 10.

Chapter 5

Starburst Evolution

5.1 Intensity Ratios of Molecular Gas in Galaxies

In chapter 2, we suggest that HCN/^{13}CO would be a good molecular gas temperature tracer, and using this ratio and other ratios (HCN/^{12}CO and ^{12}CO/^{13}CO) we revealed that starburst galaxies tend to have higher density and higher temperature molecular gas than non-starburst galaxies. Searching for the high intensity ratio objects in Our Galaxy implies that the supernova explosion would be the most effective heating source for starburst regions. In chapter 3, multi-molecular lines and continuum observations of the "prototypical" starburst galaxy M82 were done, and the results suggest that M82 would be in late phase of starburst. The detail observations of M82 show the existence of a superbubble, and suggest that the energetic starburst can terminate the starburst itself, the extension of the superbubble can turn on the new starbursts at surrounding regions, and the starburst can form the middle-mass black hole. In Chapter 4, we indicate that $\sim$ 100 GHz continuum might be dominated by free-free emission and therefore it might be a good absorption-free star formation indicator. We also suggest that molecular gas in starburst galaxies and non-starburst galaxies have different physical conditions, and even between those of the starburst galaxies have different physical conditions. In this chapter, we will discuss about the evolution of starburst from the viewpoint of the physical conditions of molecular gas using these results.

Studies of star forming regions in Our Galaxy suggest that stars are formed from dense molecular cores rather than diffuse molecular envelopes (e.g. Lada 1992). Extragalactic dense molecular gas studies show clear correlation between the amount of dense molecular gas and the star formation efficiency (Solomon, Downes, & Radford 1992, Kohno 1997). There are also spatial coincidences between the positions of dense molecular gas clouds and those of the star forming regions (Kohno, Kawabe, & Vila-Vilaró 1999, Reynaud & Downes 1999). On the other hand, post-starburst galaxies, which had experienced a starburst phase at $\sim 10^9$ year ago but have low star formation activities at present, have almost no dense molecular gas even they have a lot of diffuse molecular gas (Kohno 1997). These results indicate that vast amount of dense molecular gas is needed for the starburst activity, and if the dense molecular gas were exhausted by the formation of stars, the starburst activity would stop (Kohno 1997). We compiled all of our single-dish and interferometric data and those of Kohno (1997), and displayed in figure 5.1. All of the data except those of M82 have good correlation between the dense molecular gas fractions and star formation efficiencies (SFEs) as indicated by Solomon, Downes,

& Radford (1992) and Kohno (1997). The data points of M82 are, however, largely offset from this correlation. From the standpoint of SFEs, M82 have very high values corresponds to or higher than other starburst galaxies such as NGC 253, NGC 3504, NGC 6946, and NGC 6951. Since these SFEs are derived from free-free or Hα emission, the starburst region of M82 still have a large amount of ionizing source such as massive stars (OB stars). From the standpoint of molecular gas, however, there exist a small amount of dense molecular gas compared with total gas amount, corresponds to non-starburst galaxies such as NGC 4736, NGC 4826, NGC 5055, and NGC 5195. As mentioned above, all of the stars are formed from dense molecular gas, so that starburst region of M82 might not form stars actively hereafter. To summarize, M82 have formed vast amount of massive stars in the past and these are still exist, but no longer possible to make them. This suggests that M82 would be transient phase of starburst to post-starburst. On the other hand, the star formation of other starburst galaxies might be now ongoing.

Figure 5.2 shows a correlation diagram between HCN/^{12}CO and HCN/^{13}CO intensity ratios. Since the HCN/^{12}CO ratio is a good tracer for density (section 2.3.4, Kohno 1997) and the HCN/^{13}CO ratio for mainly temperature (section 2.2.4, 2.3.4), this diagram would correspond to the correlation between density (horizontal axis) and temperature (vertical axis). Molecular gas in non-starburst galaxies (NGC 4736, NGC 4826, and NGC 5195) have low HCN/^{12}CO (< 0.1) and HCN/^{13}CO (< 1.0) ratios which means low-density and low-temperature conditions, but that of starburst galaxies have various ratios. Intensity ratios of molecular gas in M82 (except those of the center of the super-bubble) show very interesting features. HCN/^{13}CO ratios range continuously from higher values (~ 1.75) to lower values (~ 0.5) and decrease with the decrement of HCN/^{12}CO ratios. The most important point is that the lowest ratios are very similar to those of the non-starburst galaxies. On the other hand, molecular gas in NGC 253 is rich in dense molecular gas (high HCN/^{12}CO of ~ 0.3), even the HCN/^{13}CO ratio is similar to those of M82. Intensity ratios of molecular gas in NGC 3504 are located between those of M82 and NGC 253, but are spread in wide area. The systemic velocity components VR4 is close to those of NGC 253, but have higher HCN/^{13}CO ratio (~ 2.5). The nearby systemic velocity component VR3 have much lower HCN/^{12}CO ratio (~ 0.15) and much higher HCN/^{13}CO ratio (~ 3.0) than those of VR4 and NGC 253, which suggest that VR3 have lower density but higher temperature. Other velocity component in NGC 3504 show similar intensity ratios to those of higher limit in the intensity range of M82, which have high HCN/^{13}CO ratio of ~ 1.75 and low HCN/^{12}CO ratio of ~ 1.

The top diagram of figure 5.3 shows a correlation diagram between HCN/^{12}CO and ^{12}CO/^{13}CO ratios. The non-starburst galaxies have low HCN/^{12}CO and ^{12}CO/^{13}CO ratios of < 0.1 and < 10, which are typical values for these galaxies. M82 have low HCN/^{12}CO ratios similar to the non-starburst galaxies but have high ^{12}CO/^{13}CO ratios of > 10. NGC 253 and NGC 3504 VR4, on the other hand, have high HCN/^{12}CO ratios of > 0.1 but have low ^{12}CO/^{13}CO ratios similar to non-starburst galaxies. Intensity ratios of all the velocity components of NGC 3504 except VR4 are located at the middle of those of NGC 253 and M82, but those of NGC 3504 VR1-2 and VR5-7 are located rather near to those of M82 than that of NGC 3504 VR3.

A correlation diagram between ^{12}CO/^{13}CO and HCN/^{13}CO is displayed in figure 5.3 (bottom). Molecular gas in NGC 253 and NGC 3504 VR4 have high HCN/^{13}CO (> 1) and low ^{12}CO/^{13}CO (< 10) ratios, but that in M82 has rather opposite tendencies; high ^{12}CO/^{13}CO (> 10) and high to low HCN/^{13}CO ($0.5 - 2.0$) ratios. All the velocity

components of NGC 3504 except VR4 are again located at the middle of NGC 253 and M82, which have both high HCN/^{13}CO (> 1) and high ^{12}CO/^{13}CO (> 10) ratios but are again spread in wide area; intensity ratios of NGC 3504 VR1-2 and VR5-7 are located near to those of M82, but those of NGC 3504 VR3 are largely offset from other velocity components and have high HCN/^{13}CO and ^{12}CO/^{13}CO (> 10) ratios of $\sim$ 3.0 and $\sim$ 15.

5.2 Starburst Evolution

The studies of the starburst evolution have been done mainly by Rieke and his collaborators based on their infrared observation results. Near-infrared emission line observations indicate that NGC 253 have larger Brackett γ equivalent width, stronger CO absorption and have milder shocked gas (strong H_2 and [Fe II] emission) than those of M82. These implies that younger stars are still exist and the number of supernova explosions are smaller in NGC 253 than in M82, concluding that NGC 253 is in younger phase of starburst than M82 (Rieke, Lebofsky, & Walker 1988, Rieke 1988). The extent of X-ray and dust show that NGC 253 have much smaller extent than M82 (Fabbiano 1988, Cappi et al. 1999, Alton, Davies, & Bianchi 1999, Rieke, Lebofsky, & Walker 1988, Rieke 1988), which also indicate that the number of supernova explosions are much smaller in NGC 253. From the viewpoint of dense molecular gas, NCG 253 is rich in very dense molecular gas such as HCN(4 – 3) than M82 even both galaxies have similar ^{12}CO intensities (Jackson et al. 1995), which indicate that NGC 253 is possible to make more stars than M82. These results also support the suggestion that NGC 253 is in younger phase of starburst than M82.

Rieke et al. (1988) and Rieke (1988) also suggest much older starburst phase galaxies, NGC 4736 and NGC 5195, because of their small Brackett γ equivalent widths, their slightly stronger CO absorption band than those of normal galaxies (Walker, Lebofsky, & Rieke 1988), and their stellar populations which extend up to at most A4 to A7 (Pritchet 1977, Warner 1974). Recent optical spectra of the central regions of both NGC 4736 and NGC 5195 show strong Balmer absorption lines (Ho, Filippenko, & Sargent 1995, Taniguchi et al. 1996, Sauvage et al. 1996, Greenawalt et al. 1998), which are the typical spectra of A-type stars, and have very low star formation activity (Taniguchi et al. 1996). Millimeter wave molecular gas observations indicate that in the Balmer absorption dominated regions, there are very small amount of molecular gas (Tosaki & Shioya 1997), or even exist, molecular gas is stable against gravitational instability (Shioya et al. 1998) and have almost no high density component (Kohno 1997). These observational results also suggest that these galaxies are in very late phase of starburst, or so-called "post-starburst" phase.

We compared the duration of starburst (Rieke 1988, Rieke, Lebofsky, & Walker 1988) and the intensity ratios of molecular gas (table 5.1). We put NGC 3504 at the middle of NGC 253 and M82, because the intensity ratios of NGC 3504 tend to have the middle values of those of NGC 253 and M82 (see previous subsection). Since there are gradual changes in the intensity ratios according to the changes in the duration of starburst, we propose the evolution of the intensity ratios ($\approx$ physical conditions) of molecular gas according to the starburst evolution. The HCN/^{12}CO intensity ratio tends to decrease as the starburst would evolve. The HCN/^{13}CO intensity ratio tends to increase at the early phase of the starburst, but tends to decrease at the late phase. The ^{12}CO/^{13}CO intensity ratio also tends to behave as HCN/^{13}CO ratios, but the turnover of the increment to the

Table 5.1: Comparisons between the duration of starburst and the intensity ratios of molecular gas in galaxies.

Galaxy	Duration* [yr]	W(Brγ)*	CO Absorption*	HCN/^{13}CO	HCN/^{12}CO	^{12}CO/^{13}CO
NGC 253	10^7	Large	Very Strong	1.5	0.27	6
NGC 3504	—	—	—	1.5 – 3.0	0.10 – 0.25	10 – 17
M82	5×10^7	Fairly Large	Strong	0.4 – 1.9	0.03 – 0.08	13 – 50
NGC 4736	10^8	Small	Small	0.4	0.05	9
NGC 5195	10^8	Small	—	0.1	0.02	3

* Data taken from Rieke et al. (1988) and Rieke (1988).

decrement is much later phase than that of the HCN/^{13}CO ratio. We plot the evolutional tracks on the correlation diagrams of the intensity ratios in figures 5.4.

These tendencies can explain as follows; since stars are formed from dense molecular gas such as HCN (e.g. Lada 1992), dense gas would decrease as the stars are formed by the starburst activities. The evolution of the HCN/^{12}CO intensity ratio (dense gas ratio) shows monotonically decrease, so that formation of dense gas at the shocked region (section 2.3) would be small compared with the consumption by the star formation. Dense molecular gas might be related to warm regions much closer than ^{12}CO, because stars which are formed from dense molecular gas are one of the heating sources, and because dense molecular gas can also be formed from shocked regions such as supernova remnants which would also one of the heating sources. ^{12}CO, on the other hand, is located even in much diffuse and therefore wider region than HCN, so that it might take much longer time to heat up ^{12}CO gas than HCN gas. At the end of the starburst, the amount of dense molecular gas would decrease so that HCN intensity would be relatively weaken compared with ^{13}CO intensity and therefore the HCN/^{13}CO ratio would decrease. The heating sources would still exist for a while even the dense molecular gas decrease, so that diffuse gas such as ^{12}CO would be still heated by these sources and therefore the ^{12}CO/^{13}CO ratio would still have higher value. To summarize, at the early phase of starburst, there would be a time lag that the rise of the ^{12}CO/^{13}CO ratio would be later than that of the HCN/^{13}CO ratio. At the late phase of starburst, the ^{12}CO/^{13}CO ratio would have higher value even the HCN/^{13}CO ratio decreases. These suggestions also support the idea that NGC 253 is in the young phase of starburst, M82 in the late phase, and NGC 3504 in the middle phase.

The intensity ratio of molecular gas at the central region of the superbubble in M82, especially ^{12}CO/^{13}CO ratio, have very large values (> 30) compared with other starburst galaxies. This region was the position of strong starburst, whose energy might corresponds to $\sim 10^{55}$ erg or $\sim 10^4$ supernovae (section 3.4). These ratios are similar to those of merging galaxies (Aalto et al. 1991a, Aalto et al. 1991b, Casoli, Dupraz, & Combes 1992a, Casoli, Dupraz, & Combes 1992b), which might be ongoing extensive starburst at interacting regions. This similarity strongly suggests that the starbursts in merging galaxies might quite resemble to that in M82.

The determination of the evolutional track of non-starburst to starburst is very difficult. The proposed mechanisms of the dense gas increment are the instability of gas cloud (Kohno 1997) or the compression by the enormous supernovae (section 3.4.5). The

amount of increment is, however, depends largely on the initial conditions such as large-scale kinetic structures, amount of gas at surrounding regions, and so on. Therefore, we can only suggest that non-starburst galaxies may be possible to evolve into starburst galaxies, and also the lower activity starburst galaxies may be possible to evolve into higher activity starburst galaxies, but it largely depend on their various conditions.

In concluding, we indicated the change of the physical conditions of molecular gas according to the evolution of starburst in the following and also in figure 5.5.

1. Pre-starburst phase. The amount of dense molecular gas might be increasing by the gravitational instability (Kohno 1997). It is still not clear whether the increment of dense molecular gas would be accompanied by star formation or not, so that increment of temperature might also unclear.

2. Early starburst phase. The area of starburst and the amount of supernovae are small, may be confined nearby star forming dense molecular clouds, so that HCN/^{13}CO ratio might increase but ^{12}CO/^{13}CO may have still smaller value. The possibility of sequential star formation might depend on the surrounding environment such as gas amount, galactic kinematical structures, and so on, so that it is not apparent whether starburst would evolve to sequential starburst or end with instantaneous starburst. If the sequential starburst has started, the amount of dense molecular gas and its temperature would increase by the compression of supernova explosions. Examples of this phase might be NGC 253 and systemic velocity component (VR4) of NGC 3504.

3. Middle starburst phase. The effect of the starburst might widely spread by the strong UV radiation from the vast amount of early type stars and its explosions, and therefore density and temperature might have very high values. Examples might be nearby systemic velocity component (VR3) of NGC 3504.

4. Late starburst phase. Because of a large amount of star formation and supernova explosions, the amount of dense molecular gas might decrease. A large amount of formed stars might be, however, still exist so that temperature of molecular gas might still be in warm condition. Good example might be M82. The velocity component VR1$-$2 and VR5$-$7 of NGC 3504 may be in the phase between middle and late starburst phase.

5. Post starburst phase. Almost all of the dense molecular gas is exhausted or blown out from starburst region, and therefore no more starburst would continue. OB stars are already burned out at this moment, so that there are no heating sources and gas would be in cool condition. Examples of post-starburst galaxies might be NGC 4736 and NGC 5195.

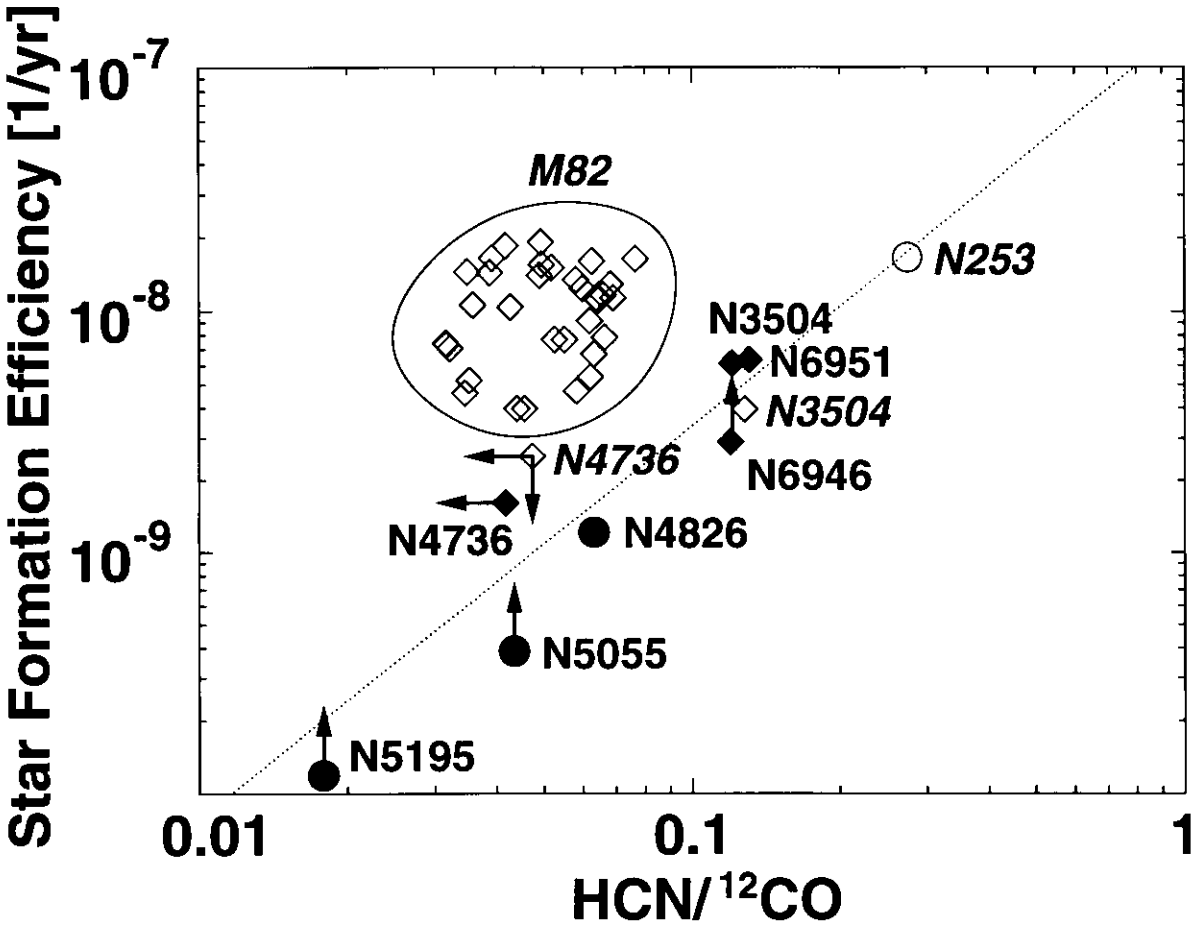

Fig. 5.1: Correlation diagram between HCN/^{12}CO and star formation efficiencies (SFEs). Open marks indicate our data whose SFEs are estimated from our interferometric 110 GHz continuum observations. Filled marks indicate the data taken from Kohno (1997) whose SFEs are estimated from Hα intensities. Diamonds and circles indicate the data taken by the interferometer (Nobeyama Millimeter Array) and the single-dish (Nobeyama 45 m), respectively. A dotted line is a linear fitting of all the data except M82.

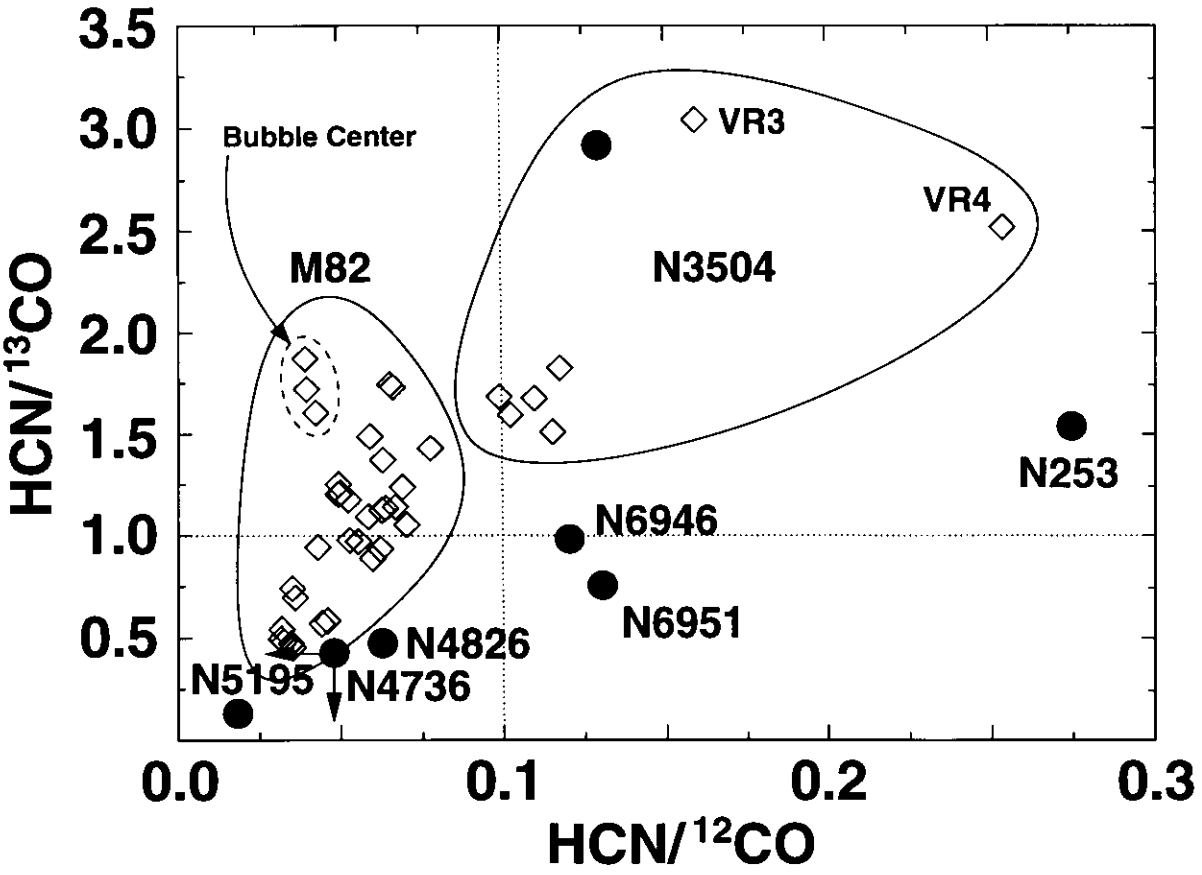

Fig. 5.2: Correlation diagram between HCN/^{12}CO and HCN/^{13}CO ratios. Filled circles indicate the integrated intensity ratios toward the galactic centers, and the open diamonds for M82 indicate intensity ratios for various points, and for NGC 3504 indicate the velocity divided intensity ratios. The velocity range of VR3, VR4, and other points are indicated in table 4.2. Vertical dotted line indicates HCN/^{12}CO ratios of 0.1, which is the rough boundary of low density ($n(H_2) < 10^4$ cm^{-3}) and high density ($n(H_2) \gtrsim 10^4$ cm^{-3}). Horizontal dotted line indicates HCN/^{13}CO ratios of 1.0, which is the rough boundary of low temperature ($T_k < 100$ K) and high temperature ($T_k \gtrsim 100$ K).

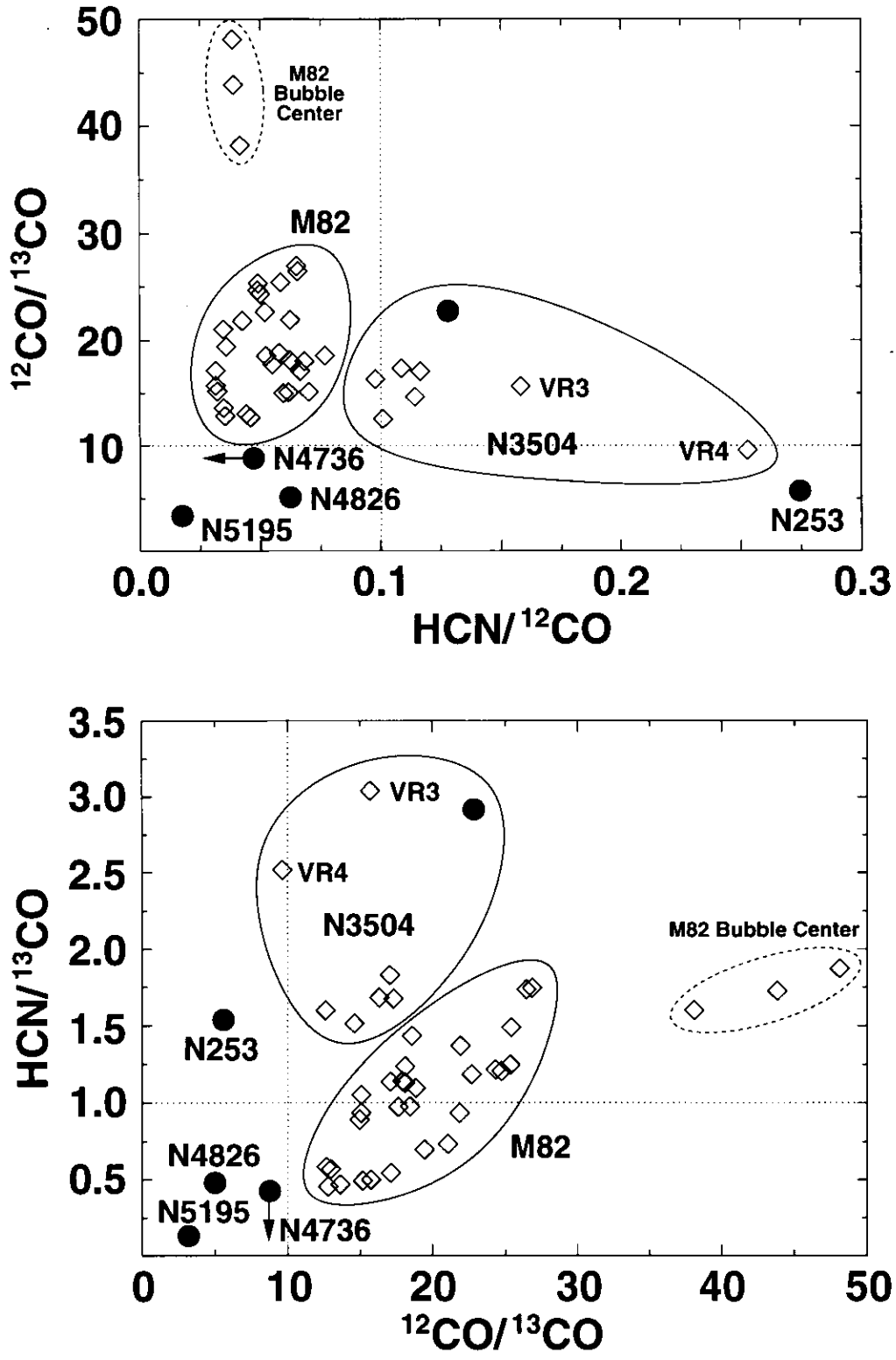

Fig. 5.3: Correlation diagrams between HCN/^{12}CO and ^{12}CO/^{13}CO ratios (top), and ^{12}CO/^{13}CO and HCN/^{13}CO ratios (bottom). Filled circles indicate the integrated intensity ratios toward the galactic centers, and the open diamonds for M82 indicate intensity ratios for various points, and for NGC 3504 indicate the velocity divided intensity ratios. The velocity range of VR3, VR4, and other points are indicated in table 4.2. The dotted line of HCN/^{12}CO = 0.1 indicates the rough boundary of low density ($n(\mathrm{H_2}) < 10^4$ cm^{-3}) and high density ($n(\mathrm{H_2}) \gtrsim 10^4$ cm^{-3}). The dotted line of HCN/^{13}CO = 1.0 indicates the rough boundary of low temperature ($T_\mathrm{k} < 100$ K) and high temperature ($T_\mathrm{k} \gtrsim 100$ K). The dotted line of ^{12}CO/^{13}CO = 10 indicates the average value of nearby galaxies, and active star forming galaxies tend to have > 10 and quiescent galaxies tend to have < 10.

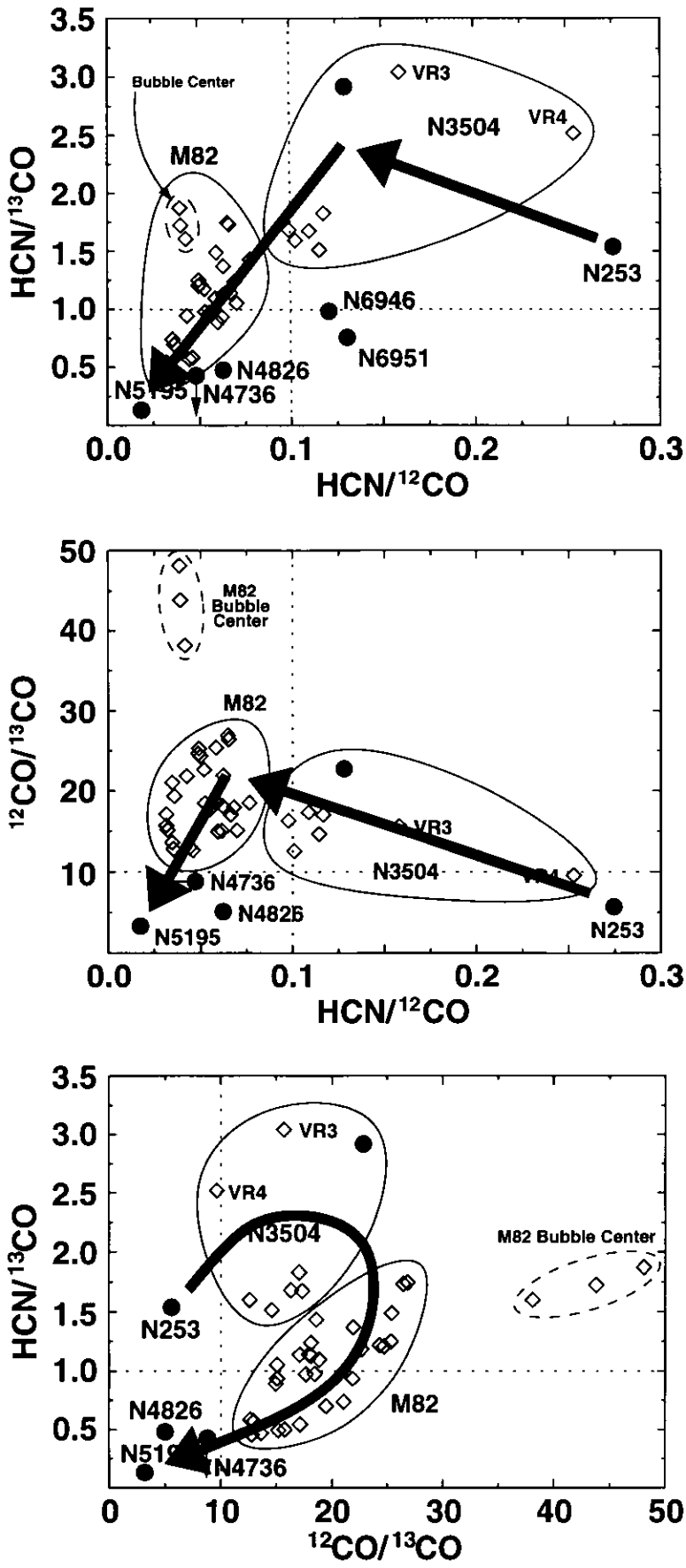

Fig. 5.4: The proposed evolutional tracks on the correlation diagrams between HCN/^{12}CO and HCN/^{13}CO ratios (top), HCN/^{12}CO and ^{12}CO/^{13}CO ratios (middle), and ^{12}CO/^{13}CO and HCN/^{13}CO ratios (bottom). Other marks and lines are same as figures 5.2 and 5.3.

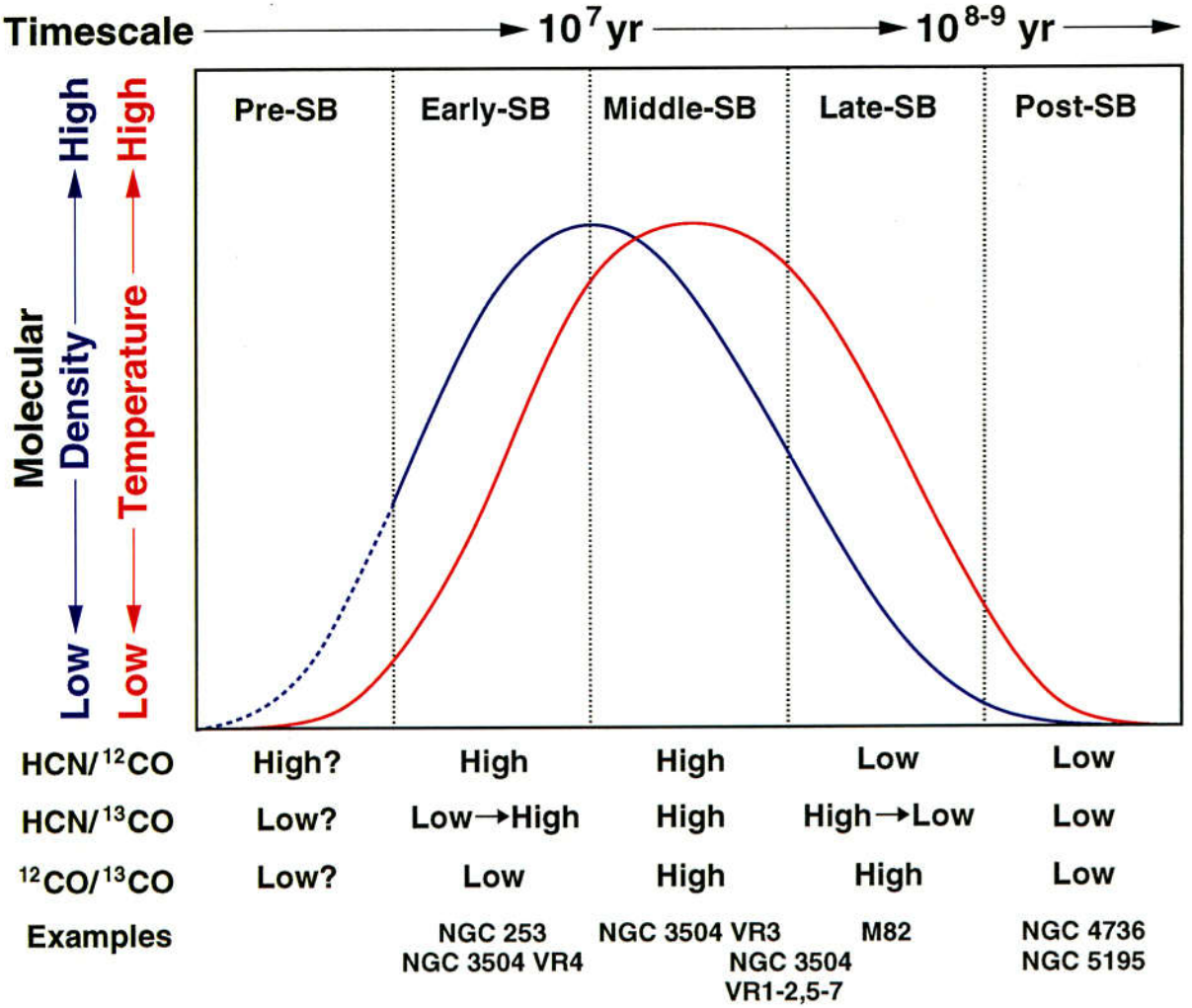

Fig. 5.5: The change of the HCN/^{12}CO, HCN/^{13}CO, and ^{12}CO/^{13}CO intensity ratios and the physical conditions of molecular gas according to the evolution of starburst. The examples of galaxies in each phase are also indicated.

Chapter 6

Summary

6.1 Estimating the Molecular Gas Temperature

In the study of the physical conditions of molecular gas around the active galactic nucleus (AGN) in M51 with interferometer (Nobeyama Millimeter Array or NMA), we find a good tracer for estimating the molecular gas temperature using low-J lines. The HCN(1 – 0)/^{13}CO(1 – 0) intensity ratio tend to show high value ($\gtrsim 1$) when the molecular gas is dense ($n(\mathrm{H_2}) \gtrsim 10^4$ cm^{-3}) and warm ($T_\mathrm{k} \gtrsim 100$ K) (figure 6.1 left). The mechanism of this ratio is as follows; HCN(1 – 0) emission is optically thick even at high temperature, but ^{13}CO(1 – 0) emission becomes optically thin when the temperature gets higher. Hence, at high temperature region (and, of course, enough dense to emit HCN line) HCN/^{13}CO ratio tend to have higher value. High-J line studies also suggest the existence of high-temperature molecular gas in the central region of M51. Comparison between the physical conditions of molecular gas derived from HCN/^{13}CO ratios and high-J lines in published data are also consistent in other galaxies.

We also observed starburst and non-starburst galaxies in HCN(1 – 0) and ^{13}CO(1 – 0) lines with a single-dish telescope (the Nobeyama 45m telescope). Compilation of the HCN/^{13}CO ratios from these data and the flux ratios of the Infrared Astronomical Satellite (IRAS) data show good correlation between the HCN/^{13}CO ratios and the ratio of IRAS 12 μm and 25 μm flux ($F_{\mathrm{IRAS12}\mu\mathrm{m}}/F_{\mathrm{IRAS25}\mu\mathrm{m}}$), which means that there are close relation between the amount of warm ($\gtrsim 100$ K) molecular gas and ~ 100 K dust (figure 6.1 right). On the other hand, correlations between the HCN/^{13}CO ratios and either $F_{\mathrm{IRAS12}\mu\mathrm{m}}/F_{\mathrm{IRAS60}\mu\mathrm{m}}$ or $F_{\mathrm{IRAS12}\mu\mathrm{m}}/F_{\mathrm{IRAS100}\mu\mathrm{m}}$ show loose or no correlations, which suggest that the amount of warm molecular gas has almost no relation with that of cold dust.

The consistency between the physical conditions of molecular gas derived from the HCN/^{13}CO ratios and high-J molecular lines, and the tight correlation between the HCN/^{13}CO ratios and the amount of 100 K dust strongly suggest that a HCN/^{13}CO ratio would be a good tracer for molecular gas temperature.

Starburst galaxies which tend to have higher HCN/^{13}CO ratios also tend to have higher HCN/^{12}CO and ^{12}CO/^{13}CO ratios than non-starburst galaxies. Search for high intensity ratio objects in Our Galaxy show that molecular gas with high HCN/^{13}CO, HCN/^{12}CO, and ^{12}CO/^{13}CO ratios is tend to reside at shocked regions such as molecular gas related with outflows from star forming dense cores or supernova remnants. Take their energetics, lifetimes, effecting areas, and numbers into consideration, we concluded

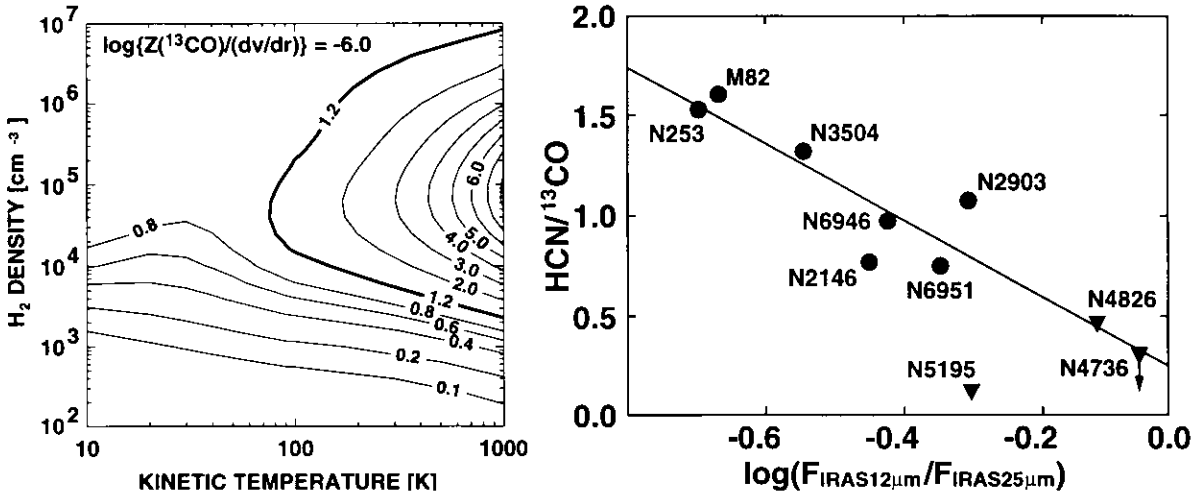

Fig. 6.1: (*Left*) **Density (vertical axis) and temperature (horizontal axis) dependence of HCN(1 – 0)/^{13}CO(1 – 0) intensity ratio based on the Large-Velocity-Gradient (LVG) calculation. Solid contours show curves of constant HCN/^{13}CO intensity ratio, and thick solid curve indicates HCN/^{13}CO ratio of 1.2. This figure clearly shows that high HCN/^{13}CO ratio indicates high-density and high-temperature.** (*Right*) **Relation between IRAS** $\log(F_{12}/F_{25})$ **flux ratios and HCN(1 – 0)/^{13}CO(1 – 0) integrated intensity ratios. Filled circles and triangles indicate starburst galaxy sample and non-starburst galaxy sample, respectively. The solid line indicates the calculated linear regression using all sample galaxies except NGC 5195, which largely offsets from the correlation.**

that supernova explosions are the most effective heating source in galaxies.

6.2 Starburst in Nearby Galaxies

Interferometric ^{13}CO(1 – 0) and 110 GHz continuum observations of the prototypical starburst galaxy NGC 253, the starburst galaxy NGC 3504, and the post-starburst galaxy NGC 4736 were done with NMA. 110 GHz continuum emission in the starburst galaxies are dominated by free-free emission, and the SFE derived from the free-free emission and that from extinction corrected Hα luminosity show good correspondence. This result suggests that free-free emission estimated from 110 GHz continuum might be a good star formation tracer. HCN(1 – 0)/^{12}CO(1 – 0) intensity ratios (the ratio of the dense gas amount to the total molecular gas amount) and SFEs show good correlation, which support the previously published results that the dense molecular gas is needed for the star formation.

We also had done high-sensitivity observations of the prototypical starburst galaxy M82 with NMA, and show detail inner (at most a few hundred parsec from the galactic disk) structures of outflowing molecular gas (spurs) for the first time. The features of spurs are quite similar to the optical dark filaments (dust filaments), which indicates that molecular gas and dust are settled in the similar regions.

We successfully imaged an expanding molecular superbubble at a first time, which located $\sim$ 140 pc westward from the nucleus of M82 (not at the nucleus) with its diameter of 210 $\times$ 140 pc in north-south and east-west direction (figure 6.2). The energy of the superbubble is about 10^{55} erg corresponds to $\sim 10^4$ supernovae. Molecular gas related with the superbubble is offset from rigid rotation, and ionized gas also shows similar kinematics but have much higher velocity. Kinematics of H_2O and OH masers also show

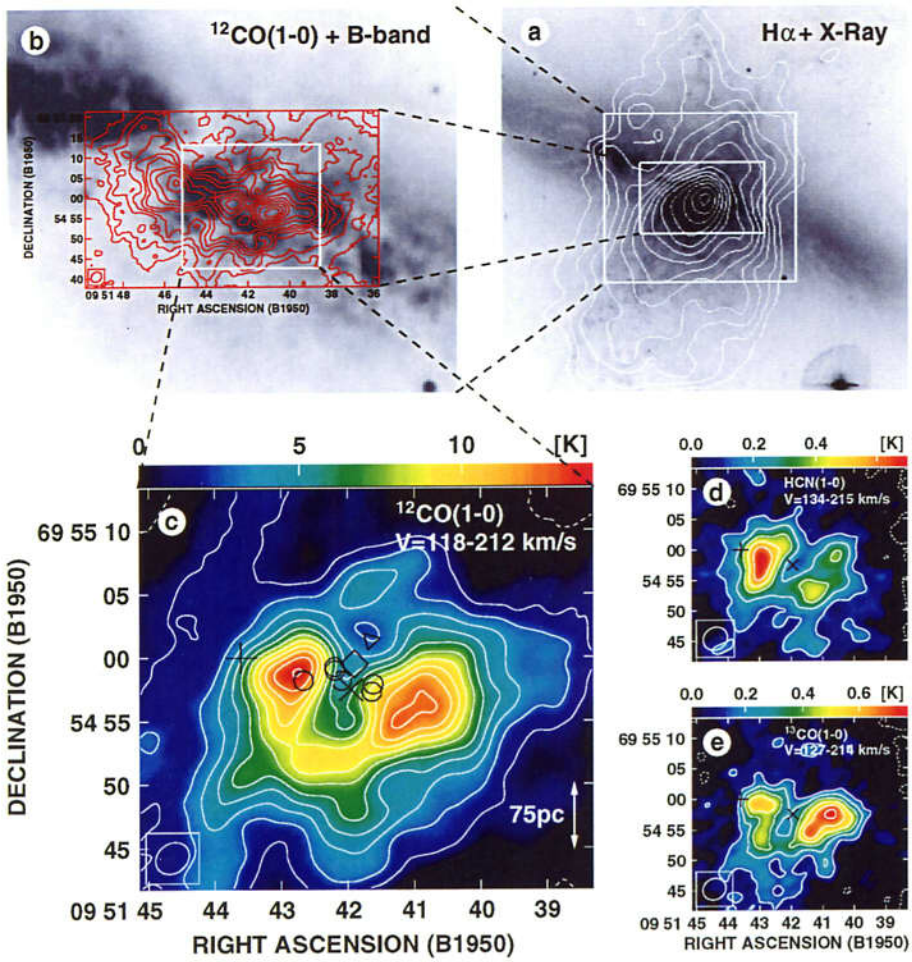

Fig. 6.2: The large-scale to small-scale views of M82. (a) The X-ray image (contours; Bregman, Schulman, & Tomisaka 1995) superimposed on the Hα image (grayscale; Shopbell & Bland-Hawthorn 1998). (b) ^{12}CO integrated intensity map (contours) superimposed on optical B-band image (grayscale; Alton, Davies, & Bianchi 1999). (c)-(e) The $^{12}CO(1-0)$, $HCN(1-0)$, and $^{13}CO(1-0)$ molecular superbubble image. Inside the superbubble, there are 2.2 μm secondary peak (diamond), X-ray peak (triangle), young supernova remnant 41.95+575 (cross), and OH and H_2O masers (circles). At this region, a strong starburst has occurred and maybe formed a middle mass black hole.

similar features, which indicate that molecular gas has undergone strong shock which maybe produced by the interaction with ionized gas and/or by induced star formations. The center of the superbubble is deficient in molecular gas, which means that no more star formation would occur at there. On the other hand, the surrounding regions show strong free-free emission, suggesting that new starburst might be occurred. From these results, we proposed new mechanisms of continuation and termination of starburst that strong starburst can blow out almost all the molecular gas in and around the starburst region and force to stop the ongoing star formations, but its strong expansion would compress the surrounding molecular gas and make new star forming regions.

Near the center of the superbubble, there are a 2.2 μm secondary peak which cluster is dominated by luminous supergiants, and a X-ray peak which may radiate from a middle mass ($\sim 10^3 - 10^4$ $M_\odot$) black hole. The stellar contents, mass, and evolution of the star cluster at 2.2 μm secondary peak based on initial mass function (IMF) suggest that

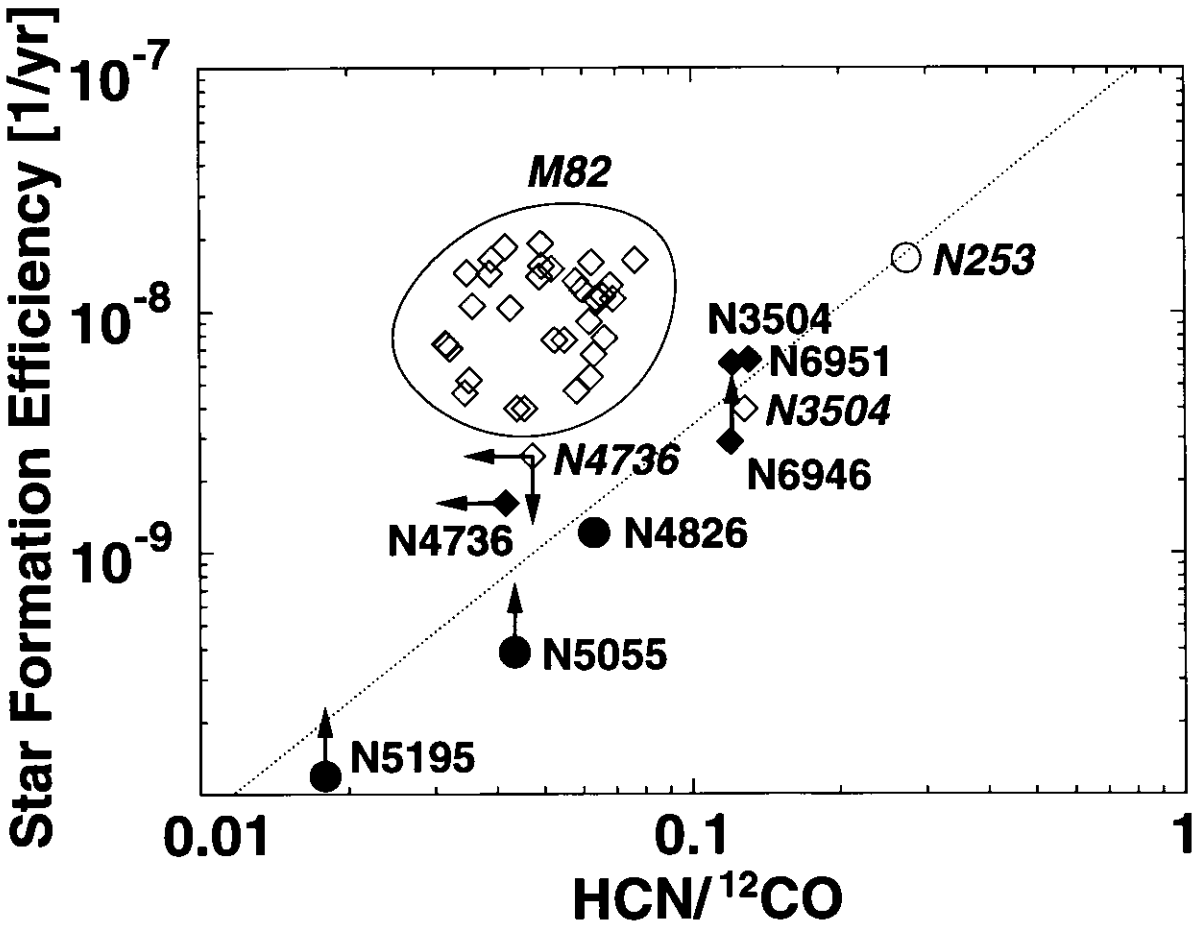

Fig. 6.3: Correlation diagram between HCN/^{12}CO and star formation efficiencies (SFEs). A dotted line is a linear fitting of all the data except M82. M82 is clearly shifted from the linear correlation, which suggest that M82 has small dense gas but high SFE.

massive stars which have already exploded can explain the energy of the superbubble. In this stellar cluster, it is possible to merge stars to several hundred solar mass with runaway merger within the similar timescale of the superbubble, and it can be a middle mass black hole after an hypernova. Also, the mass of their compact remnants (stellar black holes) are enough higher than that of the middle mass black hole, so that if some of the stellar black holes can merge into one black hole, it would be a middle mass black hole. These results indicate that an intense starburst is possible to make a middle mass black hole, and give a new explanation of the formation of AGN and/or quasars.

SFEs estimated from free-free continuum emission and HCN/^{13}CO ratios in M82 show high values similar to other starburst galaxies, but HCN/^{12}CO ratios show lower values similar to post-starburst galaxies (figure 6.3). This result strongly suggests that M82 is in the very late phase of starburst or in the very early phase of post-starburst. Other literatures based on optical and infrared observations also suggest the similar result.

We proposed the evolution of the physical conditions of molecular gas with comparison between the starburst age derived from optical and infrared observations and the change in the molecular emission line intensity ratios (figure 6.4). First, the density of molecular gas gets high by the gravitational instability. According to the increment of molecular density, the star formation might occur, and the resultant supernova explosions heat the surrounding gas. The continuance of star formation and the successive

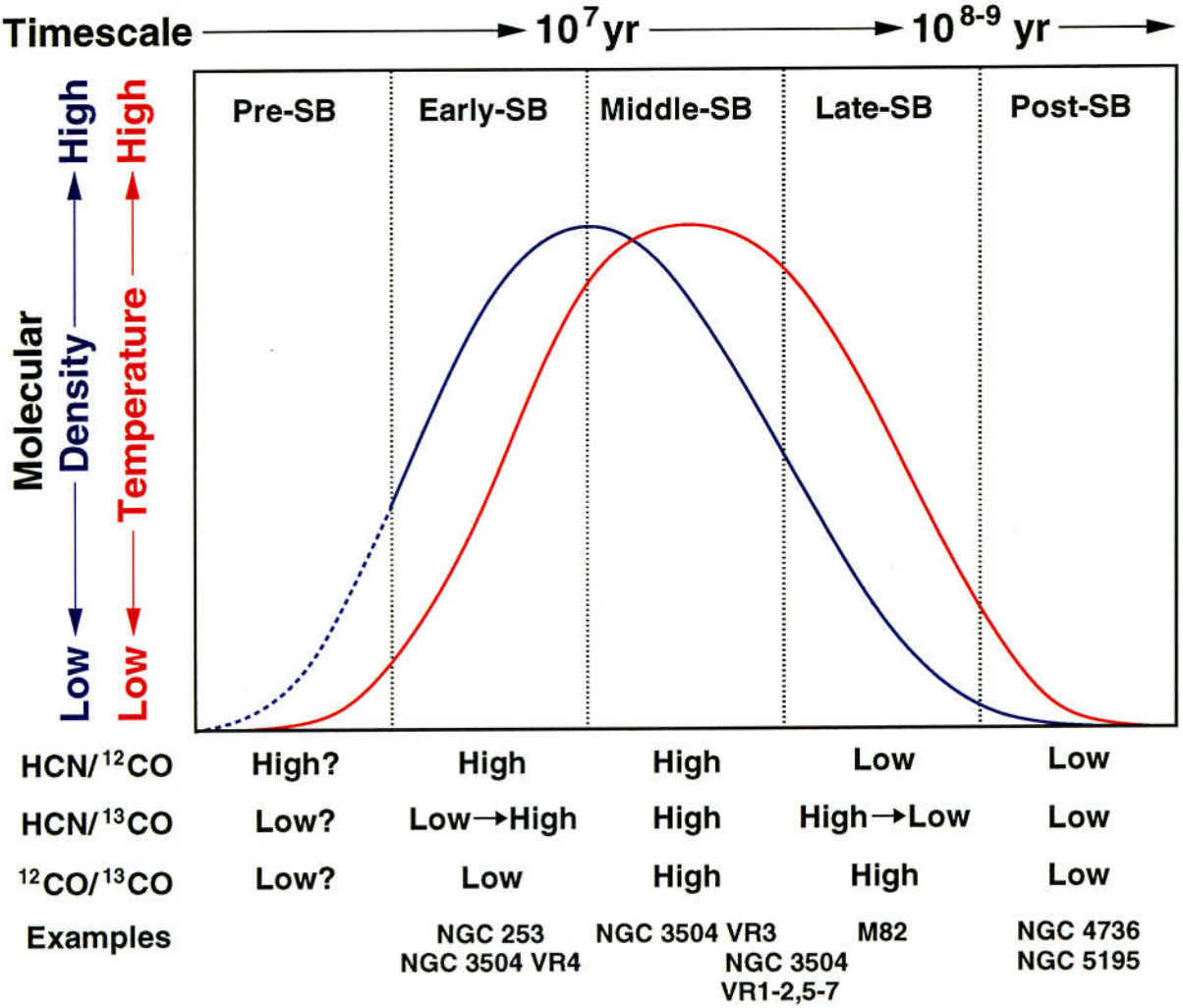

Fig. 6.4: The change of the HCN/^{12}CO, HCN/^{13}CO, and ^{12}CO/^{13}CO intensity ratios and the physical conditions of molecular gas according to the evolution of starburst. The examples of galaxies in each phase are also indicated.

supernovae might decrease the dense gas. Even all the dense gas would exhaust or blown out, however, there might still exist the massive stars and therefore the supernova explosions for a short time ($\sim 10^6 - 10^7$ yr), so the temperature of molecular gas might still high. Therefore, there might be a time offset between molecular gas density and temperature.

Using these results mentioned above, we propose a new view of starburst evolution, which is briefly shown in figure 6.5.

1. Dense gas might form by the gravitational instability (Kohno 1997). A starburst would start after the accumulation of dense molecular gas.

2. Vast amount of stars might form by the starburst, and dense molecular gas might exhaust according to the star formation.

3. Supernova explosions might occur at the end of the lifetime of massive stars. These explosions may heat up the surrounding molecular gas.

4. A large number of supernova explosions cause the blow out of dense molecular gas

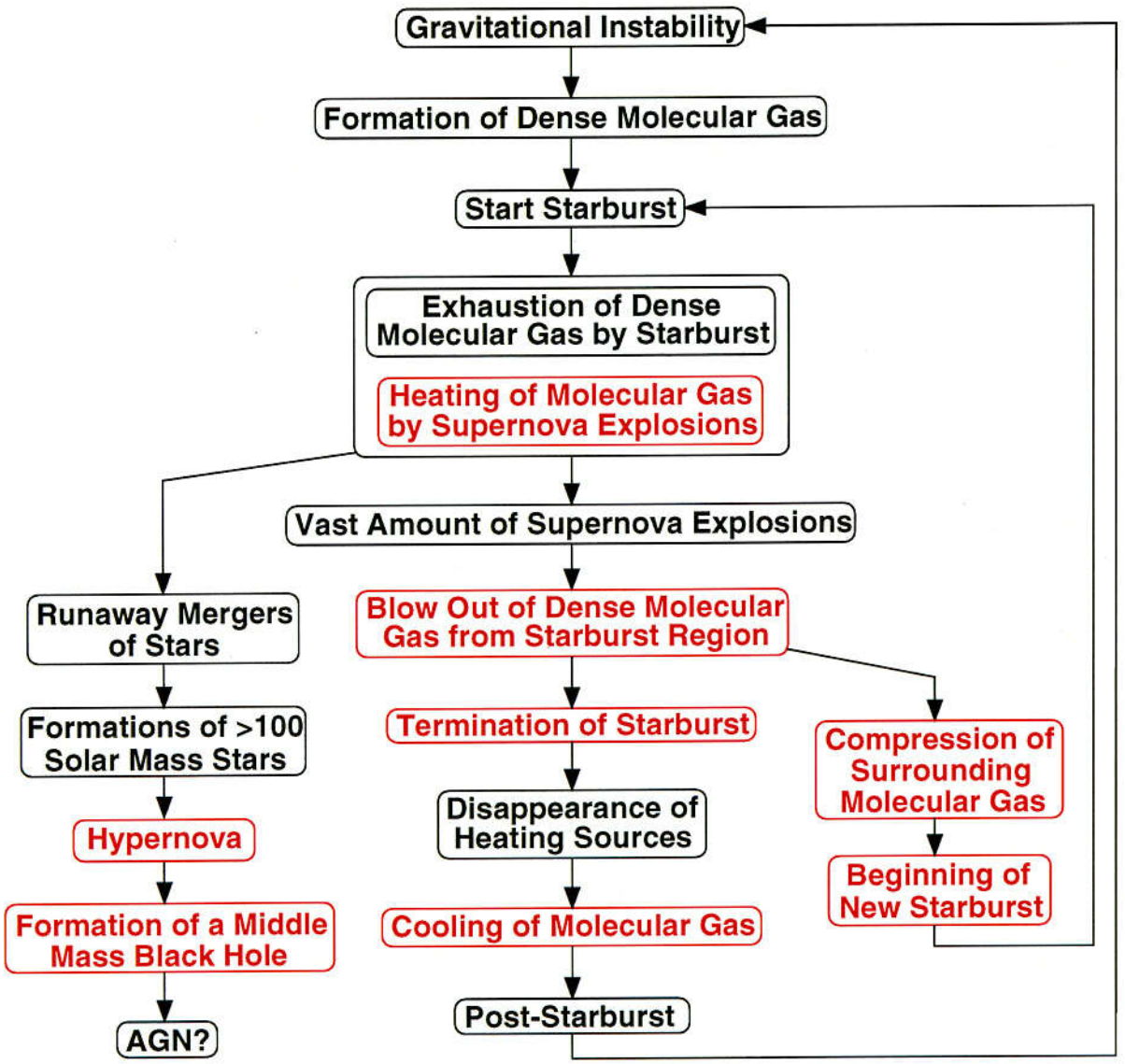

Fig. 6.5: The diagram of starburst evolution. Red sentences indicate the new features suggested by this work.

from the star burst region, and terminate the star formations.

5. After the termination of star formation, heating sources might decrease and disappear, molecular gas might cool down, and the galaxy might become a post-starburst galaxy.

Also, it is possible to merge stars to several hundred solar mass object in a dense star cluster, and the object might evolve to a middle mass black hole after the hypernova. This result also gives a new explanation of the formation of active galactic nuclei. Also, the blow out of molecular gas from starburst region would compress the surrounding molecular gas, and turn on the new star formation.

To summarize, this work mainly clarify the mechanisms about the heating of molecular gas, the termination of starburst, the formation of middle mass black hole, and sequential starburst.

Acknowledgements

First of all, I am most grateful to my supervisor Prof. Ryohei Kawabe for his helpful discussions, comments, and advice. He had introduced me to the exciting (but sometimes quite confusing) studies of starbursts and AGNs using multiple molecular lines.

I wish to thank Dr. Kotaro Kohno for his frank criticisms and encouragements. I also wish to thank Mr. Takeshi Kamazaki for his helpful discussions about the star forming regions in Our Galaxies and for providing me (and Nobeyama Radio Observatory) with useful softwares. I thank Dr. Sumio Ishizuki for teaching me all about the radio astronomy.

I gratefully acknowledge their valuable advice and comments with Profs. Y. Kobayashi, K. Makishima, K.-I. Morita, N. Nakai, M. Ohishi, S. Okumura, N. Ukita, and Drs. Y. Arikawa, R. Furuya, N. Kuno, H. Matsumoto, M. Momose, K. Nakanishi, K. Nishiyama, K. Sakamoto, S. Sakamoto, S. Shiki, K. Sorai, K. Sunada, T. Tosaki, T.G. Tsuru, and B. Vila-Vilaro.

Thanks are due to Drs. T. Umemoto and Y. Mikami for permission to use their results of molecular line observations on L1157. Thanks are also due to Dr. S. Takakuwa for providing me with the great LVG code.

I would like to thank Messrs. K. Handa, H. Iwashita, K. Nakajima, N. Satou, and T. Takahashi for their improvements and developments of Nobeyama Millimeter Array. I also thank all the staffs in Nobeyama Radio Observatory.

My special thanks are due to Dr. Justo Ossaka for introducing me to the wonderful world of astronomy and for his continuous encouragement. R.I.P.

I thank all the Hard Rock, Heavy Metal, and Industrial Rock/Metal artists who give me a lot of cool and hot music. Especially, Nine Inch Nails, PIG, KMFDM, Marilyn Manson, Rammstein, Guns'n'Roses, Black Sabbath, and Alice Cooper...You're great!!

Finally, I thank all my friends and my family for their supports and encouragement.

The author was financially supported by the Research Fellowships of the Japan Society for the Promotion of Science for Young Scientists.

References

REFERENCES

Aalto, S., Black, J.H., Booth, R.S., & Johansson, L.E.B., 1991, A&A, 247, 291

Aalto, S., Black, J.H., Johansson, L.E.B., & Booth, R.S. 1991, A&A, 249, 323

Aalto, S., Booth, R.S., Black, J.H., & Johansson, L.E.B., 1995, A&A, 300, 369

Aalto, S., Radford, S.J.E., Scoville, N.Z., & Sargent, A.I. 1997, ApJ, 475, L107

Achtermann, J.M., & Lacy, J.H. 1995, ApJ, 439, 163

Alonso-Herrero, A., Simpson, C., Ward, M.J., & Wilson, A.S. 1998, ApJ, 495, 196

Alton, P.B., Davies, J.J., & Bianchi, S. 1999, A&A, 343, 51

André, P. 1994, in The Cold Universe, ed T. Montmerle, C.J. Lada, I.F. Mirabel, J. Trân-Thanh-Vâna (Editions Frontières, France), p179

Arikawa, Y., Tatematsu, K., Sekimoto, Y., & Takahashi, T. 1999, PASJ, 51, L7

Bachiller, R. 1996, ARA&A, 34, 111

Bally, J., & Lada, C.J. 1983, ApJ, 265, 824

Bally, J., Stark, A.A., Wilson, R.W., & Henkel, C. 1988, ApJ, 324, 223

Bartel, N., Ratner, M.I., Rogers, A.E.E., Shapiro, I.I., Bonometti, R.J., Cohen N.L., Gorenstein, M.V., Marcaide, J.M., & Preston, R.A. 1987, ApJ, 323, 505

Barth, A.J., Ho, L.C., Filippenko, A.V., & Sargent, W.L.W. 1995, AJ, 110, 1009

Bash, F., Jaffe, D.T., & Wall, W.F. 1990, in Windows on Galaxies, ed G. Fabbiano, J.S. Gallagher, & A. Renzini (Kluwer, Netherland), p227

Baudry, A., & Brouillet, N. 1996, A&A, 316, 188

Beck, S.C., & Beckwith, S.V. 1984, MNRAS, 207, 671

Becklin, E.E., Beckwith, S., Gatley, I., Matthews, K., Neugebauer, G., Sarazin, C., & Werner, M.W. 1976, ApJ, 207, 770

Becklin, E.E., Gatley, I., Matthews, K., Neugebauer, G., Sellgren, K., Werner, M.W., & Wynn-Williams, C.G. 1980, ApJ, 236, 441

Binney, J., & Tremaine, S. 1987, Galactic Dynamics (Princeton University Press, Princeton)

Block, D.L., Elmegreen, B.G., Stockton, A., & Sauvage, M. 1997, ApJ, 486, L95

Boulade, O., Sauvage, M., Altieri, B., Blommaert, J., Gallais, P., Guest, S., Metcalfe, L., Okumura, K., et al. 1996, A&A, 315, L85

Boyce, P.J., Disney, M.J., Blades, J.C., Boksenberg, A., Crane, P., Deharveng, J.M., Macchetto, F.D., Mackay, C.D., & Sparks, W.B. 1996, ApJ, 473, 760

Boyce, P.J., Disney, M.J., Blades, J.C., Boksenberg, A., Crane, P., Deharveng, J.M., Macchetto, F.D., Mackay, C.D., & Sparks, W.B. 1998, MNRAS, 298, 121

Braine, J., & Hughes, D.H. 1999, A&A, 344, 779

Bregman, J.N., Schulman, E., & Tomisaka, K. 1995, ApJ, 439, 155

Bronfman, L., Bitran, M., & Thaddeus, P. 1988, in Molecular Clouds in the Milky Way and External Galaxies, ed R.L. Dickman, R.L. Snell, & J.S. Young (Springer, New York), p318

Brown, G.E., & Bethe, H.A. 1994, ApJ, 423, 659

Burton, M.G. 1987, in Supernova Remnants and the Interstellar Medium, IAU colloquium 101, ed R.S. Roger and T.L. Landecker (Dordrecht, Reidel), p399

Buta, R., & Crocker, D.A. 1991, AJ, 102, 1715

Canzian, B., Mundy, L.G., & Scoville, N.Z. 1988, ApJ, 333, 157

Cappi, M., Persic, M., Bassani, L., Franceschini, A., Hunt, L.K., Molendi, S., Palazzi, E., Palumbo, G.G.C., Rephaeli, Y., & Salucci, P. 1999, A&A, 350, 777

Carlstrom, J.E. 1988, in Galactic and Extragalactic Star Formation, ed R.E. Pudrits, & M. Fich, (Kluwer, Dordrecht), p571

Carlstrom, J.E., & Kromberg, P.P. 1991, ApJ, 366, 422

Casoli, F., Dupraz, C., & Combes, F. 1992, A&A, 264, 49

Casoli, F., Dupraz, C., & Combes, F. 1992, A&A, 264, 55

Chikada, Y., et al. 1987, Proc. IEEE, 75, 1203

Chini, R., Krügel, E., & Lemke, R. 1996, A&AS, 118, 47

Claussen, M.J., Marvel, K.B., Wooten, A., & Wilking, B.A. 1998, ApJ, 507, L79

Colbert, E.J.M., & Mushotzky, R.F. 1999, ApJ, 519, 89

Collura, A., Reale, F., Schulman, E., & Bregman, N. 1994, ApJ, 420, L63

Condon, J.J. 1992,ARA&A, 30, 575

Condon, J.J., Condon, M.A., Gisler, G., & Puschell, J.J. 1982, ApJ, 252, 102

Condon, J.J., Helou, G., Sanders, D.B., & Soifer, B.T. 1990, ApJS, 73, 359

Cox, P., Krügel, E., & Mezger, P.G. 1986, A&A, 155, 380

Crane, P.C., & van der Hulst, J.M. 1992, AJ, 103, 1146

DeNoyer, L.K. 1979, ApJ, 232, L165

DeNoyer, L.K., & Frerking, M.A. 1981, ApJ, 246, L37

Deul, E.R., & den Hartog, R.H. 1990, A&A, 229, 362

Devereux, N. 1989, ApJ, 346, 126

Devereux, N., Taniguchi, Y., Sanders, D.B., Nakai, N., & Young, J.S. 1994, AJ, 107, 2006

Dickman, R.L., Snell, R.L., Ziurys, L.M., & Huang, Y.L. 1992, ApJ, 400, 203

Dietrich, M., Appenzeller, I., Wagner, S.J., Gässler, W., Häfner, R., Hess, H.-J., Hummel, W., Muschielok, B., et al. 1999, A&A, 352, L1

Dietz, R.D., Smith, J., Hackwell, J.A., Gehrz, R.D., & Grasdalen, G.L. 1986, AJ, 91, 758

Downes, D., Radford, S.J.E., Guilloteau, S., Guélin, M., Greve, A., & Morris, D. 1992, A&A, 262, 424

Draine, B.T. 1989, in Infrared Spectroscopy in Astronomy, ed B.H. Kaldeich (ESTEC; Noordwijk), p93

Draine, B.T., & Lee, H.K. 1984, ApJ, 285, 89

Eckart, A.E., Downes, D., Genzel, R., Harris, A.I., Jaffe, D.T., & Wild, W. 1990, ApJ, 348, 434

Edwards, S., & Snell, R.L. 1982, ApJ, 261, 151

Edwards, S., & Snell, R.L. 1983, ApJ, 270, 605

Edwards, S., & Snell, R.L. 1984, ApJ, 281, 605

Ehle, M., Pietsch, W., & Beck, R. 1995, A&A, 295, 289

Elitzur, M. 1992, Astronomical Masers (Kluwer, Dordrecht)

Elmegreen, D.M., Chromey, F.R., Santos, M., & Marshall, D. 1997, AJ, 114, 1850

Elmegreen, D.M., Chromey, F.R., Sawyer, J.E., & Reinfeld, E.L. 1999, AJ, 118, 777

Engelbracht, C.W., Rieke, M.J., Rieke, G.H., Kelly, D.M., & Achtermann, J.M. 1998, ApJ, 505, 639

Engelbracht, C.W., Rieke, M.J., Rieke, G.H., & Latter, W.B. 1996, ApJ, 467, 227

Fabbiano, G. 1988, ApJ, 330, 672

Fabbiano, G., & Trinchieri, G. 1984, ApJ, 286, 491

Flower, D.R., & Launay, J.M. 1985, MNRAS, 214, 271

Ford, H.C., Crane, P.C., Jacoby, G.H., Lawrie, D.G., & van der Hulst, J.M. 1985, ApJ, 293, 132

Garcia-Burillo, S., Guélin, M., & Cernicharo, J. 1993, A&A, 274, 123

Gaume, R.A., & Mutel, R.L. 1987, ApJS, 65, 193

Gehrz, R.D., Sramek, R.A., & Weedman, D.W. 1983, ApJ, 267, 551

Goldader, J.D., Joseph, R.D., Doyon, R., & Sanders, D.B. 1997, ApJ, 474, 104

Goldreich, P., & Kwan, J. 1974, ApJ, 189, 441

Goldsmith, P.F. 1987, in Interstellar Process, ed. D.J. Hollenbach & H.A. Thronson (Reidel, Dordrecht), p51

Goldsmith, P.F., Snell, R.L., Hemeon-Heyer, M., & Langer, W.D. 1984, ApJ, 286, 599

González-Delgado, R.M., Pérez, E., Tadhunter, C., Vilchez, J.M., & Rondríguez-Espinosa, J.M. 1997, ApJS, 108, 155

Graf, U.U., Genzel, R., Harris, A.I., Hills, R.E., Russell, A.P.G., & Stutzki, J. 1990, ApJ, 358, L49

Greaves, J.S., & Holland, W.S. 1997, A&A, 327, 342

Green, S. 1993, ftp://ftp.giss.nasa.gov/pub/sgreen/astrophys/hcn_he_rates

Green, S., & Thaddeus, P. 1974, ApJ, 191, 653

Greenawalt, B., Walterbos, R.A.M., Thilker, D., & Hoopes, C.G. 1998, ApJ, 506, 135

Güsten, R., Serabyn, E., Kasemann, C., Schinckel, A., Schneider, G., Schulz, A., & Young, K. 1993, ApJ, 402, 537

Hamann, F., & Ferland, G. 1999, ARA&A, 37, in press

Harris, A.I., Hills, R.E., Stutzki, J., Graf, U.U., Russell, A.P.G., & Genzel, R. 1991, ApJ, 382, L75

Harrison, A., Henkel, C., & Russell, A. 1999, MNRAS, 303, 157

Helfer, T.T., & Blitz, L. 1993, ApJ, 419, 86

Helfer, T.T., & Blitz, L. 1995, ApJ, 450, 90

Helfer, T.T., & Blitz, L. 1997a, ApJ, 478, 162

Helfer, T.T., & Blitz, L. 1997b, ApJ, 478, 233

Helou, G. 1986, ApJ, 311, L33

Hildebrand, R.H. 1983, Quart. Jrn. Royal Astron. Soc., 24, 267

Ho, L.C., Filippenko, A.V., & Sargent, W.L.W. 1995, ApJS, 98, 477

Ho, L.C., Filippenko, A.V., & Sargent, W.L.W. 1997, ApJS, 112, 315

Hummel, E., van der Hulst, J.M., Keel, W.C., & Kennicutt Jr., R.C. 1987, A&AS, 70, 517

Hüttemeister, S., & Aalto, S. 1998, in The Physics and Chemistry of the Interstellar Medium, Proceedings of the 3rd Cologne-Zermatt Symposium, ed V. Ossenkopf, J. Stutzki, & G. Winnewisser (GCA-Verlag, Herdecke)

Irvine, W.M., Goldsmith, P.F., & Hjalmarson, A. 1987, in Interstellar Process, ed D.J. Hollenbach & H.A. Thronson (Reidel, Dordrecht), p585

Ishizuki, S. 1993, Ph.D. Thesis, University of Tokyo

Ishizuki, S., Kawabe, R., Ishiguro, M., Okumura, S.K., Morita, K.I., Chikada, Y., & Kasuga, T. 1990, Nature, 344, 224

Ishizuki, S., Kawabe, R., Ishiguro, M., Okumura, S.K., Morita, K.I., Chikada, Y., Kasuga, T., & Wright, M.C.H. 1991, in Dynamics of Galaxies and their Molecular Cloud Distributions, IAU Symp. 146, ed F. Combes & F. Casoli (Kluwer, Dordrecht), p272

Jackson, J.M., Heyer, M.H., Paglione, T.A.D., & Bolatto, A.D. 1996, ApJ, 456, L91

Jackson, J.M., Paglione, T.A.D., Carlstrom, J.E., & Nguyen-Q-Rieu 1995, ApJ, 438, 695

Jackson, J.M., Paglione, T.A.D., Ishizuki, S., & Nguyen-Q-Rieu 1993, ApJ, 418, L13

Johnston, K.J., Palmer, P., Wilson, T.L., & Beiging, J.H. 1983, ApJ, 271, L89

Jones, T.W., Rudnick, L., Jun, B.I., Borkowski, K.J., Dubner, G., Frail, D.A., Kang, H., Kassim, N.E., & McCray, R. 1998, PASP, 110, 125

Joy, M., Lester, D.F., & Harvey, P.M. 1987, ApJ, 319, 314

Jura, M., Hobbs, R.W., & Maran, S.P. 1978, AJ, 83, 153

Jura, M., & Kleinmann, S.G. 1989, ApJ, 341, 359

Kenney, J.D.P., Wilson, C.D., Scoville, N.Z., Devereux, N.A., & Young, J.S. 1992, ApJ, 395, L79

Kenney, J.D.P., Carlstrom, J.E., & Young, J.S. 1993, ApJ, 418, 687

Kennicutt, R.C. 1983, ApJ, 272, 54

Keto, E., Ball, R., Arens, J., Jernigan, G., Meixner, M., Skinner, C., & Graham, J. 1993, ApJ, 413, L23

Kikumoto, T., Taniguchi, Y., Nakai, N., Ishizuki, S., Matsushita, M., & Kawabe, R. 1998, PASJ, 50, 309

Kohno, K. 1997, Ph.D. Thesis, University of Tokyo

Kohno, K., Kawabe, R., Tosaki T., & Okumura S.K. 1996, ApJ, 461, L29

Kohno, K., Kawabe, R., & Vila-Vilaró, B. 1999, ApJ, 511, 157

Koo, B.C., & Moon, D.S. 1997, ApJ, 475, 194

Koo, B.C., & Moon, D.S. 1997, ApJ, 485, 263

Kronberg, P.P., Biermann, P., & Schwab, F.R. 1985, ApJ, 291, 693

Krügel, E., Chini, R., Klein, U., Lemke, R., Wielebinski, R., & Zylka, R. 1990, A&A, 240, 232

Kuno, N., & Matsuo, H. 1997, PASJ, 49, 265

Lada, E.A. 1992, ApJ, 393, L25

Lawrence, A. 1999, Advances in Space Research, 23, 1167

Lee, C. W. 1996, ApJS, 105, 129

Lehnert, M.D., & Heckman, T.M. 1996, ApJ, 462, 651

Lester D.F., Carr, J.S., Joy, M., & Gaffney, N. 1990, ApJ, 352, 544

Linke, R.A., Stark, A.A., & Frerking, M.A. 1981, ApJ, 243, 147

Lo, K.Y., Cheung, K.W., Masson, C.R., Phillips, T.G., Scott, S.L., & Woody, D.P. 1987, ApJ, 312, 574

Loiseau, N., Nakai, N., Sofue, Y., Wielebinski, R., Reuter, H.-P., & Klein, U. 1990, A&A, 228, 331

Lugten, J.B., Watson, D.M., Crawford, M.K., & Genzel, R. 1986, ApJ, 311, L51

Lynds, C.R., & Sandage, A.R. 1963, ApJ, 137, 1005

Magorrian, J., Tremaine, S., Richstone, D., Bender, R., Bower, G., Dressler, A., Faber, S.M., Gebhardt, K., et al. 1998, AJ, 115, 2285

Makishima, K., Ohashi, T., Kondo, H., Palumbo, G.G.C., & Trinchieri, G. 1990, ApJ, 365, 159

Maloney, P.R., Hollenbach, D.J., & Tielens, A.G.G.M. 1996, ApJ, 466, 561

Maoz, D., Filippenko, A.V., Ho, L.C., Rix, H.-W., Bahcall, J.N., Schneider, D.P., & Macchetto, F.D. 1995, ApJ, 440, 91

Matsumoto, H., & Tsuru, T.G. 1999, PASJ, 51, 321

Mauersberger, R., Henkel, C., & Sage, L.J. 1990, A&A, 236, 63

Mauersberger, R., Henkel, C., Walsh, W., & Schulz, A. 1999, A&A, 341, 256

McCall, M.L. 1989, AJ, 97, 1341

McCarthy, P.J., Heckman, T., & van Breugel, W. 1987, AJ, 92, 264

McKee, C.F., Storey, J.W.V., Watson, D.W., & Green, S. 1982, ApJ, 259, 647

McLeod, K.K., Rieke, G.H., Rieke, M.J., & Kelly, D.M. 1993, ApJ, 412, 111

Mészáros, P. 1999, Nature, 398, 368

Miller, G.E., & Scalo, J.M. 1979, ApJS, 41, 513

Muxlow, T.W.B., Pedlar, A., Wilkinson, P.N., Axon, D.J., Sanders, E.M., & de Bruyn, A.G. 1994, MNRAS, 266, 455

Nakai, N., Hayashi, M., Handa, T., Sofue, Y., & Hasegawa, T. 1987, PASJ, 39, 685

Nakai, N., Kuno, N., Handa, T., & Sofue, Y. 1994, PASJ, 46, 527

Neininger, N., Guélin, M., Klein, U., García-Burillo, S., & Wielebinski, R. 1998, A&A, 339, 737

Nguyen-Q-Rieu, Nakai, N., & Jackson, J.M. 1989, A&A, 220, 57

O'Connell, R.W., Gallagher III, J.S., Hunter, D.A., & Colley, W.N. 1995, ApJ, 446, L1

O'Connell, R.W., & Mangano, J.J. 1978, ApJ, 221, 62

Okumura, S.K., Momose, M., Kawaguchi, N., Kanzawa, T., Tsutsumi, T., Tanaka, A., Ichikawa, T., Suzuki, T., Ozeki, K., Natori, K., & Hashimoto, T. 2000, PASJ, 52, 393

Omodaka, T., Hayashi, M., Hasegawa, T, & Hayashi, S.S. 1994, ApJ, 430, 256

Paglione, T.A.D., Jackson, J.M., Ishizuki, S. 1997, ApJ, 484, 656

Paglione, T.A.D., Tosaki, T., & Jackson, J.M. 1995, ApJ, 454, L117

Palumbo, G.G.C., Fabbiano, G., Fransson, C., & Trinchieri, G. 1985, ApJ, 298, 259

Panagia, N. 1973, AJ, 78, 929

Papadopoulos, P.P., & Seaquist, E.R. 1999, ApJ, 516, 114

Pedler, A, Muxlow, T.W.B., Garrett, M.A., Diamond, P., Wills, K.A., Wilkinson, P.N., & Alef, W. 1999, MNRAS, 307, 761

Peng, R., Zhou, S., Whiteoak, J.B., Lo, K.Y., & Sutton, E.C. 1996, ApJ, 470, 821

Pickles, A.J. 1998, PASP, 110, 863

Planesas, P., Colina, L., & Pérez-Olea, D. 1997, A&A, 325, 81

Portegies Zwart, S.F., Makino, J., McMillan, S.L.W., & Hut, P. 1999, A&A, 348, 117

Pritchet, C. 1977, ApJS, 35, 397

Ptak, A., & Griffiths, R.E. 1999, ApJ, 517, L85

Puxley, P.J., Hawarden, T.G., & Mountain, C.M. 1988, MNRAS, 234, 29p

Puxley, P.J., Hawarden, T.G., & Mountain, C.M. 1990, ApJ, 364, 77

Puxley, P.J., Mountain, C.M., Brand, P.W.J.L., Moore, T.J.T., & Nakai. N. 1997, ApJ, 485, 143

Regan, M.W., & Vogel, S.N. 1995, ApJ, 452, L21

Reynaud, D., & Downes, D. 1999, A&A, 347, 37

Richer, J., Shepherd, D., Cabrit, S., Bachiller, R., & Churchwell, E. 2000, in Protostars and Planets IV, ed V. Mannings, A.P. Boss, & S.S. Russell (University of Arizona Press, Tucson), in press

Rieke, G.H. 1988, in Galactic and Extragalactic Star Formation, ed R.E. Pudrits, & M. Fich, (Kluwer, Dordrecht), p561

Rieke, G.H., & Lebofsky, M.J. 1978, ApJ, 220, L37

Rieke, G.H., & Lebofsky, M.J. 1979, ARA&A, 17, 477

Rieke, G.H., Lebofsky, M.J., Thompson, R.I., Low, F.J., & Tokunaga, A.T. 1980, 238, 24

Rieke, G.H., Lebofsky, M.J., & Walker, C.E. 1988, 325, 679

Rose, J.A., & Cecil, G. 1983, ApJ, 266, 531

Rose, J.A., & Searle, L. 1982, ApJ, 253, 556

Sage, L.J. 1989, ApJ, 344, 200

Sage, L.J. 1990, A&A, 239, 125

Sage, L.J., & Isbell, D.W. 1991, A&A, 247, 320

Saikia, D.J., Pedler, A., Unger, S.W., & Axon, D.J. 1994, MNRAS, 270, 46

Sakamoto, S. 1999, ApJ, 523, 701

Sakamoto, K., Okumura, S.K., Ishizuki, S., & Scoville, N.Z. 1999, ApJS, 124, 403

Salpeter, E.E. 1955, ApJ, 121, 161

Sandage, A., & Tammann, G.A. 1975, ApJ, 196, 313

Sanders, D.B., Scoville, N.Z., & Soifer, B.T. 1991, ApJ, 370, 158

Sauvage, M., Blommaert, J., Boulanger, F., Cesarsky, C.J., Cesarsky, D.A., Désert, F.X., Elbaz, D., Gallais, P., et al. 1996, A&A, 315, L89

Scoville, N.Z., Soifer, B.T., Neugebauer, G., Young, J.S., Matthews, K., & Yerka, J. 1985, ApJ, 289, 129

Scoville, N.Z., & Solomon, P.M. 1974, ApJ, 187, L67

Scoville, N.Z., Yun, M.S., Armus, L., & Ford, H. 1998, ApJ, 493, L63

Seaquist, E.R., Carlstrom, J.E., Bryant, P.M., & Bell, M.B. 1996, ApJ, 465, 691

Seaquist, E.R., Frayer, D.T., & Bell, M.B. 1998, ApJ, 507, 745

Seaquist, E.R., Frayer, D.T., & Frail, D.A. 1997, ApJ, 487, L131

Sérsic, J.L. 1973, PASP, 85, 103

Sérsic, J.L., & Pastoriza, M. 1965, PASP, 77, 287

Sérsic, J.L., & Pastoriza, M. 1967, PASP, 79, 152

Shen, J., & Lo, K.Y. 1995, ApJ, 445, L99

Shibatsuka, T., Matsushita, S., Kohno, K., & Kawabe, R. 2000, in Star Formation 1999, in press

Shioya, Y., Tosaki, T., Ohyama, Y., Murayama, T., Yamada, T., Ishizuki, S., & Taniguchi, Y. 1998, PASJ, 50, 317

Shopbell, P.L., & Bland-Hawthorn, J. 1998, ApJ, 493, 129

Smith, J. 1982, ApJ, 261, 463

Smith, P.A., Brand, P.W.J.L., Mountain, C.M., Puxley, P.J., & Nakai, N. 1991, MNRAS, 252, 6p

Snell, R.L., & Edwards, S. 1981, ApJ, 251, 103

Snell, R.L., Scoville, N.Z., Sanders, D.B., & Erickson, N.R. 1984, ApJ, 284, 176

Soifer, B.T., Houck, J.R., & Neugebauer, G. 1987, ARA&A, 25, 187

Solomon, P.M., Downes, D., & Radford, S.J.E. 1992, ApJ, 387, L55

Solomon, P.M., Huguenin, G.R., & Scoville, N.Z. 1981, ApJ, 245, L19

Solomon, P.M., Scoville, N.Z., & Sanders, D.B. 1979, ApJ, 232, L89

Sorai, K., Nakai, N., Kuno, N., Nishiyama, K., & Hasegawa, T. 2000, PASJ, 52, in press.

Sorai, K., Nakai, N., Kuno, N., Nishiyama, K., & Hasegawa, T. 2000, in preparation.

Suchkov, A., Allen, R.J., & Heckman, T.M. 1993, ApJ, 413, 542

Sunada, K., Kawabe, R., & Inatani, J. 1994, Int. J. Infrared Millimeter Waves, 14, 1251

Tacconi, L.J., Genzel, R., Blietz, M., Cameron, M., Harris, A.I., & Madden, S. 1994, ApJ, 426, L77

Tammann, G.A. & Sandage, A.R. 1968, ApJ, 151, 825

Taniguchi, Y., Ohyama, Y., Yamada, T., Mouri, H., & Yoshida, M. 1996, ApJ, 467, 215

Telesco, C.M. 1993, in Infrared Astronomy, ed A. Mampaso, M. Prieto, & F. Sánchez (Cambridge University Press, Cambridge), p173

Telesco, C.M., Campins, H., Joy, M., Dietz, K., & Decher, R. 1991, ApJ, 369, 135

Telesco, C.M., & Harper, D.A. 1980, ApJ, 235, 392

Telesco, C.M., Becklin, E.E., Wynn-Williams, C.G., & Harper, D.A. 1984, ApJ, 282, 427

Tenorio-Tagle, G., & Bodenheimer, P. 1988, ARA&A, 26, 145

Terashima, Y., Ptak, A., Fujimoto, R., Itoh, M., Kunieda, H., Makishima, K., & Serlemitsos, P.J. 1998, ApJ, 496, 210

Terlevich, R., Tenorio-Tagle, G., Franco, J., & Melnick, J. 1992, MNRAS, 255, 713

Tilanus, R.P.J., Tacconi, L.J., Sutton, E.C., Zhou, S., Sanders, D.B., Williams, C.G., Lo, K.Y., & Stephens, S.A. 1991, ApJ, 376, 500

Tomisaka, K., & Ikeuchi, S. 1988, ApJ, 330, 695

Tosaki, T., & Shioya, Y. 1997, ApJ, 484, 664

Tully, R.B. 1974, ApJS, 27, 437

Tully, R.B. 1988, Nearby Glalaxies Catalog (Cambridge University Press, Cambridge)

Turner, J.L., & Ho, P.T.P. 1983, ApJ, 268, L79

Turner, J.L., & Ho, P.T.P. 1994, ApJ, 421, 122

Turner, J.L., & Hurt, R.L. 1992, ApJ, 384, 72

Ulich, B.L., & Haas, R.W. 1976, ApJS, 30, 247

Ulvestad, J.S., & Antonucci, R.R. 1997, ApJ, 488, 621

Umemoto, T., Iwata, T., Fukui, Y., Mikami, H., Yamamoto, S., Kameya, O., & Hirano, N. 1992, ApJ, 392, L83

Uyama, K., Matsumoto, T., & Thomas, J.A. 1984, PASJ, 36, 477

van Dishoeck, E.F., Jansen, D.J., Phillips, T.G. 1993, 279, 541

Walker, C.E., Lebofsky, M.J., & Rieke, G.H. 1988, ApJ, 325, 687

Wall, W.F., Jaffe, D.T., Israel, F.P., & Bash, F.N. 1991, ApJ, 380, 384

Wall, W.F., Jaffe, D.T., Bash, F.N., Israel, F.P., Maloney, P.R., & Baas, F. 1993, ApJ, 414, 98

Warner, J.W. 1974, ApJ, 190, 19

Watson, M.G., Stanger, V., Griffiths, R.E. 1984, ApJ, 286, 144

Weedman, D.W. 1987, in Star Formation in Galaxies, NASA Conference Publication 2466, ed C.J. Lonsdale Persson (NASA, Washington), p351

Weiβ, A., Walter, F., Neininger, N., & Klein, U. 1999, A&A, 345, L23

Weiler, K.W., & Sramek, R.A. 1988, ARA&A, 26, 295

Weliachew, L., Fomalont, E.B., & Greisen, E.W. 1984, A&A, 137, 335

White, G.J., Rainey, R., Hayashi, S.S., & Kaifu, N. 1987, A&A, 173, 337

Wild, W., Harris, A.I., Eckart, A., Genzel, R., Graf, U.U., Jackson, J.M., Russell, A.P.G., & Stutzki, J. 1992, A&A, 265, 447

Wilkinson, P.N., & de Bruyn, A.G. 1990, MNRAS, 242, 529

Wills, K.A., Pedlar, A., Muxlow, T.W.B., & Wilkinson, P.N. 1997, MNRAS, 291, 517

Wills, K.A., Redman, M.P., Muxlow, T.W.B., & Pedlar, A. 1999, MNRAS, 309, 395

Wilson, A.S., & Ulvestad, J.S. 1982, ApJ, 263, 576

Wilson, T.L., & Rood, R.T. 1994, ARA&A, 32, 191

Wozniak, H., Friedli, D., Martinet, L., Martin, P., & Bratschi, P. 1995, A&AS, 111, 115

Wright, M.C.H., Ishizuki, S., Turner, J.L., Ho, P.T.P., & Lo, K.Y. 1993, ApJ, 406, 470

Wright, M.C.H., Plambeck, R.L., & Wilner, D.J. 1996, ApJ, 469, 216

Wynn-Williams, C.G., & Becklin, E.E. 1985, ApJ, 290, 108

Wynn-Williams, C.G., & Becklin, E.E., Matthews, K., & Neugebauer, G. 1979, MNRAS, 189, 163

Young, J.S. 1987, in Star Formation in Galaxies, NASA Conference Publication 2466, ed C.J. Lonsdale Persson (NASA, Washington), p197

Young, J.S., Allen, L.E., Kenney, J.D.P., Lesser, A., & Rownd, B.K. 1996, AJ, 112, 1903

Young, J.S., & Devereux, N.A. 1991, ApJ, 373, 414

Young, J.S., & Sanders, D.B. 1986, ApJ, 302, 680

Young, J.S., & Scoville, N.Z., 1984, ApJ, 287, 153

Young, J.S., Xie, S., Tacconi, L., Knezek, P., Viscuso, P., Tacconi-Garman, L., Scoville, N., Schneider, S., et al. 1995, ApJS, 98, 219

Ziurys, L.M., Snell, R.L., & Dickman, R.L. 1989, ApJ, 341, 857